RESEARCH ONLINE

University of Wollongong
Research Online

University of Wollongong Thesis Collection

University of Wollongong Thesis Collections

2011

Advanced materials For lithium rechargeable battery

Nurul Hayati Idris
University of Wollongong

Recommended Citation

Idris, Nurul Hayati, Advanced materials For lithium rechargeable battery, Doctor of Philosophy thesis, Faculty of Engineering, University of Wollongong, 2011. http://ro.uow.edu.au/theses/3492

Research Online is the open access institutional repository for the University of Wollongong. For further information contact Manager Repository Services: morgan@uow.edu.au.

RESEARCH ONLINE

UNIVERSITY OF WOLLONGONG

COPYRIGHT WARNING

You may print or download ONE copy of this document for the purpose of your own research or study. The University does not authorise you to copy, communicate or otherwise make available electronically to any other person any copyright material contained on this site. You are reminded of the following:

Copyright owners are entitled to take legal action against persons who infringe their copyright. A reproduction of material that is protected by copyright may be a copyright infringement. A court may impose penalties and award damages in relation to offences and infringements relating to copyright material. Higher penalties may apply, and higher damages may be awarded, for offences and infringements involving the conversion of material into digital or electronic form.

Advanced Materials For Lithium Rechargeable Battery

A thesis submitted in fulfilment of the requirements

for the award of the degree

Doctor of Philosophy

from

University of Wollongong

by

Nurul Hayati Idris

B.Sc. (Hons.), M. Sc

Institute for Superconducting and Electronic Materials

Faculty of Engineering

2011

Declaration

I, Nurul Hayati Idris, declare that the work presented in this thesis is original and was carried out at the Institute for Superconducting and Electronic Materials, Faculty of Engineering, University of Wollongong, New South Wales, Australia. This thesis is wholly my own work and contains no work previously published or written by another person, unless otherwise acknowledged and referenced. This work is original and has not been submitted to qualify for any other degree elsewhere.

Nurul Hayati Idris

Acknowledgements

I thank God for His blessings and mercy.

I would like to express my deepest gratitude to my supervisors, Prof. Hua-Kun Liu and Dr. Jia-Zhao Wang, for their invaluable advice and supervision throughout this research work. Thanks for providing me with the guidance and encouragement to finish this thesis.

The technical assistance at ISEM has been invaluable and I wish to express my gratitude to people at the University of Wollongong, such as Dr. David Wexler (TEM), Dr. Zhixin Chen (TEM), Dr. Konstantin Konstatinov (TGA, DSC, BET), Mr. Darren Attard (SEM, FESEM), Dr. Germanas Peleckis (XRD), Mr. Ron Kinnell, and Mr. Robert Morgan (mechanical workshop), and also particularly to Dr. Tania Silver for critical reading and correction of my manuscripts and thesis.

I would like to thank the Malaysian Government, especially the Ministry of Higher Education Malaysia for the scholarship support to pursue my doctoral studies at the University of Wollongong. I am also grateful to Universiti Malaysia Terengganu for granting me study leave and a generous stipend for my family.

I would also like to thank my friends from the Institute for Superconducting and Electronic Materials: Dr. Shulei Chou, Dr. Md. Mokhlesur Rahman, Dr. Mohd Faiz Hassan, Mr. Chao Zhong, Ms. Lu Lin, Ms. Xuanwen Gao, Mr. Lukman Noerochim,

Mr. Guodong Du, and Mr. Ivan Seng for helping me and giving me some ideas during the period of this research.

Last but not least, my deepest appreciation also goes to my husband and close companion, Mohammad Ismail, and my daughter, Anis Zahirah, for their love, encouragement, patience, and moral support, which were essential for the completion of my studies. Thank you for being there!

Abstract

Due to the rapid increase in the use of portable computers, mobile phones, and electric vehicles, there is an increasing demand for larger capacity, smaller size, lighter weight and lower priced rechargeable batteries. Lithium ion battery technology offers the highest energy densities by weight of all the commercial rechargeable battery technologies, with high voltage, long cycle life, and a wide environmental operation range. Commercial lithium ion battery electrodes today contain expensive and hazardous cathode (lithium cobalt oxide) and low specific capacity anode (carbonaceous materials). It is desirable to replace these materials with potentially cheaper, less toxic materials that have high specific capacity. In this doctoral work, several nanostructured materials and nanocomposites were examined and characterized as potential electrode material in lithium storage applications. In an attempt to improve the performance of nickel oxide (NiO), NiO-polypyrrole (PPy) and NiO-graphene nanocomposite were prepared and investigated as possible anode materials. Meanwhile, several cathode materials were studied: LiV_3O_8/carbon nanocomposite and nickel sulfide (NiS). The superior performance of poly(vinylidene fluoride)/poly(methyl methacrylate) (PVDF/PMMA) gel polymer electrolyte in lithium-polymer batteries was also demonstrated.

NiO-PPy nanocomposites for lithium-ion batteries were prepared by a chemical polymerization method, with sodium *p*-toluenesulfonate as the dopant, Triton X-100 as the surfactant, and $FeCl_3$ as the oxidant. The new composite material was characterized by Raman spectroscopy, thermogravimetric analysis (TGA), scanning electron

microscopy (SEM), and field-emission scanning electron microscopy (FESEM). Nanosize conducting PPy particles with a cauliflower-like morphology were uniformly coated onto the surface of the NiO powder. The electrochemical results were improved for the NiO-PPy composite compared with the pristine NiO. After 30 cycles, the capacities of the NiO and the NiO-PPy composite were about 119 and 436 mAh g^{-1}, respectively, indicating that the electrochemical performance of the composite was significantly improved.

Graphene–metal-oxide composites as anode materials for Li-ion batteries have been investigated extensively, but these attempts have been mostly limited to moderate rate charge-discharge applications. Here, NiO-graphene nanostructures have been synthesized using a controlled hydrothermal method, which enables in situ formation of NiO with a coralloid nanostructure on graphene. Graphene/NiO (20%), graphene/NiO (50%), and pure NiO show stable discharge capacities of 185 mAh g^{-1} at 20 C (1 C = 300 mA g^{-1}), 450 mAh g^{-1} at 1 C, and 400 mAh g^{-1} at 1 C, respectively. High rate capability and good stability in prolonged charge-discharge cycling permit the application of this material in fast charging batteries for upcoming electric vehicles. To the best of our knowledge, such fast rate performance of graphene/metal oxide composite as anode and such stability for pure NiO as anode have not been reported previously.

To improve the rate capability and cyclability of LiV_3O_8 cathode for Li-ion batteries, LiV_3O_8 was modified by forming LiV_3O_8/carbon nanosheet composite. LiV_3O_8/carbon nanosheet composite was successfully achieved *via* a hydrothermal route followed by a carbon coating process. The morphology and structural properties of the samples were

investigated by X-ray diffraction (XRD), TGA, SEM, and transmission electron microscopy (TEM). TEM observations demonstrated that the LiV_3O_8/carbon composite has a very flat sheet-like morphology, with each nanosheet having a smooth surface and a typical length of 400-700 nm, width of 200-350 nm, and thickness of 10-50 nm. Each sheet is surrounded by a thick layer of amorphous carbon. Electrochemical tests showed that the LiV_3O_8/carbon composite cathode features long-term cycling stability (194 mAh g^{-1} at 0.2 C after 100 cycles) and excellent rate capability (110 mAh g^{-1} at 5 C, 104 mAh g^{-1} at 10 C, and 82 mAh g^{-1} at 20 C after 250 cycles). Electrochemical impedance spectra (EIS) indicated that the LiV_3O_8/carbon composite electrode has very low charge-transfer resistance compared with pristine LiV_3O_8, indicating the enhanced ionic conductivity of the LiV_3O_8/carbon composite. The enhanced cycling stability is attributed to the fact that the LiV_3O_8/carbon composite can prevent the aggregation of active materials, accommodate the large volume variation, and maintain good electronic contact.

To reduce the reaction time, electrical energy consumption, and cost, binary α-NiS-β-NiS has been synthesized by a rapid, one-pot, hydrothermal autoclave microwave method within 15 minutes at temperatures of 160-180 ^oC. The microstructure and morphology of the α-NiS-β-NiS products were characterized by means of XRD, FESEM, and TEM. At 140 °C, pure hexagonal NiAs-type α-NiS phase was identified from the XRD patterns. With increasing reaction temperature (160-180 ^oC), the XRD evidence indicates that an increasing fraction of rhombohedral millerite-like β-NiS is formed as a secondary phase. The α-NiS-β-NiS sample synthesized at 160 ^oC yielded good electrochemical performance in terms of high reversible capacity (320 mAh g^{-1} at 0.1 C up to 100 cycles). Even at high rates, the sample operated at a good fraction of its

capacity. The most likely contributing factor to the superior electrochemical performance of the α-NiS-β-NiS sample could be the improved morphology. TEM imaging confirmed that needle-like protrusions connect the clusters of α-NiS particles, and the individual protrusions indicated a very high surface area including folded sheet morphology, which helps to dissipate the surface accumulation of Li^+ ions and facilitate rapid mobility. These factors help to enhance the amount of lithium intercalated within the material.

Microporous PVDF/PMMA membranes were prepared using the phase-separation method. Then, the membranes were immersed in liquid electrolyte to form polymer electrolytes. The effects of PMMA on the morphology, degree of crystallinity, porosity, and electrolyte uptake of the PVDF membrane were studied. The addition of PMMA increased the pore size, porosity, and electrolyte uptake of the PVDF membrane, which, in turn, increased the ionic conductivity of the polymer electrolyte. The maximum ionic conductivity at room temperature was 1.21×10^{-3} S cm^{-1} for Sample E70. The polymer electrolyte was investigated, along with lithium iron phosphate ($LiFePO_4$) as cathode for all solid-state lithium-ion rechargeable batteries. The lithium metal/E70/$LiFePO_4$ cell yielded a stable discharge capacity of 133 mAh g^{-1} after up to 50 cycles at a current density of 8.5 mA g^{-1}.

Table of contents

List of figures

List of tables

Chapter 1

Introduction

1.1 General background

There are significant concerns about the rising level of CO_2 emissions, as human activities are responsible for large impacts on the environment. The main source of the increase in CO_2 is from increasing energy demands. It is now accepted that global warming, climate change, finite fossil-fuel supplies, and emissions of greenhouse gases constitute a serious threat to the environment worldwide. Being aware of these problems, industrialized countries are examining a whole range of new policies and technology issues to make their energy futures 'sustainable'. That is, to maintain economic growth whilst providing energy security and environmental protection. For a sustainable future, energy storage technologies are expected to offer improved energy and power densities; ideally, they should also be reliable and safe, flexible in use, affordable, and limitless. Current concerns about limited energy resources have brought about the need to consider renewable energies on a large scale together with the widespread use of hybrid and electric vehicles. In this respect, lithium-ion battery technology is considered to be a mature technology with a long history of large-scale commercial applications. Applications of lithium-ion batteries have been diversified from mobile devices such as cell phones and laptop computers to electric vehicles, power tools, and stationary energy storage. Furthermore, the markets for lithium-ion batteries are likely to increase in the years ahead, as the major automobile

manufacturers are working towards electric and hybrid electric vehicles [1]. However, research to meet the application requirements is still an urgent need [2]. Table 1.1 shows the performance characteristics of some secondary battery types [3].

Table 1.1 Comparison of the performance characteristics of secondary batteries [3].

Battery type	**Nominal voltage**	**Specific energy**		**Volumetric energy**	
	(V)	**Wh kg^{-1}**	**kJ kg^{-1}**	**Wh l^{-1}**	**kJ l^{-1}**
Pb-acid	2	35	126	70	252
Ni-Cd	1.2	40	144	100	360
Ni-MH	1.2	90	324	245	882
Ag-Zn	1.5	110	396	220	792
Li-ion	3.6	125	450	440	1584

The environmental awareness and demand for high energy density have led to the popularity of lithium-ion batteries, which have gradually become an alternative power source to traditional lead-acid and Ni-Cd batteries [4]. The lithium-ion battery is a forerunner and market leader in the energy storage category due to the following outstanding properties [5]:

1) high energy in terms of gravimetric energy density and volumetric energy density;
2) high average operating voltage (3.6 V);
3) acceptably low self-discharge on standing (<10% per month);
4) no memory effect

5) easy determination of remaining capacity by virtue of having a sloping discharge curve;
6) much safer than equivalent cells which use lithium metal;
7) rapid recharging within just 2 to 3 hours;
8) stable to over 500 cycles with operation under a wide range of environmental conditions.

Although the lithium-ion battery has historically been the leading technology, Li-ion batteries are still constantly criticized for their performance due to the user's unconditional demands. Their large scale application is still limited by several barriers, including reliability, longevity, safety, and cost concerns [6-8]. An intensive quest is continuing in the search for new and improved materials for all lithium-ion battery components, including the cathode, anode, and electrolyte.

1.2 Statement of problem

1.2.1 Cathode materials

The cathode material is the main focus of enthusiastic research in the field of lithium-ion batteries. According to Whittingham [9], the most important characteristics required for cathode materials are briefly described below.

1) The material should contain a readily reducible or oxidizable ion such as a transition metal ion;
2) The material must react reversibly with lithium, with no structural changes during intercalation/de-intercalation;

3) The material must react with a high free energy of reaction for high voltage;
4) The material should react with lithium quickly on both lithium insertion and removal to give high power;
5) The material should be a good electronic conductor to alleviate the need for a conductive additive; and
6) The material should be low cost and environmentally benign.

The positive electrode material largely contributes to factors such as toxicity, costs, thermal safety, energy density, and power density. The majority of lithium-ion batteries on the market today utilize lithium cobalt oxide ($LiCoO_2$) as the positive electrode material [10]. $LiCoO_2$ forms the α-$NaFeO_2$ structure, which is a distorted rock-salt structure where the cations order in alternating (111) planes. This ordering results in a trigonal structure ($R\bar{3}m$) and, for $LiCoO_2$, planes of lithium ions through which lithiation and delithiation can occur [11]. Although it offers good electrical performance and is easily prepared, the relatively high cost of cobalt and concerns about the thermal safety and toxicity of $LiCoO_2$ have led to the development of other alternate materials. Another promising cathode material is spinel lithium manganese oxide ($LiMn_2O_4$), which forms a spinel structure ($Fd\bar{3}m$), in which manganese occupies the octahedral sites and lithium predominantly occupies the tetrahedral sites [12]. The paths for lithiation and delithiation are a 3-dimensional network of channels rather than planes, as in the α-$NaFeO_2$ structure. In spite of the fact that $LiMn_2O_4$ is low cost and safer than $LiCoO_2$, its capacity fading, Mn dissolution at high temperature, and poor high-rate capability remain severe problems [13]. Lithium iron phosphate ($LiFePO_4$), which is a compound with olivine-type (*Pnma*) structure, has received much attention owing to its potential use as cathode material because of its low cost, abundance, low toxicity, and

high theoretical capacity of 170 mAh g^{-1} [14]. However, the widespread use of $LiFePO_4$ as cathode has been hindered by its low tap density, high processing costs, and poor rate capacity [1, 15]. Although transition metal oxides based on α-$NaFeO_2$, spinel, and olivine structures have shown promising features, improvements are still needed to reduce cost and extend the lifetime.

1.2.2 Anode materials

Carbon materials such as disordered carbon [16, 17], hierarchically porous carbon monoliths [18], and acid treated graphite [19] are widely used as anode active materials for rechargeable lithium batteries. Although these materials offer a long cycle life, abundant material supply, and relatively low cost [20], the storage capacity and the rate performance still need to be improved. In addition, the lithium storage capacity in graphite is limited to 372 mAh g^{-1}, corresponding to a stoichiometric LiC_6 composition [18]. Thus, much effort has been focused in developing alternative materials with low irreversible capacity, high energy density, and long cycle life [21]. Alloy anodes (for examples, silicon (Si) and tin (Sn)) [22-24] have shown high capacity values, but generally suffer from low coulombic efficiencies (less than 60%) on the first few cycles [25]. This irreversibility could be attributed to (a) a loss of active material, (b) solid-electrolyte interface (SEI) formation, (c) Li trapping in the host alloy, (d) reaction with oxide impurities, and (e) the aggregation of active particles [20]. Recently, transition-metal oxides have shown a number of desirable properties, such as high theoretical capacity (500-1000 mAh g^{-1}), based on a novel conversion mechanism [26]. The main challenge for the implementation of transition-metal oxide anodes is their low electronic

conductivity and poor cycling performance due to the large volume changes during repeated lithium uptake and removal reactions [27-29].

1.2.3 Electrolyte

Nowadays, lithium batteries use electrolytes containing $LiPF_6$ salt dissolved in a mixed carbonate solvent, which is unsafe due to the use of flammable organic electrolyte, poor thermal stability of the cathode electrolyte interphase, and the formation of lithium dendrites. $LiPF_6$ is believed to be the main cause for poor performance of lithium-ion batteries at high temperature, while the high viscosity of ethylene carbonate limits use to above -20°C in low temperature application [30]. According to Goodenough and Kim [31], the ideal electrolyte should offers:

1) Retention of the electrode/electrolyte interface during cycling when the electrode particles are changing their volume.
2) Lithium-ion conductivity of more than 10^{-4} S cm^{-1} over the temperature range of battery operation.
3) Chemical stability over the ambient temperature range.
4) Chemical stability with respect to the electrode.
5) Safe materials, low toxicity, and low cost.

Room-temperature ionic liquids (RTILs) [32-34] have been considered as alternative electrolytes for lithium-ion batteries due to advantages such as high oxidation potential (~ 5.3 V vs. Li^+/Li^0), non-flammability, a low vapor pressure, high boiling points, and a high Li-salt solubility. However, the high viscosity of these ionic liquids reduces their

Li-ion conductivity. Rechargeable lithium cells which use solid polymer electrolytes (SPE) are considered to have a safety advantage over the organic and inorganic liquid electrolytes because of their lower reactivity with lithium and the absence of a volatile, and sometimes flammable, organic solvent. Since the polymers are light and non-combustible materials, they can be fabricated to any required size and shape. These properties allow the batteries to be fabricated in a wide range of designs [35].

1.3 Importance of study

There is an urgent need to develop new materials for lithium-ion batteries that can offer increased capacity, safety, energy, and power density, as well as compatibility with the environment. The strategies for research are the replacement of (1) graphite with alternative, higher capacity anode materials, (2) $LiCoO_2$ with lower cost and more environmentally benign cathode materials, and (3) the organic liquid electrolyte with a more reliable polymer electrolyte [36]. Exploration of nanomaterials and nanocomposites is vital to overcome these problems. The advantages associated with the usage of nanomaterials and nanocomposites include [37]:

1) better accommodation of the strain of lithium insertion/removal,
2) higher electrode/electrolyte contact area, leading to higher charge/discharge rates,
3) short path lengths for electronic transport, hence permitting operation with low electronic conductivity or at higher power and,
4) short path lengths for Li-ion transport.

Finally, properly designed nanocomposite electrodes with nanostructures may maximize the advantages while minimizing the problems associated with each component in lithium-ion batteries, hence offering higher energy and power densities and longer cycling lifetimes.

1.4 Objectives and scope of research

In order to address the some of the issues mentioned above, it is necessary to explore the effects of nanomaterials as cathode and anode in lithium-ion batteries. From the perspective of the use of nanoparticles/nanostructured materials as potential candidate electrode materials, this PhD work is aimed toward the improvement of cell performance, in terms of specific capacities and rate capabilities. The scope of this research is to synthesize nanostructured/nanocomposite cathode and anode materials, with the emphasis on understanding structural, morphological, and electrochemical changes.

Meanwhile, presentation of the research reported in this doctoral thesis will be structured as follows:

1) A thorough literature review of current state-of-the-art lithium-ion batteries is presented in Chapter 2, especially as it relates to the role of nanostuctured/composite electrode materials and possible techniques for the synthesis of those materials.

2) The overall experimental method for the anode, cathode, and gel polymer electrolyte preparation, the fabrication of cells, their characterization, and electrochemical measurements are explained in Chapter 3.
3) Synthesis of the nanostructured/composite electrode materials through different techniques, including spray pyrolysis (Chapter 4), the hydrothermal method (Chapters 5 and 6), and the hydrothermal autoclave microwave approach (Chapter 7). Preparation of gel polymer electrolytes using the phase-separation method is presented in Chapter 8.
4) As a means to accomplish the objectives in addressing the issues above, investigation of the structural and physical properties of the synthesized nanostuctured/composite materials was pursued by methods including X-ray diffraction (XRD), Raman spectroscopy, Brunauer-Emmett-Teller (BET) specific surface area measurements, attenuated total reflectance-Fourier transform infrared (ATR-FTIR) spectroscopy, differential scanning calorimetry (DSC), thermogravimetric analysis (TGA), scanning electron microscopy (SEM), field-emission scanning electron microscopy (FESEM), transmission electron microscopy (TEM), selected area electron diffraction (SAED), and energy dispersive spectroscopy (EDS).
5) The electrochemical performance of the synthesized electrode materials was investigated by cyclic voltammetry (CV), galvanostatic charge-discharge cycling, and electrochemical impedance spectroscopy (EIS).
6) Finally, the main results and achievements of this doctoral thesis are summarized in Chapter 9, followed by the list of references, a list of acronyms, and a list of publications during the period of this study.

Chapter 2

Literature Review

2.1 General backgrounds

Electrical energy is important in our daily lives, and it can universally be easily converted into light, heat, or mechanical energy. However, the main problem is that electrical energy is very difficult to store. Capacitors, for example, can allow its direct storage; however, the quantities are small when compared with the demands of most applications. In general, the storage of electrical energy requires its conversion into another form of energy. In batteries, the energy of chemical compounds acts as the storage medium, and during discharge, a chemical reaction occurs that generates energy, which can be drawn from the battery in form of electric current at a certain voltage [38]. There are a few battery systems that can reverse this process and be recharged. Therefore, battery systems can be classified into two broad categories: (1) primary batteries, which are designed to convert their chemical energy into electrical energy only once, and (2) secondary batteries, which may be recharged and used again. Before entering the topic in detail, it is necessary to gain important historical knowledge on inventions and developments in batteries up to the latest battery technology.

The earliest electrochemical energy storage system which may have served as a battery is known as Baghdad battery, which was invented between 250 BC and 640 AD [39, 40]. The next significant step in the development of batteries was the invention of the

voltaic pile by Alessandro Volta in 1799. It consisted of a pile of alternate silver (or brass or copper) and zinc (or tin) discs, with each pair of dissimilar metals separated from the next by a piece of cloth which was saturated with brine. One end of the pile terminated in a silver disc and the other in a zinc disc. A continuous current of electricity was produced as the two were connected by a wire conductor [41]. A subsequent major advance was made by John Daniell, who invented the Daniell cell in 1836. Daniell cells were adopted by commercial telegraphic systems following a rapid expansion of such services in the early 1850s [42]. In 1866, Georges Leclanche invented a primary cell that consisted of a zinc rod as the negative electrode and a carbon rod as the positive electrode. Both electrodes were immersed in a solution of ammonium chloride in a glass jar. The cell, which has been extensively developed ever since, gives a voltage of 1.5 V [43]. The first secondary cell, with an output of 2 V, was demonstrated by Gaston Plantè in 1859. This 'lead-acid battery' consisted of two concentric spirals of lead sheet, separated by porous cloth and immersed in dilute sulfuric acid within a cylindrical glass vessel. When it discharged and charged, the chemical reactions at the surface of the plates resulted in the gradual build-up of deposits of higher surface area and the current progressively improved, which was known as 'formation process' [41, 44].

Soon after, the first work on batteries with alkaline solutions was reported by Waldemar Jungner in 1899. The nickel-cadmium battery had a positive electrode of nickel hydroxide and a mixture of cadmium and iron powders as the negative electrode, and was immersed in a concentrated solution of potassium hydroxide [45]. A similar system was developed by Thomas Edison in 1905, except that it used an all-iron negative electrode rather than a cadmium-iron mixture. Both cells gave 1.2 V and were brought

into commercial use [46]. In 1932, Shlecht and Ackerman invented porous nickel electrodes, where the active materials of the batteries were deposited. This increased the contact area of the electrodes, allowing higher velocity in the charge and discharge reactions [47]. Another commercially important primary system is the zinc-mercury oxide battery, sometime also named the Ruben-Mallory battery, which was invented by Samuel Ruben in 1945 [48]. This battery was fabricated as low-drain, button cell, using amalgamated zinc as the negative electrode, a mercury oxide-carbon mixture as the positive electrode, and a concentrated potassium hydroxide aqueous electrolyte solution.

The lithium-ion battery was initially discovered by researchers at Oxford University in the late 1970s, when they found that lithium ions can be intercalated into the crystal lattice of trivalent cobalt or nickel oxides to give the compounds $LiCoO_2$ and LiNiO, respectively [49]. This discovery was followed up by researchers at Sony Corporation, and they commercialized the first lithium-ion battery that contains no metallic lithium and therefore is much safer on recharge than the earlier lithium-metal battery design. The lithium-ion battery has a respectable 3 V cell, offers high energy densities largely exceeds that of more conventional rechargeable batteries, such as lead-acid, Ni-Cd, or even Ni-MH, where M is a metal, and become the preferred choice for electrochemical storage. Figure 2.1 shows the basic electrode reactions involved in these batteries, which exhibit different voltages and capacities [50]. The characteristics of rechargeable batteries depend on both the performance of the active materials contained in the cathode and anode and on the integration technologies for the battery components.

Li-ion	(–) $Li_xC \rightarrow C + xLi^+ + xe$	$\varphi^\circ = -2.90$ V	(1)
	(+) $Li_{1-x}CoO_2 + xLi^+ + xe \rightarrow LiCoO_2$	$\varphi^\circ = 1.20$ V	(2)
	(o) $Li_xC + Li_{1-x}CoO_2 \rightarrow C + LiCoO_2$	$E^\circ = 4.10$ V	(3)
MH-Ni	(–) $MH + OH^- \rightarrow M + H_2O + e$	$\varphi^\circ = -0.83$ V	(4)
	(+) $NiOOH + H_2O + e \rightarrow Ni(OH)_2 + OH^-$	$\varphi^\circ = 0.49$ V	(5)
	(o) $MH + NiOOH \rightarrow M + Ni(OH)_2$	$E^\circ = 1.32$ V	(6)
Pb-acid	(–) $Pb + SO_4^{2-} \rightarrow PbSO_2 + 2e$	$\varphi^\circ = -0.36$ V	(7)
	(+) $PbO_2 + 4H^+ + SO_4^{2-} + 2e \rightarrow PbSO_4 + 2H_2O$	$\varphi^\circ = 1.69$ V	(8)
	(o) $Pb + PbO_2 + 2H_2SO_4 \rightarrow 2PbSO_4 + 2H_2O$	$E^\circ = 2.05$ V	(9)
Redox flow	(–) $V^{2+} \rightarrow V^{3+} + e$	$\varphi^\circ = -0.26$ V	(10)
	(+) $VO_2^+ + 2H^+ + e \rightarrow VO^{2+} + H_2O$	$\varphi^\circ = 1.00$ V	(11)
	(o) $V^{2+} + VO_2^+ + 2H^+ \rightarrow VO^{2+} + H_2O$	$E^\circ = 1.26$ V	(12)
Na-S	(–) $2Na \rightarrow Na^+ + 2e$	----------	(13)
	(+) $xS + 2e \rightarrow S_x^{2-}$	----------	(14)
	(o) $2Na + xS \rightarrow Na_2S_x$	$E = 2.08 — 1.78$ V	(15)

Figure 2.1. Electrode reactions of representative rechargeable batteries [50].

In the almost three to four decades since the emergence of these battery technologies, there has been an increase in energy density, prefiguring today's need of power sources that can deliver more energy per unit volume. Figure 2.2, which compares these batteries in an energy diagram, clearly shows the superiority of the lithium system. The energy density of the Ni-Cd battery is about 30 to 60 Wh kg^{-1} and 100 to 200 Wh l^{-1}, that of the Ni-MH battery is about 60 to 100 Wh kg^{-1} and 80 to 300 Wh l^{-1}, while the lithium-ion battery has an energy density of about 140 Wh kg^{-1} and 300 Wh l^{-1}.

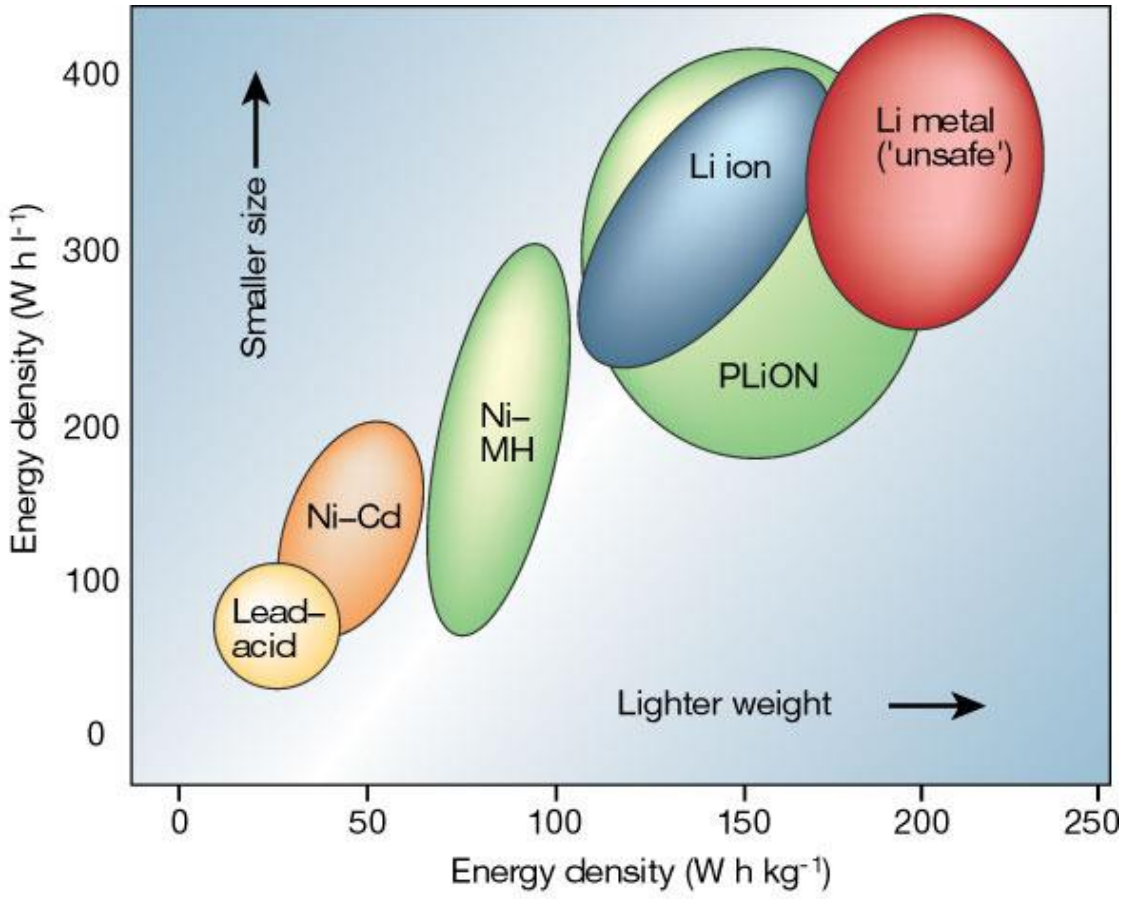

Figure 2.2. Comparison of the different battery technologies in terms of volumetric and gravimetric energy density [51].

2.2 Lithium-ion batteries

Rechargeable lithium batteries using lithium anodes were introduced onto the market on a limited scale in the 1980s for consumer applications. Unfortunately, they were withdrawn when safety problems arose. The lithium-ion cell was first marketed in 1991 and does not contain lithium in a metallic state. This battery is also known as a swing battery or rocking chair battery due to the two-way movement of lithium ions between the anode and cathode through the electrolyte during the charge-discharge processes. Most commercial lithium-ion batteries use carbon as the anode material, non-aqueous

liquid electrolyte, and a layered transition metal (M) oxide such as $LiCoO_2$ or $LiMn_2O_4$ as the cathode material. The concept of the lithium-ion battery is illustrated schematically in Figure 2.3. In the charged state, the anode contains a high concentration of intercalated lithium, while the cathode is depleted of lithium. During the discharge, lithium-ions leave the anode and migrate through the electrolyte to the cathode, while their associated electrons are collected by the current collector to be used to power an electric device. The cell voltage is determined by the energy of the chemical reaction occurring in the cell.

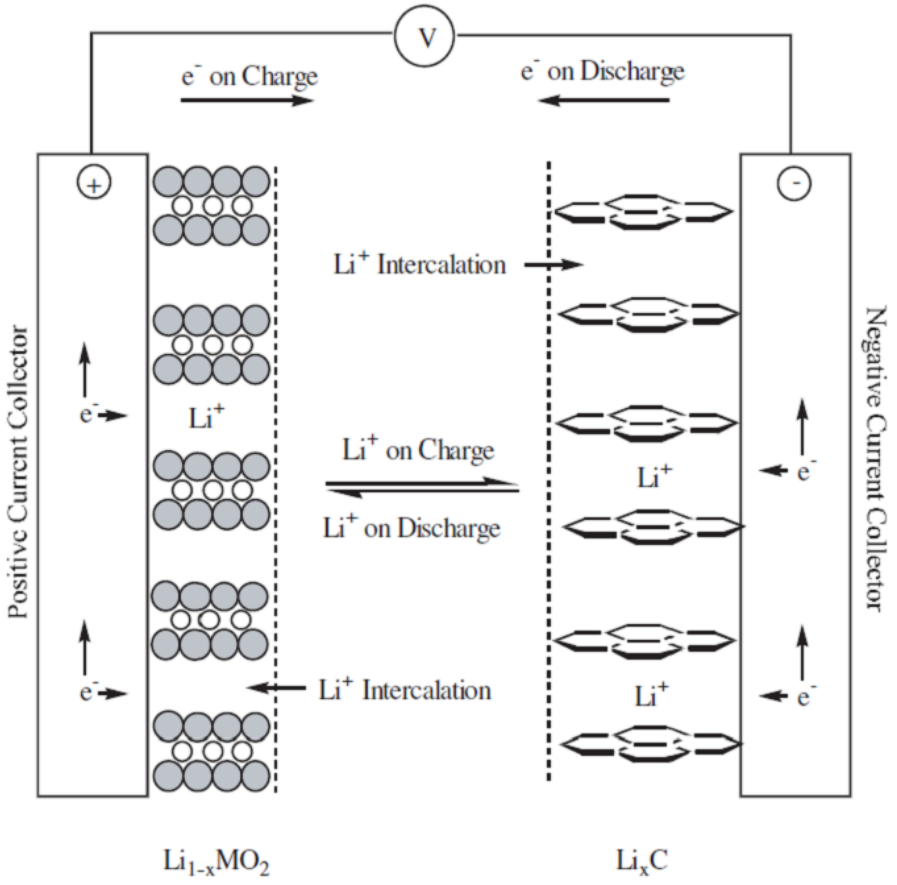

Figure 2.3. Schematic diagram of the electrochemical processes in a lithium-ion cell [52].

In practice, the anode and cathode contain polymeric binders to hold the powder structure together and conductive diluents such as carbon black to give the whole structure electronic conductivity, so that electrons can be transported to the active material. Moreover, these combinations give sufficient porosity to allow the liquid electrolyte to penetrate the powder structure and the ions to reach the reacting sites [1]. The positive electrode (cathode) has a current collector made of thin aluminum foil coated in lithium metal oxide, while the negative electrode (anode) has a current collector made of thin copper foil coated in graphite carbon. The separator is a fine porous polypropylene or polyethylene film, and the electrolyte is an organic solvent with lithium salts dissolved in it. The wound cathode/separator/anode plus electrolyte are contained within a metal (steel or aluminum) can and sealed with a cap. The cap usually contains a mechanical vent mechanism which releases internal cell pressure under abusive conditions and a positive temperature coefficient (PTC) device to limit current in a short circuit or under other abusive conditions. In many cells, an additional current interrupter is also included, which acts to remove the cell from the external circuit in an overcharge situation. The electrochemical mechanism of this battery at the electrodes and the overall reaction mechanism are shown in Figure 2.4. These rocking chair batteries do not require a stringent manufacturing environment because the starting electrode materials (i.e., lithiated oxides and carbon) are stable in ambient atmosphere. The cell is assembled in its discharged state, where the output voltage is close to 0 V, and activated during the first charge [53]. The concept is similar to that of Ni-Cd batteries that need to be charged prior to use. The lithium-ion cell delivers its capacity between 4.1-4.3 V and 2.5 V, with an average voltage of 3.5-3.7 V, and can be discharged reversibly down to 0 V [53].

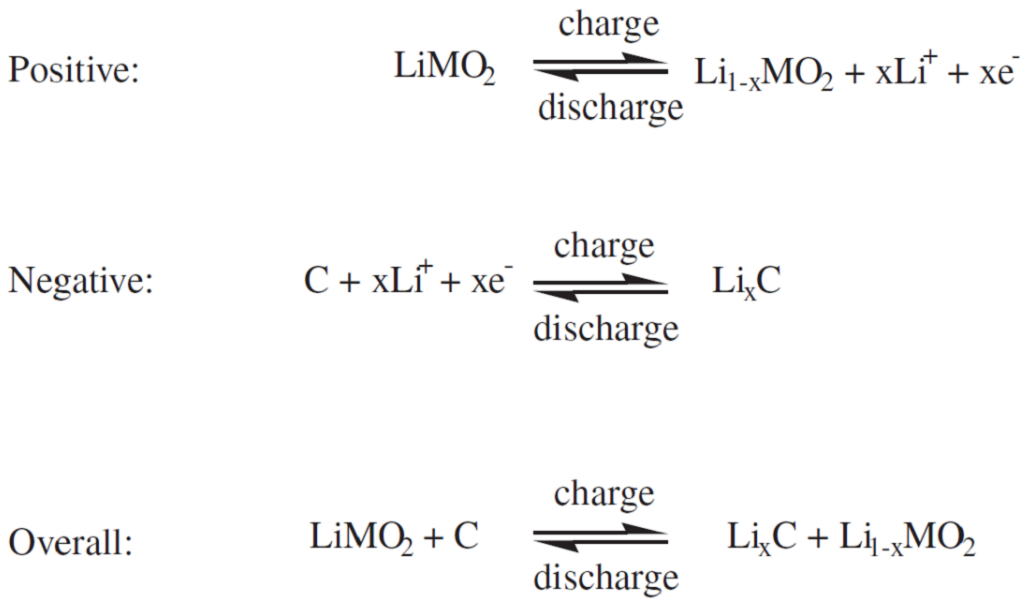

Figure 2.4. Electrode and cell reactions of lithium-ion battery [52].

2.3 Lithium polymer batteries

Rechargeable lithium batteries which use solid polymer electrolytes (SPE) are considered to have safety advantages over the liquid electrolytes due to their lower reactivity with lithium and the absence of a volatile, flammable organic solvent. The concept behind these batteries was based on a breakthrough after Wright's discovery of ionic conductivity in alkali metal salt complexes of poly(ethylene oxide) (PEO) in 1973 [54], and polymer electrolytes were proposed for batteries in 1978 [55]. Their advantages such, as no leakage of electrolyte, higher energy density, flexible geometry, and improved safety, have drawn the attention of many researchers towards the development of lithium polymer batteries [56]. The cell reaction is similar to that in the liquid organic electrolyte, intercalation of lithium into the cathode structure during discharge and de-intercalation of lithium from the charged cathode and deposition on

the anode during charge [57]. The basic structure of the solid polymer electrolyte cell can be represented as shown in Figure 2.5.

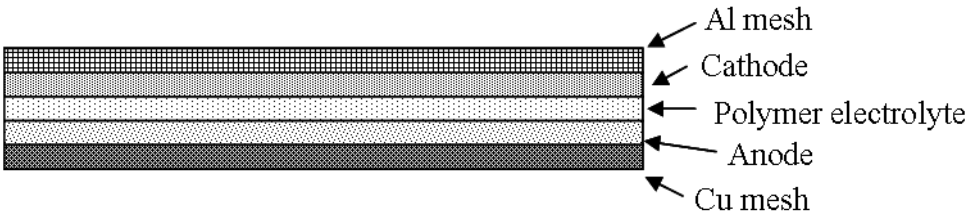

Figure 2.5. Schematic cross-section of a solid polymer electrolyte (SPE) cell.

The major problem for lithium polymer electrolyte systems is the formation of high interfacial resistance at the lithium/polymer electrolyte interphase [56], due to the reactions of lithium with water, other impurities, and the salt anions. This resistance grows with time and could be as high as 10 $k\Omega\ cm^{-2}$ [58]. A solid electrolyte interphase (SEI) also exists in non-aqueous electrolyte system, but in this case, the solid electrolyte interphase (SEI) consists of the inorganic reduction products of the polymer electrolyte and its impurities.

The energy density of the SPE batteries is projected to be close to that of the liquid electrolyte lithium rechargeable batteries. The thin cell design requires a larger percentage of construction materials and non-reactive components, which tend to lower the energy density. Larger electrode areas are also required for a given cell capacity than with the conventional battery design. The thin separator and large electrode area could adversely affect the cycle life, safety, and reliability of the battery by increasing the chance for internal short circuits, lithium dendrite penetration, and other deleterious effects [57]. A great effort has been undertaken all over the world to develop lithium polymer batteries both for small- and large-scale applications. The PolyPlus Battery in the US is a room-temperature lithium polymer battery with specific capacity as high as

500 Wh kg^{-1}. In a prototype cell using a lithium intercalated disulfide polymer as the cathode at 90°C, specific energy of 100 Wh kg^{-1} was obtained over 350 cycles [59, 60]. Moltec have reported an AA-sized battery based on organosulfur cathode with specific capacity of 180 Wh kg^{-1} [61]. In 1998, Sony introduced a lithium polymer battery onto the market which had almost equal performance to the lithium-ion battery using liquid electrolyte, as shown in Table 2.1 [62]. Thin and lightweight battery design was achieved by using aluminum-laminated polymer film as the casing materials instead of a heavy metal can (Figure 2.6).

Table 2.1. Performance of lithium polymer battery introduced by Sony [62].

Size (D×W×H)	3.8×35×62 mm
Weight	16 g
Capacity	900 mAh
Average voltage	3.75 V
Charge voltage	4.2 V
Charging time	150 min
Vol. energy density	410 Wh dm^3
Gr. Energy density	210 Wh kg^{-1}
Cyclability	85% at 1000^{th} cycle
Temperature range of operation	-20 °C ~ 60°C
Cathode	$LiCoO_2$
Anode	Graphite

Figure 2.6. Thin and lightweight lithium polymer battery [62].

2.4 Basic concepts and principles

In batteries, electrical energy is generated by conversion of chemical energy via redox reactions at the anode and cathode. Reactions at the anode usually take place at lower electrode potentials than at the cathode and the terms negative and positive electrode are used. The more negative electrode is designated the anode, whereas the cathode is the more positive one. Table 2.2 listed the electromotive series of some battery components. Batteries are closed systems, with the anode and cathode being the charge-transfer medium and taking an active role in the redox reaction as 'active mass'.

A simple galvanic cell consists of cathode and anode immersed in an electrolyte solution, as is shown in Figure 2.7. During the discharge, the anode releases electrons (is oxidized), which flow through the external load to the cathode, where they are accepted by the reduction reaction. The flow of anions and cations to the anode and cathode also occurs, respectively (Figure 2.7(a)). During the recharge, the current flow is reversed, the positive electrode is oxidized, and the negative electrode is reduced, as shown in Figure 2.7(b). As the anode is, by definition, the electrode at which oxidation

occurs and the cathode the one where reduction takes place, the positive electrode is now the anode and the negative the cathode [63].

Table 2.2 Electromotive series of some battery components [64].

Anode materials from worst (most positive) to best (most negative)	Cathode materials from best (most positive) to worst (most negative)
Gold	Ferrate
Platinum	Iron oxide
Mercury	Cuprous oxide
Palladium	Iodate
Silver	Cupric oxide
Copper	Mercuric oxide
Hydrogen	Cobaltic oxide
Lead	Manganese oxide
Tin	Lead oxide
Nickel	Silver oxide
Iron	Oxygen
Chromium	Nickel oxyhydroxide
Zinc	Nickel dioxide
Aluminum	Silver peroxide
Magnesium	Permanganate
Lithium	Bromate

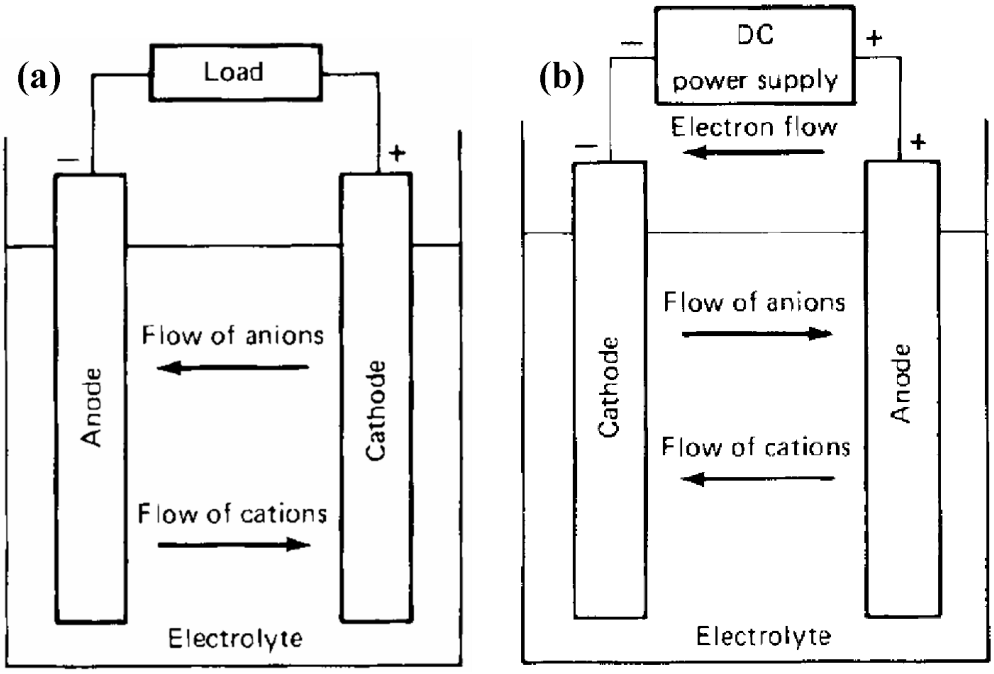

Figure 2.7. Electrochemical operation of a cell during (a) discharge and (b) charge [63].

2.4.1 Potential

It is important to note that all energy storage and power characteristics of batteries can be deduced directly from the thermodynamic and kinetic equations that arise from the properties of the active species involved. Most importantly, the Gibbs free energy serves as a measure of the net available energy from a given reactions, which is related to a standard electrode potential, E^0. Under equilibrium conditions:

$$\Delta G = -nFE^0 \tag{2.1}$$

where ΔG is the Gibbs free energy, F is the Faraday constant (96485 C), n is the number of electrons involved in a stoichiometric reaction and E^0 is the electrode potential. The amount of electricity produced, nF, is determined by the total amount of

materials available for reaction and can be thought of as a capacity factor; the cell voltage can be considered to be an intensity factor. The usual thermodynamic calculations on the effects of temperature, pressure, etc. apply directly to electrochemical reactions. Spontaneous processes have a negative free energy and a positive electromotive force (emf), with the reaction written in a reversible fashion, which goes in the forward direction [4]. For conditions other than in the standard state, the electrochemical potential of a cell is given by the Nernst equation:

$$E = E^0 - \left(\frac{RT}{nF}\right)\ln\left(\frac{A_p}{A_r}\right) \tag{2.2}$$

where R – gas constant

T – absolute temperature

A_p – the activity product of the products

A_r – the activity product of the reactants

The voltage of the cell is unique for each reaction couple, depending on which electrode materials are being used. Figure 2.8 shows the voltage versus capacity for positive and negative electrode materials for lithium-ion batteries. For cathode materials, the potential vs. Li/Li^+ varies from 2.5 V to 4.3 V, whereas anode materials show a potential vs. Li/Li^+ lower than 2.0 V.

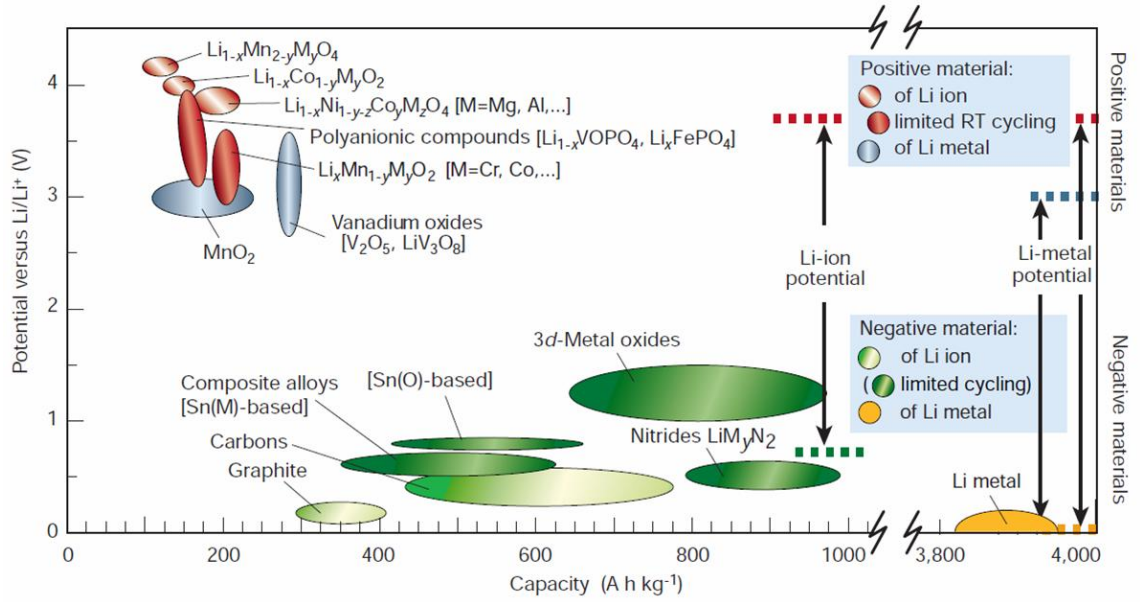

Figure 2.8. Voltage versus capacity of electrode materials [51].

2.4.2 Specific capacity

The theoretical capacity of a cell is the total quantity of electricity involved in the electrochemical reaction, which is determined by the quantity of active materials in the cell. The theoretical specific capacity, Q_s can be calculated from the equation below:

$$Qs = \frac{n \times F}{M} \tag{2.3}$$

Here, n is the number of mol of electrons transferred in the electrochemical reactions, F is the Faraday constant (96485 C), and M is the molecular weight of the active materials. Specific charge capacity (Q_c) or specific discharge capacity (Q_d) can be calculated using equation (2.4):

$$Q_c \text{ (or } Q_d) = \frac{I \times t}{m} \tag{2.4}$$

where I – is the current (A)

t – time (hour)

m – mass of the active material (kg)

2.4.3 Specific energy and energy density

The ability of a battery to deliver electrical energy is a function of the cell potential (V) and capacity (Ah kg^{-1}), which are linked directly to the chemistry of the system. It can be expressed either as

$$\text{energy density, } ED \text{ (Wh } l^{-1}) = \frac{E \times Q \times m}{V} \tag{2.5}$$

or

$$\text{specific energy, } SE \text{ (Wh } kg^{-1}) = E \times Q \tag{2.6}$$

Here, m (kg) and V (litre) are the mass and volume of the cell, respectively.

2.4.4 Specific power and power density

The amount of power that a battery is able to deliver can be expressed either per unit mass or per unit volume.

$$\text{Power density (W } l^{-1}) = \frac{ED}{t} \tag{2.7}$$

$$\text{Specific power (W kg}^{-1}) = \frac{SE}{t} \tag{2.8}$$

t is the discharge time (h).

2.4.5 Self discharge

Charged batteries will slowly lose their charge over time, even if they are not connected to a device. Moisture in the air and the slight conductivity of the battery housing will serve as a path for electrons to travel to the cathode from the anode, discharging the battery. The rate at which a battery loses power in this way is called the self-discharge rate.

2.4.6 Rate capability

A battery's rate capability is its ability to deliver a large capacity when discharged at high C rates. A rate of C/1 corresponds to the current required to completely discharge an electrode in 1 h [65]. C denotes either the theoretical charge capacity or the nominal capacity of the battery.

2.4.7 Irreversible capacity

A lithium-ion battery suffers gradual capacity loss or irreversible capacity loss with each charge-discharge cycle. For anode materials, irreversible capacity can be calculated using equation (2.9):

Irreversible capacity = $n^{th}Q_d - n^{th}Q_c$ (2.9)

For cathode materials, irreversible capacity can be calculated as follows:

Irreversible capacity = $n^{th}Q_c - n^{th}Q_d$ (2.10)

Here, Q_c and Q_d are the charge capacity and the discharge capacity, respectively, of the cell at the n^{th} cycle.

2.4.8 Coulombic efficiency

The coulombic efficiency (η) of a battery is the ratio of the amount of charge that enters the battery during charging compared to the amount that can be extracted from the battery during discharging. The coulombic efficiency (η) is given by equation (2.11):

$$\eta = \frac{n^{th}Q_c}{n^{th}Q_d} \times 100\% \quad (2.11)$$

2.4.9 Charge-transfer resistance, Warburg impedance, and equivalent circuit modeling

The cell impedance has contributions from individual electrodes as well as from other components such as the electrolyte. It is widely recognized that the presence of a solid-electrolyte interphase (SEI) layer on the electrode surface of lithium-ion batteries plays an essential role in the battery performance, and its very nature can determine an

extended (or shorter) life for the battery. The impedance response includes (a) electrolyte resistance (R_s), (b) charge-transfer resistance (R_{ct}), (c) double-layer capacitance (C_{dl}) at the electrode/electrolyte interface, and, (d) Warburg impedance (Z_w). Charge-transfer resistance (R_{ct}) at the interface between the electrolyte and the electrode constitutes a major barrier to the kinetics of lithium-ion cell chemistry, indicating slow electrochemical reactions. Diffusion also can create an impedance, called the Warburg impedance (Z_w), that depends on the frequency of the potential perturbation. The Warburg impedance is small at high frequencies, as the reactants do not diffuse very far, whereas the Warburg impedance is increased at low frequencies as the reactants have time to move farther. Capacitors in equivalent circuits in electrochemical impedance spectroscopy (EIS) experiments often do not behave ideally. Instead, they act like a constant phase element (CPE), probably due to surface roughness, a 'leaky' capacitor, non-uniform current distribution, etc, [66]. Figure 2.9 shows a typical Nyquist plot for lithium-ion batteries. The diameter of the semicircle in the medium frequency region could be assigned as R_{ct}, and Z_w appears as a diagonal line with a slope of 45°.

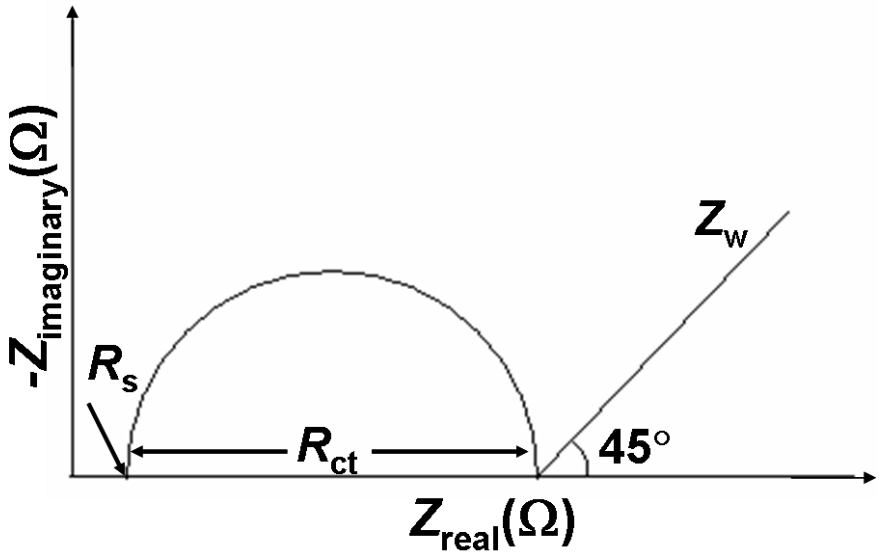

Figure 2.9. Typical Nyquist plot of lithium-ion battery.

Impedance data can be extracted physically as meaningful properties of the electrochemical system by using equivalent circuit modeling. An equivalent circuit model is an electrical circuit composed of ideal resistors (*R*), capacitors (*C*), and inductors (*L*). In the equivalent circuit analog, resistors represent the bulk resistance of a material to charge transport, such as the resistance of the electrolyte to ion transport and the resistance to the charge-transfer process at the electrode surface. Capacitors and inductors are associated with space-charge polarization regions, such as an electrochemical double layer and adsorption/desorption processes at an electrode, respectively [67]. Table 2.3 lists the circuit elements, the equation for their current versus voltage relationship and their impedance. The equivalent circuit for the Nyquist plot in Figure 2.9 is shown in Figure 2.10.

Table 2.3. The defining relations and impedance for ideal bulk electrical elements [67].

		Defining Relation	Impedance
Resistor		$V = I \times R$	$Z_R = R$
Capacitor	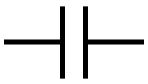	$I = C\frac{dV}{dt}$	$Z_C = \frac{1}{j\omega C} = -\frac{j}{\omega C}$
Inductor		$\mathrm{V} = \mathrm{L}\frac{\mathrm{dI}}{\mathrm{dt}}$	$\mathrm{Z_L} = \mathrm{j}\omega\mathrm{L}$

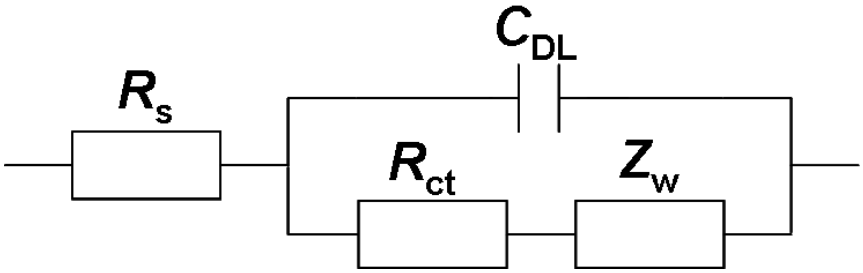

Figure 2.10. Equivalent circuit for Nyquist plot in Figure 2.9.

2.4.10 Models for ionic conductivity

It is quite difficult to interpret the conduction phenomenon in polymer electrolytes. The ion dynamics in solids can be understood through ac conductivity studies. However, there are several models that can describe the conductivity-temperature relationships in the system.

2.4.10.1 Arrhenius Model

The Arrhenius model is represented by equation (2.12):

$$\sigma = \sigma_o \exp\left(\frac{-E_a}{kT}\right) \tag{2.12}$$

Here, σ_o is the pre-exponential factor, E_a is the activation energy of the ions, k is the Boltzmann constant and T is the absolute temperature. This equation can be expressed when a plot of ln σ versus $10^3/T$ shows linear behavior. The Arrhenius behavior below the glass transition temperature (T_g) is explained by ion pair dissociation, leading to the formation of interstitial defects migrating by an indirect interstitial mechanism. Above T_g, the ionic transport involves a cooperative mechanisms of the neighboring atoms or the macromolecular chains [68].

2.4.10.2 Vogel-Tamman-Fulcher (VTF) Model

The VTF model can be explained using the free volume theory. The free volume theory assumes that the ionic transport mechanism in the polymer electrolyte results from segmental motions. This process promotes ion movement through the formation and destruction of a coordination sphere of the solvated ion, thereby creating a free volume into which the ion could diffuse under the influence of the electrical field [69]. The VTF model is represented by equation (2.13):

$$\sigma = \frac{\sigma_o}{\sqrt{T}} \exp\left(\frac{-B}{k(T_o - T)}\right) \tag{2.13}$$

where, σ_o is the conductivity pre-exponential factor, B is the pseudoactivation energy of the ion, and T_o the thermodynamic glass transition temperature or the ideal glass transition temperature, which is usually 50 K lower than the glass transition temperature (T_g). At the temperatures below the ideal glass transition temperature (T_o), the free volume is assumed to vanish.

2.5 Micro/nanotechnologies to transcend challenges

In recent years, attempts to address the capacity issue in electrode materials has still been attracting considerable attention, although great progress has been made during the last 20 years in lithium-ion batteries [20, 29, 48, 51, 53, 70-76]. To meet the technological demands in this area, the size of the materials should be reduced to the nanometer scale. Micro/nanomaterials show interesting mechanical and physical

properties, such as increased mechanical strength, enhanced diffusivity, and higher specific heat and electrical resistivity compared to conventional bulk grained materials [77]. Materials having grain size of 0.1 to 0.3 μm are classified as submicron materials, whereas nanomaterials are characterized by a grain size of up to about 100 nm [78]. The unique attributes of nanomaterials are as follows [79]:

1) Fast transport of mobile species. When the size and dimensions of materials, grains, and domains become comparable to (or less than) the characteristic length scale (such as the mean free path) of phonons, photons, electrons, ions, and molecules, the physical phenomena involving these materials are strongly influenced, such as the transport of charge, mass, and energy and in chemical and energy transformation processes. Table 2.4 shows the characteristic length and time scales for electrons, molecules, and ions under ambient condition.

Table 2.4. Characteristic length and time scales for electrons, molecules, and ions at ambient temperature [79].

Energy carriers	Wavelength/ nm	Mean free path/nm	Relaxation time/ns
Electrons			
In semiconductors/dielectrics	~1–50	~1–500	$\sim10^{-3}$ to 10^{-2}
In conductors/metals	~0.1–1	~1–10	$\sim10^{-5}$ to 10^{-4}
Molecules/ions			
In gas/plasma	$\sim10^{-2}$ to 1[a]	$\sim10^{3}$ to 10^{7}	~1–100
In liquid/electrolyte	–	~0.1–1	$\sim10^{-3}$
In solid/electrolyte	–	~0.1–1	$\sim10^{-3}$

[a] Refers to de Broglie wavelength

It can be seen that the mobile species (electrons, ions, and molecules) in batteries have length scales on the order of 0.1 – 100 nm in typical

electrochemical systems, suggesting that some unique physicochemical properties of materials and novel reaction pathways may become operative in the nanoscale regime. The transport of these mobile species associated with cycling of batteries has a significant impact on the rate of chemical and energy transformation processes.

2) Surface reactivity. The ratio of the number of surface atoms to that of the bulk atoms for a nanomaterial is far greater than for a bulk material (> 100 nm). In bulk materials, the surface atoms contain fewer neighbors than the atoms in the bulk, leading to lower coordination numbers and unsatisfied bonds. The chemical reactivity of materials could be affected by large surface free energy, surface defects, and surface states [80]. The large surface free energy and stress/strain of nanomaterials may influence the phase stability and structural transformations, which in turn influence the electrochemical and catalytic activities. The surface free energy of nanomaterials can be estimated as:

$$\mu\circ(r) = \mu\circ(r=\infty) + 2\left(\frac{\gamma}{r}\right)V \tag{2.14}$$

Here, $\mu°(r)$ and $\mu°(r = \infty)$ refer to the chemical potential of nanoscale and bulk materials, respectively, γ is the effective surface tension, r is the effective grain radius, and V is the partial molar volume. As can be seen from eq. (2.14), the surface energy increases with decreasing particle size. Therefore, phases that may not be stable in bulk materials are more stable in nanostructures.

3) Mechanical robustness. Nanostructured materials are known to exhibit high mechanical strength, toughness, and structural integrity [81-83]. Some naturally

evolved nanostructures (e.g., diatom shells) are resilient to mechanical stress and strain, and exceptional stresses and strains are required to break them [84].

In recent years, the possible roles of nanomaterials in electrode materials have been emphasized in lithium-ion batteries, as these strategies have dramatically enhanced battery performance, including capacity, rate capability, cycling life, and safety. The advantages of nanomaterial electrodes in lithium-ion batteries include [85, 86]:

1) Large surface to volume ratio increases the contact area between the electrode and the electrolyte and thus, provide more active sites for electrode reactions. Therefore, the power density (or rate capability), energy efficiency, and energy density are improved, and the electrode polarization loss is reduced.
2) The nanosized dimensions reduce the distance for lithium-ion transport within the particles, which in turn increases the rate of lithium insertion/removal processes. For solid-state diffusion of lithium in electrode materials, the characteristic time constant for diffusion is given by

$$\tau = \frac{L^2}{D} \tag{2.15}$$

where L is the diffusion length and D the diffusion constant. The time for lithium intercalation, τ, decreases with the square of the diffusion length, L, illustrating the remarkable effect of manipulating nanostructures.

3) Enhanced electron transport within the particles as described for lithium ions.
4) The formation of nanocomposites or thin film deposition of electronic/ionic conductors could also enhance the ionic and electronic conductivity of the

electrode materials, where the surface of each phase or the interfaces between phases support fast transport of ionic and electronic species.

5) Structural integrity is improved by well-designed nanomaterials such as nanowires, nanotubes, nanobelts, and nanorods. These structures have high mechanical strength and more resistance to mechanical damage.
6) Hierarchical architecture of nanoporous materials can improve electrocatalytic activity and stability due to the high surface area for surface modifications and the robust structure for durability. The electrocatalytic activity is enhanced due to the increased number of active reaction sites and facile transport of electro-active species to the reaction sites.
7) Higher capacities could be achieved by using nanostructured materials, due to new lithium storage mechanisms. Recent studies show that lithium ions can be stored on the surface [87], interface [88-90], and nanopores [91, 92], without causing any mechanical crumbling in the electrode, thus leading to excess lithium storage. In particular, surface/interfacial lithium storage mechanisms will play critical roles in transition metal oxide and newly emerging graphene-based electrodes.
8) The chemical potentials of electrode materials for lithium ions and electrons may be modified, resulting in a change in the electrode potential [93].

Meanwhile, the disadvantages related to the use of nanomaterials as electrode materials in the lithium-ion battery are listed as follows [85]:

1) Nanoparticles may be more complicated to synthesize, and their dimensions are rather difficult to control.

2) High electrolyte/electrode surface area may lead to undesired side reactions with the electrolyte, and it will be more difficult to maintain the interparticle contact.
3) Nanopowders have less density when compared with the same material formed from micrometer-sized particles. The volume of the electrode increases for the same mass of material, thus reducing the volumetric energy density.

2.6 Negative electrode for lithium-ion batteries

2.6.1 Carbonaceous materials

Carbonaceous materials are the earliest materials that have been examined and successfully used as anode in lithium-ion batteries. After being commercialized by Sony in 1991, the performance of carbon-based anode materials has been significantly improved, in terms of energy density, rate capability, and cost. The physical, chemical, and electronic properties of carbonaceous nanomaterials are strongly dependent on carbon's structural conformation and its hybridization state [94]. Carbon atoms can bind covalently with three, five, and seven neighboring carbon atoms, leading to the possible formation of pentagonal and heptagonal faces. These faces allow the existence of complex solids and macromolecules [95]. The oldest carbon allotropes are amorphous carbon (such as coal and soot), graphite and, diamond as shown in Figure 2.11. Later, scientists have synthesized new allotropes, including carbon nanotubes (CNTs), fullerenes, and graphene, all of which have had a significant scientific and technological impact. Today, graphite-based anodes with a theoretical capacity of 372 mAh g^{-1} (for a stoichiometry of LiC_6) are still dominating current commercial batteries [96, 97].

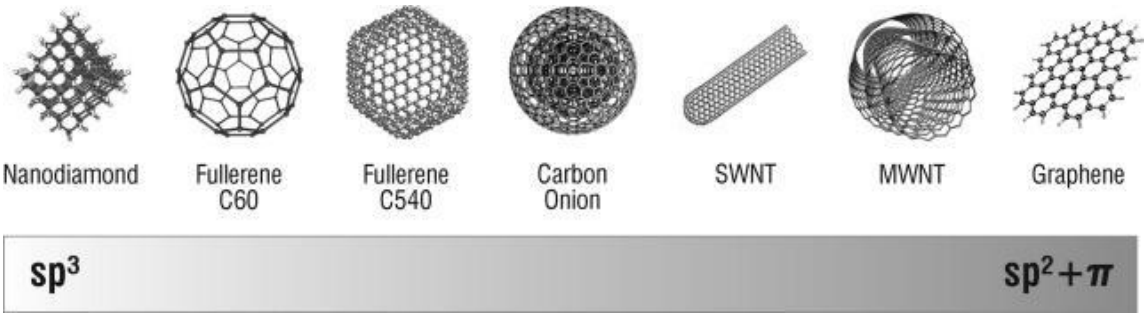

Figure 2.11. Carbon allotropes [98].

Carbonaceous nanomaterials share the same bonding configurations as macroscopic carbon structures, however, their properties and morphology are controlled by the stability of particular resonance structures rather than the bulk of their crystalline forms [98]. Graphite nanosheets are thermodynamically stable as three-dimensional structures on the nanoscale. The curvature of the planar graphite will generate strain energy which is compensated by the reduction of unfavorable dangling bonds [99]. Therefore, fullerenes and nanotubes share many properties of graphite and exhibit a distinct and tunable set of properties due to quantum effects at the nanoscale, enhanced sp^3 character of the bonds, quantum confinement on wave functions in one or more dimensions [100], and closed topology. More recently, Novoselov and Geim discovered the allotrope of carbon which was called graphene in 2004 [101]. They used adhesive tape to detach a single layer of atoms from graphite to produce the new allotrope. Graphene consists of a single layer of graphite (Figure 2.12) with a thickness of one atom and is a good electrical and thermal conductor. Due to the high quality of its sp^2 carbon lattice, electrons were found to move ballistically in a graphene layer, even at ambient temperature [102, 103].

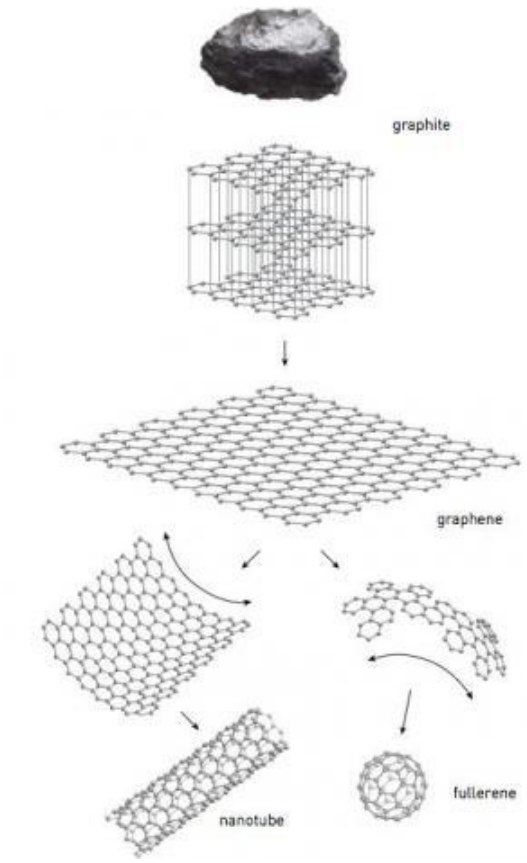

Figure 2.12. Graphene from graphite [104].

Owing to its large surface-to-volume ratio and highly conductive nature, graphene may have properties that make it suitable for reversible lithium storage in lithium-ion batteries. This is because lithium ions could be bound on both sides of graphene sheets, as well as on the edges and covalent sites of the graphene nanoplatelets. Therefore, it is expected that graphene could overtake its three-dimensional counterpart (graphite) for enhanced lithium storage in lithium-ion batteries.

Yoo et al. [105] have studied the lithium storage properties of graphene nanosheet (GNS) materials as anode materials for rechargeable lithium-ion batteries. The charge/discharge capacities of GNS are much higher than the theoretical capacity of graphite (372 mAh g^{-1}), as shown in Figure 2.13. Two possible explanations has been

proposed: (1) different electronic structures of GNS, GNS + CNT, and GNS + C60 from that graphite, and (2) the expansion of *d*-spacing of the graphene layers provides more sites for accommodation of lithium ions.

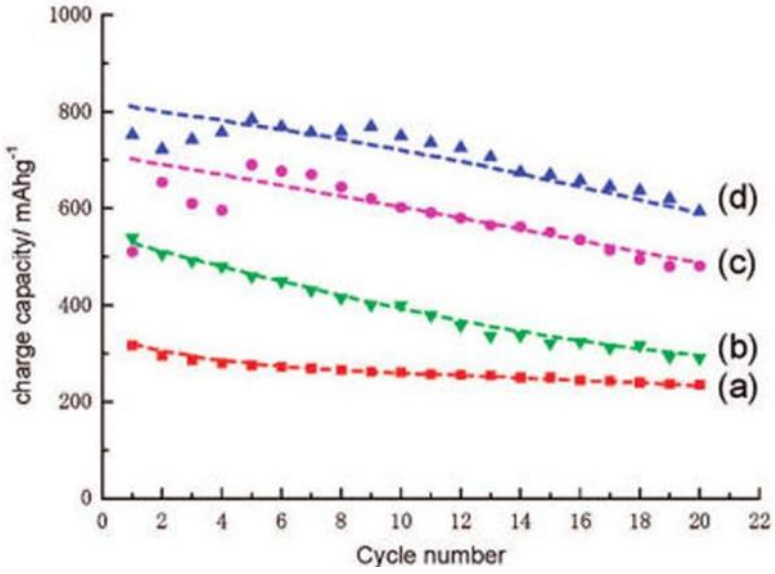

Figure 2.13. Charge/discharge cycling performances of (a) graphite, (b) GNS, (c) GNS + CNT, and (d) GNS + fullerenes (C_{60}) [105].

High capacity graphene materials have also been reported by Wang et al. [106] (Figure 2.14). It has been proposed that lithium ions can be absorbed on both sides of a graphene sheet that is arranged like a "house of cards" in hard carbons, leading to two layers of lithium for each graphene sheet, with a theoretical capacity of 744 mAh g^{-1} through the formation of Li_2C_6 [107, 108]. However, large irreversibility, the absence of a voltage plateau during discharge, and large hysteresis in voltage between charge and discharge currently limit the usage of graphene-based anode materials. Further improvements are awaited before this material can be commercialized in lithium-ion batteries.

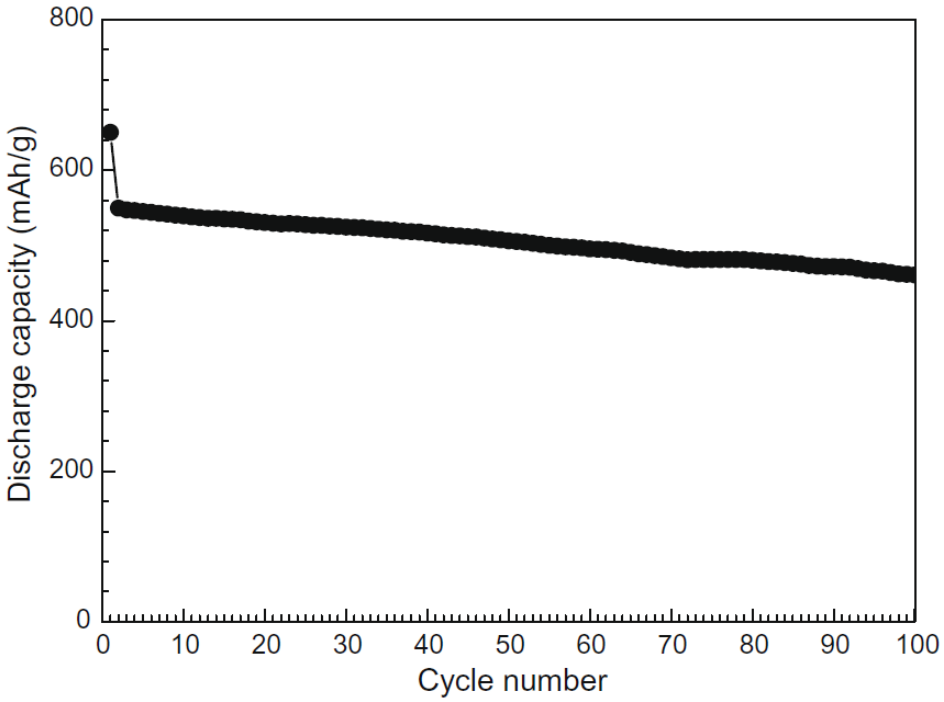

Figure 2.14. Discharge capacity of graphene nanosheet electrode versus cycle number [106].

2.6.2 Lithium alloys

Lithium alloys are possible alternatives for the anode due to their high theoretical capacity and their similar potential range to graphite materials. The concept was introduced by Dey [109] in 1971 when he demonstrated the feasibility of electrochemical formation of lithium alloys in liquid organic electrolytes. The reaction usually proceeds reversibly according to the general scheme shown in Eq. (2.16) [110].

$$\mathrm{Li}_x\mathrm{M} \underset{\text{charge}}{\overset{\text{discharge}}{\rightleftharpoons}} x\,\mathrm{Li}^+ + x\,\mathrm{e}^- + \mathrm{M} \qquad (2.16)$$

Some metals, such as Sn, Sb, Si, Al, Zn, and Ge, can form alloys with lithium at low potential [111, 112]. Table 2.5 shows a comparison of the theoretical specific capacities

of alloy anodes, lithium metal, and graphite. Si-based and Sn-based nanocomposites are more attractive due to their high capacity, and much attention has been paid to improving their performance. Si and Sn can generate lithium alloys with lithium compositions up to $Li_{4.4}M$, giving high theoretical capacities of 4200 and 994 mAh g^{-1}, respectively.

Table 2.5. Comparison of the theoretical specific capacity, charge density, volume change, and onset potential of various anode materials [20].

Materials	Li	C	Si	Sn
Density (g cm^{-3})	0.53	2.25	2.33	7.29
Lithiated phase	Li	LiC_6	$Li_{4.4}Si$	$Li_{4.4}Sn$
Theoretical specific capacity (mAh g^{-1})	3862	372	4200	994
Theoretical charge density (mAh cm^{-3})	2047	837	9786	7246
Volume change (%)	100	12	320	260
Potential vs. Li (~V)	0	0.05	0.4	0.6

While attractive in terms of gravimetric capacity, however, these materials generally suffer from low coulombic efficiencies (< 60%) on the first few cycle [25] and huge volume changes during the electrochemical lithiation/delithiation process [113]. Furthermore, these types of materials have poor electronic conductivity, which impedes fast lithiation. It has been reported that a volume expansion on the order of 400% occurred during the formation of $Li_{4.4}Si$ alloy, which causes disintegration and hence a loss of electrical contact between particles [113]. Alloy anodes also had high initial irreversible capacities and rapid capacity fade during cycling [22, 114-116]. Figure 2.15 shows an example where the charge capacity is much lower than the discharge capacity at the first cycle [24].

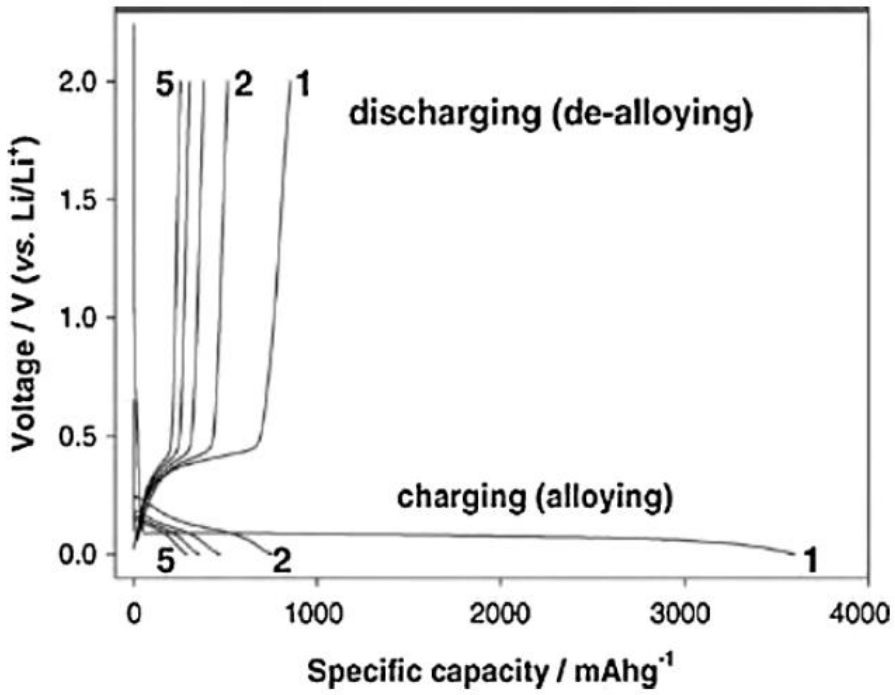

Figure 2.15. Charge-discharge voltage profiles for the first 5 cycles of a pure silicon anode with an average powder size of 10 μm [24].

This serious drawback is caused by several factors [20]:

1) Loss of active material due to large volume change during cycling, and cracking and pulverization of active particles and the surrounding matrix, leading to the disconnection of some alloy particles from the conductive carbon or current collector [114, 115, 117, 118]. The disconnection of the conductive network between active particles and the carbon matrix was confirmed by the sharp rise in the internal resistance of a Si anode at ~0.4 V during the Li-extraction process [119, 120] and verified by scanning electron microscopy (SEM) observation [121]. Atomic force microscopy (AFM) was also used to study the anode surface and has revealed that cracking occurs mainly during the Li-extraction process [122]. As the Si particles become isolated and large internal resistance

occurs, the delithiation process is not completed, with some Li remaining in the Si particles. Therefore, an irreversible capacity loss was observed.

2) Formation of solid-electrolyte interphase (SEI) films on alloy anodes contribute to the process of breaking off and reforming due to the constant volume changes of the alloy particles upon cycling [114, 123-125]. The SEI films consist of Li_2CO_3, various lithium alkylcarbonates ($ROCO_2Li$), LiF, Li_2O, and non-conductive polymers. The thickness of SEI films and the amount of salt-degradation products increase with the cycle number [121, 123], contributing to the first cycle irreversible capacity and the later capacity fade.
3) Generally, Li insertion/extraction in alloys is reversible; however, some lithium ions may be permanently trapped in the alloys. This could be due to slow lithium release kinetics, the formation of highly stable lithiated compounds, or strong bonding with less coordinated atoms at defect sites [117, 118, 126-130]. Lithium ions could be trapped irreversibly at defect sites at the surface, interface, or grain boundaries in alloy particles that result from large volume change and the complicated structural transformation during Li insertion/extraction processes [128, 130, 131].
4) Formation of a passivation oxide layer on a metal or alloy particle surface occurs during material preparation, since many metals are reactive with oxygen or water. It was reported that lithium reacts irreversibly with many oxides to form Li_2O at the potential of ~ 0.8-1.6 V [123, 132, 133].
5) Aggregation of alloy particles has been observed in alloy anodes during cycling, which could be attributed to the welding effect induced by the pressure resulting from the large volume expansion [132]. Therefore, the diffusion length of lithium is increased, leading to irreversible capacity loss [132].

To overcome these problems, several approaches have focused on using porous and nanoscale materials and/or dispersing the active components in a rigid matrix to form composite structures [134]. Nanocomposite anodes could offer two or more functional components while preserving the small particle sizes [50]. Composite anodes can be classified as (1) inactive matrix, (2) active matrix, and (3) carbon-matrix composite, and (4) conducting polymer-based composite [20].

1) Inactive-matrix composites. This type of composite anode employs intermetallic phases, MM′, where M is the active element that can electrochemically alloy with Li and M′ is an inactive or less active metal (e.g., Fe, Ni, Cu, and Co) to suppress the volume change [135]. Fan et al. [136] have prepared amorphous Sn-Co, and its electrochemical behavior was comparable to that of crystalline Sn and Sn-Co materials. Amorphous Sn-Co shows excellent electrochemical performance, and the capacity was found to be stabilized at 400 mAh g^{-1} for 30 cycles at 0.5 mA cm^{-2}, in contrast to crystalline Sn, which rapidly lost capacity after 10-12 deep cycles.
2) Active-matrix composites. Basically, this active composite anode is composed of one component that is lithiated while the other acts as a buffer to alleviate the volume change, as they react with Li at different onset potentials. Yang et al. [137] have prepared SnSb alloy, where lithium first inserts into the more active SnSb phase at ~ 0.82 V vs. Li/Li^+, forming Li_3Sb and Sn phases, and then inserts into the Sn phase below 0.66 V vs. Li/Li^+. Such a stepwise Li-insertion process can buffer the volume expansion of the active material and thereby enhance the mechanical and cycling stability of the electrode.

However, this type of composite has low reversibility upon cycling, and the cycling stability depends on the charge depth.

3) Carbon-based composites. A carbon-matrix composite seems to be an attractive route to enhance the capacity and capacity retention of many electrode materials [25, 138-141]. The beneficial effects of the carbon coating include enhancement of the conductivity of materials, low volume expansion, tolerance to mechanical stress, Li-storage capability, and suppression of the formation of SEI layers [142-145]. Although carbon coating leads to improve cyclability, it will still reduce the specific capacity and increase the irreversibility loss [138, 140, 144, 146]. Typically, along with particle size control, Si-C nanocomposites exhibited stable cycling up to 100 cycles at the 1 C rate, as reported by Magasinski et al. [147]. Reversible capacities over five times higher than for state-of-art anodes (1950 mAh g^{-1}) and stable performance are attained, as shown in Figure 2.16. More recently, graphene-based composites have gained enormous attention and appear very promising for the advanced lithium-ion batteries [76, 106, 148-159]. Graphene is suitable for composite nanostructures due to its atomically thin layers high electronic conductivity, chemical stability, and high surface area [156, 160]. Paek et al. [161] have synthesized graphene nanosheet (GNS) via the chemical reduction of exfoliated graphite oxide materials, followed by dispersing the SnO_2 with GNS in a suspension to obtain SnO_2-graphene composite. As shown in Figure 2.17, the cycling performance of SnO_2-GNS electrode shows a remarkable enhancement in comparison with the bare SnO_2 nanoparticles, with reversible capacity of 810 mAh g^{-1}.

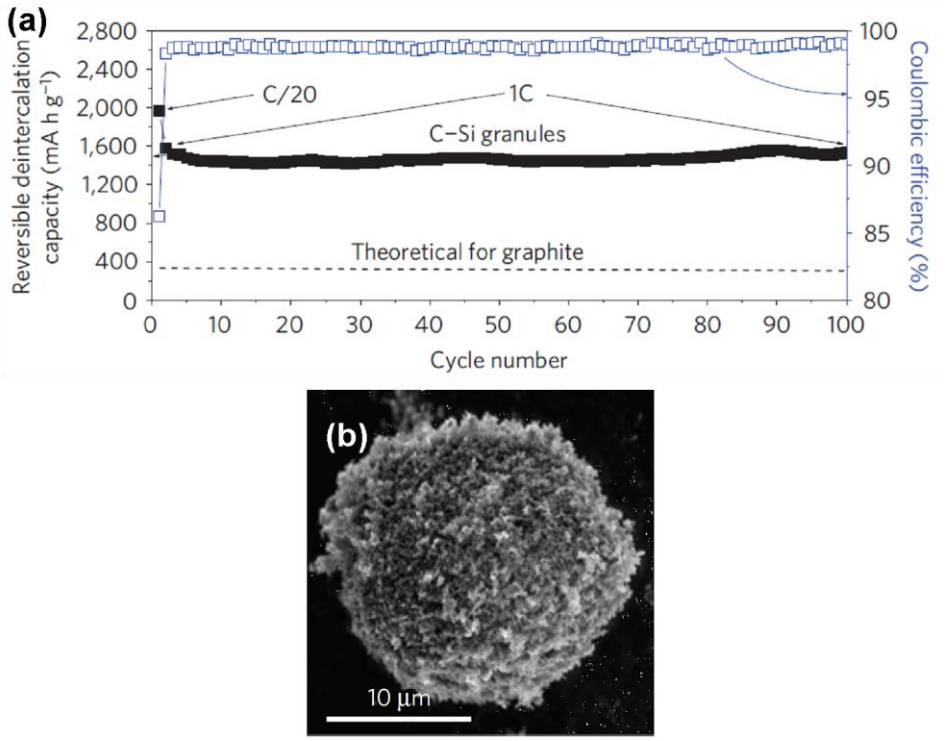

Figure 2.16. (a) Electrochemical performance of Si-C at 1 C rate, and (b) SEM image of Si-C nanocomposite spherical granule [147].

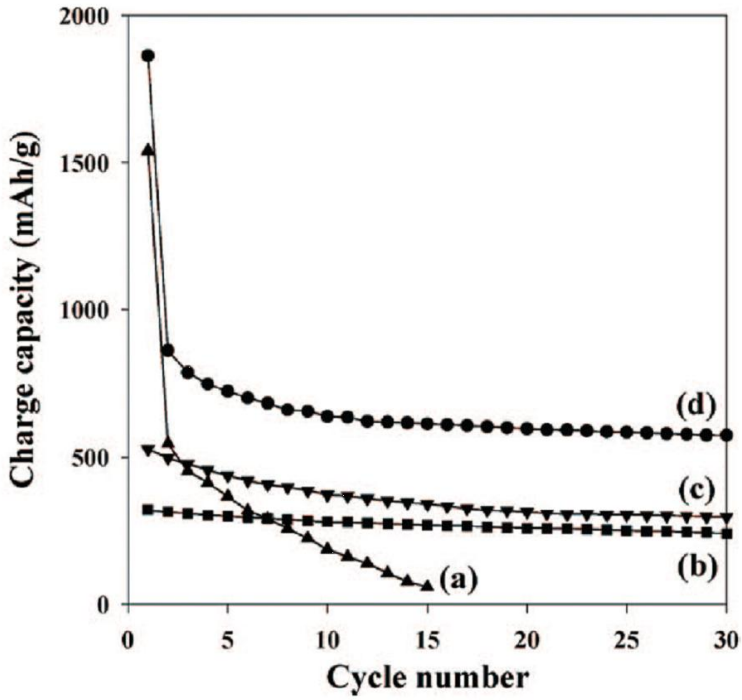

Figure 2.17. Cyclic performances for (a) bare SnO_2 nanoparticles, (b) graphite, (c) GNS, and (d) SnO_2/GNS [161].

4) Conducting polymer-based composite. Another approach to circumvent the volume expansion and low conductivity of alloy anode is by coating with conducting polymers such as polypyrrole (PPy), polyaniline (PANI), and polythiophene (PTh) [162-166]. Previous studies have shown that SnO_2-PPy composite showed improved capacity and cycle life compared with pure SnO_2, since the conductive PPy in the composite could effectively buffer the volume changes during the lithium insertion/extraction process [163]. PPy also acts as an efficient host matrix to prevent cracking and pulverization of the SnO_2 electrode due to the phase transitions, thus improving the cycling stability of the electrode. This has been confirmed by SEM images (Figure 2.18), where the cracks in the SnO_2-PPy electrode are much smaller than in the bare SnO_2 electrode.

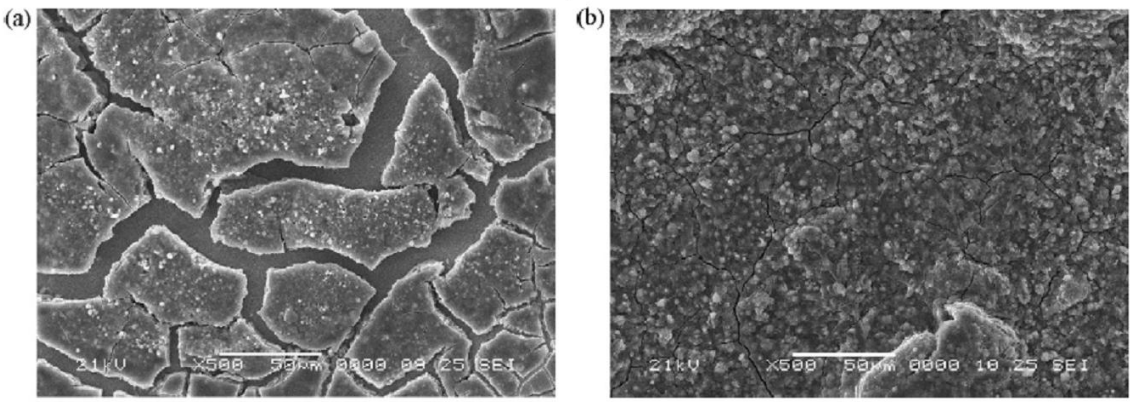

Figure 2.18. SEM images of (a) bare SnO_2 electrode, and (b) SnO_2-PPy electrode after 20 cycles [163].

2.6.3 Transition metal oxides

Numerous transition metal oxides have been proposed for negative electrodes in rechargeable lithium-ion batteries after Poizot et al. [26] reported reversible Li storage

in several transition metal oxides (M = Fe, Ni, Co, and Cu) by a reduction to the metal. This type of compound, which has a rock salt structure, exhibited capacities much higher than those of carbon, with 100% capacity retention for up to 100 cycles [51]. Table 2.6 shows the theoretical electromotive force (EMF) values, Gibbs free energy of formation ($\Delta_f G$), and the theoretical Li storage capacities of binary metal compounds [167].

Table 2.6. EMF values, Gibbs free energy of formation, and Li storage capacities for binary metal compounds [167].

MX	$\Delta_f G$ (kJ/mol)	EMF (V)	Li storage capacity (mAh/g)	MX	$\Delta_f G$ (kJ/mol)	EMF (V)	Li storage capacity (mAh/g)	MX	$\Delta_f G$ kJ/mol	EMF (V)	Li storage capacity (mAh/g)
LiF	−589	⋯	0	MnO_2	−465	1.708	1233	Ga_2O_3	−998	1.188	858
TiF_3	−1361	1.396	767	Mn_2O_3	−881	1.431	1018	GeO_2	−521	1.562	1025
VF_3	−1227	1.863	745	MnO	−363	1.032	756	Al_2O_3	−1582	0.180	1577
MnF_2	−807	1.919	577	FeO	−251	1.61	746	MgO	−569	−0.0354	1330
MnF_3	−1000	2.647	719	Fe_2O_3	−742	1.631	1007	SiO_2	−856	0.694	1784
FeF_2	−663	2.664	571	CoO	−214	1.802	715	B_2O_3	−1194	0.850	2300
FeF_3	−972	2.742	712	NiO	−212	1.954	718	Ce_2O_3	−1708	−0.038	490
CoF_2	−627	2.854	553	CuO	−128	2.248	674	Li_2S	−439	⋯	0
CoF_3	−719	3.617	694	Cu_2O	−148	2.147	375	TiS_2	−402	1.233	957
NiF_2	−604	2.964	554	ZnO	−320	1.252	659	CoS_2	−146	1.898	871
CuF_2	−492	3.553	528	SnO	−257	1.566	398	Co_3S_4	−487	1.644	703
ZnF_2	−714	2.404	518	SnO_2	−520	1.582	711	CuS	−53	1.998	561
SnF_2	−601	2.984	342	Ag_2O	−11.2	2.855	231	Cu_2S	−86	1.827	337
AgF	−187	4.156	211	RuO_2	−280	2.12	805.6	FeS	−102	1.747	610
PbF_2	−617	2.903	218	MoO_2	−533	1.669	838.2	FeS_2	−160	1.861	893
CaF_2	−1173	0.0259	686	MoO_3	−668	1.75	1117	MnS	−218	1.144	616
BaF_2	−1158	0.104	306	SrO	−561	0.005	517	MnS_2	−225	1.692	900
Li_2O	−562	⋯	0	SrO_2	−573	1.428	896	MoS_2	−226	1.69	670
TiO	−513	0.253	839	Y_2O_3	−1817	−0.226	712	Ag_2S	−40.7	2.06	216.3
TiO_2-R	−890	0.608	1342	ZrO_2	−1040	0.217	870	Li_3N	−129	⋯	0
TiO_2-A	−883	0.625	1342	NbO	−392	0.881	492	TiN	−309	−0.623	1301
VO	−404	0.819	801	NbO_2	−795	0.852	858	Co_3N	−34	0.326	421
V_2O_3	−1139	0.945	1073	Nb_2O_5	−1766	1.082	1008	Fe_4N	−3.722	0.432	338.7
VO_2	−1318	−0.502	1293	In_2O_3	−831	1.477	579	Mn_4N	−105	0.083	459
V_2O_5	−1419	1.441	1474	Sb_2O_3	−634	1.817	552	Mn_5N_2	−155	0.176	531
Cr_2O_3	−1058	1.085	1058	PbO	−189	1.933	721				
Cr_3O_4	−1531	~0.93	975	CeO_2	−1025	0.257	623				

Furthermore, these transition metal oxides do not alloy with Li, and their mechanism of Li reactivity differs from the classical processes. The conversion reaction proceeds according to equation (2.17).

$$M_xO_y + 2yLi^+ + 2ye \leftrightarrow yLi_2O + xM \quad (2.17)$$

The reaction is reversible in the voltage range of 0-3 V, where the highly reactive metallic nanodomains are embedded in a Li_2O matrix, which is generated in situ during the first reduction of the metal oxide [26]. Similar to the Li-alloying process, the conversion reaction leads to volume variation upon electrochemical cycling. Therefore, the efficient approaches discussed above to overcome this problem, such as by using nanoscale and nanocomposite materials, are applicable to metal oxide based anode materials as well.

NiO has a theoretical capacity of 718 mAh g^{-1} when it is used as anode in lithium-ion batteries. However, NiO exhibits low electrical conductivity (< 10^{-13} Ω^{-1} cm^{-1}) at room temperature and is classified as a Mott-Hubbard insulator [168, 169]. Nanocrystalline nickel oxide (NiO) was prepared using the spray pyrolysis method as reported by Oh et al. [170]. The NiO powders sintered at 500 °C, which consist of spherical particles with a mean diameter of 0.5-2 μm, delivered a first discharge capacity of 1031 mAh g^{-1}. However, this material displays fast capacity fade (Figure 2.19(a)). Another example was spherical NiO nanoshafts synthesized through chemical precipitation, followed by thermal decomposition [171]. Similarly, capacity fading was observed for the spherical NiO nanoshaft electrode, as shown in Figure 2.19(b). Several works on NiO-carbon nanocomposite [172-174] and NiO-PANI [175] nanocomposite have improvements in the performance of NiO.

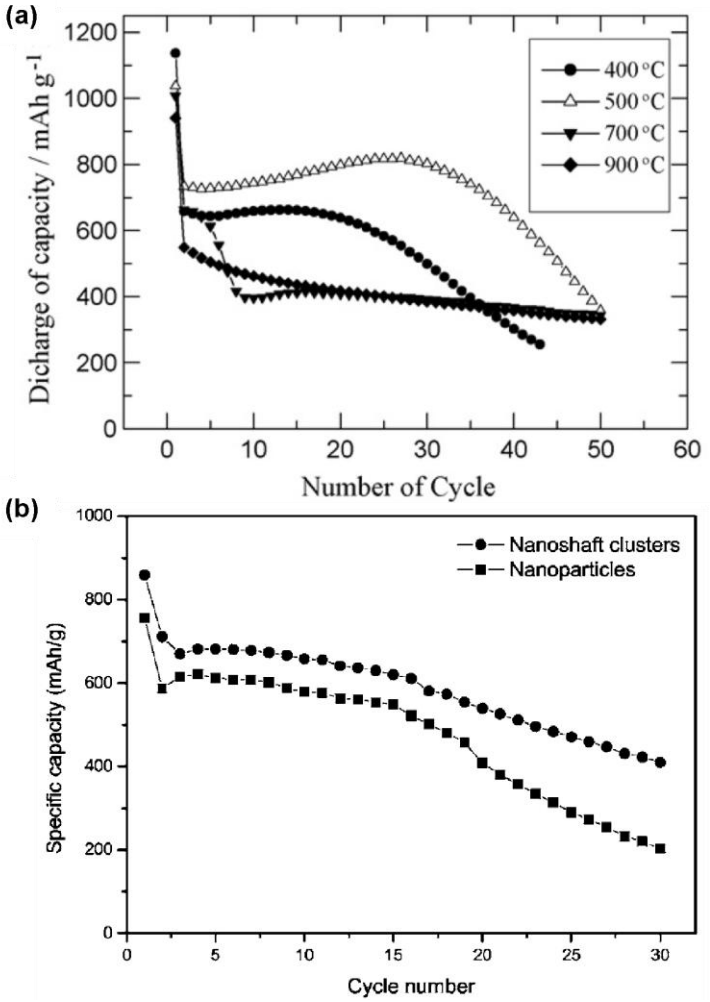

Figure 2.19. Discharge capacity vs. number of cycles for NiO electrode at a current density of (a) 1 mA cm^{-1} [170], and (b) 50 mA g^{-1} [171].

2.7 Positive electrode for lithium-ion batteries

2.7.1 Layered-type transition-metal dioxides

Several types of transition metal oxides, $LiMO_2$ (M = Co [10, 11, 176], Mn [177-179], Ni [180-182], and Fe [183-185]), which show the α-$NaFeO_2$-type structure (Figure 2.20), have been proposed as positive electrode.

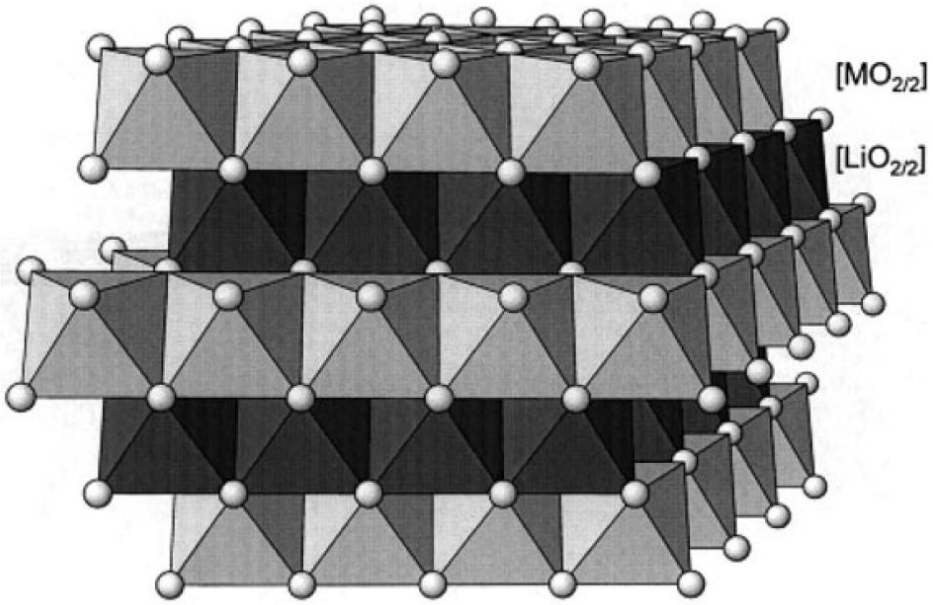

Figure 2.20. The two-dimensional crystal structure of $LiMO_2$ (M = Ni, Co, V, etc.) of the α-$NaFeO_2$ type [110].

In a cubic close-packed oxygen array, the lithium and transition-metal atoms are distributed in the octahedral interstitial sites in such a way that MO_2 layers are formed consisting of edge-sharing $[MO_6]$ octahedra. Lithium resides in octahedral $[LiO_6]$ coordination between these layers, leading to alternating (111) planes of the cubic rock salt structure. This (111) ordering induces a slight distortion of the lattice to hexagonal symmetry. Complete de-insertion of the lithium ions results in the layered $CdCl_2$ structure type. The oxides are thermodynamically stable only in the intercalated state $LiMO_2$, due to the high electronegativity of oxygen, which leads to a higher ionic character of the metal-oxygen bonds in comparison to the covalent nature of the metal-chalcogen bonds. The resulting negative charge of the transition metal-oxygen layers causes repulsive interactions between adjacent layers, which have to be compensated for by positively charged ions between the adjacent oxygen layers [110].

So far, $LiCoO_2$ has been successfully commercialized due to its high theoretical capacity of 274 mAh g^{-1}, ease of preparation, and excellent cyclability [186, 187]. $LiCoO_2$ shows excellent cyclability when cycled in the composition range $0.5 < x < 1.0$ in Li_xCoO_2. Lithium intercalation beyond this range degrades the layered structure of $LiCoO_2$, resulting in poor cyclability. As a result, only half of the theoretical capacity can be used in a practical battery. Nevertheless, the toxicity and the scarcity of cobalt sources have accelerated the development of alternative positive materials with higher specific capacities and lower costs.

Layered $LiNiO_2$ was also considered as 4 V class positive material, as it showed promising specific capacity and lower cost when compared to $LiCoO_2$. Unfortunately, this compound shows structural and compositional variations depending on the preparation conditions [188-190]. $LiNiO_2$ is difficult to synthesize during the sintering process at temperatures above 600 °C, which is necessary to complete the oxidation from Ni^{2+} to Ni^{3+} in oxygen atmosphere and to obtain a high degree of crystallinity. At high temperatures, $LiNiO_2$ tends to decomposed from $LiNiO_2$ to $Li_{1-x}Ni_{1+x}O_2$ ($x > 0$) which has partially disordered cation occupation at the lithium ion sites [181]. Therefore, optimum conditions are necessary to prepare $LiNiO_2$ in order to have high cycling performance.

The concept of substitution of Co for Ni in $LiNi_{1-x}Co_xO_2$ was adopted, as delithiated $LiCoO_2$ was found to be thermodynamically more stable than its $LiNiO_2$ counterpart. It also inhibits the formation of Ni^{2+} impurities and stabilizes the two dimensional character of the structure [191]. This compound is of particular interest as a safe and inexpensive Li-host material with a high capacity [192]. Due to the modifying of its

crystal structure, $LiNi_{0.5}Mn_{0.5}O_2$ showed higher discharge capacity than $LiCoO_2$ and $LiNiO_2$, as shown in Figure 2.21 [193].

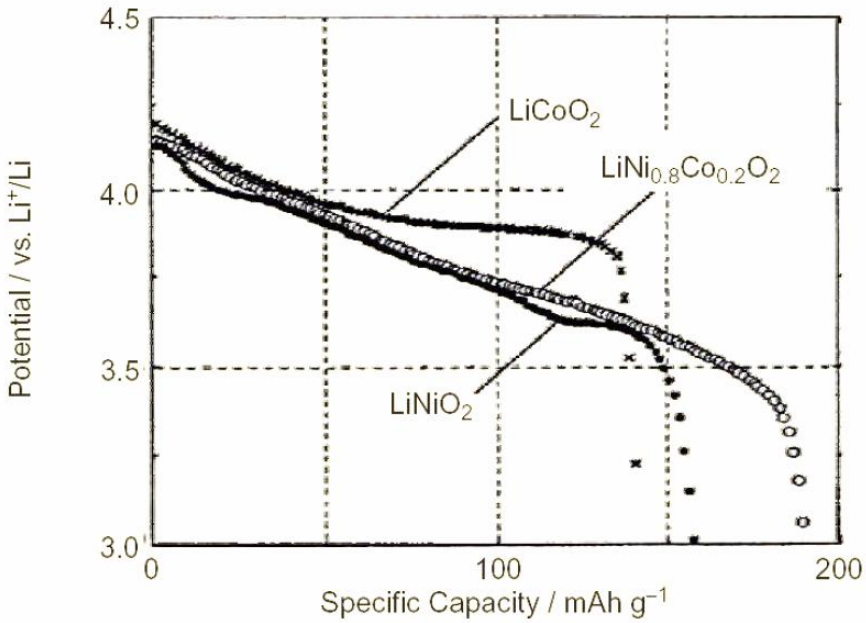

Figure 2.21. Discharge curves of $LiCoO_2$, $LiNiO_2$, and $LiNi_{0.8}Co_{0.2}O_2$ electrode [193].

Another promising candidate cathode materials is layered $LiMnO_2$ which, shows advantages in cost, safety, a high theoretical capacity of 285 mAh g^{-1}, and thermodynamic stability when crystallized in the orthorhombic space group (*Pmmn*) [194]. The structure of orthorhombic $LiMnO_2$ (*o*-$LiMnO_2$) could be described as a modified rock salt type with a distorted cubic close-packed oxygen anion array, as illustrated in Figure 2.22. The distribution of lithium and manganese cations in the octahedral interstitial sites in such a way generates zig-zag layers of edge-sharing [LiO_6] and [MnO_6] octahedra [110].

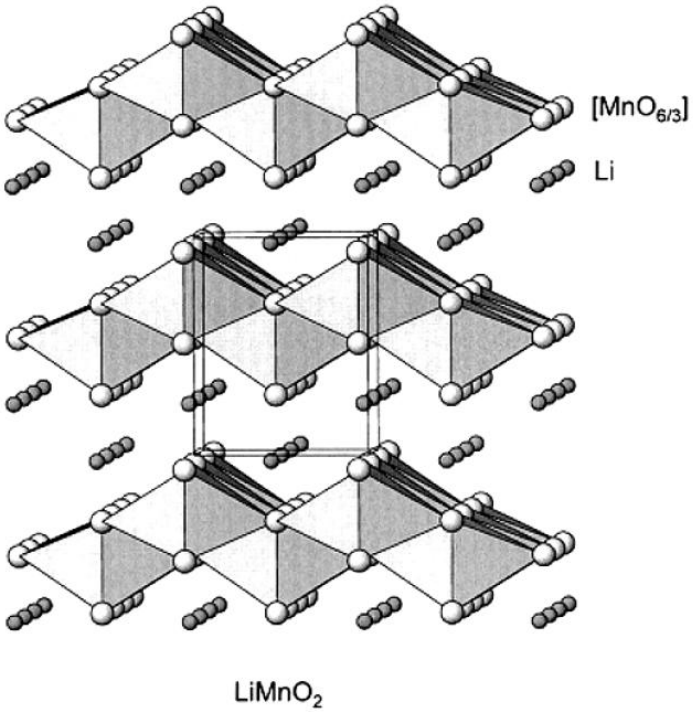

Figure 2.22. The two-dimensional crystal structure of $LiMnO_2$ [110].

Several reports have demonstrated that *o*-$LiMnO_2$ has good cyclability, although this material exhibits phase transformation into spinel-like $Li_xMn_2O_4$ during prolonged cycling [177-179, 195]. In addition, the effects of Jahn-Teller distortion on the deterioration of the *o*-$LiMnO_2$ structure are hardly noticeable in comparison with the case for spinel $LiMn_2O_4$ [196, 197]. Much effort is still needed to develop a more economically efficient route to synthesize *o*-$LiMnO_2$ with well-defined morphology. Recently, electrochemical investigation of *o*-$LiMnO_2$ showed that the capacity and cyclic behavior are greatly influenced by the synthetic route and that low temperature synthesized *o*-$LiMnO_2$ offered better properties than the cathode materials prepared at high temperature [198]. Therefore, some hydrothermal routes that operated at low temperature were developed to prepare the material on the nanoscale [179, 199-201]. Wu et al. [202] have prepared *o*-$LiMnO_2$ via a hydrothermal process consisting of two steps. The first step is the formation of Mn_3O_4 precursor, which is followed by the

hydrothermal conversion from Mn_3O_4 precursor to the final product of *o*-$LiMnO_2$, which is a time-consuming step. A one-step hydrothermal method has been reported by Liu et al. [179], employing Mn_2O_3 and LiOH as the starting materials. Under optimized hydrothermal conditions, pure-phase *o*-$LiMnO_2$ was obtained and showed higher capacity when compared with the commonly prepared *o*-$LiMnO_2$.

2.7.2 Polyanionic materials

Polyanion-based compounds, $Li_xM_y(XO_4)_z$ (M = metal; X = P, S, Si, Mo, W, etc.) have been proposed as promising cathode materials for Li-ion batteries. Since the pioneering work of Padhi et al. [14], $LiFePO_4$ is gaining significant attention and perceived as being 'green'. $LiFePO_4$ has advantages in terms of high specific capacity (170 mAh g^{-1}), good thermal stability, and excellent cycling performance. Additionally, $LiFePO_4$ possesses a flat voltage plateau at 3.4 V vs. Li^+/Li, which is compatible with most existing organic electrolytes [203].

$LiFePO_4$ forms in the orthorhombic olivine structure with *Pnma* space group, in which the strong P-O covalency stabilizes the Fe^{3+}/Fe^{2+} redox couple through the Fe-O-X inductive effect [203], as shown in Figure 2.23. Oxygen atoms shows a slightly distorted hexagonal close packed arrangement [14]. FeO_6 and PO_4 form the zigzag skeleton by sharing oxygen, and Li-ions are located in the octahedral channel. The FeO_6 octahedra are connected through the corners in the *bc* plane, and LiO_6 grows as a linear chain along the *b*-axis, while each PO_4 tetrahedron shares edges with one FeO_6 and two LiO_6 [204]. The PO_4 tetrahedral structure is the reason for the good phase stability during lithium de-intercalation [14, 205-207].

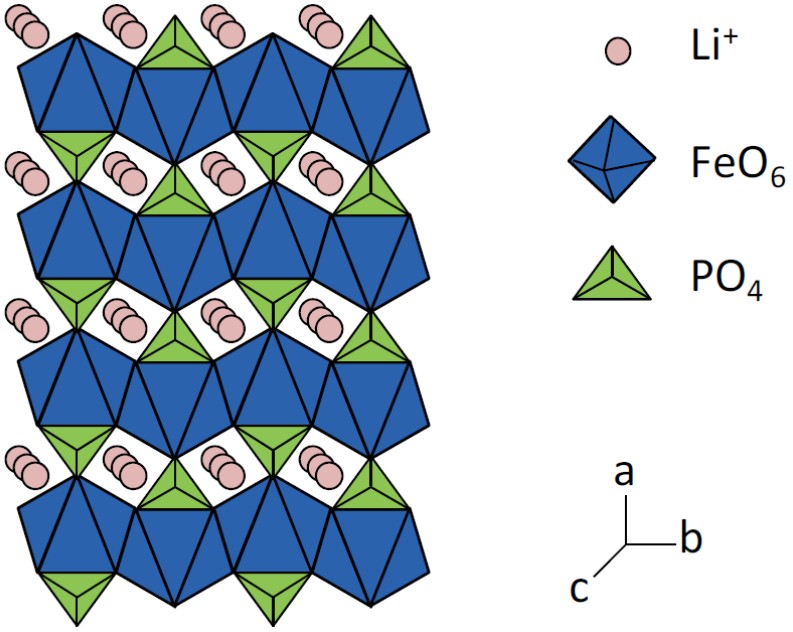

Figure 2.23. Crystal structure of $LiFePO_4$ [204].

$LiFePO_4$ power performance is limited by low electronic conductivity (10^{-9}-10^{-10} S cm^{-1}) as well as by the slow one-dimensional lithium ion diffusion, which is an impediment to realize high rate capability [14, 208], a parameter critical for high power applications. Therefore, much attention has been focused on doping or coating $LiFePO_4$ with an electronically or ionically conductive component, as well as downsizing the particles to the nanoscale, which has proven to be an efficient strategy because of the greatly reduced distance for ionic and electronic transport [50]. Jin et al. [209] have shown that the electronic conductivity of $LiFePO_4$ was significantly improved from 10^{-9} S cm^{-1} to 1.08×10^{-1} S cm^{-1} for $LiFePO_4$/multi-walled carbon nanotubes (MWCNTs). A facile method has been developed by Wang et al. [210] to synthesize nanosized $LiFePO_4$ completely coated with carbon from a low cost Fe^{3+} salt. High power performance was achieved, with the discharge capacity of the composite delivering a capacity of 90 mAh g^{-1} at the current density of 60 C. In addition, a highly ordered mesoporous $LiFePO_4$/C

nanocomposite has been developed [203], and the the composite exhibited a high capacity of 166 mAh g^{-1} at the 0.1 C rate, which nearly approaches the theoretical capacity of $LiFePO_4$. These results showed that particle morphology or architecture has a great influence on the performance of materials. Other than carbon, conducting polymers were also proposed as a good conductive matrix to improve the electrochemical performance of $LiFePO_4$ [75, 211, 212]. Huang and Goodenough [211] have systematically investigated the enhancement of capacity of $LiFePO_4$ at high rates of charge and discharge by substitution of PPy and PANI. The overall electrochemical properties of the composites are improved by this approach.

Other attractive species in the polyanionic family include fluorophosphates, fluorosulphates, and silicates [50]. Shifting from $[PO_4]^{-3}$ to $[PO_4F]^{4-}$, $[SO_4F]^{3-}$, or $[SiO_4]^{4-}$ permits tuning of the electrode properties, such as voltage, through changes in the charge balance and lattice structure [213-216]. However, the drawback of the polyanion-based cathodes is low material packing density, which is not suitable for practical application in large batteries.

2.7.3 Vanadates

The vanadates $Li_{1+x}V_3O_8$, $Na_{1+x}V_3O_8$, and $Mg(V_3O_8)_2$ are insertion compounds, where the alkaline or alkaline-earth metal atoms act as pillars between the vanadium oxide units. They stabilize the oxide structure during insertion/de-insertion processes and optimize the space between the vanadium oxide units, thus enhancing the lithium diffusion rate [110]. The monoclinic structure of $Li_{1+x}V_3O_8$ and $Na_{1+x}V_3O_8$ is illustrated in Figure 2.24. These compounds have a layered structure composed of octahedral and

trigonal bipyramidal ribbons that can swell, just as in other layered compounds, and can intercalate lithium [9].

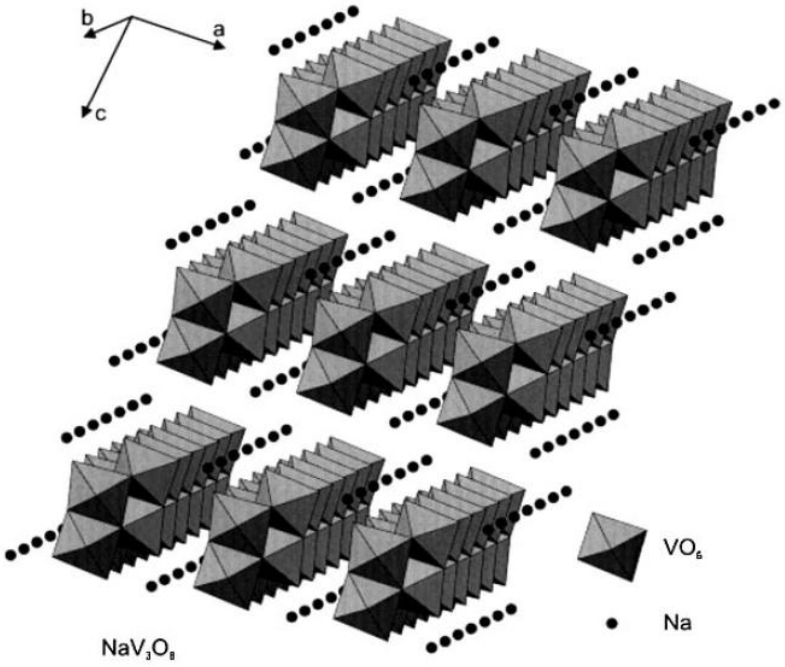

Figure 2.24. Crystal structure of NaV_3O_8 [110].

Lithium vanadium oxide, LiV_3O_8, has attracted considerable interest as excellent alternative candidates to the $LiCoO_2$ cathode that is presently commercially used. This oxide has a layered structure with attractive characteristics such as low cost, large specific capacity, and facile preparation [70, 217], which is of practical interest for lithium-ion battery application. It is generally agreed that the electrochemical performance of LiV_3O_8 mainly depends on the preparation process [218]. The earliest method used to synthesize LiV_3O_8 was by reacting Li_2CO_3 and V_2O_5 at high temperature for 10 h [219, 220], which yields material with a low capacity of 180 mAh g^{-1} in the range of 1.8-4.0 V. The effect of the synthesis method on the electrochemical performance was studied systematically by West et al. [221]. They reported that

amorphous material increased the capacity above 2.0 V from 3-4 lithium per mole of LiV_3O_8 at 6-200 μA cm^{-2}.

Recently, numerous works have been focused on the preparation of LiV_3O_8 nanostructures such as nanorods [222, 223], nanosheets [224, 225], and nanotubes [226]. It has been shown that using nanoparticles and nanostructures for the positive electrode material greatly improves charge/discharge rates by increasing the electrode/electrolyte interface area [227]. Xu et al. prepared $Li_{1+x}V_3O_8$ nanorods by the hydrothermal reaction from LiOH and V_2O_5 precursor. The results showed high discharge specific capacity of 302 mAh g^{-1} with 278 mAh g^{-1} retained after 30 cycles for the sample annealed at 300 °C [222]. More recently, Cui et al. used a combined sol-gel reaction and hydrothermal treatment to prepare LiV_3O_8 nanotubes [226]. However, the disadvantage of these materials was the capacity fading, which took place very rapidly upon cycling. Doping with conductive agent such as carbon or conducting polymers seems to be an attractive route to overcome these problems.

2.7.4 Metal sulfides

Metal sulfides (MS_x) (M = Fe, Ni, Cu, Mo, and Ti) are considered as promising cathode materials for high energy rechargeable lithium batteries because of their high theoretical capacities and relatively low cost [228-235]. They showed higher electronic conductivity and higher utilization in Li/MS_x cells with liquid electrolytes as compared with elemental sulfur. In addition, the potential of the transition-metal sulfides versus lithium in the conversion process reactions can be tuned continuously from 0 to 3.5 V by changing the nature of the anion chalcogenide. This also depends in the

ionocovalence of the bonding between the transition metal and the chalcogenide [167]. Unfortunately, the Li/MS_x cells with liquid electrolytes demonstrated degradation with cycling. Poor cyclability of the Li/MS_x cells could be related to (1) the structural irreversibility of the active materials for the Li insertion/extraction; (2) the formation of polysulfides during the charge-discharge process, which were soluble in non-aqueous liquid electrolyte, leading to the loss of the active materials; (3) the partial loss of the electrical contact among the cathode active materials and current collector; and (4) the formation of metal sulfates at the surface of MS_x by exposure to oxygen and moisture, which could form a barrier for migration of Li-ions inside the active materials, as well as degrading the electrolyte during the electrochemical tests [236].

Choi et al. [237] have reported the electrochemical performance of pyrite (FeS_2) using three types of organic electrolytes: 1 M lithium bis(trifluoromethylsulfonyl)imide (LiTFSI) in tetra(ethylene glycol) dimethyl ether (TEGDME) or a mixture of TEGDME and 1,3-dioxolane (DOX), and 1 M $LiPF_6$ in a mixture of ethylene carbonate (EC) and dimethyl carbonate (DMC). It was found that TEGDME based electrolyte is better suited for performance of Li/FeS_2 cells at room temperature compared to EC/DMC, as shown in Figure 2.25.

Systematic studies of covellite (CuS) cells with the electrolyte consisting of 1 M $LiPF_6$ in a mixture of ethyl carbonate and ethyl methyl carbonate (EC-2EMC) were reported by Chung and Sohn [238]. CuS undergoes a two-stage reaction, as can be observed in the voltage profile in Figure 2.26. However, the second plateau reactions are not reversible, which is partially due to the formation of soluble Li_2S, resulting in poor cyclability when cycling between 2.6 and 1.5 V.

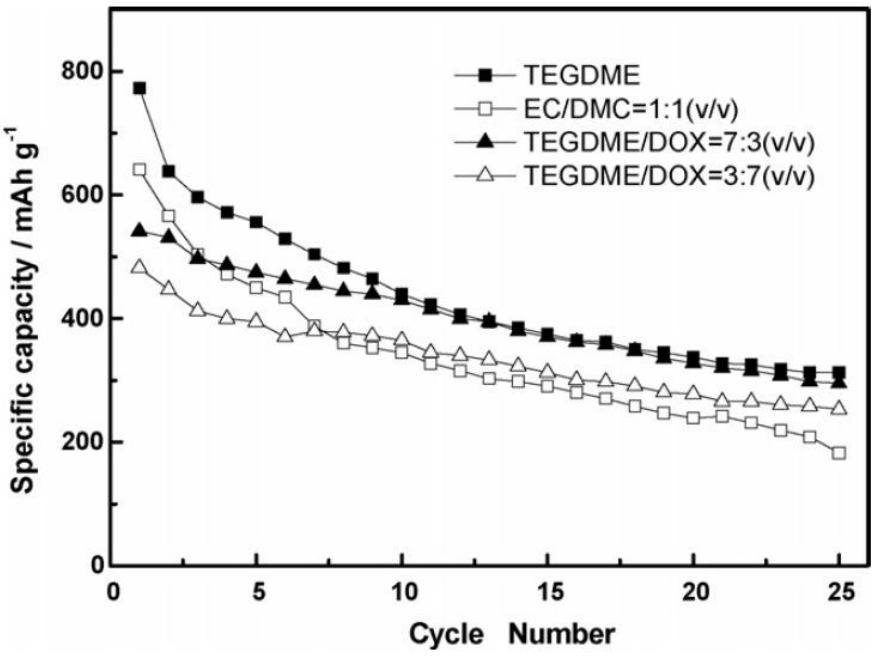

Figure 2.25. Cycling performance of Li/FeS_2 cells using various electrolytes at room temperature [237].

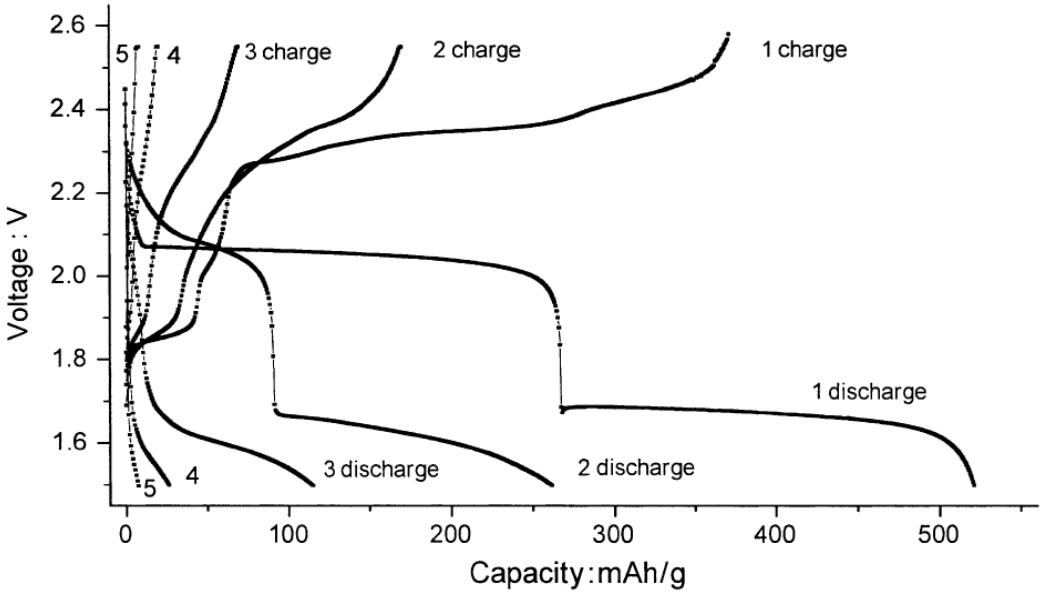

Figure 2.26. Charge-discharge profile of CuS electrode at room temperature [238].

Nickel sulfide (NiS) has attracted considerable attention because of its outstanding features, including a theoretical capacity of 590 mAh g^{-1} and good electronic conductivity [229]. NiS exists in two phase: the high-temperature phase, α-NiS (hexagonal), and the low-temperature phase, β-NiS (rhombohedral). The α-β phase transformation takes place between 282 and 379 °C [239]. Recently, several methods have been developed to prepare NiS with various morphologies. Zhu et al. [240] have prepared hierarchical NiS hollow spheres by using silica nanospheres as templates with large surface area and enhanced structural stability. NiS nanotubes obtained by the directional infiltration self-assembly route in anodized aluminum oxide (AAO) templates were also reported [241]. Wang et al. [235] have reported that the capacity and cycle life of the NiS electrode in electrolyte consisting of 1 M LiTFSI in polyethyleneglycol dimethylether (PEGDME) was significantly improved. This may be because the dissolution of the active material in this electrolyte is reduced compared with the conventional organic solvent-based electrolyte.

2.8 Polymer electrolytes

The science of polymer electrolytes, which encompasses the disciplines of electrochemistry, polymer science, organic chemistry, and inorganic chemistry, is a highly specialized interdisciplinary field. Ion-conducting polymers (or polymer electrolytes) have attracted considerable attention due to their vast applications in the development ionic devices in the solid state. These materials have useful chemical and mechanical properties that allow ease of fabrication in thin film form at desired sizes. They also have the ability to form proper electrode-electrolyte contact [242].

The development of the polymer electrolyte began because scientists recognized the potential that polymers could be electronically insulating elements with low ionic resistance and could eventually be used as the electrolyte in a battery. Fenton et al. [54] launched the study of polymer electrolytes in 1973, but their technological significance was not appreciated until the research undertaken by Armand et al. [243] in the late seventies. Since then, various type of polymer electrolyte films have been developed using various methods, such as casting from a polymer solution [244], evaporation methods [245], and in situ plasma polymerization techniques [246]. The electrolyte material must show high ionic conductivity and be dimensionally stable, since it will also act as separator in the battery. Therefore, it is necessary to prepare polymer electrolyte with adequate mechanical strength. In addition, polymer electrolyte with high cationic transport number, rather than anionic, is also important because concentration gradients caused by the mobility of both cations and anions in the electrolyte arise during discharging, which may result in premature battery failure [247]. Basically, polymer electrolytes can be classified into the following categories [35, 248].

1) Solid polymer electrolytes (SPEs). In SPEs, the polymer host itself is used as a solid solvent along with Li salt and does not contain any organic liquids. The SPEs suffer from poor ionic conductivities (10^{-5} S cm^{-1} at 20 °C), but are safer due to the absence of any organic solvent which can cause environmental hazards. SPE films can be prepared either using the solution cast technique [249-251] or the hot-press technique [252, 253].
2) Plasticized solid polymer electrolytes. Due to the low ionic conductivity of SPEs, plasticizers such as ethylene carbonate (EC), propylene carbonate (PC),

poly (ethylene glycol) (PEG), and dibutyl phthalate (DBP) are incorporated into the SPEs. Such an addition not only decreases the degree of crystallinity, but also increases the segmental motion of the polymer chain. They also support ion dissociation, resulting in greater numbers of migrating ions for charge transport.

3) Gel polymer electrolytes (GPEs). GPEs are also known as hybrid polymer electrolytes, formed by trapping liquid electrolytes in a polymer matrix. The advantage of this type of electrolyte is that higher ionic conductivity can be obtained as compared with SPEs. The ion conduction in these electrolytes takes place through the liquid electrolyte, with the host polymer mostly providing the structural support. Unfortunately, a loss of mechanical properties is observed in GPEs, and liquid electrolytes tend to provoke undesired interfacial reactions of the GPEs with electrodes during cell operation [254, 255]. This may induce vigorous proliferation of a resistive layer on the electrodes, which hinders ionic transport at the interface of the GPE and the liquid electrolyte.
4) Composite polymer electrolytes (CPEs). More attention has been focused on CPEs, wherein nanosized fillers are added to the SPEs. It has been reported that addition of nanosize fillers, such as zeolites, super-acid sulfated zirconia, alumina (Al_2O_3), silica (SiO_2), and titania (TiO_2), not only improved the transport properties, but also the mechanical and electrochemical properties of the SPEs [256-258].

There are numerous polymers that have been developed such as poly (ethylene oxide) (PEO) [259-261], poly (acrylonitrile) (PAN) [262, 263], poly (vinyl chloride) (PVC) [264, 265], poly (methyl methacrylate) (PMMA) [266, 267], and polyvinylidene difluoride (PVdF) [268, 269]. Poly (ethylene oxide) (PEO) is a semi-crystalline

polymer, and about 80% of the bulk is crystalline at room temperature [35]. The donor oxygen atoms in the PEO backbone can solvate the metal cation M^+, and the structure of the complex depends on the ion concentration and the temperature. PEO was the first polymer reported to exhibit high ionic conductivity (10^{-3}-10^{-4} S cm^{-1}) at elevated temperatures when complexed with alkali metal salts [69, 270, 271], however, these electrolytes suffer from low ionic conductivity values in the range of 10^{-7}-10^{-8} S cm^{-1} due to the high crystallinity of PEO [272]. Furthermore, the lithium transference number is generally low, of the order of 0.2–0.4, and may result in concentration polarization, limiting the rate (power) of the battery [85]. Investigations on PEO with various amounts of lithium bis(trifluoromethanesulfonyl) imide (LiTFSI) have been carried out. It was found that crystallization and melting phenomena were identified as the main factors determining the ionic conductivity of the system [273]. Therefore, better understanding of crystallization is necessary for the use of PEO as a solid polymer electrolyte.

Poly (vinylidene fluoride) (PVDF) as a host has drawn the attention of many researchers due to its excellent mechanical properties, high chemical resistance, good thermal stability, and high piezoelectric and pyroelectric coefficients [274]. PVDF also exhibits high anodic stability and a high dielectric constant (ε_r = 8.4) which helps in greater ionization of lithium salts [275] and strongly electron-withdrawing fluorine atoms (-C-F). Watanabe et al. [276] have reported that PVDF can form homogeneous SPE films with a lithium salt, along with EC and/or PC, in the proper compositions. In later studies, Chiang et al. [277] revealed that the ionic conductivity of PVDF/$LiPF_6$ gel polymer electrolyte was enhanced by three orders of magnitude by plasticization with EC/PC solution, when compared with PVDF solid polymer electrolyte. Such

improvement in ionic conductivity can be explained by the conduction mechanism in PVDF gel polymer electrolyte, which is associated with swollen polymer network chains via EC/PC molecules, which also form a solid amorphous polymer region.

Poly (methyl methacrylate) (PMMA) is one of the polyethers extensively studied due to its ability to solvate inorganic salts to form a polymer-salt complex. PMMA as a gelatinization agent in the electrolyte was first reported by Iijima et al. [278] in 1985, and a conductivity of 10^{-3} S cm^{-1} at 25 °C was attained with 15 wt.% PMMA. Bohnke et al. [279] examined the rheological and electrochemical properties of PMMA-$LiClO_4$/PC films. Their results showed that the addition of PMMA in various proportions increased the viscosity of the polymer solution. In contrast to previous results, the ionic conductivity was considerably reduced upon the addition of PMMA. However, the room temperature conductivity remained close to that of a liquid electrolyte.

Over the past few years many papers have been published which describe the introduction of polymer blends as matrices in SPEs [280-284]. The main objective of these studies was to improve the mechanical properties of polyether-salt complexes. This strategy was originally disclosed by Tsuchida et al. [280] who studied the PEO-$LiClO_4$ system supported by poly(methacrylic acid). The formation of hydrogen bonds between PEO and poly(methacrylic acid) makes this system is fully miscible. The first electrolytes based on immiscible blends were described by Gray et al. [282]. They consisted of PEO/polystyrene and lithium salts. The mechanical properties of these electrolytes are far better than those of the pristine PEO-based system. High porosity of the GPE membrane usually leads to fading mechanical strength. To bypass this limitation, a similar approach was undertaken to improve the mechanical strength of

GPEs. The structure and properties of PVDF/PEO membranes have been studied previously [285, 286]. The addition of PEO to the PVDF improves the porosity and pore connectivity for electrolyte uptake, contributing to high ionic conductivity. However, the mechanical strength of PVDF/PEO blend membranes is lower than for pure PVDF. In addition, blending of poly (acrylonitrile) (PAN) and PVDF-hexafluoropropylene (HFP) increases the mechanical stability and structural rigidity of the porous polymer electrolyte [287]. The phase behavior of PMMA/PVDF is likewise of fundamental interest, since it involves a crystallizable polymer, PVDF, in the presence of chemically dissimilar, amorphous PMMA, which is capable of site-specific intermolecular interaction [288]. There is also evidence that an intermediate amorphous PVDF interphase exists between the crystalline PVDF and the mixed amorphous phases [289]. Furthermore, PVDF has crystallinity, leading to the formation of a spherulitic structure with large holes between them in the PVDF membrane. By adding PMMA into PVDF, the amorphous domain of the membrane is increased by retarding the crystallization of PVDF [290, 291].

Polymer electrolytes represent one of the cornerstones of future development in the area of materials for conversion and storage of energy, which are assumed to gain an increasing importance in the scientific and technological panorama of the current century. Future research efforts should enable significant progress to be made in the next several years. Nevertheless, engineering of the all the battery components in the lithium-ion battery, including the cathode, anode, and electrolyte, is the key factor for the final properties.

Chapter 3

Experimental

3.1 Materials and chemicals

Chemicals and materials used throughout the experiments are listed in Table 3.1.

Table 3.1. List of chemicals and materials used in this thesis.

Materials/chemicals	Chemical formula	Purity (%)	Supplier
1-methyl-2-pyrrolidinone	C_5H_9NO	99.5	Sigma-Aldrich
Acetone	CH_3COCH_3	≥ 99.5	Sigma-Aldrich
Ammonia solution	NH_3	28-30	Merck
Argon gas	Ar		
Carbon black	C	-	Timcal, Belgium
Citric acid trisodium salt dehydrate	$Na_3C_6H_5O_7 \cdot 2H_2O$	99	Aldrich
Cyclohexane	C_6H_{12}	99.5	Sigma-Aldrich
Diethyl carbonate	$C_5H_{10}O_3$	99	Sigma-Aldrich
Ethanol	C_2H_5O	Reagent	Q-Store Australia
Ethylene carbonate	$C_3H_4O_3$	99	Sigma-Aldrich
Ethylene glycol	$HOCH_2CH_2OH$	99.8	Sigma-Aldrich
Glycerin	$HOCH_2CH(OH)CH_2OH$	-	Fluka
Graphite	C	-	Fluka

Hydrochloric acid	HCl	37	Sigma-Aldrich
Hydrogen peroxide	H_2O_2	≥ 30	Fluka
Iron (III) chloride	$FeCl_3$	97	Sigma-Aldrich
Lithium hexafluorophosphate	$LiPF_6$	99.99	Aldrich
Lithium hydroxide monohydrate	$LiOH·H_2O$	98	Aldrich
Lithium iron phosphate	$LiFePO_4$	-	DLG Battery Co. Ltd., China
Lithium metal	Li	99.9	China
LP30 electrolyte	$LiPF_6$ in EC:DMC (1:1 by volume)	-	MERCK KgaA, Germany
Malic acid	$C_4H_6O_5$	99%	Sigma-Aldrich
Methanol	CH_3OH	Reagent	Sigma-Aldrich
N,N-dimethyl formamide	$HCON(CH_3)_2$	99.8	Sigma-Aldrich
n-butanol	$CH_3(CH_2)_3OH$	>99.0	Sigma-Aldrich
Nickel (II) acetate tetrahydrate	$Ni(CH_3COO)_2·4H_2O$	98	Sigma-Aldrich
Nickel nitrate hexahydrate	$Ni(NO_3)_2·6H_2O$	≥ 97	Sigma-Aldrich
Poly(methyl methacrylate)	$(CH_2C(CH_3)(CO_2CH_3))_n$	-	Sigma-Aldrich
Poly(vinylidene fluoride)	$(CH_2CF_2)_n$	-	Sigma-Aldrich
Polypropylene separator	$(C_3H_6)_n$	Celgard 2500	Hoechst Celanese Corporation, USA
Potassium permanganate	$KMnO_4$	≥ 99	Sigma-Aldrich
Pyrrole	C_4H_5N	98	Sigma-Aldrich

Sodium *p*-toluenesulfonate	$CH_3C_6H_4SO_3Na$	95	Aldrich
Sulfuric acid	H_2SO_4	95-98	Sigma-Aldrich
Thiourea	N_2SCH_4	≥ 99	Sigma-Aldrich
Toluene	C_7H_8	99.5	Sigma-Aldrich
Triton X-100	$(C_2H_4O)_nC_{14}H_{22}O$	100	Aldrich
Vanadium pentoxide	V_2O_5	Puriss	Riedel-de Haën

3.2 Experimental procedures

The experiments in this thesis can be classified under three broad categories, including synthesizing of materials (anode, cathode, and gel polymer electrolytes), structural and physical characterizations, and fabrication and electrochemical characterizations. Figure 3.1 shows the overall framework of the experiments.

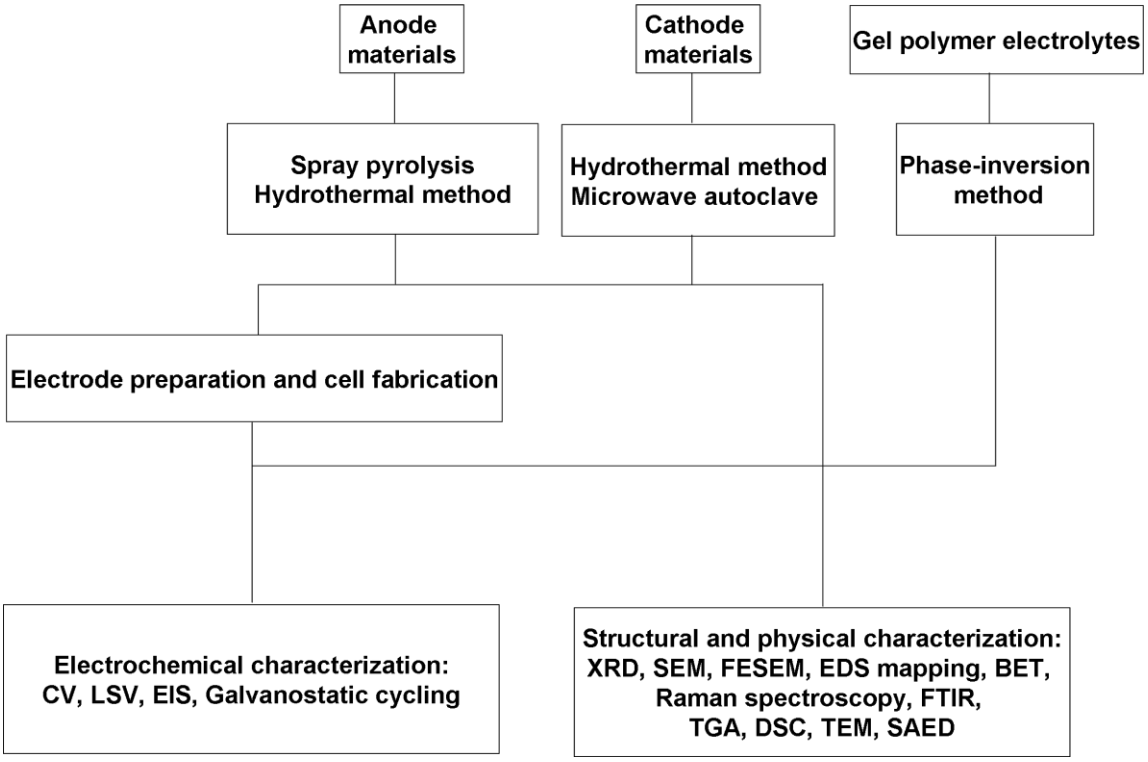

Figure 3.1. The overall procedure of the experiments.

3.3 Synthesis method

Several methods have been adopted to synthesize the anode and cathode materials in this thesis. In this section, the methods are explained in detail.

3.3.1 Spray pyrolysis

Spray pyrolysis equipment consists of a peristaltic pump, a nozzle, the air compressor, a three zone vertical tube furnace, the sample collector, and a suction system, as shown in Figure 3.2. The reaction is carried out by subjecting the precursor solution to temperatures at which pyrolysis of the solute will occur. First, the solution is peristaltically pumped into three-zone spray pyrolysis furnace at an operating

temperature from room temperature to 600 °C, using compressed air as the carrier. The resultant powder is separated from the hot gas steam via a collecting jar through a suction system and collected into an airtight sample bottle. The morphology and crystal structure of the materials can be controlled by modifying the precursor concentration and the temperature parameters.

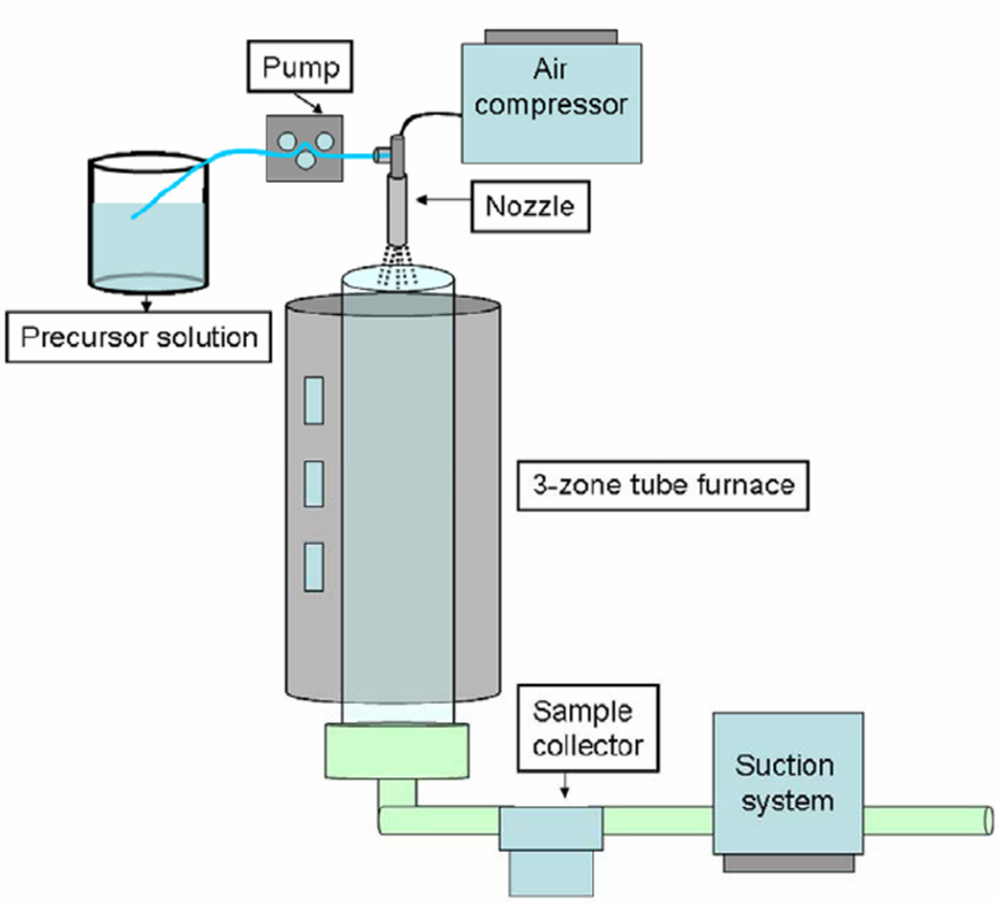

Figure 3.2. Schematic diagram of spray pyrolysis apparatus.

3.3.2 Hydrothermal method

The hydrothermal method is considered as a low temperature method and has been well established. In this thesis, the 4748 Acid Digestion Bomb autoclave from Parr

Instruments was used, as shown in Figure 3.3. It has a 125 mL removable Teflon cup in a stainless steel body with six cap screws in the screw cap to seal the flanged Teflon cup. An expandable wave spring maintains continuous pressure on the seal during the cooling cycle when Teflon parts might otherwise relax and leak. The synthesis reactions can be carried out at temperatures below 250 °C and pressures less than 1900 psi. In a typical experiment, the precursor solution was transferred to the Teflon cup, filling up to 80% of the whole volume, and the autoclave was then kept in an oven for the preset temperature and time. The resultant powder was filtered, washed, and centrifuged to remove the remaining ions.

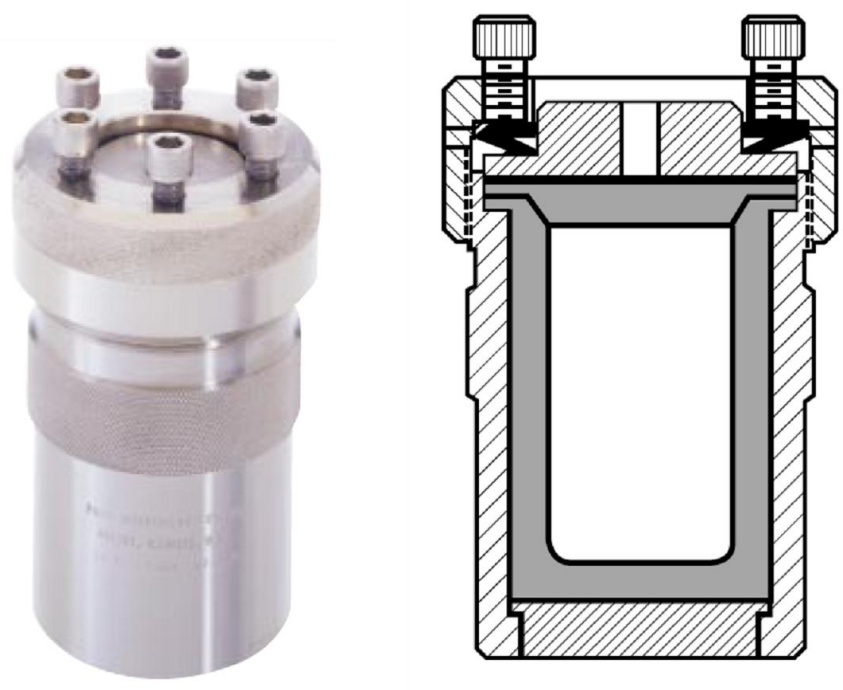

Figure 3.3. 4748 Acid Digestion Bomb from Parr Instruments.

3.3.3 Microwave autoclave method

Another method of synthesis of nanostructures which is receiving considerable interest lately is the use of microwave heating in place of conventional heating. Use of

microwaves for synthesis was first reported in 1986 by Gedye et al. [292]. Here, the MicroSYNTH microwave system (Milestone) controlled by a Labterminal 800 Controller was used (Figure 3.4). It has a 45 mL quartz vessel where reactions take place at temperatures up to 250°C and pressures up to 40 bar. The vessel is hosted in a safety shield which features a built-in pressure control through a preloaded spring with a vent-and-reseal mechanism. In a typical procedure, the precursor solution was transferred into the Teflon lined digestion vessel and fitted with a pressure and temperature probe. The sealed vessels were placed inside the microwave at preset power, time, and temperature.

Figure 3.4. MicroSYNTH microwave system (Milestone) controlled by a Labterminal 800 Controller.

3.4 Structural and physical characterization

3.4.1 X-Ray diffraction (XRD)

X-ray diffraction (XRD) is a non-destructive analytical method which can yield the unique fingerprint of Bragg reflections associated with a crystal structure. The nature of the powders, whether crystalline or amorphous, can be determined using XRD. A crystalline powder is a material that has an internal structure in which the atoms are arranged in an orderly three-dimensional configuration. An amorphous powder is a non-crystalline material that has no definite order or crystallinity. X-rays with a similar wavelength to the distances between planes of the crystal structure can be reflected such that the angle of reflection is equal to the angle of incidence. This is called 'diffraction' and can be described by Bragg's law:

$$2d \sin \theta = n\lambda \tag{3.1}$$

where d is the interplanar spacing, θ the Bragg angle, n is the order of reflection, and λ is the X-ray wavelength. When Bragg's law is satisfied, constructive interference of diffracted X-ray beams occurs, and a 'Bragg reflection' will be detected by a detector scanning at this angle. The position of these reflections is related to the inter-layer spacings of atoms in the crystal structure. The crystal size also can be calculated from the broadening of the peaks according to the Scherrer equation:

$$L = \frac{0.9\lambda}{B\cos\theta} \tag{3.2}$$

where L - crystallite size

λ - 1.5418 Å

B - the peak full-width at half maximum (FWHM) in radians.

In this work, XRD was performed with a GBC-MMA generator and diffractometer using Cu Kα radiation and a graphite monochromator. The systems were interfaced with Visual XRD and Traces software for graphical processing and data manipulations. Powders adhered onto cleaned glass slides, and were dropped with ethanol and left to dry. The glass slide was then placed in the sample holder of the diffractometer and directly scanned at 2θ angles between 5° and 90° at a scan rate of 2° min^{-1}.

3.4.2 Scanning electron microscopy (SEM) or field-emission scanning electron microscopy (FESEM) with energy dispersive spectroscopy (EDS)

A scanning electron microscope (SEM) is a type of electron microscope that captures images of a sample by scanning it with a high-energy beam of electron. The electrons interact with the atoms that make up the sample, producing signals that contain information about the sample's surface morphology, composition, etc. The types of signals produced by an SEM include secondary electrons, back-scattered electrons (BSE), characteristic X-rays, light, the specimen current, and transmitted electrons. The signals result from interactions of the electron beam with atoms at or near the surface of the sample. High magnification images could be obtained using a field-emission scanning electron microscope (FESEM). In the most common or standard detection mode, secondary electron imaging (SEI), the FESEM can produce very high-resolution images of a sample surface, revealing details less than 1 nm in size. Energy dispersive

spectroscopy (EDS) is an accompanying elemental analysis technique that detects atomic numbers 6 through 92 with a detectability limit of approximately 0.1 weight percent. The analysis diameter and depth for EDS is typically a few micrometers. Images obtained in backscatter electron mode offer quick identification of areas with different atomic number. EDS mapping illustrates the distribution of species in the near-surface region. In this experiment, a JEOL JSM 6460A scanning electron microscope (SEM) and JEOL 7500 field-emission scanning electron microscope (FESEM) were used. The sample was mounted onto copper tape for observation.

3.4.3 Transmission electron microscopy (TEM)

The transmission electron microscope (TEM) operates on the same basic principles as the SEM and FESEM. The electron source emits the electrons that travel through vacuum in the column of the microscope. TEM also uses electromagnetic lenses to focus the electrons into a very thin beam, interacting with the sample as it passes through. The TEM is capable of forming a focused electron probe, as small as 20 Å, which can be positioned on very fine features in the sample for diffraction information or analysis of X-rays for compositional information. The brighter areas of the image represent areas where more electrons have passed through the sample. The darker areas represent areas where fewer electrons have passed through as a result of higher specimen density. A TEM can magnify up to about 500,000 times. In this work, TEM investigations were performed using a 200 kV JEOL 2011 instrument, with a JEOL-Energy Dispersive X-ray Spectroscopy (EDS) detector and a JEOL EDS software analysis system. TEM powder samples were prepared by dispersion onto holey carbon support films.

3.4.4 Thermogravimetric analysis (TGA) and differential scanning calorimetry (DSC)

Thermogravimetric analysis (TGA) is a type of thermal analysis technique which measures the amount and rate of change in the mass of a sample as a function of temperature or time in a controlled atmosphere. The measurements are used to determine the thermal and/or oxidative stabilities of materials as well as their compositional properties. In this doctoral work, a Mettler-Toledo thermogravimetric analysis/differential scanning calorimetry (TGA/DSC 1) Star^{e} System was used to determine the amount of carbon, graphene, or polypyrrole (PPy) in the composite samples. The temperature ranged from 25 to 1000 °C at 5 °C min $^{-1}$.

Differential scanning calorimetry (DSC) is another type of thermoanalytical technique in which the difference in the amount of heat required to increase the temperature of a sample is recorded. Basically, when the sample undergoes a physical transformation such as at the glass-transition temperature (T_g), the melting temperature (T_m), and solid-solid transitions, more (or less) heat will need to flow to the sample, depending on whether the process is exothermic or endothermic. DSC also can be used to determine the polymer crystallinity by quantifying the heat associated with melting (fusion) of the polymer. The melting curve of a partially crystalline polymer contains information on the size distribution of the crystallites present in the material. This heat is reported as percent crystallinity by normalizing the observed heat of fusion to a 100% crystalline sample of the same polymer. The crystallinity of the polymer can be calculated from the integral area of the baseline and each melting curve. Therefore, the degree of crystallization of polymer is given by the equation:

$$X_c = \frac{\Delta H_m}{\Delta H_{m,p}} \times 100\% \quad (3.3)$$

where ΔH_m is the heat of fusion for the sample and $\Delta H_{m,p}$ is the heat of fusion for the 100% crystalline sample. In this work, DSC was performed to investigate the degree of crystallization of poly(vinylidene fluoride)/poly(methyl methacrylate) (PVDF/PMMA) gel polymer electrolytes.

3.4.5 Raman spectroscopy

Raman spectroscopy is a spectroscopic technique based on inelastic scattering of monochromatic light, usually from a laser source. Inelastic scattering means that the frequency of photons in monochromatic light changes upon interaction with a sample. Photons of the laser light are absorbed by the sample and then reemitted. The frequency of the reemitted photons is shifted up or down in comparison with the original monochromatic frequency, which is called the Raman effect. This shift provides information about vibrational, rotational, and other low frequency transitions in molecules. Typically, a Raman system consists of four components, including the excitation source (laser), the sample illumination system and light collection optics, the wavelength selector filter (filter or spectrophotometer), and detector (photodiode array, charge-coupled device (CCD) or photomultiplier tube (PMT)). A sample is normally illuminated with a laser beam in the ultraviolet (UV), visible (Vis) or near infrared (NIR) range. Scattered light is collected with a lens and delivered through an interference filter to obtain the Raman spectrum of a sample. Here, Raman spectra of the samples were collected using a JOBIN YVON HR800 Confocal Raman system

from HORIBA Ltd., France with 632.8 nm diode laser excitation on a 300 lines mm^{-1} grating at room temperature.

3.4.6 Fourier transform infrared (FTIR) spectroscopy

Fourier transform infrared (FTIR) is the preferred method for identifying types of chemical bonds in a molecule by producing an infrared (IR) absorption spectrum that is like a molecular fingerprint. In FTIR spectroscopy, IR radiation is passed through a sample. Some of the infrared radiation is absorbed by the sample and some of it is passed through (transmitted). The resulting spectrum represents the molecular absorption and transmission, which is characteristic of the chemical bonds in the sample. By interpreting the infrared absorption, the chemical bonds in the molecule can be determined. There are two common forms of sample preparation for FTIR measurements. First, the fine powder is dispersed in a liquid such as mineral oil (nujol) to form a paste. Secondly, the fine powder is mixed with potassium bromide (KBr), transferred to a die that has a barrel, and pressed. These two methods of sample preparation can be very time consuming and are complicated by difficulties in getting sample to matrix ratios correct and homogeneous throughout the sample. Therefore, the technique of using attenuated total reflectance (ATR) is suitable by placing the powder directly onto the ATR crystal. An ATR operates by measuring the changes that occur in a totally internally reflected infrared beam when the beam comes into contact with a sample. In this doctoral work, the FTIR spectroscopy analyses were carried out using a Shimadzu IRPrestige-21 model. Samples were analysed in ATR mode using a Pike MIRacle accessory equipped with a germanium crystal (Pike Technology).

3.4.7 Brunauer-Emmett-Teller (BET) measurement

Brunauer-Emmett-Teller (BET) is a well known method for the measurement of the specific surface area of a material. This technique is based on gas absorption, in which gas molecules of known sizes are condensed onto the unknown sample surface. After completely covering the surface and opening the pores of each particle with a condensed gas, the surface area analyzer can characterize the surface, including irregularities and pore interiors down to the atomic level. Nitrogen gas is usually used, as its molecular size is well established, and it is inert and high purity. The 'outgassed' sample under high vacuum in its sample tube is immersed in a coolant bath of liquid nitrogen and ready to attract gas molecules into it when they are admitted to the sample tube. The amount of gas adsorbed and the resultant sample pressure are recorded for data manipulation. Here, the specific surface area of the synthesized powders were measured using a NOVA 1000 high-speed gas sorption instrument by Quantachrome Instruments, USA. The BET specific surface area was determined through the 15-points nitrogen adsorption isotherm at 77 K after degassing the powders with nitrogen at 150 °C.

3.5 Electrode preparation and cell fabrication

In electrode preparation, the synthesized powders were mechanically mixed with binder and carbon black, which was followed by dispersion in N-methyl-2-pyrrolidone (NMP) or distilled water. The slurry was spread onto aluminum foil substrates for cathode materials and copper foil substrates for anode materials, and the dried at 100 °C for 24 h in vacuum. After being cut into 1×1 cm^2 sizes, the electrodes was transferred to an

argon-filled glove box to fabricate a coin cell. CR 2303 coin cells were assembled by stacking the electrodes with lithium metal as the counter and reference electrode and polypropylene separator. The liquid electrolyte used in this thesis was either 1 M $LiPF_6$ in ethyl carbonate: diethyl carbonate (EC:DEC, 1:2 by volume), 1 M $LiPF_6$ in EC: dimethyl carbonate (DMC, 1:1 by volume), or 1 M lithium bis(trifluoromethanesulfonyl)imide (LiTFSI) in polyethyleneglycol dimethylether (PEGDME 500).

3.6 Electrochemical characterization

3.6.1 Linear sweep voltammetry (LSV) and cyclic voltammetry (CV)

Voltammetry is one of the techniques preferred to investigate the general electrochemical behavior of the electrodes in lithium-ion batteries. There are several forms of voltammetry such as potential step, linear sweep, and cyclic voltammetry. For each method, a voltage or series of voltages are applied to the electrode and the corresponding current that flows is monitored. Linear sweep voltammetry (LSV) involves a single sweep, measuring the electric response at a constant rate from an initial potential to a final potential. Initially, the analyte is unaffected by the electrode, but as the potential sweeps by the formal potential, it begins to be oxidized (or reduced) by the electrode. This produces a concentration gradient, and a current transient is observed. Cyclic voltammetry (CV) is a reversible LSV measurement which scans electric potential and returns by the reverse direction after reaching the final potential, scanning back to the initial potential. Similar to LSV, the analyte is oxidized (or reduced) during the initial sweep, but during the return sweep it is reduced (or oxidized) back to its original form. Therefore, CV exhibits two peaks of equal size but opposite

sign, because one process is anodic and the other is cathodic. In a typical procedure, LSV and CV were conducted using a CHI 660 electrochemical workstation from Shanghai Chenhua Apparatus, China.

3.6.2 Galvanostatic testing

Galvanostatic cycling is often used for testing the cyclability and coulombic efficiency of electrodes over long periods on time. The measurements of capacity during charge and discharge using this method are more reliable, because the current may be kept rigorously constant and the time may be determined with accuracy. Therefore, the electrodes prepared in this doctoral work were subjected to galvanostatic charge and discharge at constant current rate and also multiple current rates (for rate capability tests). The instrument used for this measurement was a Land battery tester (Wuhan Land Electronic Co. Ltd.).

3.6.3 Electrochemical impedance spectroscopy (EIS)

Electrochemical impedance spectroscopy (EIS) is a direct technique for studying electrode processes by measuring the change in the electrical impedance of an electrode. This method, with wide frequency scope, is associated with only small disturbance and is a good means of studying the electrode process dynamics, electrode superficial phenomena, etc. Since EIS can reflect the electrochemical characteristics and inner structure more accurately, determination of and hence classification of the properties of the battery can give accurate results. Fundamental aspects of EIS related to electrode materials for the lithium-ion battery have been discussed in detail in Chapter

2. In addition, this technique has been used to determine the ionic conductivity of electrolytes or thin films of polymers. EIS of the gel polymer electrolytes was conducted using the CHI 660 electrochemical workstation (Shanghai Chenhua Apparatus, China), which was interfaced to a computer in the frequency range from 10 mHz to 100 kHz. The software controlling the measurement also calculates the real and imaginary parts of the impedance. Conductivity was also studied in the temperature range between 303 and 373 K. The films were cut into 1 cm^2 sizes and sandwiched between two blocking stainless steel electrodes of a conductivity cell. The impedance was measured six times for each sample and also at different portions of the same sample. The ionic conductivity of the sample was calculated from

$$\sigma = \frac{t}{R_b A} \tag{3.4}$$

where A is the area of film-electrode contact, t is the thickness of the film, and R_b is the bulk resistance of the film in ohms obtained from the complex impedance measurements. This experiment involves measuring the impedance as a function of frequency of the applied signal over a wide frequency range. This is because impedance is precisely frequency dependent. The complex impedance is represented as a complex impedance plot, in the form of $Z(\omega)$, using the Cole-Cole plot. In the Cole-Cole plot, the imaginary impedance component Z_i is plotted against the real impedance component Z_r.

Chapter 4

Effects of polypyrrole on the performance of nickel oxide anode materials for rechargeable lithium-ion batteries

4.1 Introduction

Rechargeable lithium-ion batteries have been the most widely used batteries in the portable electronics market for many years. Although carbon-based materials are the accepted anode used in the majority of commercial lithium-ion batteries so far, various new higher capacity anode materials are still required to meet increasing energy demands, such as for electric and hybrid electric vehicles.

Recently, transition metal oxides (M_xO_y, where M is Co, Ni, Cu, or Fe) have shown a number of desirable properties, such as high theoretical capacity (500-1000 mAh g^{-1} compared with 372 mAh g^{-1} for conventional graphite), on the basis of a novel conversion mechanism [293-296]. The new mechanism can be written as $M_xO_y + 2yLi \leftrightarrow yLi_2O + xM$. During the discharge, the M_xO_y particles are disintegrated into highly dispersed metallic nanoparticles, consisting of M and Li_2O matrix, and then the highly divided, high surface energy nature of the nanoparticles facilitates the back reaction with oxygen from the lithium oxide matrix to reform the metal oxide on charge [26]. Although the transition metal oxides are attractive, there are still obstacles to their

commercial application. One of the most critical problems is their poor cycling performance, resulting from large volume expansion and contraction during the Li^+ insertion and extraction reactions, respectively, resulting in the aggregation of small particles into large particles in the host matrix [297-299]. Thus, the electrode suffers from pulverization, as well as from consequent loss of electrode interparticle contact.

It has been widely demonstrated that to overcome the volume changes during the Li^+ insertion and extraction reactions, it is necessary to embed the active materials in a cushioning medium, which maintains particle connectivity. The well-known media for this purpose are amorphous carbon or conducting polymers [25, 163, 172, 175]. The carbon or conducting polymer medium serves multiple purposes in the composite when it is used in anode [163, 235]. It serves as (i) an electrically conducting agent to improve the conductivity of the electrode, (ii) a diluting agent to prevent particles from aggregating, and (iii) an efficient matrix to protect the electrode from cracking and pulverization. Recently, conducting polypyrrole (PPy) has been studied as an additive to improve the performance of cathode and anode materials in lithium-ion batteries [75, 162, 300, 301]. However, using PPy powder as an additive in transition metal oxide anode materials for lithium ion batteries has not been explored. In this study, nickel oxide (NiO)-PPy composite was synthesized and evaluated as an anode material. The conducting PPy was used as a cushioning medium and an electrically conducting agent to improve the cycling performance of NiO in lithium-ion batteries.

4.2 Experimental

4.2.1 Preparation of materials

Nanocrystalline NiO powders were synthesized by a spray pyrolysis method [25]. Aqueous solution (0.2 M) of nickel nitrate hexahydrate ($(Ni(NO_3)_2 \cdot 6H_2O$, ≥97.0%,Sigma-Aldrich) was used as the precursor. The solution was peristaltically pumped into a three-zone spray pyrolysis furnace. This procedure was carried out at an operating temperature of 600 °C using compressed air as the carrier gas. Then, the powder was separated from the hot gas stream via a collecting jar and collected into an airtight sample bottle.

NiO-PPy composite was prepared using a chemical polymerization method. $FeCl_3$ was used as the oxidant and sodium *p*-toluenesulfonate (NaPTS) as the dopant. The molar ratio of monomer pyrrole to dopant and pyrrole to oxidant was 3:1 and 1:3, respectively. NiO was dispersed into a solution of pyrrole, Triton-X, and NaPTS and exposed to ultrasonic vibrations for 1 h. Then, $FeCl_3$ was slowly added to the suspension and stirred overnight to complete the polymerization. The resulting NiO-PPy precipitate was filtered and washed with distilled water several times. The final product was dried at 50 °C under vacuum for 12 h.

4.2.2 Material characterization

The crystalline phases of NiO and NiO-PPy were examined by x-ray powder diffraction (XRD; GBC Difftech XRD-MMA, USA) using Cu Kα radiation at 40 kV and 25 mA. Raman spectra were collected using a JOBIN YVON HR800 Confocal Raman system

(HORIBA Ltd., France) with 632.8 nm diode laser excitation on a 300 lines/mm grating at room temperature. The specific surface areas of the NiO and NiO-PPy powders were measured by nitrogen adsorption according to the Brunauer-Emmett-Teller (BET) method with a NOVA 1000 high-speed gas sorption instrument (Quantachrome Instruments, USA). Scanning electron microscopy (SEM) with energy dispersive spectroscopy (EDS) mapping and field-emission SEM (FESEM) were performed using JEOL JEM-3000 and JEOL JSM-7500FA instruments (JEOL Ltd., Japan), respectively. The amounts of PPy in the samples were estimated using a Mettler-Toledo thermogravimetric analysis/differential scanning calorimetry (TGA/DSC 1) equipped with the STARe System from room temperature to 1000 °C at 10 °C min^{-1}.

4.2.3 Electrochemical measurements

The working electrodes were fabricated by mixing 80 wt% active material, 10 wt% carbon black, and 10 wt% polyvinylidene fluoride with *N*-methyl-2-pyrrolidinone. The slurry was pasted onto the copper foil substrates and dried under vacuum. Then, the electrodes were pressed and cut to a size of 1 cm × 1 cm. Coin cells (CR2032) were assembled using lithium metal foil as the counter electrode in an argon-filled glove box. The electrolyte solution was 1 M $LiPF_6$ in 1:2 v/v ethylene carbonate: diethyl carbonate. Constant-current charge-discharge tests were performed in the range of 3.00-0.01 V at a current density of 100 mA g^{-1}. Electrochemical impedance spectroscopy (EIS) was conducted in the frequency range between 0.01 Hz and 100 kHz, and the AC amplitude was 5 mV. Cyclic voltammetry was carried out using a CHI 660B electrochemical workstation instrument (Shanghai Chenhua Apparatus, China) at a scanning rate of 0.1 mV s^{-1}.

4.3 Results and discussion

Figure 4.1 shows the XRD pattern for the nanocrystalline NiO powder. The characteristic peaks of NiO correspond well with standard crystallographic data (JCPDS No. 04-0835). The structure is a nanocrystalline cubic structure with diffraction peaks at 37.46°, 43.44°, 63.08°, and 75.72° ((111), (200), (220), and (311) reflections, respectively) [174, 302]. The average crystal size of the NiO powder was calculated from the largest diffraction peak (200) using Scherrer's equation, and the estimated crystal size was about 3 nm.

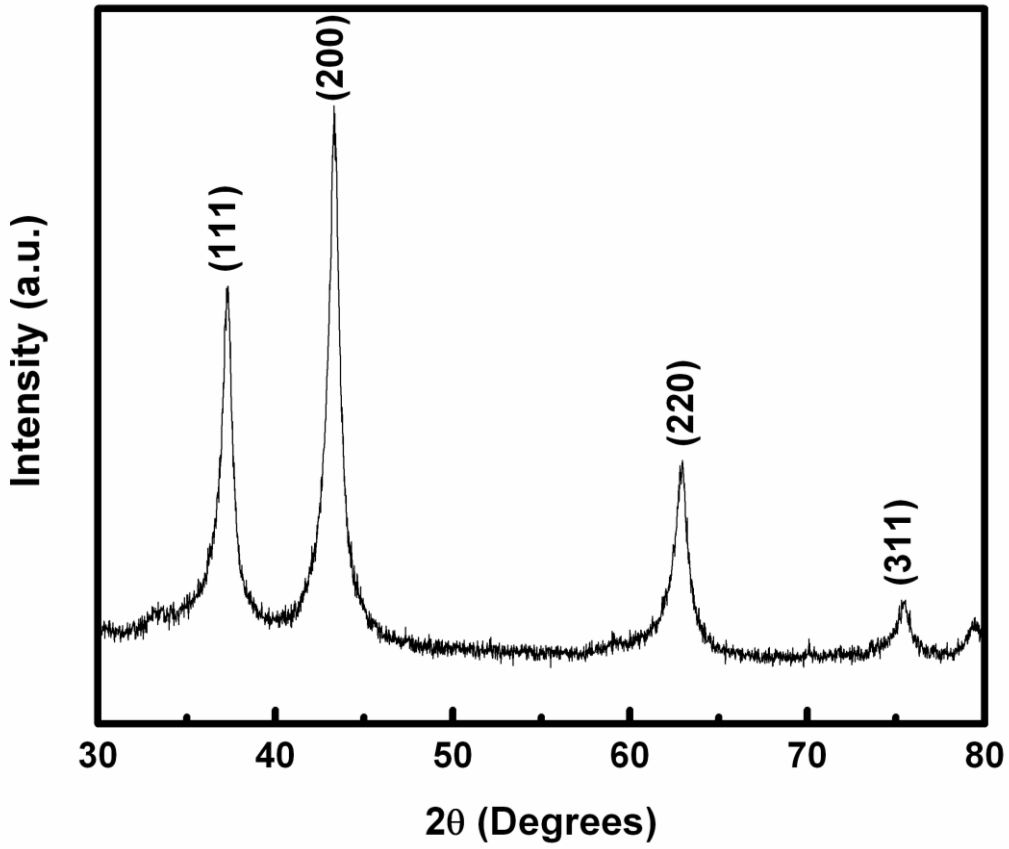

Figure 4.1. X-Ray diffraction pattern of nickel oxide (NiO) powder.

Figure 4.2 presents the Raman spectrum of the NiO-PPy nanoparticles obtained with 632.8 nm diode laser excitation on a 300 lines/mm grating at room temperature. The peak at ~500 cm^{-1} is typical of NiO, and the peaks between 800 and 1700 cm^{-1} match up with the Raman spectrum of pure PPy nanoparticles. The peak at about 1085 cm^{-1} is attributed to the N-H in-plane deformation, and the peaks at about 1375 and 1599 cm^{-1} are attributed to the ring stretching and the backbone stretching of the C=C bonds of PPy, respectively [303]. This indicates that the NiO-PPy composite was successfully synthesized by a simple chemical polymerization method, with the PPy coated on the surfaces of the NiO particles. This result has been further confirmed by FESEM and SEM-EDS.

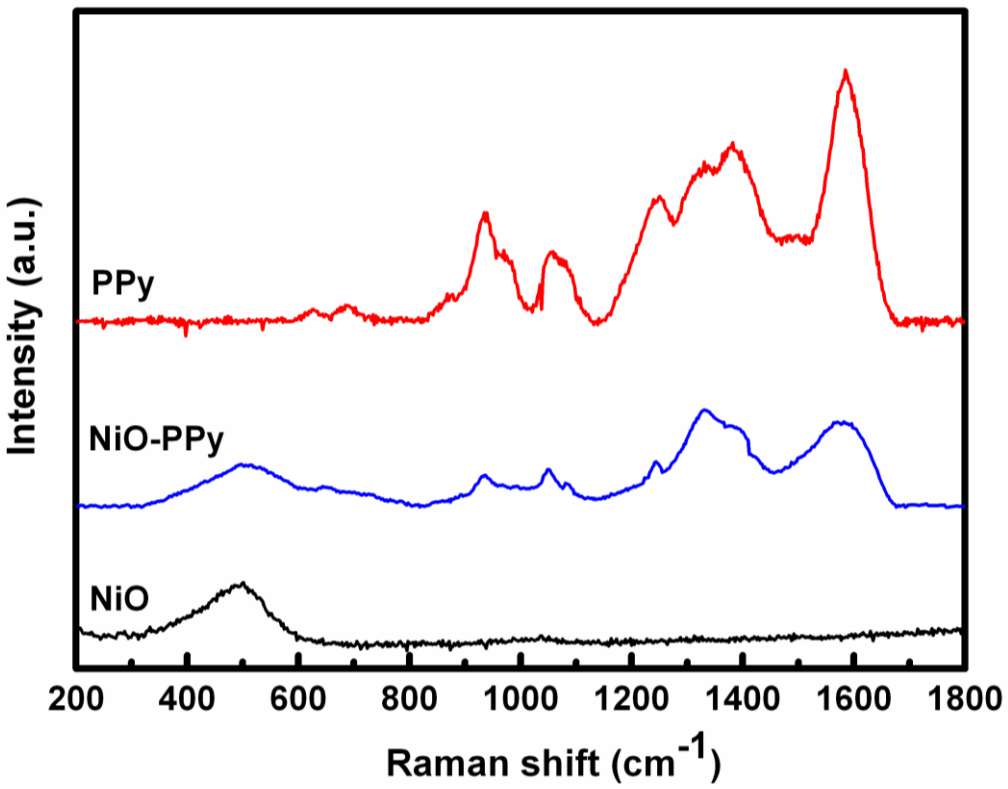

Figure 4.2. Raman spectra of NiO, NiO-polypyrrole (PPy), and PPy particles.

Figure 4.3 presents the FESEM images of the NiO-PPy composite. The NiO particles are mainly spherical agglomerates with sizes in the range of 2-4 μm (Figure 4.3(a)], which is a typical structure for products from the spray pyrolysis method. From the broken spherical particles, we found that the NiO particles are spherical hollow balls with a wall thickness of 200 nm. It has been reported that the specific surface area of NiO prepared by the spray pyrolysis method is larger than that prepared by other methods [302]. The spherical agglomerated structure of NiO exhibits a remarkably high BET surface area of 15.8 m^2 g^{-1}. The NiO-PPy composite was synthesized using an in-situ chemical polymerization method. NiO was dispersed into a solution of pyrrole and NaPTS and then $FeCl_3$ was slowly added to the suspension to complete the polymerization. The thickness and uniformity of the PPy layer depends on the surface area of the suspended NiO particles. A thinner and more uniform PPy coating layer can be easily formed on the larger BET area of the suspended NiO particles. The PPy layer is about 50 nm thick with the typical PPy cauliflower morphology (Figure 4.3(b) and 4.3(c)) [304]. From Figure 4.3(c), it can be seen that the spherical hollow balls of NiO consist of small spherical particles with sizes less than 10 nm.

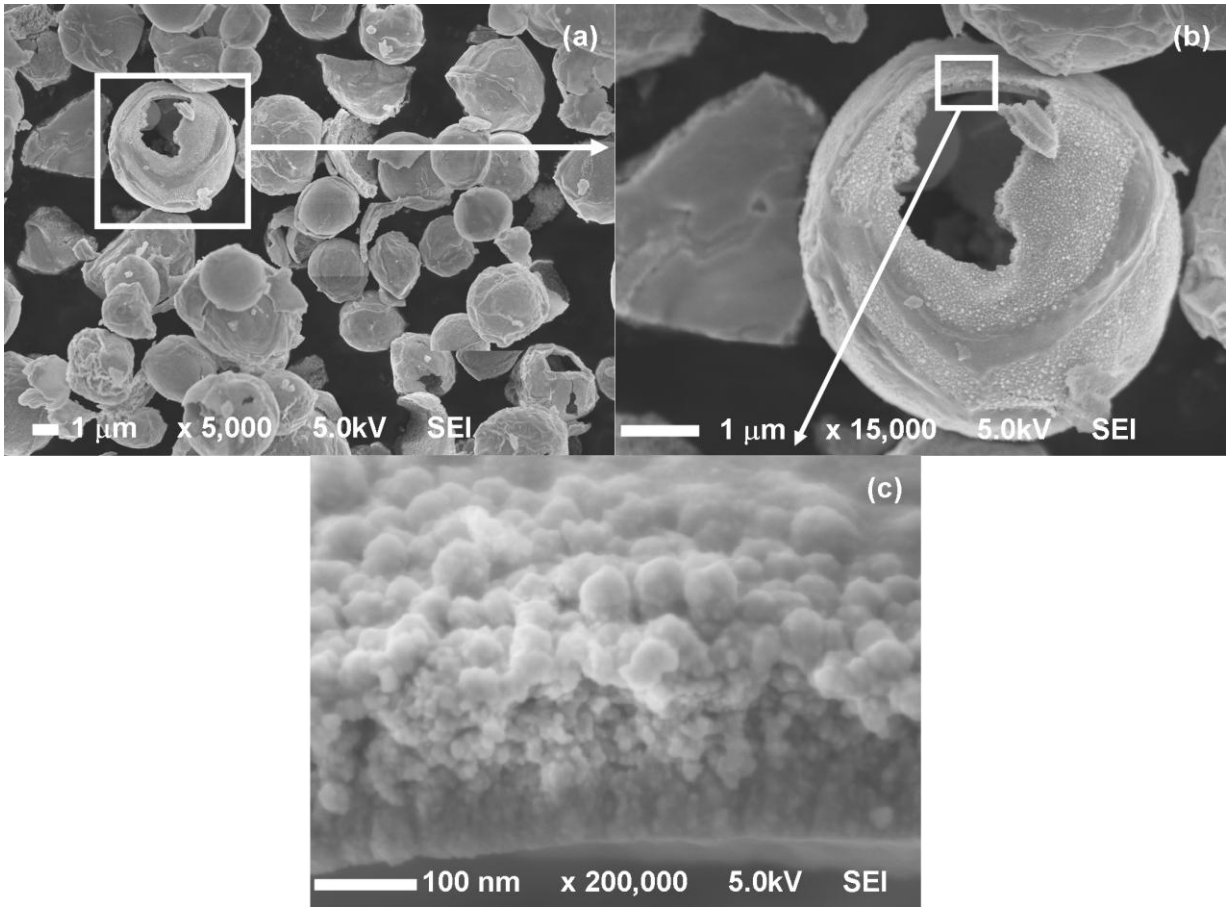

Figure 4.3. Field-emission scanning electron microscopy images of NiO-PPy composite.

To verify that the PPy is uniformly coated on the NiO particles, EDS mapping analysis was used (Figure 4.4). Both the blue and the red dots in Figure 4.4(b) represent the element Ni, with the red dots indicating higher intensity. The dark green dots and the light green dots represent the element N (Figure 4.4(c)) and the element C (Figure 4.4(d)), respectively, in which the N and C are elements of the PPy. The results show that the N and C are distributed uniformly throughout the whole area, which indicates that the nanosized PPy particles have uniformly coated the surface of the NiO powder.

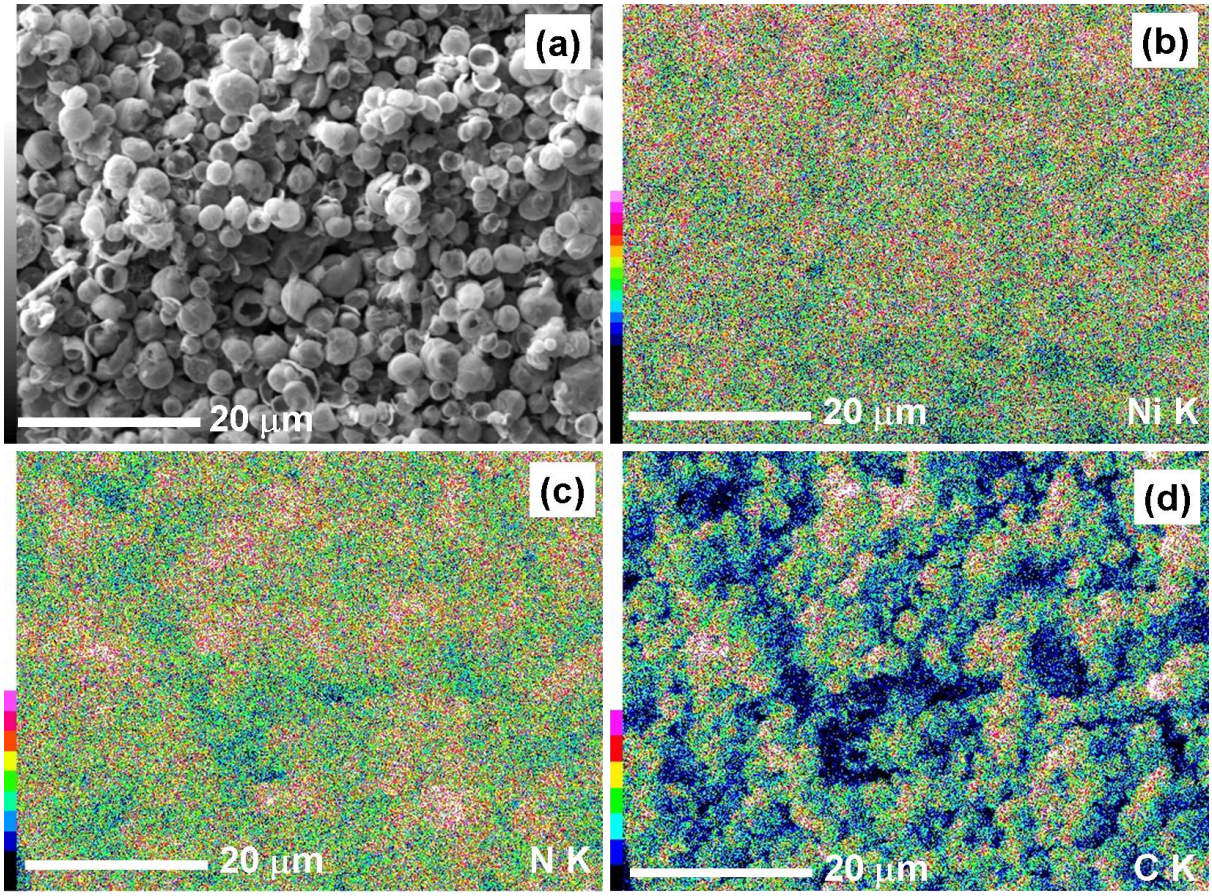

Figure 4.4. Scanning electron microscopy (SEM) images of (a) the NiO-PPy composite, with corresponding energy dispersive spectroscopy maps for elements (b) Ni, (c) N, and (d) C.

For quantifying the amount of PPy in the NiO-PPy composite materials, TGA analysis was carried out in air. Figure 4.5 shows the TGA analysis of the NiO-PPy composite along with bare NiO and PPy powders. As can be seen from Figure 4.5, the bare PPy powder burns off at 640 °C, whereas the bare NiO powder remains stable over the temperature range used for this experiment. It can also be seen that the composite shows weight loss over the temperature of 200 °C, which corresponds to the oxidation of PPy. There is no further weight change in the composite after the initial oxidation of PPy. Therefore, the change in weight before and after the oxidation of PPy directly translates

into the amount of PPy in the NiO-PPy composite. It was found that the amount of PPy in the composite was about 8.08 wt%.

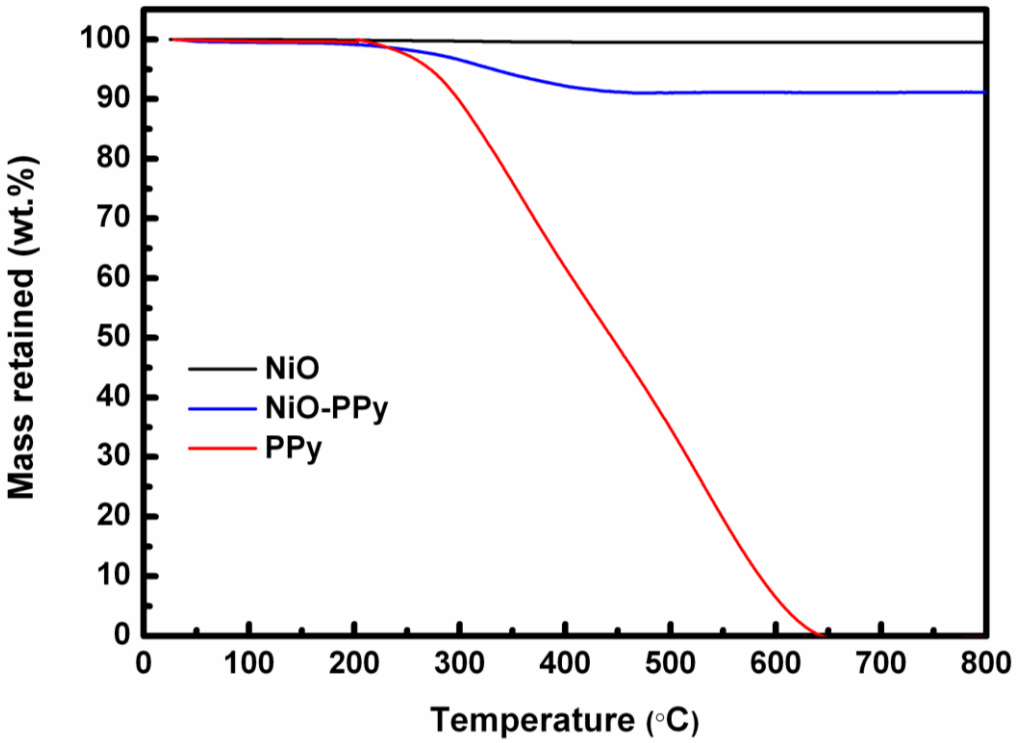

Figure 4.5. Thermogravimetric analysis curves of NiO-PPy composite, bare NiO powder, and bare PPy powder.

Figure 4.6 shows the cyclic voltammograms of the NiO and NiO-PPy electrodes. Both samples exhibit similar curves, as reported previously [174, 294]. For the first cathodic process, high intensity peaks are located at about 0.3 and 0.4 V for the NiO and NiO-PPy electrodes, respectively, corresponding to the decomposition of NiO into Ni, formation of amorphous Li_2O, and formation of the solid electrolyte interphase (SEI)[174]. This peak shifts to 0.9 V for the NiO electrode and 1.0 V for the NiO-PPy electrode in the subsequent process. However, a low-density peak at around 1.3 V is observed for the NiO-PPy electrode, which could be attributed to the reduction of NiO to metallic Ni and the formation of the SEI layer [305, 306].

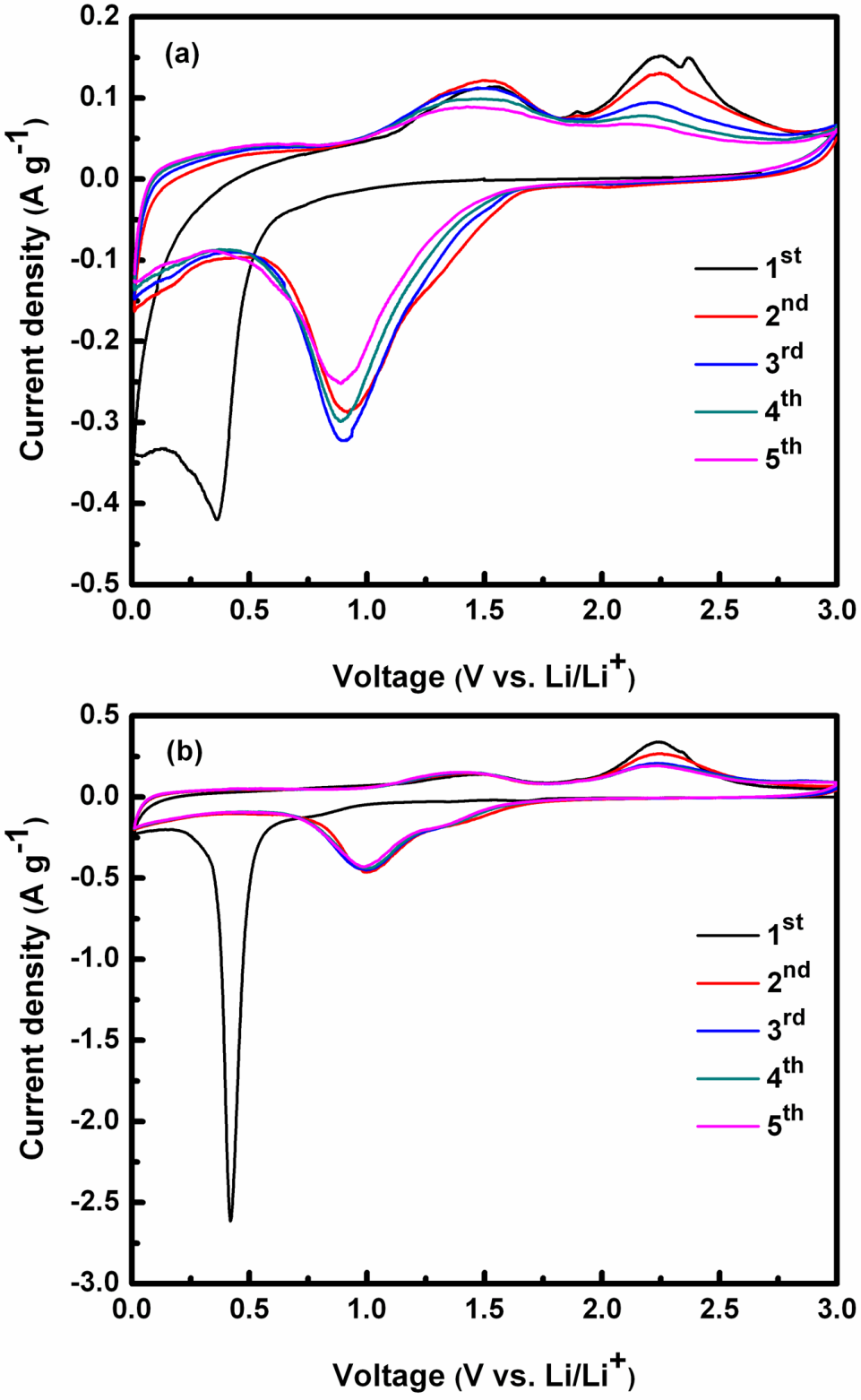

Figure 4.6. Cyclic voltammograms of (a) NiO and (b) NiO-PPy electrodes measured between 0 and 3 V at the scan rate of 0.1 mV s^{-1}.

In the anodic process, two oxidation peaks at about 1.4 and 2.3 V for the NiO and the NiO-PPy composite were observed. These peaks can be attributed to the decomposition of the SEI and Li_2O, respectively [306]. The separation between the reduction and oxidation peaks of the NiO-PPy is decreased as compared with the NiO in subsequent cycles, demonstrative of weaker polarization and better reversibility. This is because the high electronic conductivity of the PPy in the composite is beneficial for the diffusion of lithium ions [173]. No additional peak was found during the redox reactions for the NiO-PPy composite, indicating that the PPy did not contribute any capacity in the charge-discharge process and only acted as a conductive additive [163].

The discharge capacity versus the cycle number for cells with the NiO and NiO-PPy electrodes is presented in Figure 4.7. It can be seen that the composite electrode shows a better cycling performance than the NiO electrode. The initial reversible capacity of the NiO electrode was 571 mAh g^{-1}, and the capacity was reduced rapidly within 10 cycles. After 30 cycles, the capacity was only 119 mAh g^{-1}. However, the electrode prepared from NiO-PPy composite shows much better capacity retention. The initial reversible capacity was as high as 638 mAh g^{-1}. The material utilization almost reached 100%, based on the mass of NiO in the composite. Subsequently, the reversible capacity was maintained above 436 mAh g^{-1} beyond 30 cycles. The specific capacity retained for the NiO-PPy composite electrode after 30 cycles was 66% compared with 21% for the bare NiO electrode. The improvement in the capacity and the cycling stability of the cell with NiO-PPy composite electrode may be due to the following factors: (i) the conductive PPy coating on the surface of the NiO particles can improve the conductivity of the NiO-PPy electrode, while PPy can also act as a binder, increasing the contact between the particles; (ii) the conducting PPy serves as a diluting agent to

prevent nickel regions from aggregating; and (iii) the PPy can act as a cushioning medium that can accommodate the volume changes via the polymer viscoelasticity during the cycling process [175], and consequently, the PPy host matrix can prevent cracking and pulverization of the NiO electrode.

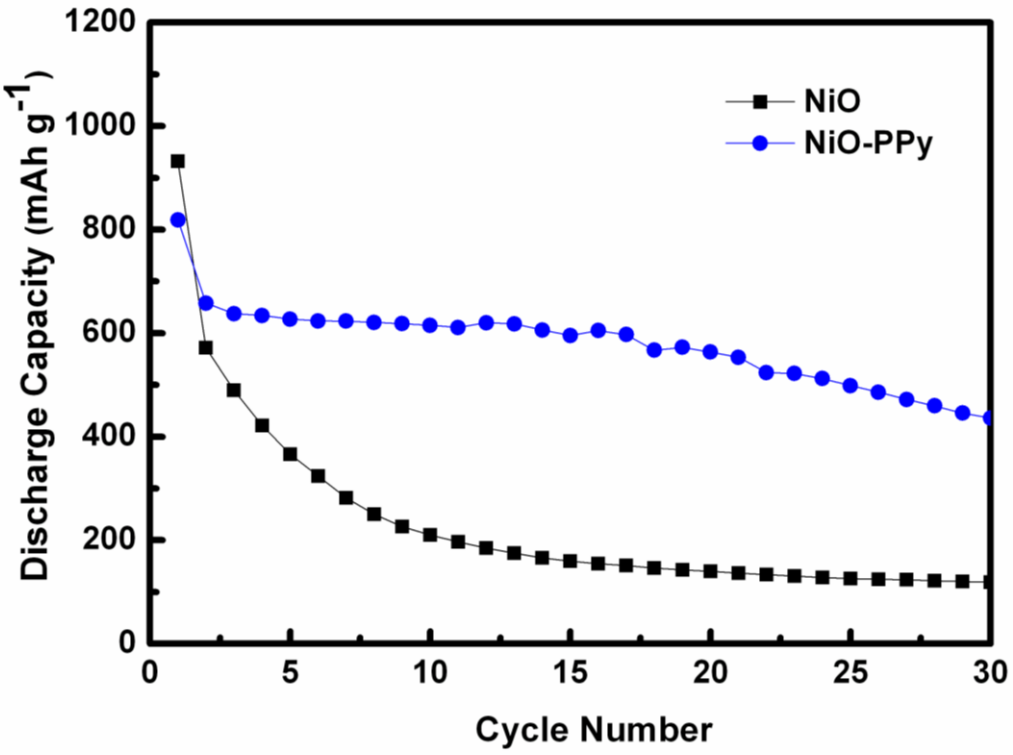

Figure 4.7. Discharge capacity of NiO and NiO-PPy electrodes as a function of the cycle number.

To verify that the PPy coating is responsible for the good performance of the NiO-PPy electrode in the cell, EIS measurements were performed. The Nyquist plots obtained for the nanocrystalline NiO and the nanocomposite electrodes after 5 and 30 cycles are compared in Figure 4.8. The thickness of the electrodes was controlled at 50 μm and the coated area of the electrodes at 1 cm^2. Impedance of the anode in the Li-ion cell depends strongly on the lithium content inside the electrode. To maintain uniformity, EIS experiments were performed at 2.25 V in the charged state.

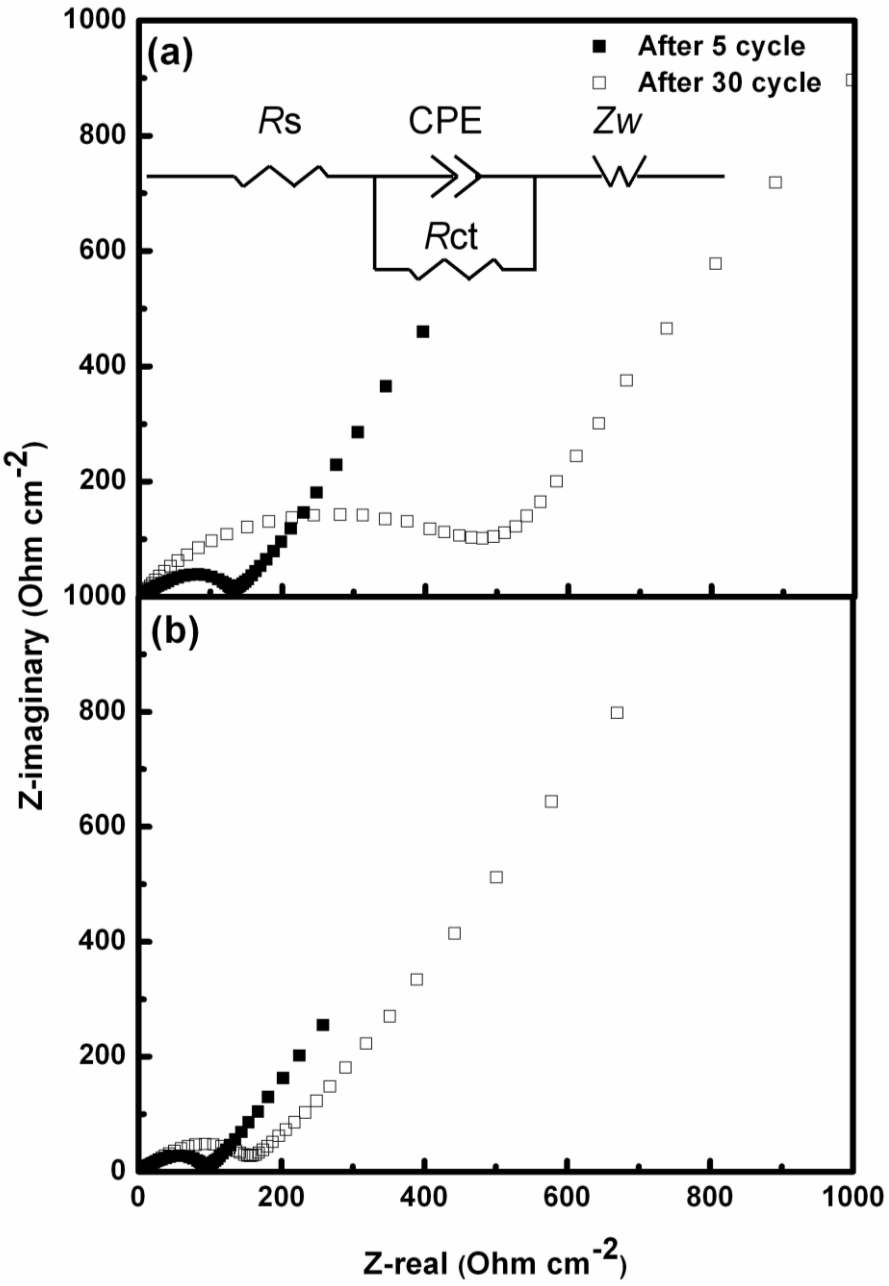

Figure 4.8. Impedance plots of (a) NiO and (b) NiO-PPy electrodes after 5 and 30 cycles. Inset: Equivalent circuit for NiO and NiO-PPy electrodes, which is explained in the text.

According to the experimental results obtained in this work, an equivalent circuit, shown as the inset in Figure 4.8, is proposed to fit the impedance spectra during the charge process. The equivalent circuit model includes electrolyte resistance (R_s), a

constant phase element (CPE), charge transfer resistance (R_{ct}), and the Warburg impedance (Z_w). The values of the parameters from the impedance data are summarized in Table 4.1. The impedance response exhibits a semicircular loop in the medium frequency region. The diameter of this semicircle gives the charge-transfer resistance (R_{ct}), which is a measure of the charge-transfer kinetics [307]. We found that the diameter of the semicircle in the medium frequency region for the NiO-PPy composite is smaller than for the NiO cells after 5 and 30 cycles. The reduction in the diameter of the semicircle for the composite could be attributed to a decrease in the interparticle contact resistance [308, 309]. It should also be noted that the CPE is constant for the NiO-PPy electrode after 5 and 30 cycles, suggesting that a compact and chemically/mechanically stable film forms on the SEI layer [138]. This result has been confirmed from the SEM images (Figure 4.9). The morphology of the NiO electrode (Figure 4.9(a)) shows large cracks when compared to the NiO-PPy electrode (Figure 4.9(b)). These SEM images were captured after the cells completed their 30^{th} cycle of discharge/charge.

Table 4.1. Various impedance parameters of nickel oxide (NiO) and NiO-polypyrrole (PPy) electrodes after 5 and 30 cycles.

Samples	R_s (Ω)	Constant phase element (10^{-4} F)	R_{ct} (Ω)
NiO after 5 cycles	3.30	1.33	137.90
NiO after 30 cycles	3.87	19.10	484.90
NiO-PPy after 5 cycles	2.20	1.28	96.64
NiO-PPy after 30 cycles	5.14	1.14	150.50

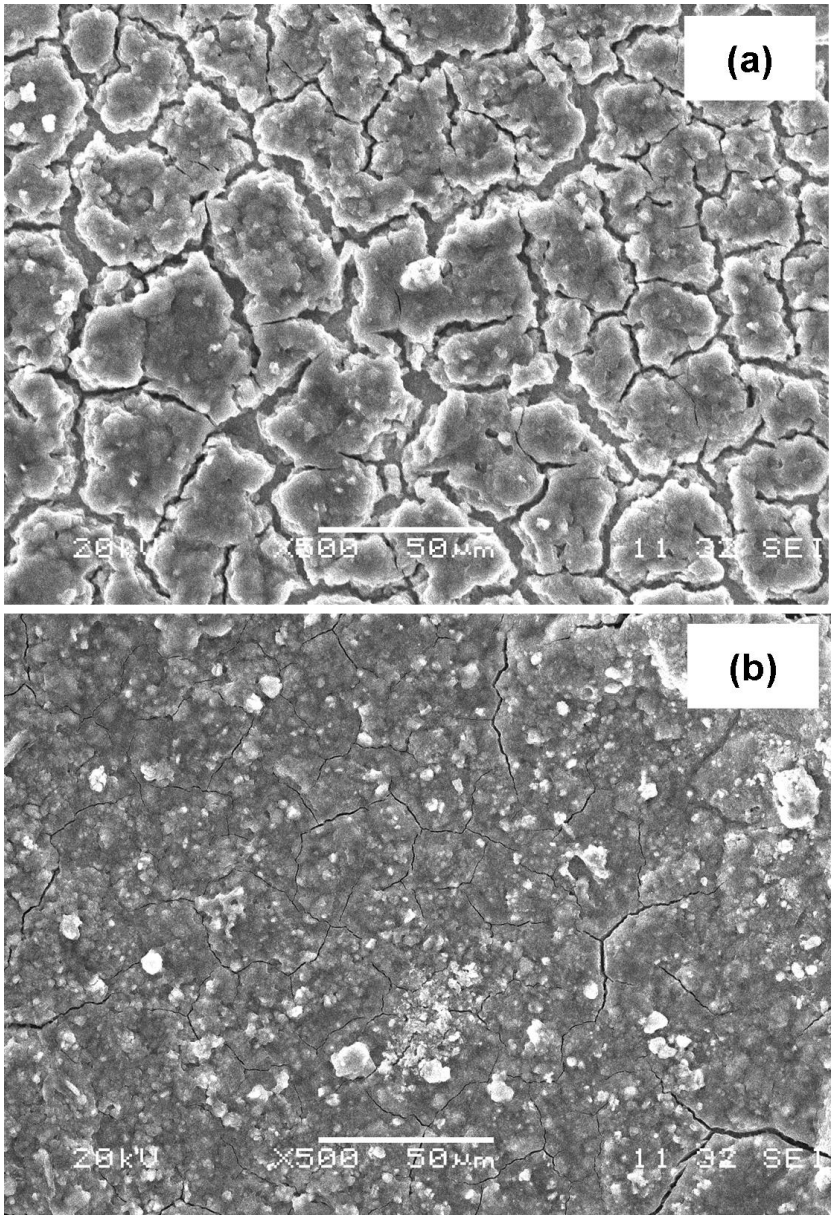

Figure 4.9. SEM images of (a) NiO and (b) NiO-PPy electrodes after 30 cycles.

4.4 Summary

Hollow spherical NiO powders were prepared by the spray pyrolysis method, and then a NiO-PPy nanocomposite was successfully prepared using a simple in-situ chemical polymerization method. The nanosized PPy, with a cauliflower-like morphology, formed a coating on the surface of the NiO. The PPy serves multiple purposes in the

composite when it is used in a lithium cell: as a conducting medium, binder, diluting agent, and cushioning medium to protect the electrode from pulverization during electrochemical reactions. Capacities and cycle lives obtained from the cells constructed from NiO-PPy composite are much better than those from cells constructed using pure NiO. The use of PPy and other conducting polymers to improve battery performance can be extended to other electrode materials, especially for materials that suffer from low conductivity and large volume changes during repeated charging and discharging.

Chapter 5

Synthesis and characterization of graphene-nickel oxide nanostructures for fast charge-discharge application

5.1 Introduction

Lithium-ion batteries for hybrid and plug-in hybrid electric vehicles are currently under intensive investigation. The storage and release of electrical energy depend mainly on how fast the electrons and ions can move through the electrodes. In practice, it is hard to meet all the battery performance requirements, such as high specific energy, high rate capability, long cycle life, low cost, perfect safety, and minimal environmental impact, at the same time. The Li-ion battery is attractive in terms of specific energy and power, and also has the potential to be "the battery of choice" for electric vehicles [110, 310, 311]. Graphite and $LiCoO_2$ are commonly used as anode and cathode, respectively, in commercial Li-ion battery for portable consumer electronics [51]. The intrinsic properties of the electrodes limit the lithium insertion rate, the charge-discharge current, and the energy density. To circumvent the rate issues, several alternative approaches have been pursued, in which either the existing electrodes were replaced by better materials or modified to nanostructured form. For the anode, quite recently, graphene (a single atomic layer of graphite) has emerged and attracted wide attention in materials science and condensed matter physics [101, 152, 153, 312, 313]. The most interesting

feature of graphene nanostructures is the possibility that they can be synthesized from natural graphite, which is perceived as "green". Graphene has shown faster charge-discharge rates than graphite as an anode in Li-ion battery, fulfilling major performance requirements [105, 106, 149, 155, 314]. Being a single atomic sheet, graphene can accommodate Li-ions on both sides of the sheet, providing high lithium storage capacity above 600 mAh g^{-1} at the 1 C rate, which is higher than the theoretical capacity of graphite (372 mAh g^{-1}). Recently, graphene has been utilized to improve the electrochemical properties of metal alloys [76, 150, 158] and metal oxides [29, 154, 156, 157, 159, 161, 315-317], the theoretical capacities of which are much higher (700-4000 mAh g^{-1}) than that of graphene. Considerable fast charge-discharge capability has been shown by graphene/TiO_2 [156] and graphene/Co_3O_4 [316] composites.

Reports on graphene composites with Si [150], TiO_2 [156], Co_3O_4 [316], Fe_3O_4 [29], SnO_2 [157, 159, 161], Cu_2O [317], and CuO [318] claim that a uniform distribution of metal oxide on graphene sheets can eliminate restacking of the sheets during the synthesis and stabilizes the volume changes in the metal/metal oxide during charge-discharge cycling. Studies based on alternatively assembled graphene and nanocrystalline metal oxides such as SnO_2 or NiO reveal similar explanations for their improved electrochemical performances [157]. However, the preparation method in this report was not an in situ method, and the performance at high current densities such as 300-6000 mA g^{-1} was not investigated. Quite recently, graphene/NiO composite with 45% NiO has been synthesised using an in situ method [154]. However, this particular study was limited to the preparation and characterization of the composite. We have focused on synthesizing graphene/NiO composite with lower NiO content (20 wt%), enabling a battery based on graphene/NiO anode to be charged within a few minutes.

NiO synthesised by the same method also gave good stability in prolonged charge-discharge cycling at moderate current densities. To the best of our knowledge, the effectiveness of using lower percentage of metal oxide for higher charge/discharge current application has not been reported.

5.2 Experimental

5.2.1 Preparation of materials

Graphite oxide was synthesised by the Hummers method [319]. 1 g of natural graphite was added to 20 cm^3 of C. H_2SO_4 at 0 °C. 3 g of $KMnO_4$ was added gradually to the mixture while stirring. The mixture was then stirred at room temperature for 30 min. 50 cm^3 of water was added slowly and heated at 90 °C for 15 min. 150 cm^3 of distilled water was added, followed by 10 cm^3 of 30% H_2O_2 solution. The solids were separated by centrifuging and washed repeatedly with 5% HCl until sulphate could not be detected with $BaCl_2$. The product was washed 3-4 times with acetone and dried in an oven at 65 °C for 12 h. Graphite oxide synthesized as above was used to synthesize graphene and graphene/NiO composites. Hydrothermal method was used to reduce graphite oxide to graphene as described below [317, 320, 321]. Graphite oxide is dispersed in ethylene glycol by ultrasonic agitation for 30 min before autoclave the mixture. To synthesize the composite, an appropriate ratio of nickel acetate tetrahydrate and graphite oxide was dispersed in ethylene glycol. The mixtures were then transferred to stainless steel autoclaves filled with Ar and kept at 160 °C for 16 h. The resulting products (graphene and graphene composites) were washed with acetone followed by water and then dried at 65 °C in air. The samples were finally thermally annealed at 500 °C in Ar. For comparison, nickel acetate tetrahydrate was treated under similar

conditions (hydrothermal reaction in ethylene glycol at 160 °C and pyrollysis at 500 °C) to synthesize NiO. Graphite oxide converts to graphene and nickel acetate turns to an intermediate product at the end of the hydrothermal reaction. Therefore, heat treatment is necessary to convert the intermediate product to NiO.

5.2.2 Material characterization

The morphology of the samples was investigated using a JEOL JSM 6460A scanning electron microscope (SEM) with an energy dispersive X-ray spectroscopy detector with X-ray mapping capability. X-ray diffraction (XRD) analysis was carried out using a GBC MMA generator and X-ray diffractometer with Cu Kα radiation and a graphite monochromator. Raman spectroscopy was carried out to monitor the nature of the disorder in the graphene using a JOBIN YVON HR800 Confocal Raman system with 632.8 nm diode laser excitation on a 300 lines/mm grating at room temperature. Thermogravimetric analysis (TGA) was performed in air via a Mettler-Toledo TGA/DSC 1 Star^{e} System to determine the actual weight ratio of graphene and NiO. Fourier transform infrared (FTIR) spectra were collected using a SHIMADZU-84005.

5.2.3 Electrochemical measurements

The electrodes were prepared on Cu foil using slurry of 80 wt.% active material and 10 wt.% (each) carbon black and poly(vinylidene fluoride) dissolved in *N*-methyl-2-pyrrolidinone (NMP). The coated electrodes were dried in a vacuum oven at 100 °C for 24 h, pressed, and cut into 1×1 cm^2 sizes. The resulting electrodes were assembled into CR2032 coin-type cells (half cells) in an Ar-filled glove box (Mbraun, Unilab,

Germany), using lithium metal as the counter electrode and 1M $LiPF_6$ in ethylene carbonate/dimethyl carbonate (EC/DMC, 1:1 by volume) provided by MERCK as the electrolyte. The cells were galvanostatically charge-discharge cycled between 2.5 V and 0.01 V vs. Li/Li^+ on a LAND battery tester at 25 °C. Different current rates ranging from 300 mA g^{-1} to 6000 mA g^{-1} were used to cycle the cells and for simplicity 300 mA g^{-1} rate was used as 1 C rate for all cells irrespective to their real theoretical values.

5.3 Results and discussion

Figure 5.1 shows X-ray diffraction (XRD) patterns of graphite oxide, graphene, NiO, and the graphene/NiO composites. Fairly high interplanar spacing (*d*-spacing) of about 0.85 nm was observed in graphite oxide in contrast to the typical value of about 0.70 nm, probably due to the high ratio of graphite oxide to H_2O [322, 323]. Complete conversion of graphite oxide into graphene was observed from the disappearance of the characteristic peak of graphite oxide at $2\theta \approx 11°$. Both graphene and the composites show the typical 2θ peak for graphene at about 26°, corresponding to *d*-spacing of about 0.36 nm. Although the *d*-spacing is higher than that of natural graphite (~0.33 nm) the values are similar for pristine graphene and the composites, suggesting that the NiO nanocrystallites have not greatly affected the orientation of the graphene layers. This evidence was confirmed by Raman spectroscopy, which can be used to investigate the nature of disorder in graphene as shown in Figure 5.2. Raman spectroscopy is a powerful non-destructive technique to study carbonaceous materials such as graphene and also for examining the ordered and disordered crystal structures and distinguishing the single and multilayer characteristics of graphene layers [155, 324, 325].

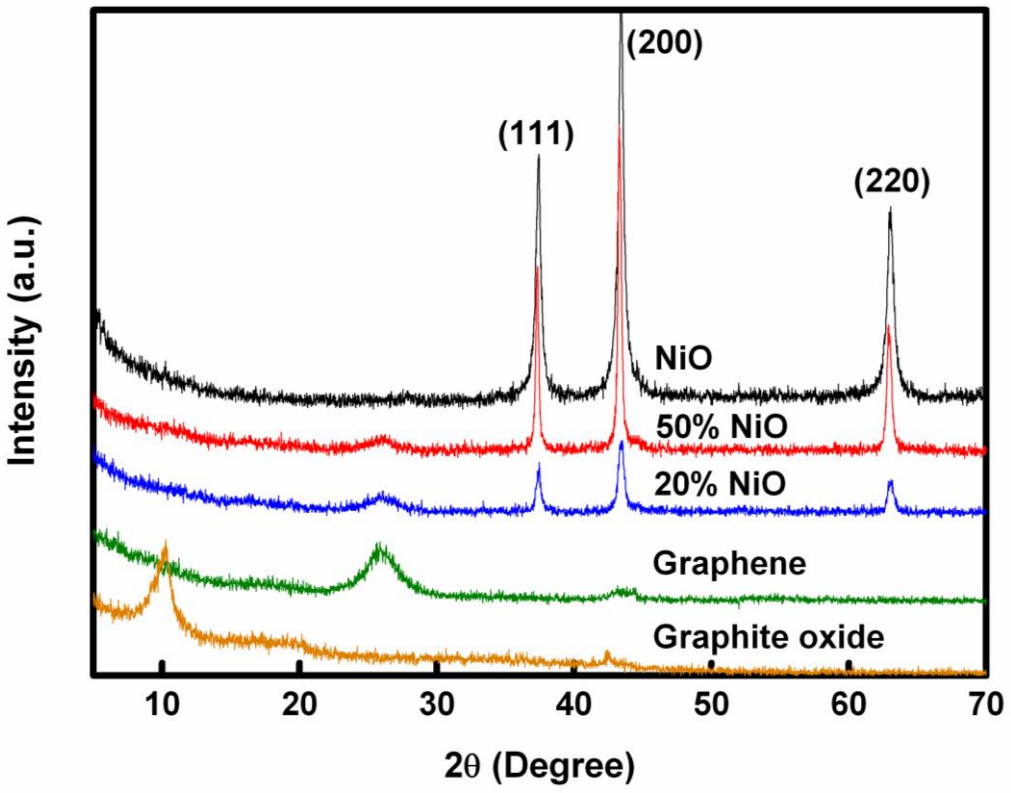

Figure 5.1. XRD spectra of graphite oxide, graphene, and graphene/NiO composites with different quantities of NiO.

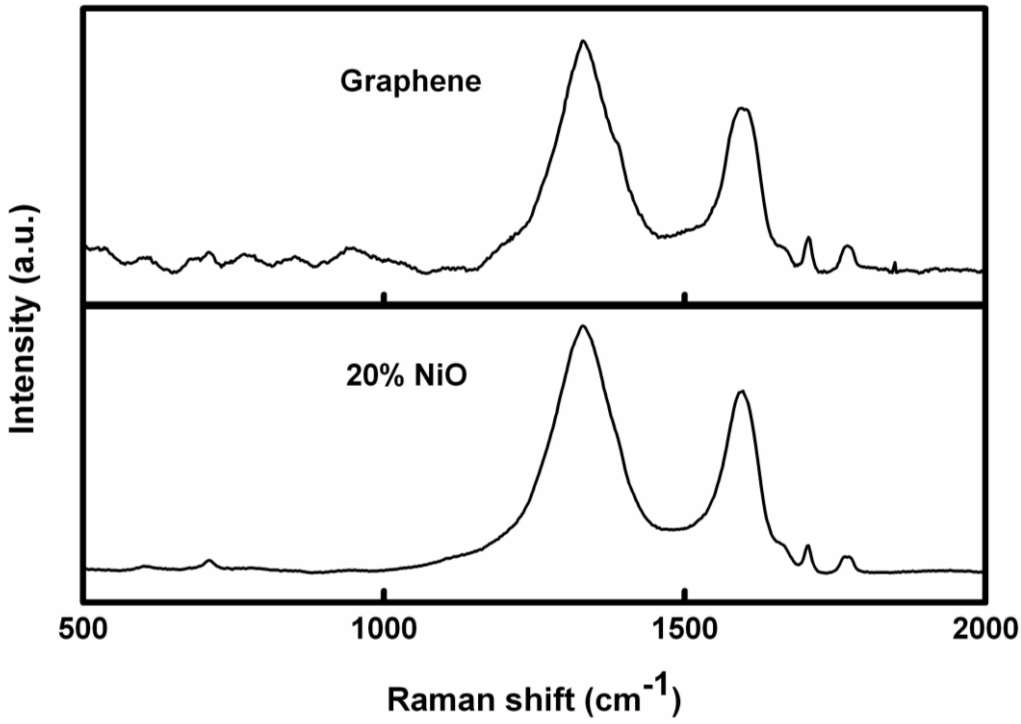

Figure 5.2. Raman spectra of graphene and of the composite with 20% NiO.

In perfect graphite, the G band is highly intense (in-plane bond stretching motion of C sp^2 pairs), whereas the D band is generally active in the presence of high disorder in the graphene. The D/G ratio of the band intensities for the composite has not increased compared to the pristine graphene, suggesting that no significant increase in disorder has occurred due to the presence of NiO crystallites in graphene. Furthermore, G band observed at about 1582 cm^{-1} during the present study. It had been shown that the peak frequency of the G band of the single layer graphene at 1585 cm^{-1} shifts about 6 cm^{-1} into lower frequencies after stacking several graphene layers. For 2-6 layers of graphene the G band have even shifted to 1579 cm^{-1}. Therefore the G band at 1582 cm^{-1} is attributable to mostly single graphene [155, 324, 325]. The above concept was supported by FESEM as shown later. Crystal sizes of the NiO were also compared from the XRD peaks in Figure 5.1. The pristine NiO and the composites show (111), (200), and (220) crystal planes of strongly crystalline NiO with space group *R*3*m* [174]. The crystal sizes of NiO, which were calculated using the Scherrer equation applied to the (200) plane, followed the order 32, 43, and 120 nm for samples containing 20%, 50%, and 100% NiO, respectively.

Graphene, when imaged via field emission scanning electron microscopy (FESEM), shows disassembly of graphite stacks into nanosheets with a flower petal-like appearance (Figure 5.3(a) and (b)). Generally, attempts made to synthesize nanometer sized crystallites fail as their lateral size increases. The thermal vibrations rapidly build up, which diverts the nanoparticles to the macroscopic scale and changes the two-dimensional (2D) crystallites into a variety of stable 3D structures [152]. Accordingly, graphene layers are naturally crumpled and flexible, in contrast to graphite. The graphene layers are substantially thin and disordered according to the Figure 5.3(a)

which is consistent with the results of Raman. The composites consisting of 20% and 50% NiO show NiO nanocrystallites a few nanometers in size attached firmly to certain sites on graphene sheets (Figure 5.3(c) and (d)). This phenomenon was confirmed by energy dispersive spectroscopy, where NiO particles at high concentrations were observed at certain sites (Figure 5.4).

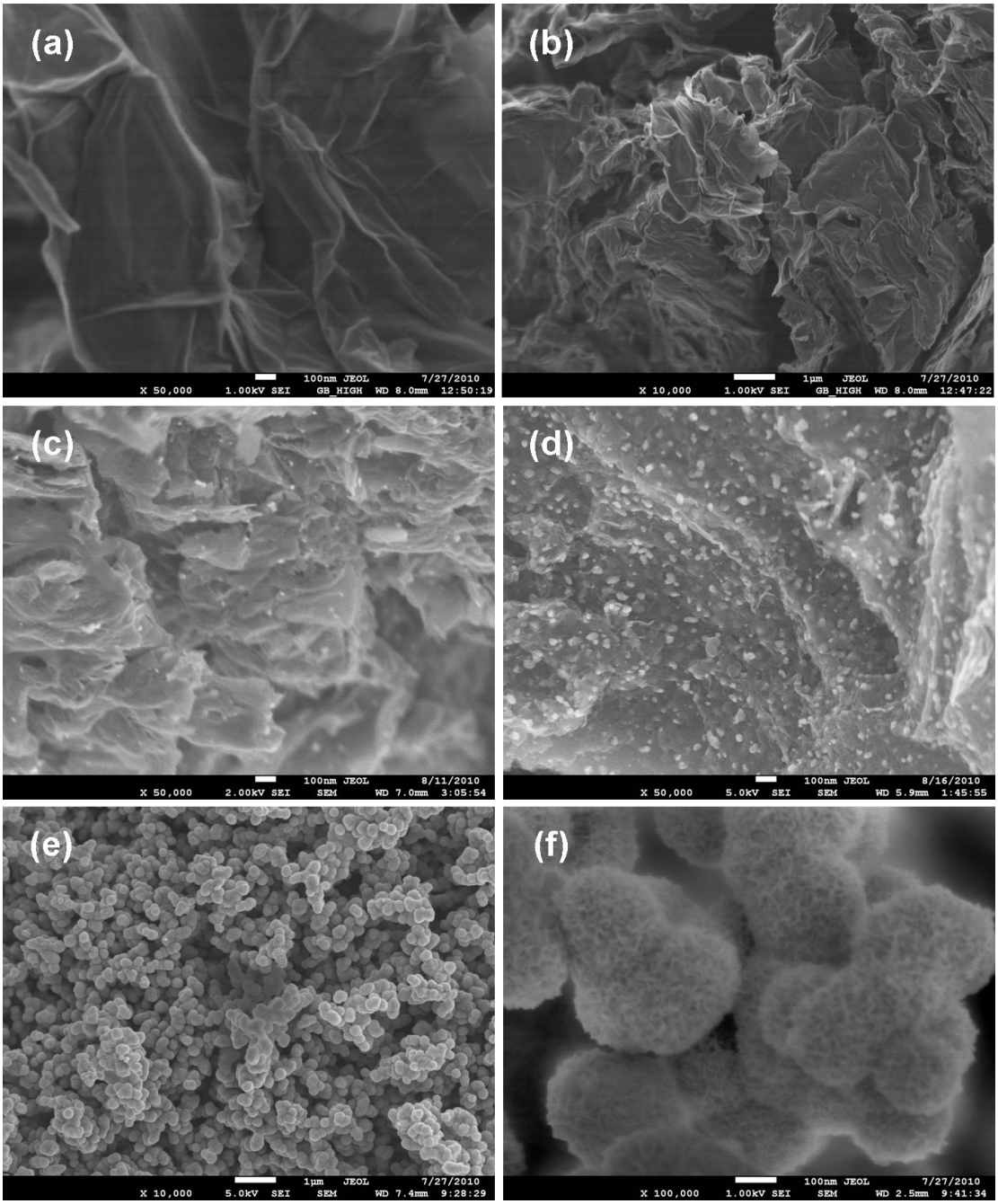

Figure 5.3. FESEM images of (a) and (b) graphene, (c) 20% NiO composite, (d) 50% NiO composite, and (e) and (f) pure NiO.

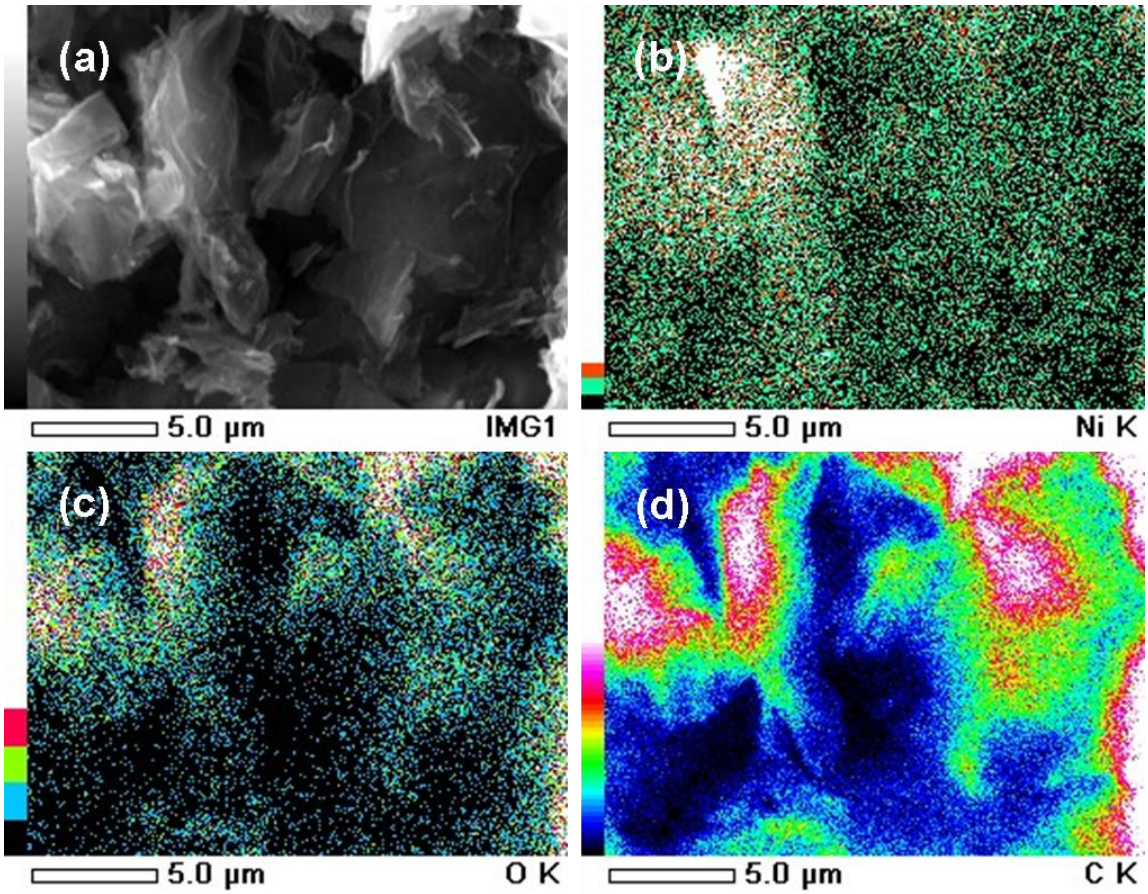

Figure 5.4. EDS spectra for graphene and the composite (50% NiO).

The growth pattern of NiO nano-structures as observed in Figure 5.3(e), and (f) is not visible in the composite and agglomerations of NiO nanoparticles are not much prominent either. Presumably the growth of nano-structures could exist in limited manner which is not visible through scanning electron microscope. We believe that interconnections of the graphene layers are not entirely interspaced by NiO nanocrystallites at 20% NiO in graphene. If all such contacts incorporated NiO, the electrical resistance would be too extreme to deliver such stable capacity as we observed for the composite, as discussed later, and a high charge-transfer rate would not be attainable either. Obviously electrical contacts can be lost due to the insulating nature of NiO in high doses. A completely different growth pattern of NiO was observed in the

pristine NiO, the particle size of which is much bigger (100-300 nm) than in the composites (Figure 3(e) and (f)). Coralloid-type nanostructures of NiO are formed. Higher magnification revealed that a flower petal-like morphology on the order of 1 nm thick grew radially from the core. Formation of stable 3D structures is common to all the nanoparticles. Such striking morphology may presumably lead to high Li-ion storage capacity, as shown later. The preparation process for the graphene, the NiO, and the composite involved two steps. The hydrothermal method was used to reduce graphite oxide (present in the composite and in the pristine graphite oxide) to graphene, and thermal annealing was then necessary to convert the intermediate product of the composite to graphene/NiO. Solvothermal reduction of colloidal dispersion of graphite oxide by various solvents was investigated in literature and has been used to synthesize graphene and graphene composites from graphite [317, 320, 321]. Hydrothermal reaction of graphite oxide dispersed in ethylene glycol at lower temperature (120-200 °C) has lead to reduction of graphite oxide to graphene. Ethylene glycol performs as the solvent and the reducing agent for the reduction of graphite oxide. Ultrasonic agitating of graphite oxide in ethylene glycol resulted in highly dispersed brown-yellow colour graphite oxide in ethylene glycol. The presence of oxygen containing functional groups in graphite oxide facilitates anchoring of various polar molecules such as ethylene glycol and water [317, 321]. The reduction of graphite oxide anchored to ethylene glycol takes place at low temperature with the development of high pressure in the autoclave. The complete reduction has observed even at 120 °C with ethylene glycol [320] although the present study used 160 °C for complete reduction. Thermal annealing at 500 °C was employed after the hydrothermal reaction to convert the intermediate nickel hydroxide to NiO and also to remove any residues such as chemically and physically bonded ethylene glycol from all materials. It is interesting to

understand the intermediate products resulting from the hydrothermal reaction before production of the graphene/NiO composite and the pure NiO. Figure 5.5 shows FESEM micrographs of the intermediate products. Similar morphology has been observed for the microwave-assisted hydrothermal synthesis of nickel hydroxide [326]. The morphology of the intermediate is similar to those of NiO, suggesting that the nucleation and growth of the nanostructure have begun before conversion of the intermediate product to NiO.

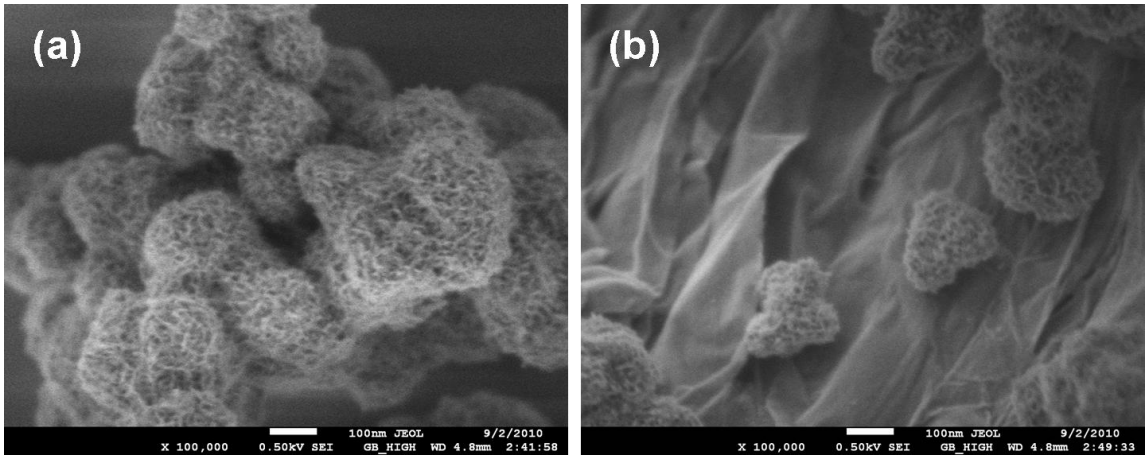

Figure 5.5 FESEM images of the intermediate for (a) NiO and (b) NiO/graphene composite.

FESEM micrographs further reveal that NiO intermediate in the composite has a similar morphology to the intermediate of pure NiO, implying that the synthesis of both pure NiO and the composite involves the same intermediate. However, after the heat treatment of the composite, the morphology of NiO is completely different from the intermediate. We suggest that, the pyrollysis of the composite at 500 °C in an Argon flow lead to cleavage of agglomeration of NiO and attachment to new cites or functional groups on the surface of graphene which presumably created from the heat

treatment. Therefore, dispersion of NiO throughout the graphene sheets is visible after the heat treatment as revealed in Figure 5.3(c) and (d) instead of the growth and agglomeration observed in the intermediate stage (Figure 5.5(b)). Detailed investigation is underway for further clarification of the morphology and the mechanism of formation of the composite which would be published separately.

The typical XRD peaks corresponding to the (003), (006), (101), and (110) planes (Figure 5.6) confirmed the formation of α-$Ni(OH)_2 \cdot xH_2O$ from nickel acetate precursor [326-329]. Therefore, the intermediate product of both graphene/NiO and pristine NiO is $Ni(OH)_2 \cdot xH_2O$. The interlayer spacing, which was derived from the (003) plane, is about 0.89 nm, suggesting that the acetate and ethylene glycol have intercalated into the layered nickel hydroxide. Generally, α-nickel hydroxide stacks with intercalated ions such as the above to restore its charge neutrality [326-329]. Such stacking obviously stabilizes nickel hydroxide in ethylene glycol. We propose that the intermediate of the composite is nickel hydroxide bonded to the graphene surface.

From Figure 5.7, Fourier transform infrared spectroscopy (FTIR) showed vibrational bands at about 3644, 3405, 1623, 1358, 1280, 990, 645, and 484 cm^{-1}, which is typical for α-type hydroxides [326, 327]. Although the broadness of the peaks for the composite is not the same as for the nickel hydroxide, the characteristic peaks are common to both samples. Vibration bands for free hydroxyl groups at 3644 cm^{-1} and for H bonded to water at 3405 cm^{-1} seem to be well separated and small in the composite compared to the broad band of the pure NiO intermediate sample, although there is no apparent shift of the band position. This result suggests that the free OH vibrations low in the composite.

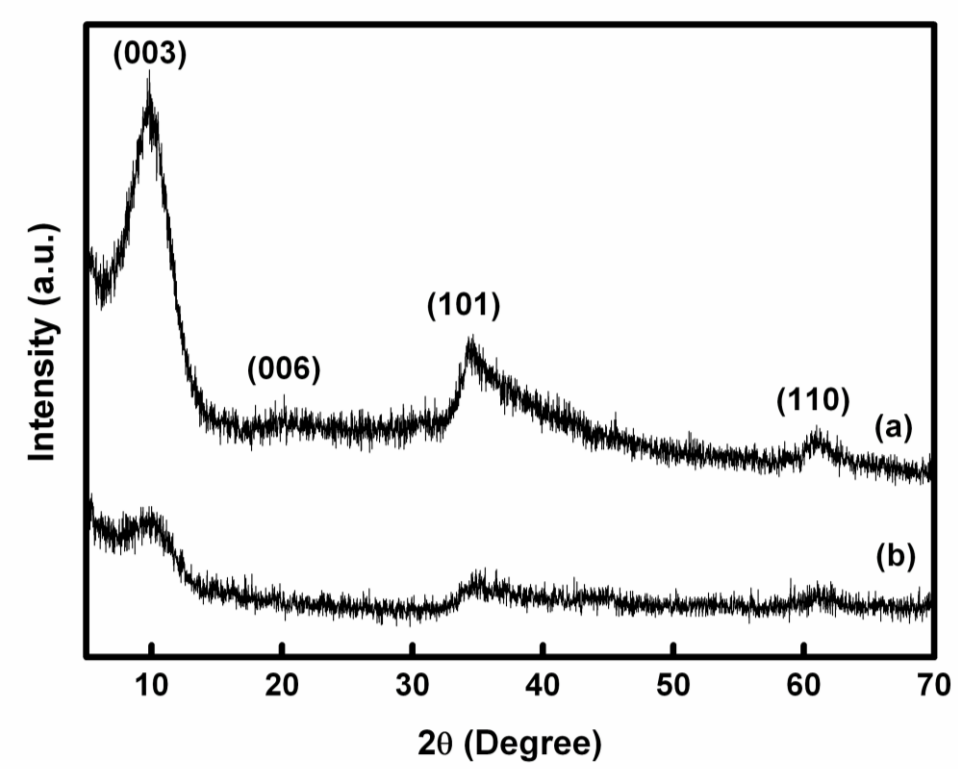

Figure 5.6. XRD spectra of intermediate products for (a) NiO and (b) NiO/graphene composite.

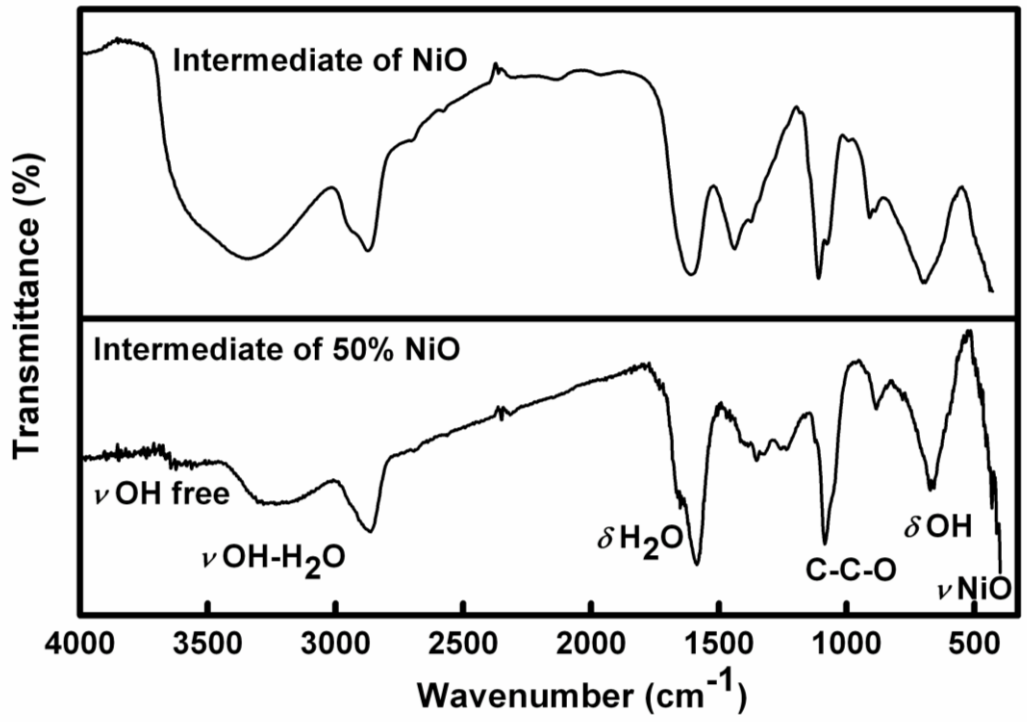

Figure 5.7. FTIR spectra of intermediates for NiO and the composite with 50% NiO.

Figure 5.8 shows a schematic representation of the formation of NiO and NiO/graphene composite. The intermediate product for both the composite and the pristine NiO is nickel hydroxide, the thermal annealing of which converts it to NiO:(1)$Ni(OH)_2 \cdot xH_2O \rightarrow NiO \cdot xH_2O + H_2O$. In the composite, graphene edge surfaces and defect sites can act as nucleation sites for nickel hydroxide. Obviously, nickel hydroxide selectively attaches to the edge surfaces and defect sites, as shown in the schematic diagram. This is because the edge surfaces and any other defects present on the surface of the graphene are more reactive towards various chemical reactions [330]. A recent study on atomic layer deposition of Al_2O_3 reveals that Al_2O_3 is preferentially grown at the edge surface of graphene [331]. The authors suggest that the method can be used to detect defects and edge sites in graphene. Graphene has a high surface to volume ratio, and various defects appear after exfoliation of graphite. Therefore, we suppose that the higher quantity of NiO (50%) can firmly attach to the reactive sites of graphene.

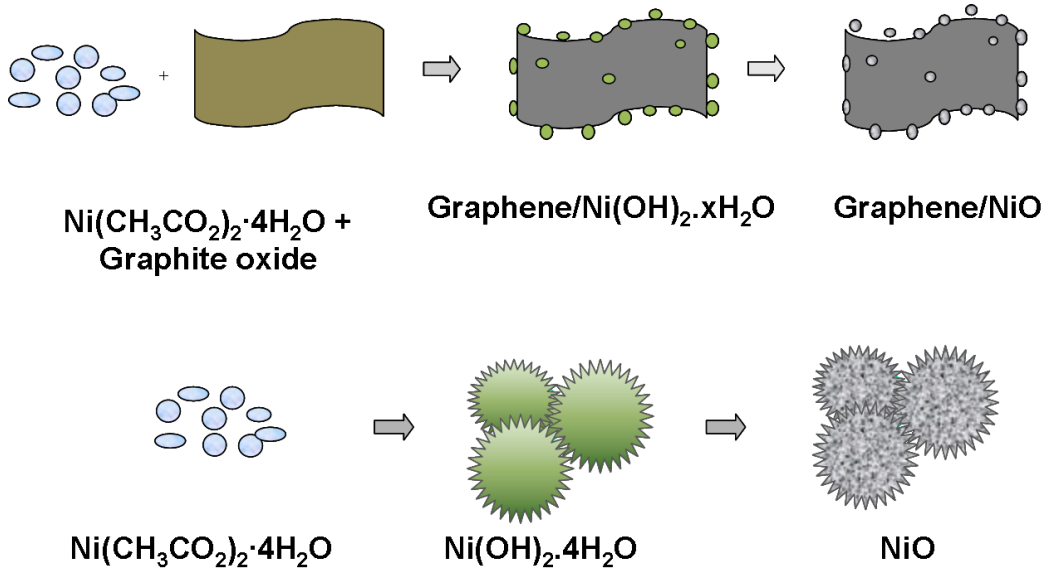

Figure 5.8. Schematic illustration of the formation of nickel hydroxide and NiO, including the formation of $Ni(OH)_2$/graphene composite and the phase transformation to NiO/graphene.

In the present investigation, the graphene and NiO precursor ratio was chosen so that free nickel hydroxide was not formed among the graphene sheets, which would affect adversely the conductivity of the graphene. As explained previously, high reactive sites such as edge surface and defect sites of graphene attach metal oxide crystallites as much as possible. Free NiO is obviously formed after attachment of all such reactive sites on graphene surface. At higher concentrations of NiO precursor (above 60%), free nickel hydroxide is observed, even by the naked eye, due to the unique green colour of the intermediate. The composite with 80% NiO shows metallic nickel in the composite, the performance of which is also interesting and different from the present systems, as will be discussed separately. The actual weight percent of NiO in the composite was investigated using thermo-gravimetric analysis (TGA) (not shown here).

Figure 5.9 shows the charge-discharge behaviour of the graphene/NiO composites, graphene, and NiO when assembled as an anode in a coin type Li-ion cell. The charge-discharge current density used provides capacity of 300 mAh g^{-1} in 1 h, which is denoted as the 1 C rate for each half cell. All cells show high irreversible capacity loss during the first charge-discharge cycle and improvement of stability during the subsequent cycles. The initial capacity loss is attributed to the surface film formation [332]. NiO generally shows a voltage plateau at about 0.6 V during the first discharge, corresponding to the reaction of Li-ions and NiO according to $2Li + NiO \rightarrow Li_2O + Ni$ and formation of the surface films [174]. The plateau shifts to about 1.2 V in subsequent charge-discharge cycles and becomes smaller in prolonged charge-discharge cycling. The peak at 2.25 V during the charge cycle corresponds to the reverse reaction of formation of NiO from Ni and Li_2O. However, such voltage hysteresis, as is observed in NiO based cells, is unsuitable for practical application. Graphene does not show such

hysteresis, which starts appearing only with increasing content of NiO in the composite. The composite with 20% NiO shows similar charge-discharge behaviour to graphene, which is useful in practical application. It is one of the advantages of using lower percentage of metal oxide in a composite. The charge-discharge behaviour is not much deviate from the pristine graphene. Generally, composites at high percentage of metal oxide show voltage plateaus [156, 316] which are unfavourable in practice.

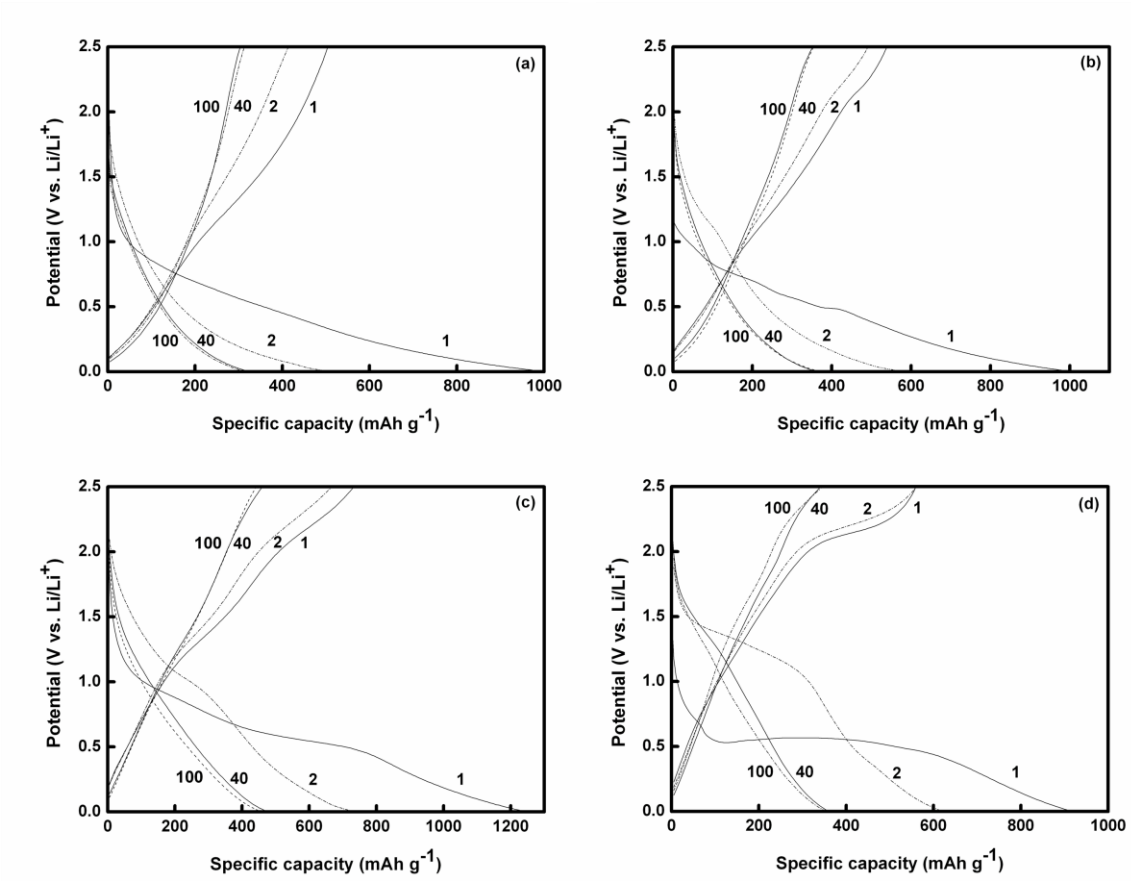

Figure 5.9. Voltage profiles showing the 1st, 2nd, 40th, and 100th charge-discharge cycle behaviour of (a) graphene, (b) 20% NiO composite, (c) 50% NiO composite, and (d) pure NiO half cells at 1 C rate.

Cyclic voltammograms (CV) of the cells also show high irreversibility during the first cycle (Figure 5.10), corresponding to the formation of the surface film. Graphene edge

surface is highly exposed compared to that of graphite due to the exfoliation of the graphite stacks; consequently, the surface area is also higher than graphite. As a result, higher initial capacity loss is observed which is common to all graphene based anodes [29, 76, 150, 154, 156-159, 161, 315-317]. NiO also showed high initial capacity loss presumably due to high surface area resulting from the growth of nanostructures. Nevertheless high initial is not suitable for practical application.

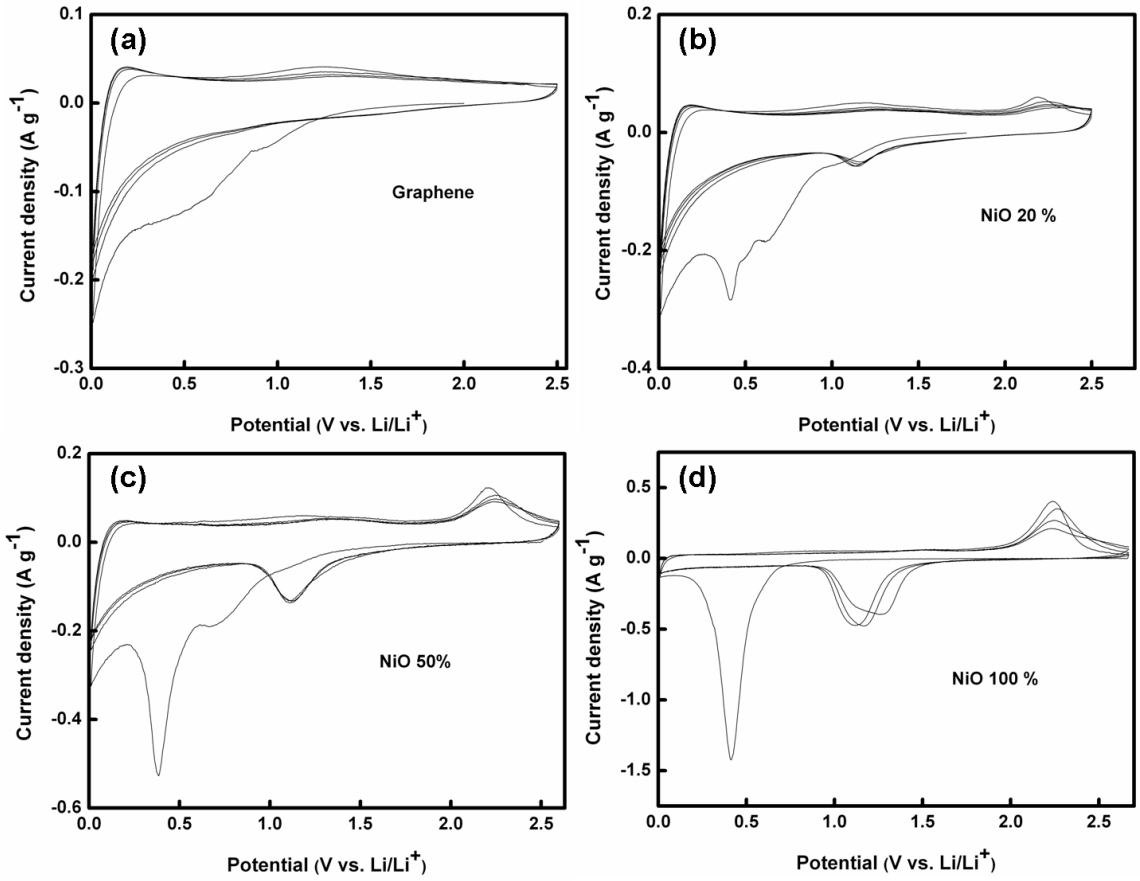

Figure 5.10. Cyclic voltammograms of (a) graphene, (b) 20% NiO composite, (c) 50% NiO composite, and (d) 100% NiO.

Extensive work has been done to reduce the initial capacity loss as well as the capacity fade on charge-discharge cycling of graphite and other materials [332]. Similar work is necessary to solve the problems associated with graphene and composites which needs

to address separately. The present work aimed at investigation long term cycle stability and high rate capability which is also equally important in practical application.

Figure 5.11 shows the Li-ion storage capacity of the half cells consisting of graphene, NiO, and composites as anode in charge-discharge cycling at 1 C rate. Continuous irreversibility in varying degree is evident during the initial charge-discharge cycles. Such irreversibility occurs until a stable surface film is formed, which prevents further capacity loss. In the present study, almost all constituents were used without further purification. Using clean dried constituents or using alternative ones obviously decreases the irreversibility resulting from those constituents. However, the performance of the materials in the present system can be compared, as any fault that occurs during the preparation of the electrodes is common to all cells. The capacity observed for the graphene is less than for the graphene synthesised by exfoliation of graphite oxide at 1050 °C in Ar [155]. Nevertheless, the present graphene can be used for comparison with the composite. The composite with 50% NiO showed capacity as high as 450 mAh g^{-1} for 100 cycles. All the cells show good stability in cycling at the 1 C rate after the cell was stabilized, implying that all of them are suitable for charge-discharge at moderate current densities. In other words, the battery can be charged to its full capacity in 1 h. The performance of even pristine NiO is good at the 1 C rate, implying that reversible insertion of lithium is possible at the 1 C rate. The charge-discharge performance of pristine NiO was further tested up to 300 charge-discharge cycles and the cell showed good stability at the 1 C rate (not shown here). NiO generally suffers many morphological changes during continuous charge-discharge cycling. Therefore much effort has been made to improve the performance by modification of the NiO [174, 333]. However, the pure NiO obtained in the present

study showed better performance than reported modified NiO [172, 174, 333, 334]. The unique nanostructure observed in the present NiO obviously gave good reversible capacity at moderate current densities.

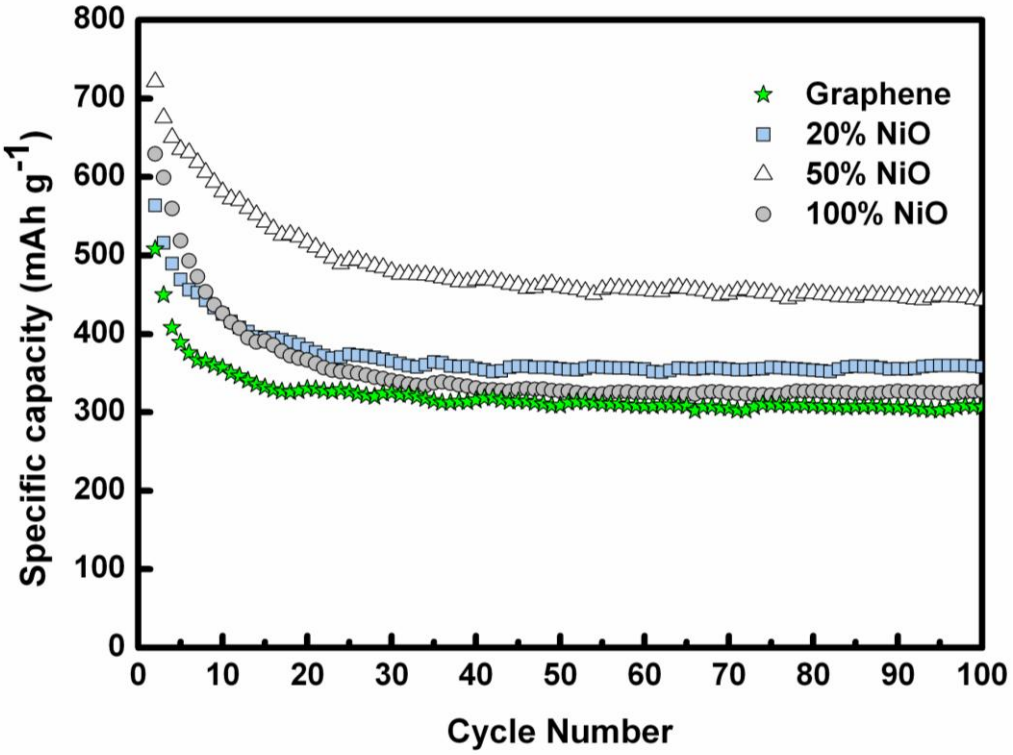

Figure 5.11. Charge-discharge cycling performance of graphene, 20% NiO composite, 50% NiO composite, and 100% NiO half cells at 1 C rate.

Figure 5.12 shows the charge-discharge performance of the half cells at different current densities varying from 0.5 C to 20 C. Although the cell with pristine NiO showed good performance at the 1 C rate, it shows poor performance at higher rates. The cell with 50% NiO shows good capacity only at the 1 C and 2 C rates, it shows low capacity at higher current densities, such as the 10 C and 20 C rates. It is clear that, NiO contributed to the additional capacity which has high theoretical capacity. However, it stands solely at lower current rates. The cells containing 20% NiO show the best performance, with Li-storage capacity of 185 mAh g^{-1} at the 20 C rate. As we have

taken the current density of 300 mA g^{-1} as the 1 C rate, the 20 C rate corresponds to 6000 mA g^{-1}. Such high rate performance has been recently shown for $LiFePO_4$ as a cathode material [335].

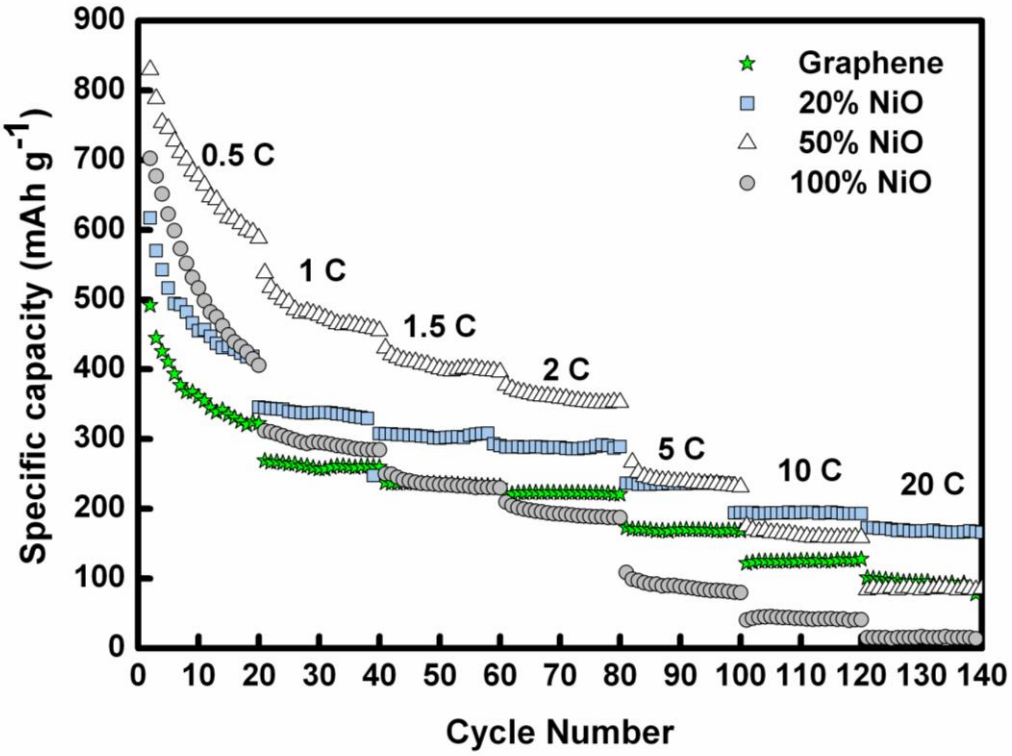

Figure 5.12. The rate capability of graphene, 20% NiO composite, 50% NiO composite, and 100% NiO half cells (1 C = 300 mA g^{-1}).

The present cell can store energy to considerable capacity within 3 min, suggesting that the present anode is suitable for fast charge-discharge requirements. Further increase of the rate performance needs increase of the conductor used in the electrode as indicated in the above Ref. [335]. The fact can be explained as follows. The rate capability of the electrodes generally increases by addition of high percentage of the conductor. Especially for high rate application, higher percentage of conductor is used. The above publication reveals using of even 30% of the conductor in the electrode at very higher current rates such as 20 C, 30 C, etc. The main reason is high rate charge transfer which

is a stringent requirement for high rate application. It is clear that a high content of NiO (50%) leads to attachment of NiO throughout the graphene surface, wherever there are reactive sites such as edges and defects. Presumably, such morphology leads to higher electrical impedance and low capacity when charge-discharge takes place at high current densities. Detailed investigation of impedance spectra is underway. However, the fact that 20% NiO composites deliver higher rate capability can be explained as follows. Graphene is an atomic or nano layers. Therefore it shows good charge transfer rates at higher charge-discharge rates than graphite as observed from recent studies on graphene. Although graphene shows good rate capability, it does not show high capacity as shown by graphene/NiO 20% composite even at low rates. As a result, graphene shows lower capacity at higher rates, yet the rate capability of both half cells is similar. Although, the presence of more NiO leads to high capacity, it obviously limits the charge transfer rate at fast charge-discharge currents as NiO is not conductive. Consequently, the rate capability of both pure NiO and 50% NiO is not satisfactory. The lower percentage of NiO in the composite is therefore more suitable for higher rates. Furthermore, scanning electron micrographs reveal the existence of NiO nano-crystallites mainly at the edge surface of the graphene in 20% NiO composite, presumably due to high reactivity at the edge surface of graphene. Whereas, the 50% NiO composite shows a distribution of NiO throughout the surface due to higher amount of NiO which may be adversely affect for the inter particle conduction of the electrode. Nevertheless, the addition of higher amount of conductor is necessary for fast rate application of such materials. The present study used 10% conductor for fabrication of each electrode. Further investigation is underway to elucidate the mechanism through impedance spectra analysis of each material at different C-rates and different charge-discharge cycle. Therefore higher percentage of NiO is not suitable for application at

higher current densities. The better performance of the 20% NiO composite at higher charge/discharge rates may be a result of the good mechanical stability and the electrical conductance at lower level of NiO. Similar results were obtained for natural graphite surfaces modified with zirconia (ZrO_2) [336, 337]. High rate capabilities have been observed from the presence of zirconia at lower levels. X-ray absorption near edge surface studies showed that zirconia was present at the edge surface. In the composite, NiO contributes to additional capacity by being attached to the defect and edge sites of graphene without much morphological change from continuous lithium insertion and de-insertion during cycling.

5.4 Summary

Graphene/NiO (20%) nanocomposite synthesised by a controlled hydrothermal method delivers high rate capability and long cycle life as anode in Li-ion batteries. Graphene plays a dual role in delivering good performance. Firstly, graphene works as a supporting material for the nanostructured NiO particles to give good mechanical stability for lithium insertion and de-insertion. Secondly, as a lithium ion insertion material, the graphene provides good energy storage capacity. The unique nanostructure of NiO in the composite and of the pure NiO facilitates reversible Li-insertion and de-insertion during the charge-discharge processes. Lower content of NiO in the composite (20%) is suitable for fast charge-discharge application where as higher content of NiO (50%) is suitable for high capacity requirements at moderate rate charge-discharge.

Chapter 6

Synthesis and electrochemical performance of LiV_3O_8/carbon nanosheet composite as cathode material for lithium-ion batteries

6.1 Introduction

Recently, vanadium-based oxides as cathode materials have drawn remarkable attention because they offer great promise for increasing the energy density of the lithium ion battery [9, 338, 339]. As a candidate cathode material, LiV_3O_8 has been the particular object of attention in the past 20 years due to its high theoretical capacity (~280 mAh g^{-1}), facile preparation, and excellent stability in air [340]. LiV_3O_8 with layered structure has been thought to be one of the most promising cathode materials for lithium ion batteries due to its low cost, high discharge rate, and long cycle life [341]. It should be noted that the preparation methods, as well as the material's morphology, can strongly influence the electrochemical performance of LiV_3O_8 electrode, in aspects such as charge-discharge capacity, rate capacity, cyclability [73, 221, 342-344], etc. In fact, up to now, many methodologies have been developed to prepare LiV_3O_8 with the aim of improving its electrochemical performance, for example, the sol-gel method, rapid cooling, efficient grinding, the hydrothermal method, and so on [345-347]. However, the reported rate capacity and cycling properties in all these references are still far from its optimal target performance, and therefore, there is still interest in new synthesis

methods for LiV_3O_8 that might improve its electrochemical properties. However, nanoscale and well-ordered structures with various morphologies of LiV_3O_8 materials have also been extensively studied, for instance, nanorods [222, 223], nanosheets [225, 348], and nanotubes [226]. It is generally accepted that the nanomaterials provide short diffusion pathways for lithium ion insertion/extraction from host materials, together with high specific surface areas, which often afford more active intercalation sites [349, 350]. It has been shown that using nanoparticles and nanostructures for the positive electrode material greatly improves charge/discharge rates by increasing the electrode/electrolyte interface area [86]. Xu et al. prepared $Li_{1+x}V_3O_8$ nanorods by hydrothermal reaction from LiOH and V_2O_5 precursor. The results showed a high initial discharge capacity of 302 mAh g^{-1}, with 278 mAh g^{-1} retained after 30 cycles for the sample annealed at 300°C [222]. More recently, Cui et al. used a combined sol-gel reaction and hydrothermal treatment to prepare LiV_3O_8 nanotubes [226]. However, the disadvantage of these materials was the very fast capacity fading with cycling. In general, the prevalent approach to overcome these problems was doping with a conductive agent such as carbon [351-353], carbon nanotubes [354-357], graphene [148, 358, 359], or conducting polymer [360, 361]. Different conductive fillers have been extensively explored for composite components, and these fillers effectively improve the conductivity of the materials. A significant improvement in electrical conductivity arising from increased filler content was observed for most composites, and it was explained by the better percolation of the conductive network [362, 363]. However, in contrast to the other additives, carbon has a low mass density, and carbon is a cheap way to enhance the conductivity of materials. Carbon coating seems to be an attractive route to enhance the capacity retention and capability of many cathode materials, such as $LiFePO_4$ [210], $LiMnO_2$ [364], and $LiCoO_2$ [365]. Carbon with a

high proportion of sp^2 linkages is usually chosen for coating, since it can provide good electronic transport between the particles, affecting the morphology and the electrochemical performance of the composite material [366].

In this study, LiV_3O_8 nanosheets were synthesized by a hydrothermal method followed by a calcination process. A carbon coating process was also successfully adopted to coat the LiV_3O_8 nanosheets with amorphous carbon. The LiV_3O_8 nanosheets were simply coated by amorphous carbon obtained from malic acid dispersed in toluene. The coating process involved here is a quite different method compared to the others reported in the literature. Furthermore, the role of binders has become increasingly important in terms of the energy density of the whole battery. Recently, aqueous binders have been widely applied for the fabrication of anodes and cathodes for Li-ion cells [367, 368]. Carboxymethyl cellulose (CMC) is one such binder which is an environmentally friendly and inexpensive material compared to the conventional binder, polyvinylidene difluoride (PVdF). The water solubility of CMC also decreases the processing costs during the production of negative electrodes [369]. Electrode using CMC binder is herein reported for the first time for this material. So, the structural and electrochemical properties of the LiV_3O_8/carbon nanosheet composite are presented and characterized with the aim of application as cathode material for lithium-ion batteries.

6.2 Experimental

6.2.1 Preparation of materials

First, VO_2 (B) nanosheet precursor was prepared by a hydrothermal method. In a typical procedure, VO_2 (B) was prepared first by the hydrothermal method, by mixing 0.365 g V_2O_5 (puriss, Riedel-de Haën®) in a solution of *n*-butanol (10 ml, > 99.0%, Sigma-Aldrich) and de-ionized water (30 ml). The mixture was then stirred for 4 h before being transferred to a 125 ml autoclave and kept in an oven for 48 h at 180 °C. The precipitate was washed several times with ethanol and anhydrous cyclohexane, dried at 80 °C in vacuum for 12 h, and annealed at 250 °C in flowing argon for 10 h. In order to prepare LiV_3O_8 nanosheets, stoichiometric VO_2 (B) and $LiOH{\cdot}H_2O$ (Aldrich, 98%) were mixed in methanol and stirred for 12 h. Then, the mixture solution was heated to 50 °C to evaporate the methanol. The product was heated at 150°C for 10 h in vacuum and further annealed at 450 °C for 10 h in air. In the preparation of LiV_3O_8/carbon nanosheet composite, an appropriate quantity of malic acid ($C_4H_6O_5$, 99%) was dissolved in toluene (C_7H_8, 99.5%) and stirred for 2 h. LiV_3O_8 nanosheet powder was added to the solution, which was continuously stirred for 12 h. The mixture solution was heated at 50 °C in vacuum for 12 h and then heated again at 180 °C for 6 h.

6.2.2 Material characterization

X-ray diffraction analysis (XRD) was carried out on the synthesized powders with a GBC MMA generator and diffractometer using Cu Kα radiation and a graphite monochromator. The Traces™ software package in combination with the Joint Committee on Powder Diffraction Standards (JCPDS) powder diffraction files was used to identify the phases present. The amount of amorphous carbon in the composite sample was estimated using a Mettler-Toledo thermogravimetric analysis/differential scanning calorimetry (TGA/DSC) 1 Star^e System from 25-600 ^oC at 5 ^oC $min^{-1.}$ The

morphologies and energy dispersive spectroscopy (EDS) mappings of the samples were obtained with a JEOL JSM 6460A scanning electron microscope (SEM). Transmission electron microscopy (TEM) investigations were performed using a 200 kV JEOL 2011 instrument, with a JEOL-Energy Dispersive X-ray Spectroscopy (EDS) detector and a JEOL EDS software analysis system. TEM powder samples were prepared by dispersion onto holey carbon support films.

6.2.3 Electrochemical measurements

To test the electrochemical performance, sample powders were mixed with acetylene black (AB) and a binder, carboxymethyl cellulose (CMC), in a weight ratio of 75:20:5 in a solvent (distilled water). The slurry was spread onto aluminum foil substrates. The coated electrodes were dried in a vacuum oven at 110 ^{o}C for 24 hours to remove water molecules. The electrode was then pressed using a disc with a diameter of 14 mm to enhance the contact between the aluminum foil, active materials, and conductive carbon. CR 2032 coin-type cells were assembled in an Ar-filled glove box (Mbraun, Unilab, Germany) using lithium metal foil as the counter electrode. The electrolyte was 1 M $LiPF_6$ in a mixture of ethylene carbonate (EC) and dimethyl carbonate (DMC) (1:1 by volume, provided by MERCK KgaA, Germany). Charge/discharge cycling tests were conducted in the voltage range of 1.5-4.0 V using a Land battery tester. Electrochemical impedance spectroscopy (EIS) was conducted in the frequency range between 0.01Hz and 100 kHz using Parstat® 2273 equipment.

6.3 Results and discussion

Structural analysis of LiV_3O_8 and LiV_3O_8/carbon nanosheet composite materials was conducted by XRD studies. The XRD patterns of the samples, shown in Figure 6.1, are in good agreement with the structure of LiV_3O_8 (JCPDS 72-1193).

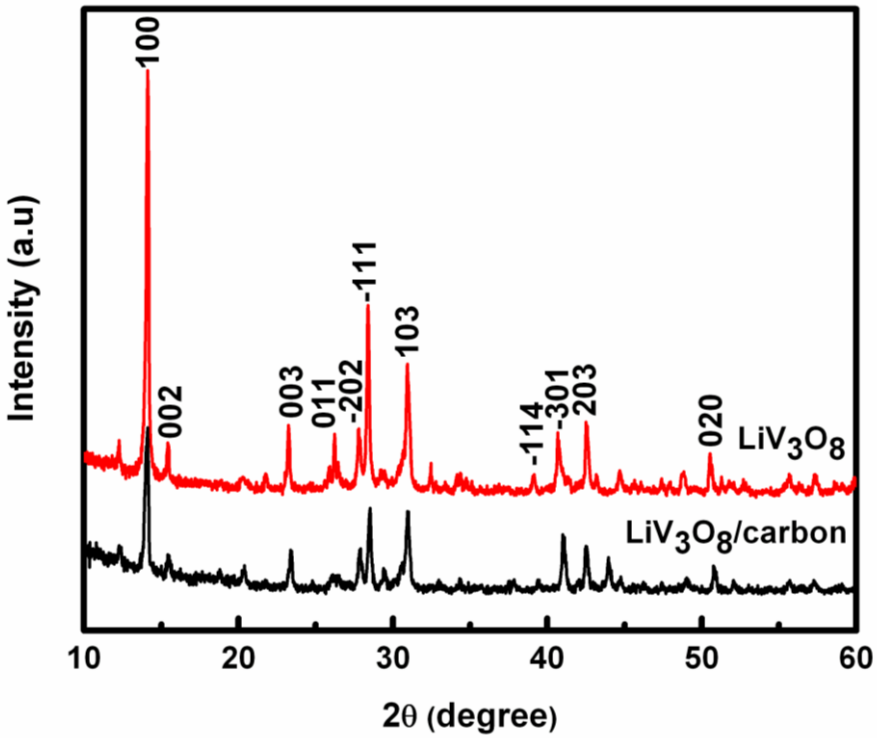

Figure 6.1. X-ray diffraction patterns of LiV_3O_8 and LiV_3O_8/carbon nanosheet composite powders.

The (100) peak at ~ 14° is assigned to the layered structure of LiV_3O_8, where trigonal bipyramids of VO_2 share a corner with the VO_6 octahedra, and the Li^+ is intercalated between such layers [219]. It can be observed that the intensities of the diffraction peaks are decreased for the LiV_3O_8/carbon composite powder, indicating that the material is likely to be more amorphous compared to the pristine LiV_3O_8.

Energy dispersive spectroscopy (EDS) elemental analysis of the LiV_3O_8/carbon nanosheet composite was carried out for the main elements of V, O, and C. Figure 6.2(a) shows the agglomerated LiV_3O_8/carbon composite together with the distribution of the individual elements V, O, and C (Figure 6.2(b)-(d)) . There is no remarkable segregation of carbon in the mapping area, which convincingly proves that the carbon is uniformly distributed among the LiV_3O_8 nanosheets.

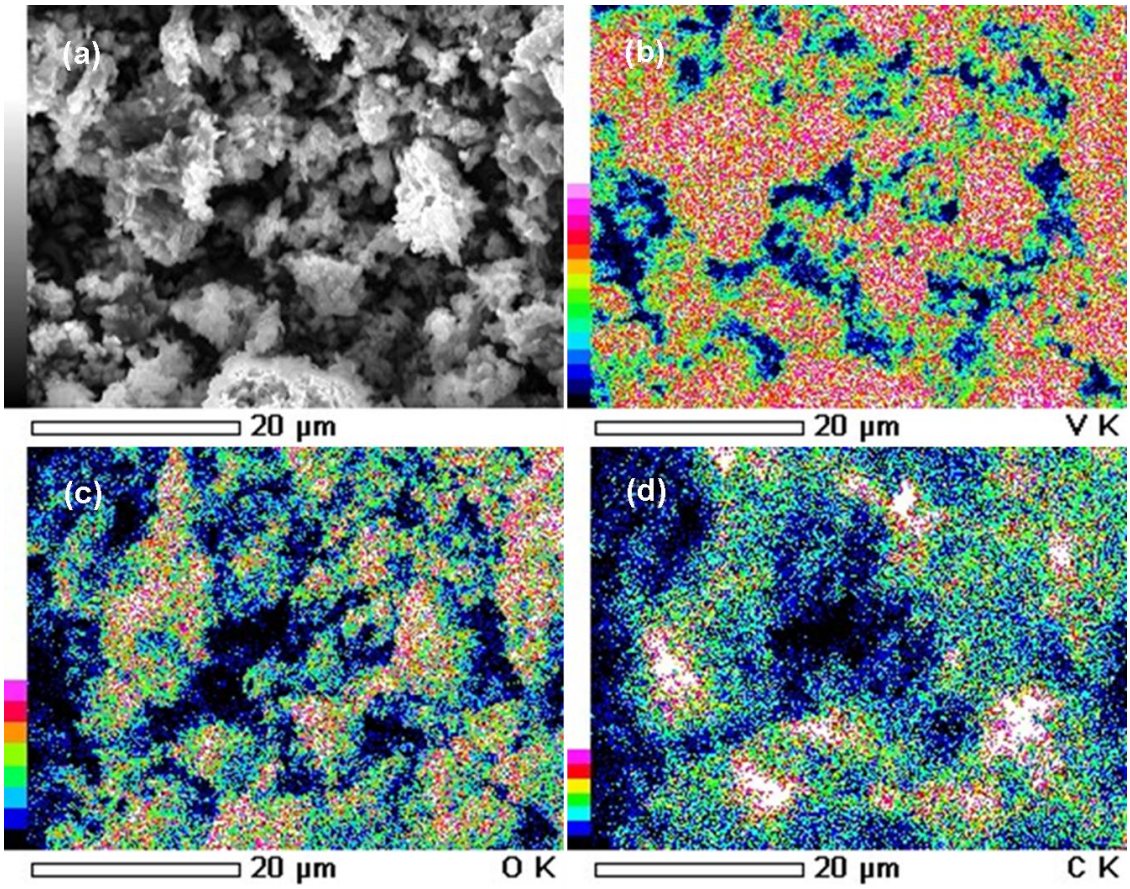

Figure 6.2. SEM image of (a) LiV_3O_8/carbon nanosheet composite powder and its corresponding EDS mapping as follows: (b) V mapping, (c) O mapping, and (d) C mapping.

For quantifying the amount of amorphous carbon in the LiV_3O_8/carbon nanosheet composite, TGA analysis was carried out in air. Figure 6.3 shows the TGA analysis of

the LiV_3O_8 and LiV_3O_8/carbon nanosheet composite. The samples were heated from 25 to 600 °C at the rate of 5 °C min^{-1}. As can be seen from Figure 6.3, LiV_3O_8/carbon nanosheet composite starts to lose weight slowly in air at a temperature of approximately 200 °C, while the pristine LiV_3O_8 powders remain stable over the temperature range used for this experiment. As the pristine LiV_3O_8 powders remain stable from 200 to 600 ^oC, any weight change can be assigned to amorphous carbon. Therefore, the amount of amorphous carbon in the LiV_3O_8/carbon nanosheet composite can be estimated to be approximately 11 wt.%.

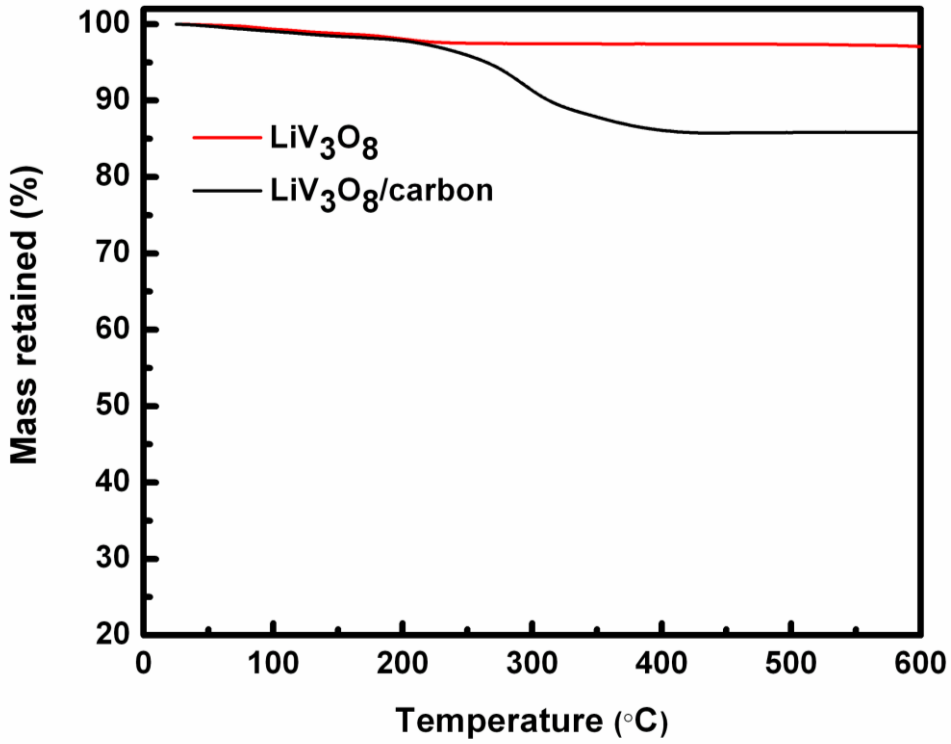

Figure 6.3. TGA analysis of LiV_3O_8 and LiV_3O_8/carbon nanosheet composite powders.

To obtain additional information on the structural and morphological evolution of the samples, field emission SEM (FESEM) and TEM measurements were carried out (Figure 6.4). As shown in Figure 6.4(a), the pristine LiV_3O_8 sample exhibited a very long sheet-like morphology, with each sheet having a smooth surface with a typical

width of 50-150 nm and a length of several micrometers. On the other hand, the LiV_3O_8/carbon sample (Figure 6.4(b)) exhibited a very flat sheet-like morphology, with each sheet having a smooth surface and a typical length of 400-700 nm, width of 200-350 nm, and thickness of 10-50 nm. The selected-area electron diffraction (SAED) pattern (inset) was also collected from the individual nanosheet region of Figure 6.4(b).

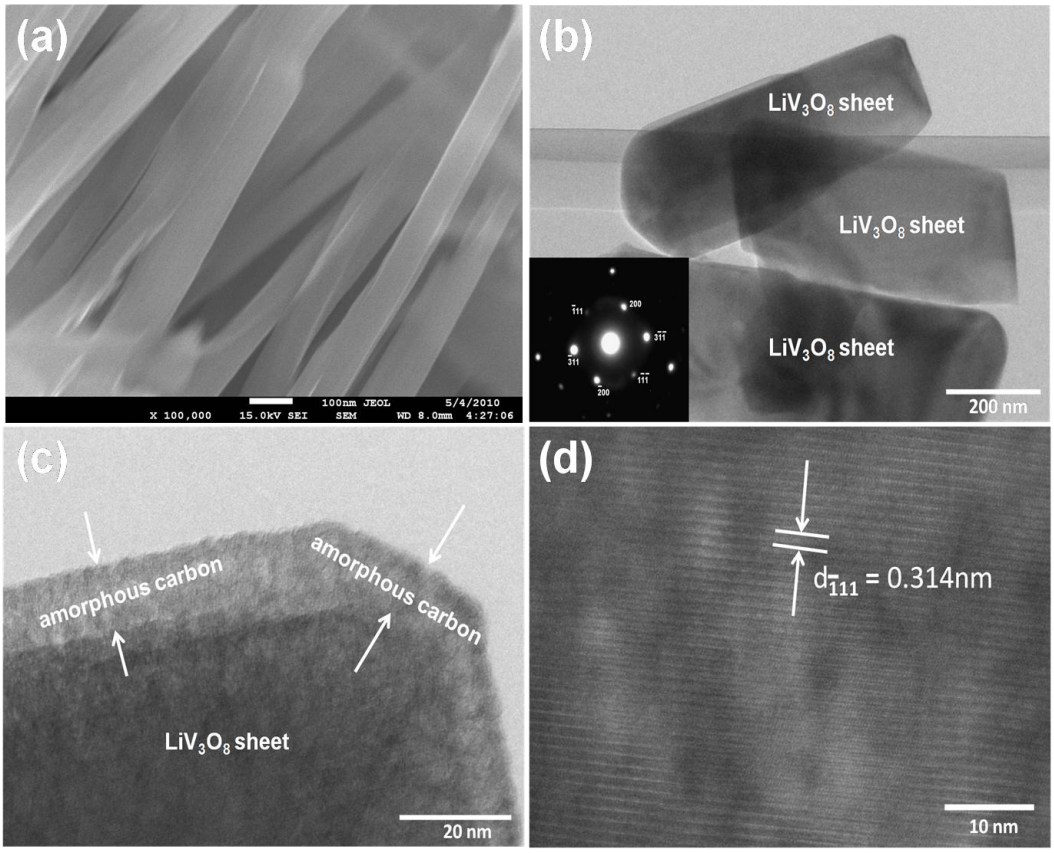

Figure 6.4. Typical FE-SEM image of (a) pristine LiV_3O_8 nanosheets; TEM images of (b) LiV_3O_8/carbon nanosheets and the corresponding SAED pattern (inset); (c) an individual sheet located over a hole in the holey carbon support film and surrounded by a layer of amorphous carbon ~5-10 nm thick; (d) HRTEM image showing lattice fringes of an individual LiV_3O_8 nanosheet.

To confirm how the amorphous carbon is distributed within the LiV_3O_8 nanosheet powder, an individual nanosheet from the region of Figure 6.4(b) was scanned at higher magnification, as shown in Figure 6.4(c). It can be clearly observed that the sheet is surrounded by a layer of amorphous carbon ~5-10 nm thick, as marked in Figure 6.4(c). Furthermore, the high-resolution TEM (HRTEM) image of the individual nanosheet shown in Figure 6.4(d) clearly exhibits lattice fringes, where the lattice planes with a *d* spacing of 0.314 nm correspond to the (-111) planes, which is in good agreement with the structure of LiV_3O_8 (JCPDS 72-1193), as was confirmed by XRD.

The Li-ion intercalation/deintercalation properties in the LiV_3O_8/carbon nanosheet composite were studied in order to examine the effectiveness of carbon in improving the cycling behavior of the electrode. Figure 6.5(c) compares the cycling performance of the LiV_3O_8/carbon electrode at 0.2 C with that of the LiV_3O_8 in the voltage range of 1.5-4.0 V, and their corresponding galvanostatic discharge-charge voltage profiles are shown in Figure 6.5(a, b). Figure 6.5(a) and (b) shows the 1^{st}, 2^{nd}, 5^{th}, 50^{th}, and 100^{th} cycle discharge-charge curves for the LiV_3O_8 and LiV_3O_8/carbon electrodes, respectively. The discharge capacities at the 2^{nd}, 5^{th}, 50^{th}, and 100^{th} cycle of the bare LiV_3O_8 electrode were measured to be 335, 318, 202, and 130 mAh g^{-1}, whereas in the case of the LiV_3O_8/carbon electrode, the discharge capacities were 227, 225, 209, and 194 mAh g^{-1} at the 2^{nd}, 5^{th}, 50^{th}, and 100^{th} cycle, respectively. It can be seen that the discharge capacity for the bare LiV_3O_8 electrode was higher than that of the LiV_3O_8/carbon composite electrode at 0.2 C below 50 cycles. However, the specific capacity of the bare LiV_3O_8 electrode was further decreased with increasing cycle number. This trend is clearly seen in Figure 6.5(c). It can be observed that after coating with carbon, the capacity is actually reduced. It is suggested that this might be due to

the fact that inactive carbon materials are coated on the LiV_3O_8 material [352]**.** Basically, carbon coating is a compromise between cycle life and capacity, and has very limited lithium storage capacity [139]. After 100 cycles, the discharge capacity for the LiV_3O_8 electrode was only 130 mAh g^{-1} at 0.2 C, whereas it was 194 mAh g^{-1} for the LiV_3O_8/carbon electrode. Such a big difference in the electrochemical performance implies that the electrochemical properties of the LiV_3O_8 are greatly influenced by the carbon coating. In order to fully estimate the electrochemical performance of the LiV_3O_8 and LiV_3O_8/carbon composite electrodes, the consecutive cycling behavior at various current densities of 0.5, 1, 2, and 5 C was examined, as shown in Figure 6.5(d). The initial (considering the 2^{nd} cycle) discharge capacities at the low current density of 0.5 C were measured to be 296 mAh g^{-1} and 157 mAh g^{-1}, and at the 10^{th} cycle, 275 and 175 mAh g^{-1} for the LiV_3O_8 and LiV_3O_8/carbon electrodes, respectively. This trend was continued up to 50 cycles for both electrodes, and capacity retention measured at every 10^{th} cycle was only 78% at 1 C, 66% at 2 C, and 73% at 5 C of the initial discharge capacity for the LiV_3O_8 electrode. In the case of the LiV_3O_8/carbon composite electrode, capacity retention was 97% at 1 C, 99% at 2C, and 91% at 5 C of initial discharge capacity. On returning to 0.5 C, the LiV_3O_8 and LiV_3O_8/carbon composite electrodes delivered a discharge capacity of 155 mAh g^{-1} and 173 mAh g^{-1}, respectively. It should be noted that the LiV_3O_8/carbon composite electrode shows more stable cycling performance at each current density, although it shows a lower discharge capacity than the LiV_3O_8 electrode in the beginning. At the high current densities of 2 C and 5 C, the LiV_3O_8/carbon composite electrode shows larger discharge capacity than the LiV_3O_8 electrode. This kind of behavior was also reported by Du et al. [140] and Wu et al. [316], which leads to the conclusion that the LiV_3O_8/carbon composite electrode possesses better electrochemical performance compared with pristine LiV_3O_8.

We believe that this carbon coating was responsible for improving the electrical conductivity of the LiV_3O_8 material, as well as preventing aggregation and effectively accommodating the volume variation [141]. Carbon addition also has been shown to improve the performance of $LiFePO_4$ [351, 370] and $LiMn_2O_4$ [371] materials, especially at high discharge rates, where the carbon coating provides a path for electrons without blocking access for Li^+ ions.

We further investigated the cycling performance of the LiV_3O_8/carbon nanosheet composite electrode at the high current densities of 5, 10, and 20 C. The cycling behavior for the composite is sustained at high current density up to 200 cycles, implying that the carbon coating contributes to the better capacity retention. As shown in Figure 6.5(e), the specific capacity of LiV_3O_8/carbon composite electrode at 5, 10, and 20 C after 250 cycles was measured to be 110 mAh g^{-1}, 104 mAh g^{-1}, and 82 mAh g^{-1}, respectively. The capacity retention after 250 cycles from the second cycle was 93% at 5 C and 100% at 10 C. For the second cycle, the discharge capacity at 20 C was 65 mAh g^{-1}, and it increased to 82 mAh g^{-1} at the 50^{th} cycle. Then, the discharge capacity becomes steady for up to 250 cycles. It can be observed that the capacity increases with cycle number, possibly because of the processes of activation and stabilization that are going on in the electrode materials [344]. The morphological effects in the compound are likely to lead to diffusion limitations, where all the lithium ions might not be able to take part in the initial cycling, but with increasing cycle number, more active material may be able to participate due to electrochemical grinding, leading to an increase in capacity with increasing cycle number [372]. Another reason may be the slight fragmentation of the grains induced by the electrochemical grinding. The smaller grain

size reduces the diffusion path for the lithium ions [373]. This result shows that good cycling stability has been achieved for the LiV_3O_8/carbon electrode.

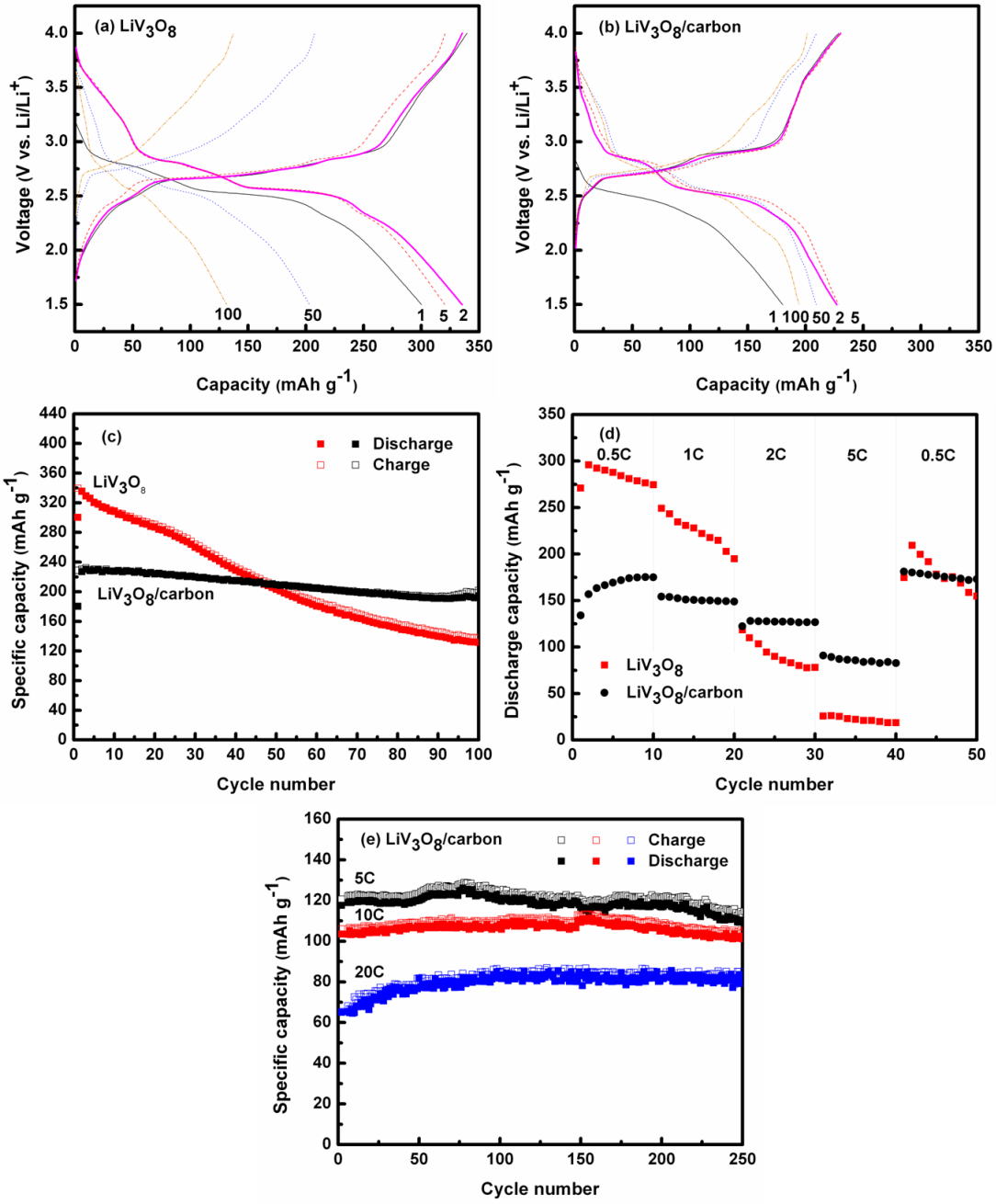

Figure 6.5. Electrochemical performances of LiV_3O_8 and LiV_3O_8/carbon composite electrodes: (a, b) galvanostatic charge-discharge voltage profiles at 0.2 C for selected cycles; (c) cyclic performance beyond 100 cycles at 0.2 C; (d) consecutive cyclic behavior at different rates; (e) long-term cycling performance of LiV_3O_8/carbon nanosheet composite electrode at different rates of 5, 10, and 20 C, respectively.

Essential information on the anodic/cathodic processes in the pristine LiV_3O_8 and the composite electrodes can be extracted from the charge/discharge curves by translation into differential capacity curves. In Figure 6.6, comparative plots for the pristine LiV_3O_8 and the composite electrodes for the 5^{th}, 50^{th}, and 100^{th} cycles are presented. The patterns for both profiles are nearly identical, suggesting that the carbon was not involved during intercalation/deintercalation processes and is only providing paths for electrical conduction [374]. Basically, there are several cathodic peaks at 2.6-2.8 V that are related to the insertion of Li^+ into LiV_3O_8. The anodic peaks are located at 2.7-2.8 V, which are related to the extraction of Li^+ from LiV_3O_8 [344]. From Figure 6.6(a), the intensity of the peaks decreases with cycling, indicating poor cycling stability. However, for the composite electrode, it is clearly seen from Figure 6.6(b) that the anodic and cathodic peak intensities remain stable upon cycling. This result is consistent with the cycling performance results, demonstrating that the composite electrode has excellent kinetic activities for Li^+ insertion/extraction.

The impedance spectra for the pristine LiV_3O_8 and the composite electrodes were collected in the fully charged state (4.0 V) after 50 cycles. The Nyquist plots (Figure 6.7) show a semicircle in the high to medium frequency range, which describes the charge transfer resistance (R_{ct}) for both electrodes. The intercept value is considered to represent the total electrical resistance offered by the electrolyte (R_s). The inclined line represents the Warburg impedance (Z_w) at low frequency, which indicates the diffusion of Li^+ in the solid matrix. The impedance plots were fitted using the equivalent circuit model shown in the inset in Figure 6.7, where C_{DL} represents the double layer capacitance. The values of R_{ct} for the LiV_3O_8 and the composite electrodes are 324.2 and 121.8 Ω, respectively. Obviously, the R_{ct} of the LiV_3O_8/carbon electrode is much

smaller than that of the pristine LiV_3O_8 electrode. Therefore, the presence of carbon in LiV_3O_8 improved the battery performance upon extended cycling, as the R_{ct} decreased.

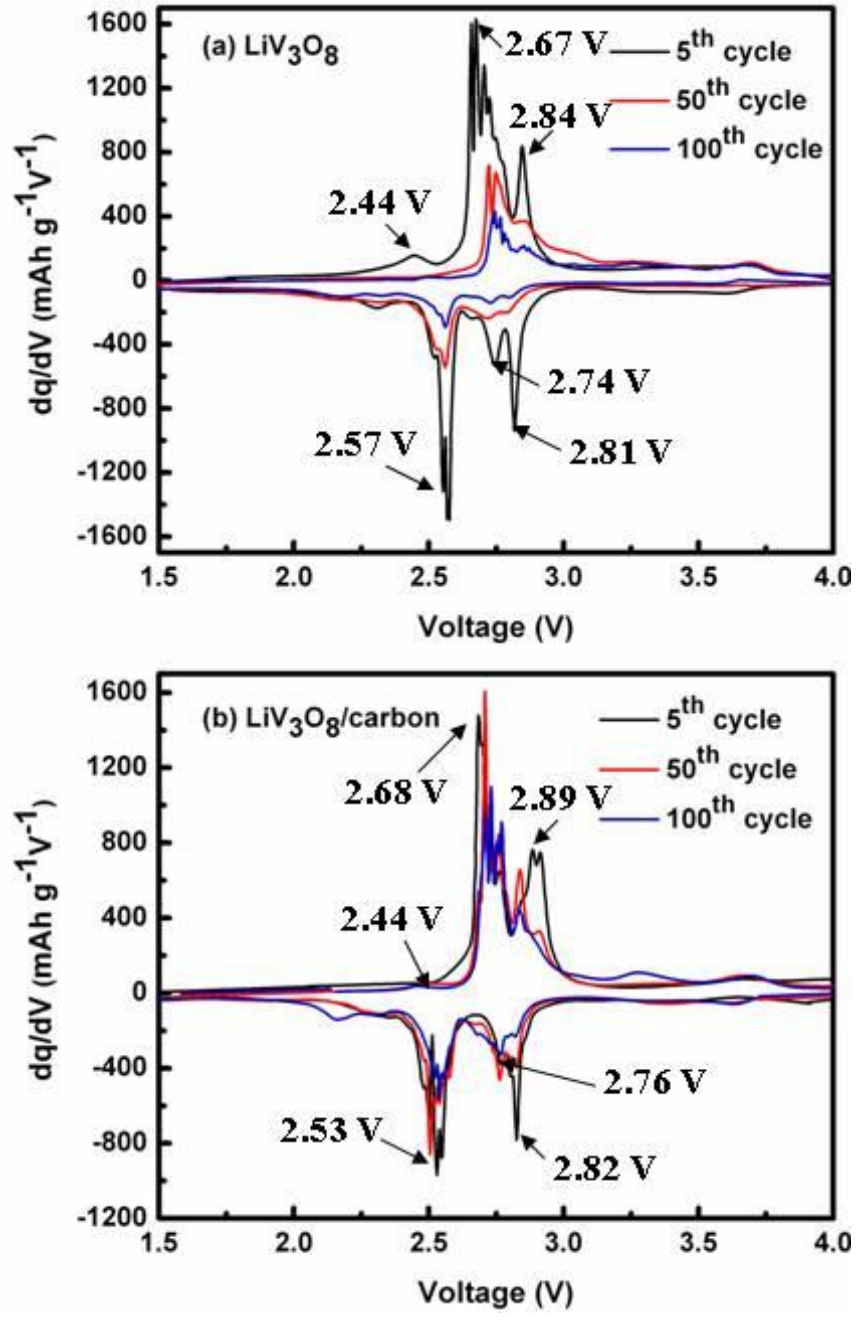

Figure 6.6. Differential capacity plots for LiV_3O_8 (a) and LiV_3O_8/carbon (b) at the 5th, 50th, and 100th cycle.

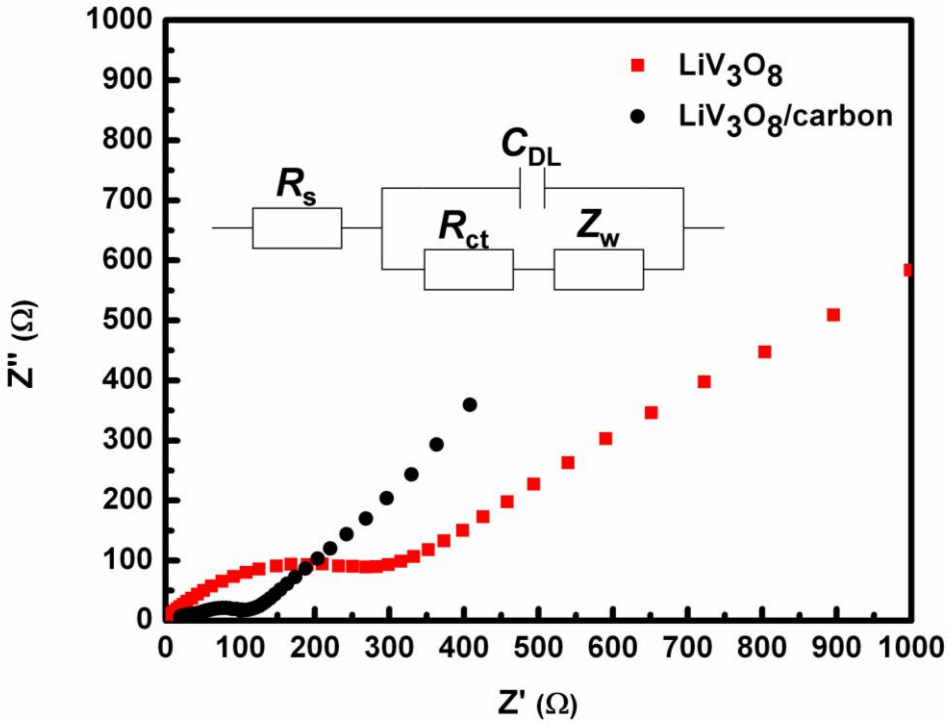

Figure 6.7. Electrochemical impedance spectra of the samples after 50 cycles of charge/discharge and the equivalent circuit (inset) used for fitting the EIS spectra.

6.4 Summary

In summary, LiV_3O_8/carbon nanosheet composite has been successfully synthesized via *in-situ* hydrothermal treatment followed by a carbon coating process, and the material was investigated, along with the bare LiV_3O_8, as cathode for lithium-ion batteries. TEM observations confirmed that the composite exhibited a flat sheet-like morphology, with the nanosheets covered by a layer of amorphous carbon ~5-10 nm thick. It was found that the carbon coated composite showed better electrochemical performance in terms of rate capability and cycling stability compared with the LiV_3O_8 sample. This high performance can be ascribed to the combined effects of nanosize sheets and good interface behavior between the carbon layer and the nanosheets, which improved the

electrical conductivity and decreased charge transfer resistance, as was confirmed by cyclic voltammetry and EIS. This research suggests that the LiV_3O_8/carbon nanosheet composite could be suitable for use as cathode material for lithium-ion batteries.

Chapter 7

Rapid Synthesis of Binary α-NiS-β-NiS by Microwave Autoclave for Rechargeable Lithium Batteries

7.1 Introduction

There is an urgent need for renewable clean energy sources at a much higher level than is presently in force. The CO_2 issue, and the consequent air pollution in large urban areas, may be only solved by replacing internal combustion engine (ICE) cars with ideally, zero emission vehicles, i.e. electric vehicles (EVs) or, at least, by controlled emission vehicles, i.e. hybrid electric vehicles (HEVs) and/or plug-in hybrid electric vehicles (PHEVs). In this respect, lithium-ion battery technology could be the most promising approach. Thus, achieving the goals of low cost combined with higher energy density, better cycling stability, and non- or less toxic and more environmentally friendly materials as electrodes for lithium ion batteries has become mandatory if clean renewable technologies are to be developed for the future [375, 376]. Presently, $LiMO_2$ or LiM_2O_4 (M: transition metal) compounds are widely employed as positive electrode for lithium-ion batteries due to their high reversibility in Li-ion intercalation/de-intercalation processes [176, 177, 377-379]. Although $LiCoO_2$ is still being used as a successful cathode material in most commercial lithium-ion batteries, it is less available in terms of raw materials, more toxic, and more costly than other transition metals, such as manganese, nickel, and iron. In addition, $LiCoO_2$ is not as stable as other potential electrode materials and can undergo performance degradation or failure when

overcharged [380-382]. $LiNiO_2$, which also forms a distorted rock-salt structure, is lower in cost and has a higher energy density [383], but is less stable [384, 385] and less ordered [386], as compared to $LiCoO_2$. $LiMn_2O_4$ has shown excellent cycling performance at room temperature in the region of 4 V, but still suffers from capacity loss, particularly at elevated temperature [364]. Various strategies have been proposed and tested to avoid some of these drawbacks, and scientists are still struggling to minimize these problems. Besides these types of positive materials, sulfur and metal sulfides are known to be promising cathode materials because of their low cost and high theoretical capacity, assuming complete discharge to Li_2S [300, 387-391]**.** Among the various metal sulfides, nickel sulfide is the one of the most promising cathode materials. Nickel sulfide (NiS) has a high theoretical capacity of 590 mAh g^{-1} with good electronic conductivity [229]. At present, only a few studies on NiS as a battery material have been reported [228-230, 235, 392, 393]. Studies based on the ex-situ X-ray diffraction method by Han et al. [230] indicated that the cathode reaction of NiS could be explained as follows:

$$3NiS + 2Li \leftrightarrow Ni_3S_2 + Li_2S \quad (7.1)$$

$$Ni_3S_2 + 4Li \leftrightarrow 3Ni + 2Li_2S \quad (7.2)$$

The total charge-discharge mechanism is represented as:

$$NiS + 2Li \leftrightarrow Ni + Li_2S \quad (7.3)$$

To this end, various synthesis techniques have been adopted to synthesize NiS in order to improve the electrochemical performance of NiS electrodes, such as ball-milling [229, 230, 393], high-boiling-point solvent [228], polyol [235], spark plasma-sintering [236], and solvothermal [392] techniques, in which most of the methods require extensive mechanical mixing, high temperature, and long reaction time. Wang et al. [392] have prepared NiS by the solvothermal method, which needs 24 hours to

complete the reaction. In addition, homogeneous NiS readily forms after 12 hours of ball milling, as reported by Han et al. [230]. Quite recently, microwave-assisted synthesis methods have been particularly proved to be effective for many types of cathode materials [195, 394-396]. Microwave-assisted synthesis requires much shorter reaction times and saves energy, which is favorable for industrial manufacturing when compared with the conventional solvothermal and hydrothermal synthesis. Manthiram et al. have successfully synthesized a series of $LiMPO_4$ (M: Fe, Mn, Co, Ni) nanocrystallites within 5 to 15 min at temperatures below 300 °C [394, 395, 397, 398], and the preparation of $LiMnO_2$ using conventional and microwave hydrothermal routes has also been reported by Ji et al. [195]. It was observed that the electrochemical performance of $LiMnO_2$ obtained from the microwave hydrothermal method was improved compared to the conventional method.

It is well known that electronic transport properties can be tuned by interfacial design and by varying the spacing of interfaces down to the nano-regime [399-401]. In recent reports, the interface in some dual-phase materials is demonstrated to be more sensitive for storing the extra lithium [228, 392, 399, 402, 403]. There are many hybrid systems reported due to some great advantages which possibly could not be found in the single system, such as higher catalytic activity, capability to absorb the volume variation of the active material during lithium insertion, and ability to react reversibly with a larger amount of lithium, and these factors can greatly improve the electrochemical performance compared to the single component systems [392, 399, 402]. Morphological stability can also be further improved if several materials are combined in an appropriately structured composite [404, 405]. When two compounds with different crystal structures combine and form a composite, the crystal lattice mismatch causes

numerous lattice defects in the structure of the composite. As a result, channels for Li^+ transfer in the composite will be much more abundant than in either of the constituent compounds [399]. Based on this approach, we attempted to incorporate β-NiS phase into α-NiS, with the aim of improving the electrochemical performance of α-NiS cathode.

In this study, we report binary α-NiS-β-NiS compound prepared *via* the microwave hydrothermal method within a short period of time. In addition, an electrolyte consisting of 1 M lithium bis(trifluoromethanesulfonyl) imide (LiTFSI) in poly(ethylene glycol) dimethyl ether 500 g/mol (PEGDME 500) is also reported in this work. It was previously reported that the electrochemical performances of nickel sulfide electrodes were improved by using this electrolyte when compared with conventional electrolyte composed of 1 M $LiPF_6$ in ethylene carbonate (EC) and dimethyl carbonate (DMC) [235, 392].

7.2 Experimental

7.2.1 Preparation of materials

In a typical procedure for the preparation of NiS powders [405], 0.01 mol nickel (II) acetate tetrahydrate ($Ni(CH_3COO)_2{\cdot}4H_2O$, 98%, Sigma Aldrich), 0.03 mol thiourea (N_2SCH_4, ≥ 99%, Sigma-Aldrich), and 0.01 mol citric acid trisodium salt dehydrate ($Na_3C_6H_5O_7{\cdot}2H_2O$, 99%, Aldrich) were added to 40 mL deionized water under stirring. Afterward, 20 mL ammonia solution (28-30%, MERCK) was added dropwise to tune the pH value to 12, and the dark blue solution was further stirred for 30 min. Then, the solution was transferred into three Teflon lined digestion vessels, each with a volume of

20 mL, and fitted with a pressure and temperature probe. The sealed vessels were placed inside a MicroSYNTH microwave system (Milestone). The power, time, and temperature of the reaction system were controlled by a Labterminal 800 Controller. To get single phase α-NiS, the sealed vessel was heated at 140 °C for 15 min, whereas binary α-NiS-β-NiS was obtained at 160 °C and 180 ^{o}C for 15 min. The power was kept at 300 W throughout the experiment. The precipitate was washed several times with de-ionized water and ethanol, and dried at 50 °C in vacuum for 12 hours.

7.2.2 Material characterization

The phase formations of the synthesized powders were investigated using X-ray diffraction (XRD) with a diffractometer using Cu Kα radiation and graphite monochromator (GBC Difftech MMA instrument). The Brunauer-Emmett-Teller (BET) surface areas were measured by a NOVA 1000 high-speed gas sorption analyzer (Quantachrome Instruments, USA). The morphologies of the samples were examined using field emission scanning electron microscopy (FE-SEM, JEOL 7500FA) and transmission electron microscopy (TEM, JEOL 2011 200 keV instrument).

7.2.3 Electrochemical measurements

A mixture composed of 70 wt.% of the powder sample, 20 wt.% of carbon black, and 10 wt.% of polyvinylidene fluoride (PVDF) was mixed with *N*-methyl-2-pyrrolidone (NMP). The slurry was spread onto aluminum foil substrates and dried at 100 °C for 24 hours in vacuum. After being cut to a 1 × 1 cm^2 size, the electrode was mounted as the positive electrode versus lithium metal as the counter and reference electrode in CR

2032 coin-type cells. The cells were assembled in an argon-filled glove box. The electrolyte used to test the electrochemical performance of the electrodes was an organic solvent-based electrolyte composed of 1 M lithium bis(trifluoromethanesulfonyl) imide (LiTFSI) in poly(ethylene glycol) dimethyl ether 500 g/mol (PEGDME 500). Charge-discharge testing was performed galvanostatically between 1.0 and 3.0 V on a Land battery tester (Wuhan Land Electronic Co. Ltd.). Cyclic voltammetry (CV) measurements were carried out using a CHI 660B Electrochemical Workstation (Shanghai Chenhua Apparatus, China) at a scanning rate of 0.05 mV s^{-1}.

7.3 Results and discussion

The XRD patterns of the samples synthesized at 140 °C, 160 °C, and 180 °C for 15 min are shown in Figure 7.1. Microwave hydrothermal treatment of the mixture at 140 °C produced a pure hexagonal NiAs-type α-NiS phase, which shows good agreement with JCPDS data (JCPDS File Card No. 75-0613, space group: $P6_3/mmc$, a = 3.4200 Å and c = 5.3000 Å). Liu has reported that the synthesis of single-phase α-NiS was obtained at a longer reaction time of 24 hours by a conventional hydrothermal route [404]. In our case, α-NiS single-phase could be prepared within 15 min at low temperature. The direct heating in the microwave autoclave system can increase the kinetics of the reaction by one or two orders of magnitude, as the microwave energy is dissipated by the reactants and the reaction is completed within several minutes [195, 406, 407]. This is different from the conventional autoclave method, which gives indirect heating to the reactants, thus requiring longer time to complete the reactions. On increasing the reaction temperature to 160 °C and 180 °C, the formation of a secondary phase of

rhombohedral millerite β-NiS was evidenced by the appearance of additional XRD reflections which matched well with the standard data (JCPDS File Card No. 12-0041, space group: *R*3*m*, *a* = 9.6200 Å and *c* = 3.1600 Å) [229, 235, 392]. The intensities of α-NiS peaks decreased, and those associated with β-NiS started to grow at this temperature.

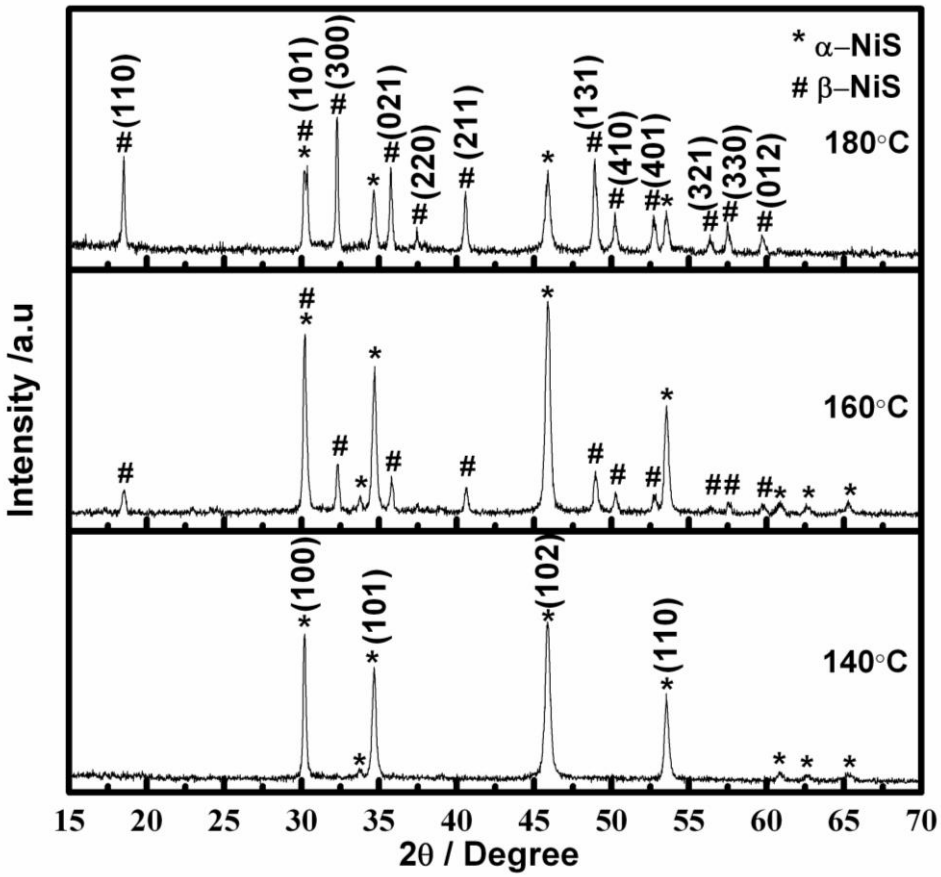

Figure 7.1. XRD patterns of the NiS powders synthesized at 140 °C, 160 °C, and 180 °C.

The calculated cell parameters for each sample are close to those reported in the literature, as shown in Table 7.1. The approximate crystallite sizes for the samples were estimated using the Debye-Scherrer formula, which was applied to the (102) peak of α-NiS and the (300) peak of β-NiS. The specific surface areas of the synthesised products

were also measured by the 15 points BET N_2 adsorption method. Approximate crystallite sizes and specific surface areas of the samples are also shown in Table 7.1. The measured BET specific surface area for the α-NiS-β-NiS prepared at 160 °C shows the highest value of 4.67 m^2 g^{-1}, while the α-NiS synthesized at 140 °C and the α-NiS-β-NiS synthesized at 180 °C have specific surface areas of 2.66 and 1.82 m^2 g^{-1}, respectively. Generally, high surface area powders are beneficial to the intercalation/de-intercalation of Li^+, and thus improve the cycling stability and electrochemical performance of the electrode [85].

Table 7.1. Calculated cell parameters, approximate crystallite size, and BET specific surface area of synthesized NiS at different temperatures.

Calculated cell parameters of α-NiS		Calculated cell parameters of β-NiS		Crystallite size of α-NiS from peak (102) (nm)	Crystallite size of β-NiS from peak (300) (nm)	BET specific surface area (m^2 g^{-1})
a (nm)	*c* (nm)	*a* (nm)	*c* (nm)			
0.34246	0.53181	-	-	41	-	2.66
0.34285	0.53232	0.96185	0.31538	47	53	4.67
0.34274	0.53225	0.96191	0.31557	32	87	1.82

FESEM images of the products synthesized at different temperatures are shown in Figure 7.2. A single morphology is formed for the product after heating at 140 ^oC (Figure 7.2(a, d)), comprising, predominately, prismatic particles around 500-900 nm in size, consistent with XRD evidence for the formation of α-NiS. The morphologies obtained at 160 ^oC (Figure 7.2(b, e)) and 180 ^oC (Figure 7.2(c, f)) comprised a duplex coarse nanostructure, with core particles of similar morphology to those formed at 140

^{o}C and additional fine needle-like protrusions, resulting in product of higher surface area. Compared to the monophase sample formed at 140 °C, when the reaction temperature is raised to 160 °C, the core particles (assumed to be α–NiS) appear to take on a more refined hexagonal prism shape, while the nanoneedles (assumed to be predominately β-NiS) appear to originate from facets and facet corners of the hexagonal prisms (Figure 7.2(e)). The sizes of the hexagonal prism shaped particles were found to be in the range of 1-2 μm, while the average diameter of the nanoneedles was about 80-200 nm.

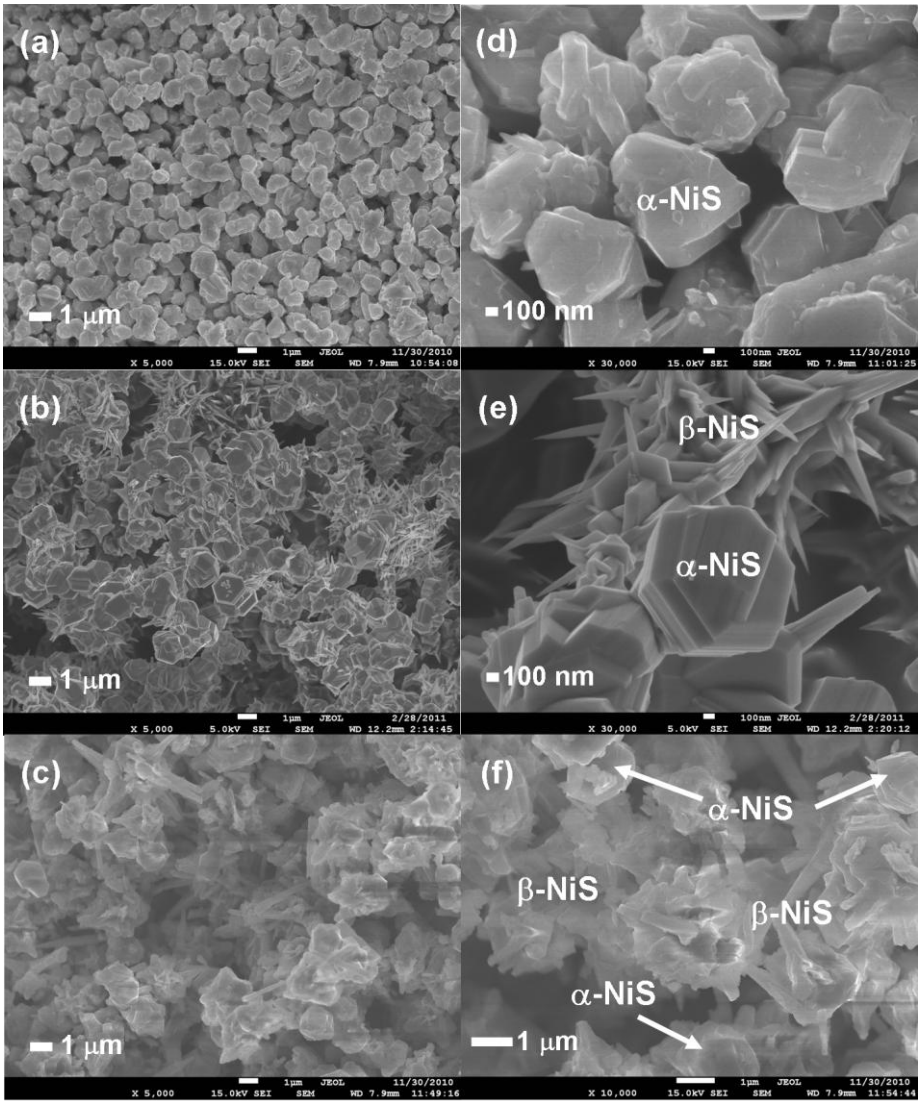

Figure 7.2. FESEM images of NiS powders synthesized at (a), (d) 140 °C; (b), (e) 160 °C; and (c), (f) 180 °C.

We also observed that when the reaction temperature was increased up to 180 °C, there appeared to be an increase in the amount of needle-like phase at the expense of α-NiS grain size, consistent with increased transformation of α-NiS to β-NiS. The size of the agglomerated clusters, up to about 2-3 μm, is believed to be responsible for the decrease in the surface area compared to the sample formed at 160 °C. Close observation of the high-magnification FESEM image (Figure 7.2(f)) reveals that the nanoneedle shape increases in size to a diameter of about 400-600 nm. These results are consistent with the calculated crystallite sizes and measured BET specific surface areas.

Figure 7.3 shows TEM and preliminary high resolution TEM (HRTEM) observations of the samples prepared at 160 °C and dispersed onto holey carbon support film. Bright field imaging confirmed that the needle-like protrusions connect the clusters of α-NiS particles (Figure 7.3(a)). Close examination of individual protrusions (Figure 7.3(b) and (c)) indicated a very high surface area morphology including sheets folded up into the features described as nanoneedles that were observed using lower resolution TEM (Figure 7.3(c)). Preliminary HRTEM combined with a Fast Fourier Transform (inset in Figure 7.3(d)) revealed a faulted structure containing a significant proportion of microtwins (Figure 7.3(e)), consistent with early TEM observations of rhombohedral NiS phase [408]. However, further investigation is required to determine the true structure of these needle-like protrusions producing the β-NiS XRD reflections, firstly, because β-NiS can transform to α-NiS as a result of electron beam heating [408] and because non-stoichiometric $Ni_{(1-x)}S$ can also occur with a range of different atomic stacking sequences and associated structure variants [409].

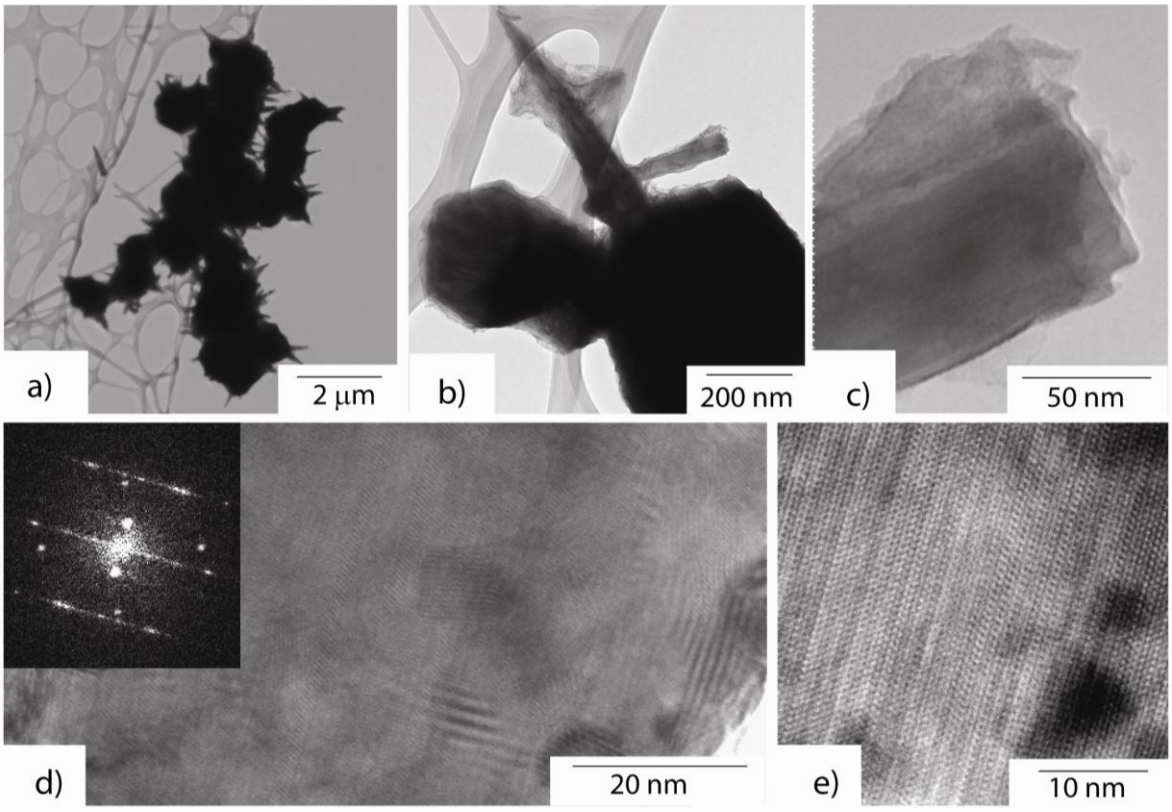

Figure 7.3. TEM and HRTEM images of sample prepared at 160 °C; (a-c) bright field images; (d-e) HRTEM images and fast Fourier transform (diffractogram inset in (d)).

Figure 7.4 shows a typical cyclic voltammogram of the α-NiS electrode prepared at 140 °C, recorded at a scan rate of 0.05 mV s^{-1} between 1.0 and 3.0 V. Han et al. [230] have reported the ex-situ XRD profile of NiS electrode during electrochemical charge-discharge cycling. It is considered that the anodic and cathodic processes of NiS undergo the same reaction mechanism. Cathodic peaks are present at around 1.75 V and 1.20 V, which might be related to two different electrochemical reactions between NiS and lithium. On the other hand, the anodic peak occurs at around 2.00 V, which could be related to the regeneration of NiS. The cathodic peaks in the cyclic voltammograms are in good agreement with the plateaus observed in the voltage-capacity profiles (Figure 7.5(a-c)). It is suggested that the Li/NiS cell discharges in a two-step process.

The first step could be the transformation of NiS to Ni_3S_2 at higher potential around 1.75 V (eq. (7.1)) and the second step could be the conversion of Ni_3S_2 to Ni at lower potential around 1.20 V (eq. (7.2)) [230, 235]. In the anodic process, we can find a large charging current peak at 2.10 V, which represent the regeneration of NiS in the fully charged state. This phenomenon is consistent with the previous report about charge-discharge mechanism study of NiS used as cathode in rechargeable lithium batteries [230].

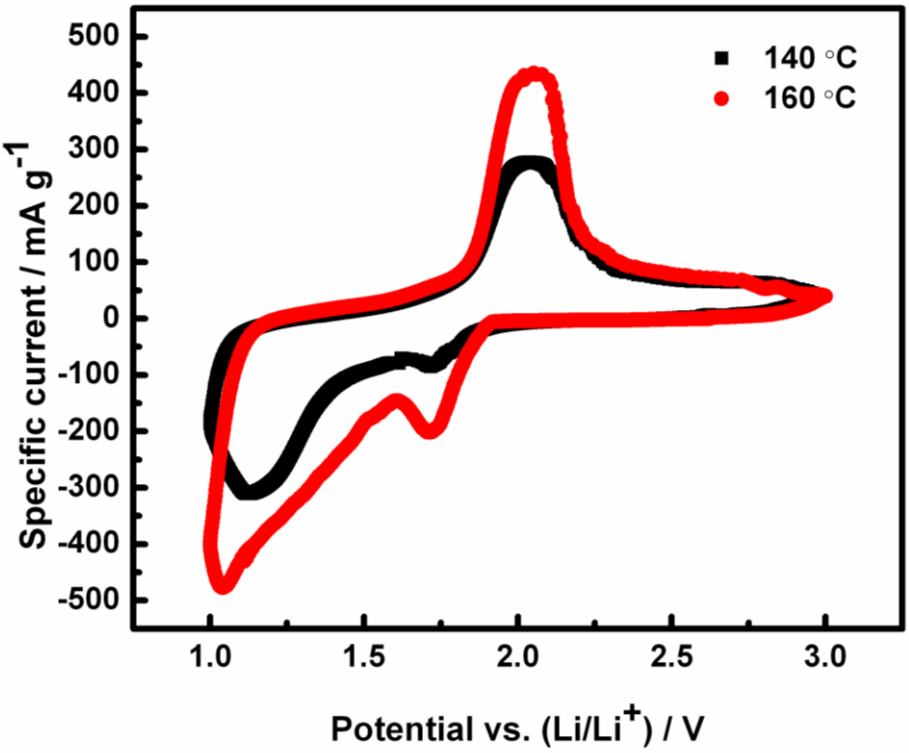

Figure 7.4. Cyclic voltammogram of NiS synthesized at 140 °C and 160 °C with scan rate of 0.05 mV s^{-1}.

Figure 7.5(a-c) shows the 1st, 2nd, 10th, and 50th cycle discharge voltage profiles at 0.1 C of the electrodes prepared at 140 °C, 160 °C, and 180 °C. The discharge curves show two voltage plateaus which are consistent with the CV curve. The initial discharge capacity for the NiS electrode prepared at 140°C, 160°C, and 180°C was measured to

be 535, 581, and 585 mAh g^{-1}, with an initial coulombic efficiency of 98%, 96% and 84%, respectively. It can be seen that all the cells show irreversible capacity loss during the first charge-discharge cycle and improvement of stability during the subsequent cycles. The initial capacity loss is attributed to the surface film formation [332]. The discharge capacities were measured to be 447, 408, and 342 mAh g^{-1} at the 2^{nd}, 10^{th}, and 50^{th} cycle for the electrode prepared at 140 °C, whereas in the case of α-NiS-β-NiS electrode prepared at 160 °C, the discharge capacities were 486, 452, and 385 mAh g^{-1} at the 2^{nd}, 10^{th}, and 50^{th} cycle, respectively. However, the discharge capacity for the electrode prepared at 180 °C decreased rapidly and was measured to be 349, 165, and 86 mAh g^{-1} at the 2^{nd}, 10^{th}, and 50^{th} cycle, respectively. The overpotential of NiS synthesized at 160 °C was found to be smaller than pure α-NiS. This may because the sample prepared at 160 °C has higher BET surface area than the sample prepared at 140 °C, the contact surface area between NiS and carbon black are increased, therefore increase the conductivity and electrochemical accessibility of NiS prepared at 160 °C electrodes. The cycling stability of the electrodes at 0.1 C is shown in Figure 7.6(a). The electrode prepared at 160 °C shows a higher discharge capacity and better cycling performance. After 100 cycles, the discharge capacities were measured to be 281 and 320 mAh g^{-1} for the electrodes prepared at 140 and 160 °C, with capacity retention of 63% and 65% of the 2^{nd} cycle discharge capacity, respectively. The discharge capacity degradation rate was about 0.37% per cycle for the NiS electrode prepared at 140 °C and 0.35% per cycle for the α-NiS-β-NiS electrode prepared at 160 °C. Rapid capacity decay of the electrode prepared at 180 °C was observed. The coulombic efficiency for α-NiS synthesized at 140 °C and α-NiS-β-NiS synthesized at 160 °C was reached 96%

and 99% over 100 cycles respectively, whereas it was 90% for the α-NiS-β-NiS synthesized at 180 °C over 68 cycles (Figure 7.6(b)).

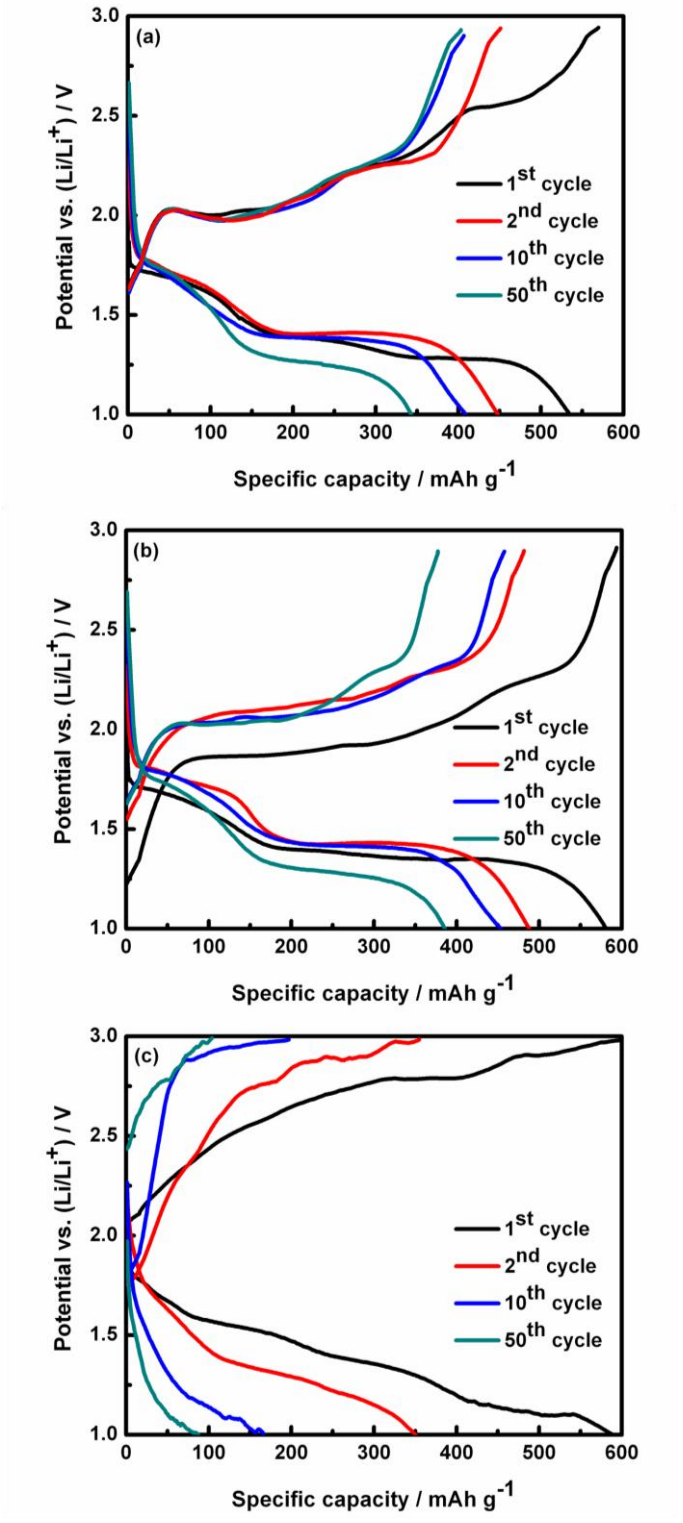

Figure 7.5. Charge-discharge profiles vs. lithium at 0.1 C for NiS synthesized at (a) 140 °C, (b) 160 °C, and (c) 180 °C for selected cycles.

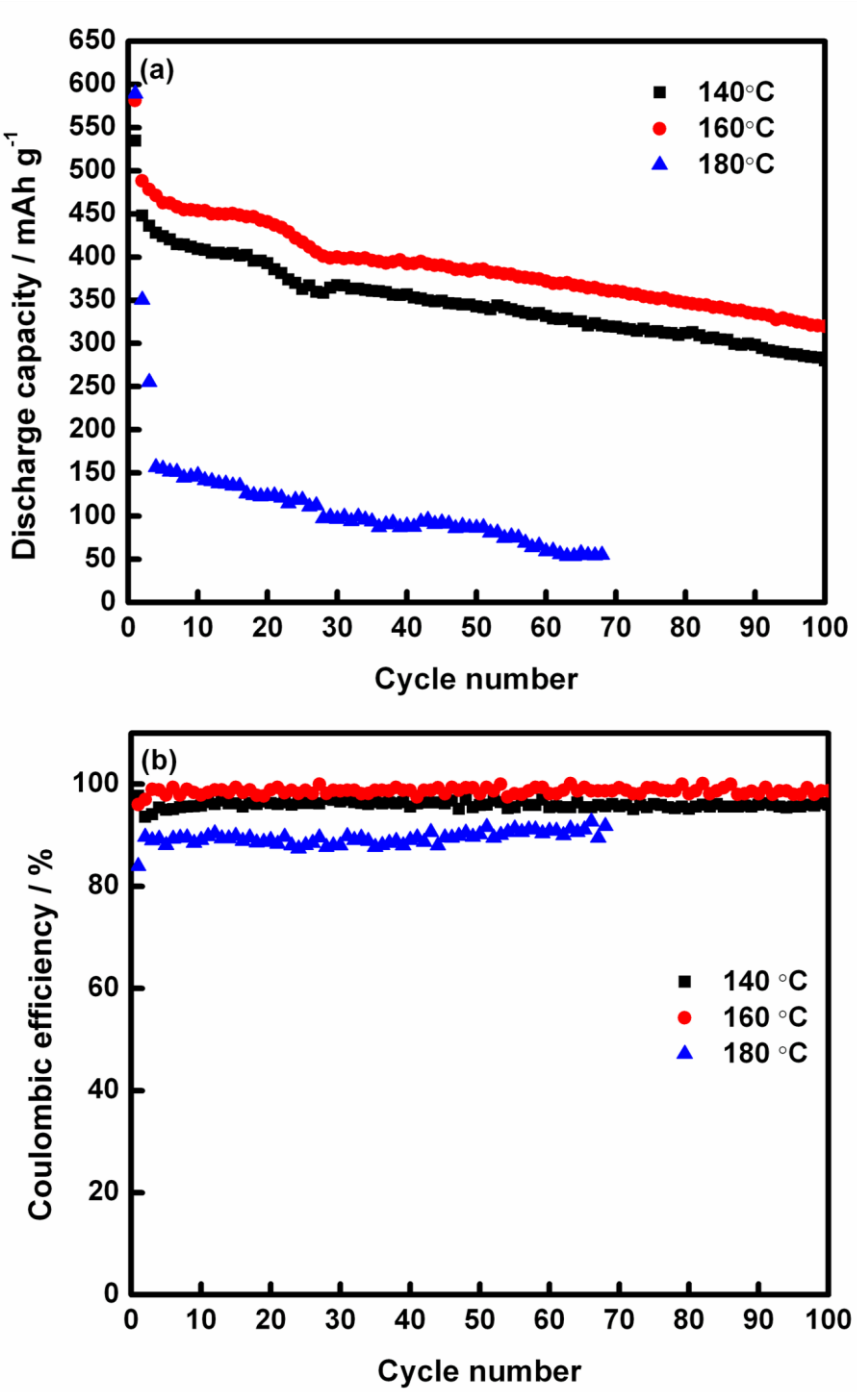

Figure 7.6. (a) Cyclic performance and (b) coulombic efficiency at 0.1 C of NiS synthesized at 140 °C, 160 °C, and 180 °C.

Furthermore, the consecutive cycling behavior at different current densities of 0.1, 0.3, 0.5, 1, and 2 C in an ascending order, followed by a return to 0.1 C, is shown in Figure 7.7. The electrode prepared at 160 °C presents good cycling stability at each rate, and

reversible capacities were measured to be 475, 456, 383, 223, and 56 mAh g^{-1} at the rate of 0.1, 0.3, 0.5, 1, and 2 C, respectively. After 60 cycles, the reversible capacity of the electrode prepared at 160 °C was still 407 mAh g^{-1} at 0.1 C, illustrating its good cycling performance, clearly much better than the performance of the other electrodes. The discharge capacity after returning to 0.1 C is 77% of the capacity at 0.1 C (from the second cycle) for the α-NiS-β-NiS electrode obtained at 160 °C.

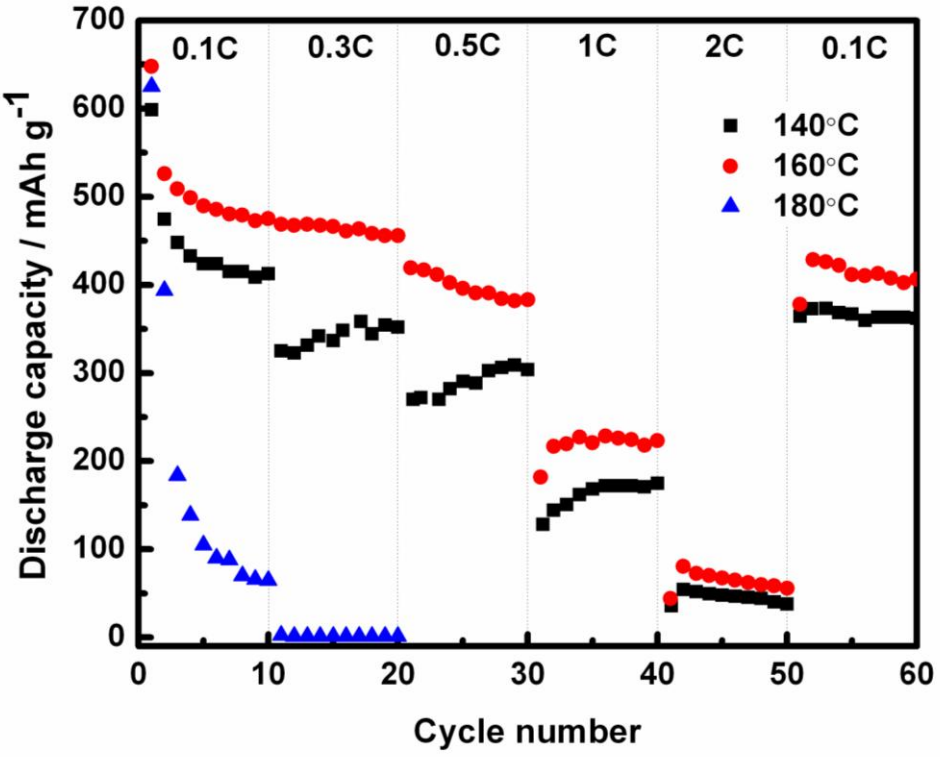

Figure 7.7. Consecutive cyclic behavior of NiS synthesized at 140 °C, 160 °C, and 180 °C at different rates.

Why does the α-NiS-β-NiS material synthesized at 160° C show the best electrochemical performance? The important factors that govern electrochemical performance of a cell relate to the solid-state diffusion length and diffusion rate. Diffusion length depends on particle microstructure and particle size distribution.

Smaller particles with high surface area will help to dissipate the surface accumulation of Li^+ ions and facilitate rapid mobility. This helps to enhance the amount of lithium intercalated within the material, resulting in increased energy density and higher rate capability [176, 399, 410]. The surface area for the three samples is in the descending order of α-NiS-β-NiS (160^o C) > α-NiS (140^o C) > α-NiS-β-NiS (180^o C). Since the number of insertion sites is directly proportional to the surface area, a larger number of lithium insertion sites would be expected in the samples with higher surface area [306]. Under these considerations, the electrochemical performance is in the descending order of α-NiS-β-NiS (160^o C) > α-NiS (140^o C) > α-NiS-β-NiS (180^o C).

7.4 Summary

Nanocrystalline α-NiS-β-NiS powder has been successfully synthesized in a simple microwave autoclave within a short period of time. The results indicate that hexagonal NiAs-type α-NiS phase can be partially converted to a β–NiS millerite-like secondary phase with increasing heat-treatment temperature. In a sample prepared at 160 ^{o}C, a duplex crystallite size (α-NiS ~ 47 nm and high surface area β-NiS ~ 53 nm) is observed. Electrochemical testing demonstrates that the sample synthesized at 160 ^{o}C has a high reversible capacity with good rate capability. This finding strongly suggests that the synthesis process is very simple and convenient, and also requires only a low treatment temperature and a very short period of time as well. The motivation for using this method is to decrease the reaction time as compared to the conventional hydrothermal method. Therefore, the electrical energy consumption for materials synthesis is significantly reduced.

Chapter 8

Microporous gel polymer electrolytes for lithium rechargeable battery application

8.1 Introduction

Polymer electrolyte may generally be defined as a membrane that possesses transport properties comparable to those of common liquid ionic solutions. The development of polymer electrolytes has drawn the attention of many researchers over the last three decades, as they find applications not only in lithium batteries, but also in other electrochemical devices such as supercapacitors, electrochromic devices, etc. [411]. Lithium batteries use liquid electrolytes with organic solvents, which are flammable and easy to ignite on exposure to high temperatures. To solve this safety problem, there is a strong desire to move to non-flammable electrolytes [268]. In the case of the lithium-ion battery, numerous studies have been conducted to improve its safety performance, since scaled-up forms have promising applications in electric vehicles. Still, one of the main challenges is the electrolytes, because they will react with the active electrode materials [412]. As a result, polymer electrolyte is a promising candidate, as these polymer electrolytes have several advantages over their liquid counterparts. The advantages of these electrolytes include no internal shorting, no leakage of electrolytes, and non-combustible reaction products at the electrode surface, in contrast to the liquid electrolytes [56, 413-417]. However, the prerequisites for a polymer electrolyte for lithium-ion batteries are (i) high ionic conductivity at ambient and sub-ambient

temperatures, (ii) good mechanical strength, (iii) appreciable transference number, (iv) thermal and electrochemical stability, and (v) better compatibility with electrodes [414-416]. The polymer electrolyte should also allow good cycle lives at low temperatures and must withstand the internal pressure build-up during battery operation.

Since 1973 [270], many studies on solid polymer electrolytes have been carried out that involve such techniques as blending, co-polymerizing, cross-linking, and adding nanofillers to modify the polymer host to increase the ionic conductivity [413, 418-420]. However, the main obstacle is still the ionic conductivity, which is generally below 10^{-3} S cm^{-1} and not enough for practical application. As a result, gelled polymer electrolytes (GPEs) were developed [413, 421, 422]. Much recent attention has turned to microporous gel polymer electrolytes, which can be regarded as an intermediate state between typical liquid electrolytes and dry solid polymer electrolytes. Microporous gel polymer electrolytes usually exhibit ionic conductivities ranging from 10^{-4} to 10^{-3} S cm^{-1} at room temperature, near to that of commercial liquid electrolytes. In microporous gel polymer electrolytes, the liquid component is trapped in the polymer matrix, thereby preventing leakage of liquid electrolyte. Consequently, the safety of Li-ion batteries is greatly improved [423]. The pore structure of the polymer membrane is the key component and especially important for the ionic conductivity. The larger the amount of trapped liquid electrolyte in the pores, the higher the ionic conductivity of the membrane [424].

Generally, porous membrane materials are prepared by the phase inversion method [425]. Some polymer electrolytes are prepared by template imprinting or the sol-gel process [426], but the preparation process for polymer electrolytes is very tedious, and

the pores are also too small to observe, so that such polymer membrane materials are generally classified as non-porous or continuous membranes. Nowadays, researchers are very keen to develop microporous polymer membranes, which can be activated as polymer electrolyte by soaking in an electrolyte solution [427]. The Bellcore technique has been widely used to prepared porous polymer membrane based on poly (vinylidene fluoride)-co-hexafluoropropene (PVDF-HFP), which showed favorable ionic conductivity (~ 1 mS cm^{-1}) at room temperature after soaking with liquid electrolyte [428]. However, the extraction process for dibutyl phthalate (DBP) needs large volumes of organic solvents, which increases the production costs, and the removal of DBP is not 100 % efficient [429-431]. On the other hand, Pasquier et al. [432] have shown that the phase-inversion method is a valid method to use in preparing microporous PVDF-HFP co-polymers by casting a polymer solution and evaporating the solvent and nonsolvent. Research and development in this field have involved a variety of polymer matrices such poly (ethylene oxide) (PEO) [259-261], poly (acrylonitrile) (PAN) [262, 263], poly (vinyl chloride) (PVC) [264, 265], poly (methyl methacrylate) (PMMA) [266, 267], and polyvinylidene difluoride (PVdF) [268, 269]. In particular, much attention has been devoted to increasing the liquid electrolyte content in the polymer matrix by controlling the components and morphology, as the ionic conductivity of the solid polymer electrolyte increases with increasing amount of the liquid electrolyte trapped in the polymer matrix. In addition, several features of the polymer electrolyte, such as porosity, pore size, crystallinity, chain structure, and the degree of polymerization, contribute to the conduction properties of the carriers [433]. However, high porosity usually leads to fading mechanical strength, and it has been shown that the addition of PEO to the PVDF can improve the porosity and pore connectivity for electrolyte uptake [285, 286], although the mechanical strength of PVDF-PEO blends is

lower than that of pure PVDF. In addition, blending PAN and PVDF-HFP can increase the mechanical stability and structural rigidity of the porous polymer electrolyte [287].

In this study, we report PVDF-PMMA blends for polymer electrolyte prepared via the phase-separation method in a mixture of N, N-dimethylformamide (DMF) as a solvent and glycerin as a nonsolvent. The effects of PMMA at different ratios on the morphology, porosity, and electrochemical performance have been characterized with the aim of obtaining better microporous gel polymer electrolyte for lithium-ion rechargeable battery application.

8.2 Experimental

8.2.1 Preparation of PVDF/PMMA membranes and polymer electrolytes

The polymer blend membranes were prepared by the phase-separation method. Poly(vinylidene fluoride) (PVDF, Mw = 534,000, Sigma-Aldrich) and poly(methyl methacrylate) (PMMA, Mw = 350,000, Sigma-Aldrich) were dried for 24 h at 100 °C in vacuum. The required amounts of PVDF and PMMA were dissolved in a mixture of N,N-dimethyl formamide (DMF, > 99.8%, Sigma-Aldrich) and glycerin (Fluka) (10:1 by volume), and stirred for 3 h at 80 °C. Then, the solution was cast onto a glass plate and dried at 120 °C for 24 h in vacuum. During this process, DMF and glycerin evaporated in turn, and the voids left by the glycerin formed micropores. The polymer electrolytes were obtained by soaking the obtained membranes in 1 M $LiPF_6$ in a mixture of ethylene carbonate (EC) and dimethyl carbonate (DMC; 1:1 by volume, MERCK, Germany). The compositions of the PVDF/PMMA membranes and the corresponding polymer electrolytes that were prepared are listed in Table 1. M0, M30,

M50. M70, M90, and M100 designate the membranes with PVDF to PMMA (wt.%:wt.%) weight ratios of 100:0, 70:30, 50:50, 30:70, 10:90, and 0:100, respectively. The corresponding polymer electrolytes are designated as E0, E30, E50, E70, E90, and E100, respectively.

Table 8.1. Compositions of PVDF/PMMA membranes and corresponding polymer electrolytes.

Composition PVDF/PMMA (wt.%/wt.%)	**Porous membrane**	**Polymer electrolyte**
100/0	M0	E0
70/30	M30	E30
50/50	M50	E50
30/70	M70	E70
10/90	M90	E90
0/100	M100	E100

8.2.2 Characterization of the membranes and polymer electrolyte

The morphology of the membranes was observed by scanning electron microscope (SEM; JOEL JEM-3000). Fourier transform infrared (FTIR) spectroscopy was carried out using a Shimadzu FTIR spectrometer, IRPrestige-21 model. Samples were analyzed in attenuated total reflectance (ATR) mode using the Pike MIRacle accessory equipped with a germanium crystal (Pike Technology). Differential scanning calorimetry (DSC)

measurements were carried out under argon atmosphere using a Mettler-Toledo thermogravimetric analysis/ differential scanning calorimetry (TGA/DSC) 1 Star^e system from 50 to 200 °C at 10 °C min^{-1}. Porosity of the membranes was measured as follows: after weighing, the membrane was immersed in 1-butanol for 2 h. Then, the surface of the membrane was dried with filter paper and weighed again. The porosity was calculated using the following equation:

$$\text{Porosity (\%)} = \frac{w_t - w_o}{\rho V} \times 100 \tag{8.1}$$

where V is the apparent volume of the membrane, ρ is the density of 1-butanol, and w_t and w_o are the weights of the wet and dry membranes, respectively. The liquid electrolyte uptake of the membranes was measured according to the following procedure: after weighing, the membrane was immersed in liquid electrolyte for 10 min and weighed again. The electrolyte uptake was calculated as follows:

$$\text{Electrolyte uptake (\%)} = \frac{w_t - w_o}{w_o} \times 100 \tag{8.2}$$

where w_t and w_o are the weights of the wet and dry membranes, respectively. The impedance of the polymer electrolytes was measured using a CHI 660B electrochemical workstation instrument (Shanghai Chenhua Apparatus, China) in the frequency range from 10 mHz to 100 kHz. The polymer electrolytes were cut into 1 cm^2 sizes and sandwiched between two blocking stainless steel electrodes. The ionic conductivity of the polymer electrolytes was calculated based on the following equation:

$$\sigma = \frac{t}{R_b A} \tag{8.3}$$

Here, σ is the ionic conductivity, R_b is the bulk resistance, and t and A are the thickness and area of the polymer electrolyte, respectively. Impedance measurements were also carried out in the temperature range between 303 and 373 K. The electrochemical

stability window of the polymer electrolyte was determined by linear sweep voltammetry using a stainless steel working electrode and lithium foil as the counter electrode at the scanning rate of 1 mV s^{-1}.

8.2.3 Electrochemical characterization

A mixture composed of 80 wt.% $LiFePO_4$ powder (DLG Battery Co., Ltd., China), 10 wt.% carbon black, and 10 wt.% polyvinylidene fluoride (PVDF) were mixed with *N*-methyl-2-pyrrolidone (NMP). The slurry was spread onto aluminum foil substrates and dried at 100 °C for 24 h in vacuum. After being cut to a 1 × 1 cm^2 size, the electrode was mounted as the positive electrode versus lithium metal as the counter and reference electrode in CR 2032 coin-type cells. Here, Sample E70 was chosen as the polymer electrolyte. The Li/E70/$LiFePO_4$ cell was assembled in an argon-filled glove box. Charge-discharge testing was performed galvanostatically between 2.5 and 4.2 V at room temperature on a Land battery tester (Wuhan Land Electronic Co. Ltd.).

8.3 Results and discussion

A comparison of the cross-sectional morphology of the pure PVDF, pure PMMA, and PVDF/PMMA blend films after extraction of glycerin and DMF from the polymer matrix are shown in Figure 8.1. The presence of PMMA leads to change in the size of the pores in the membrane. It was found that the pore size of the membrane increases with the addition of PMMA up to 70 wt.%, and then the pore size starts to decrease. Sample M70 showed the largest diameter pores (about 10 μm), which is enough to trap more liquid electrolyte and provide a path for ion migration. This trend agrees well with

the porosity and liquid electrolyte uptake measurements, as shown in Figure 8.2. It can be seen that Sample M70 has the highest porosity of 64% when compared with pure PVDF (Sample M0) and pure PMMA (Sample M100), which have only 24% and 41% porosity, respectively. Such large porosity will help the liquid electrolyte to more easily penetrate into Sample M70, with subsequently more liquid electrolyte embedded in the pores of the membrane.

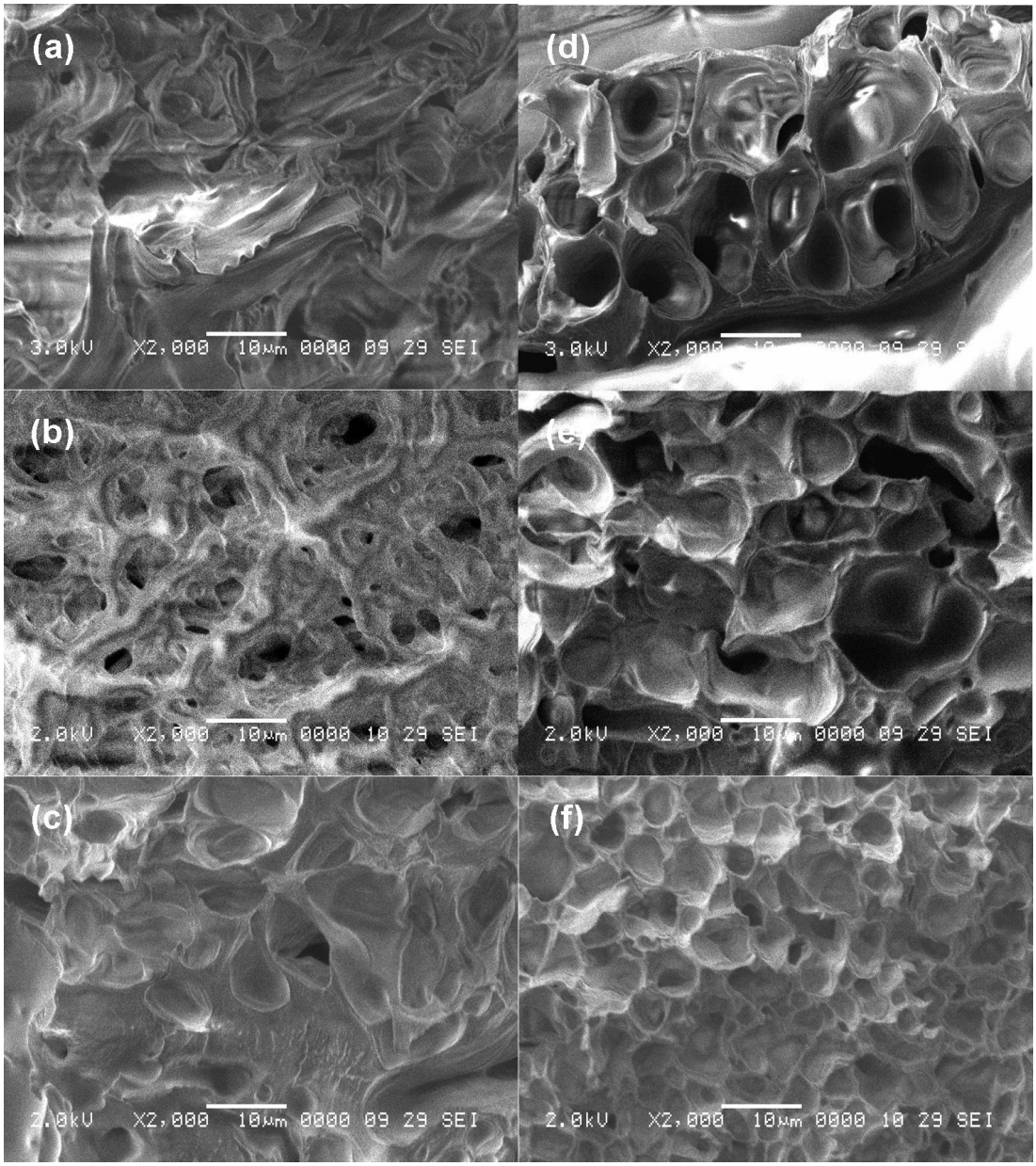

Figure 8.1. Cross-sectional SEM images of porous membrane for Samples (a) M0, (b) M30, (c) M50, (d) M70, (e) M90, and (f) M100.

For liquid electrolyte uptake measurements, pure PVDF polymer electrolyte (Sample E0) reaches saturation with a weight uptake ratio of 15%. With addition of PMMA to the polymer matrix, the liquid electrolyte uptake ratio increases due to the high porosity of the PVDF/PMMA blended film. Sample E70 reaches saturation with a maximum liquid electrolyte uptake ratio of 204%. Therefore, the addition of PMMA not only controls the porosity, but also is correlated with the liquid electrolyte uptake of the film, resulting in high ionic conductivity of the membrane.

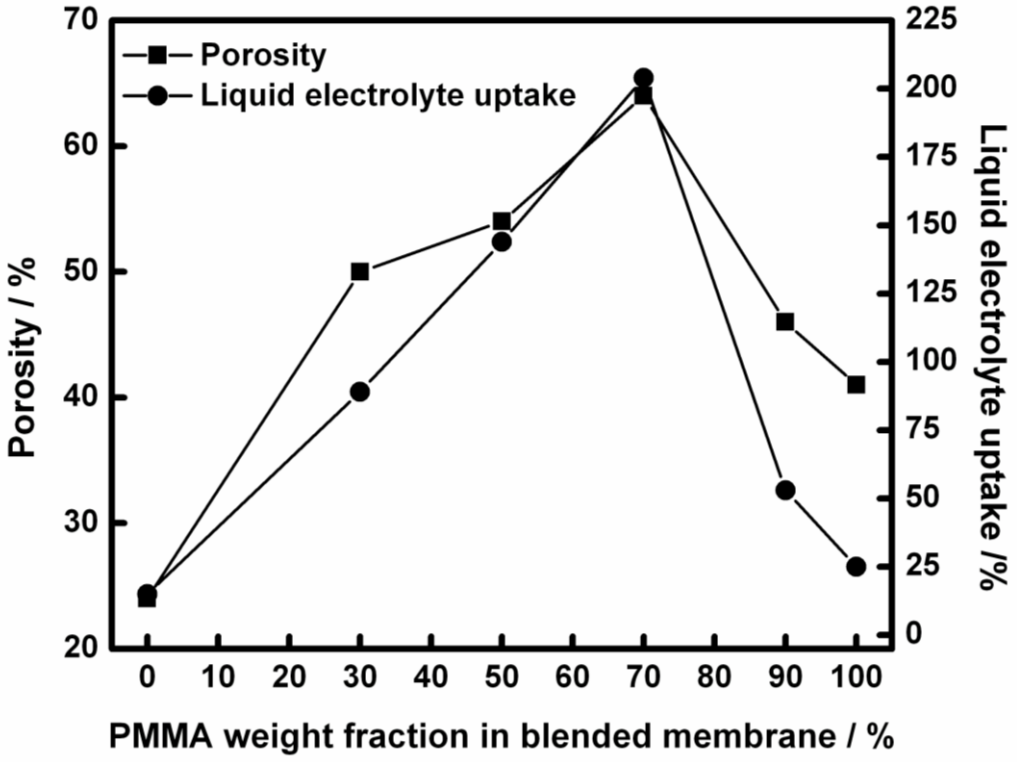

Figure 8.2. Porosity and liquid electrolyte uptake as a function of PMMA weight fraction in blended porous membranes with polymer electrolyte.

Figure 8.3 shows the ATR-FTIR spectra of Samples M0, M30, M50, M70, and M100. The characteristic peaks observed are common to both pure PVDF and pure PMMA membranes [249, 274, 434]. From Figure 8.3(a), the vibrational band at 1406 cm^{-1}

corresponds to CH_2 wagging deformation of pure PVDF membrane. It can be seen that the intensity of this peak decreases with the addition of PMMA and finally disappears, as shown in Figure 8.3(d, e). For pure PMMA membrane, a peak reflecting the stretching of the carbonyl (C=O) group is present at 1730 cm^{-1}, as shown in Figure 8.3(e). From the inset in Figure 8.3, it can be clearly seen that the intensity of this peak gradually decreases, while the peak is slightly shifted to 1734 cm^{-1} in the PVDF/PMMA blend membrane. This result suggests that there is a specific interaction between the carbonyl groups of PMMA and the CH_2 groups of PVDF, and indicates the formation of a PVDF/PMMA blended membrane [249, 274].

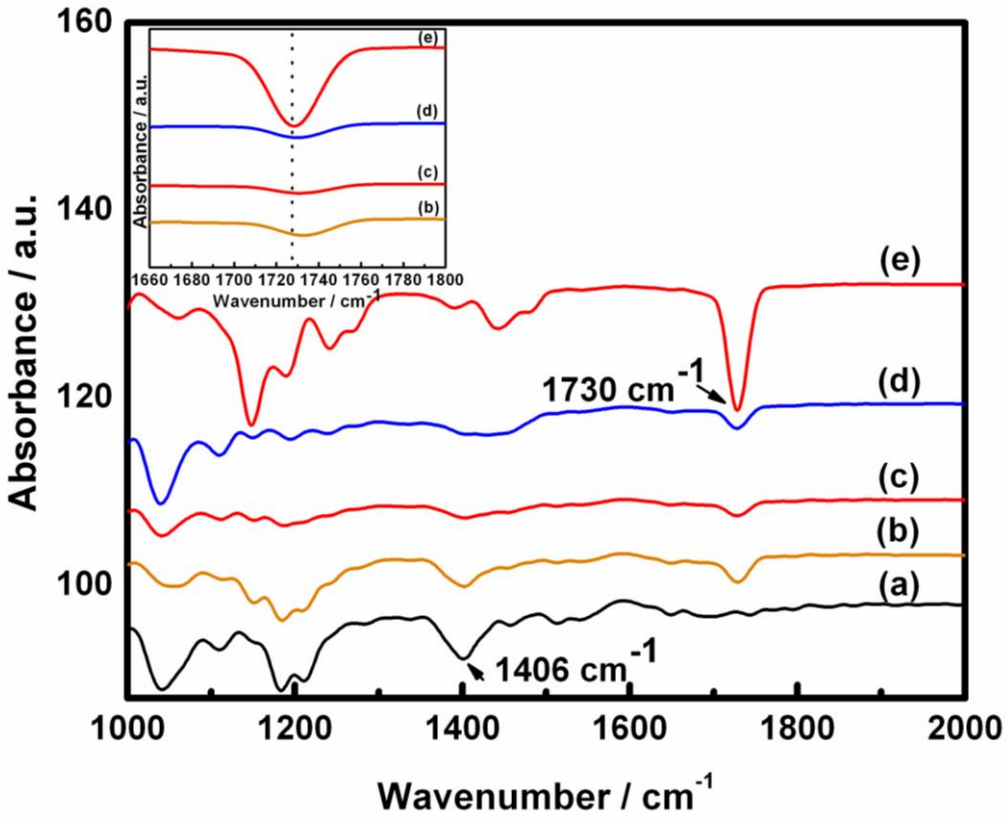

Figure 8.3. ATR-FTIR spectra of Samples (a) M0, (b) M30, (c) M50, (d) M70, (e) M90, and (f) M100 from 1000-2000 cm^{-1}. The inset shows the ATR-FTIR spectra of Samples M30, M50, M70, and M100 in the range of 1660 to1800 cm^{-1}.

Figure 8.4 shows the differential scanning calorimetry (DSC) curves of the pure PVDF, pure PMMA, and polymer blend membranes. Pure PVDF (Sample M0) shows a characteristic endothermic peak at 159.4 °C, corresponding to the melting temperature of the crystalline form, T_m. With the addition of PMMA, the melting temperature of the polymer blend membrane is depressed markedly. However, in the rich PMMA concentration (Sample M90), there was no trace of melting behavior of PVDF. Similar results were obtained by Ma et al. [290]. They reported that the decrease in T_m with increasing PMMA concentration could be related to the melting temperature depression of the crystalline components, suggesting that the growth of crystals is affected by the interaction of the components. The integral peak area under the T_m curve is correlated with the degree of crystallinity. Therefore, the degree of crystallization of the polymer membranes could be calculated from the enthalpy of fusion from the DSC measurements, using the following equation:

$$X_c = \frac{\Delta H_m}{\Delta H_m^{\phi}} \times 100\% \tag{8.4}$$

where ΔH_m^{ϕ} is the enthalpy of fusion for pure PVDF, 104.7 J g^{-1} [435], and ΔH_m is the enthalpy of fusion of the PVDF/PMMA blended membrane. The data for T_m, ΔH_m, and the degree of crystallization, X_c, are tabulated in Table 8.2. It shows that the amount of PMMA has a slight influence on the X_c. The crystallinity of the polymer blend membranes is lower than that of pure PVDF, suggesting that the amorphous domain of the membranes was increased, as the PMMA in the polymer blend membrane progressively retards the crystallization of PVDF [290, 436]. This facilitated the absorption and swelling of the liquid electrolyte, resulting in high ionic conductivity of the polymer electrolyte [435].

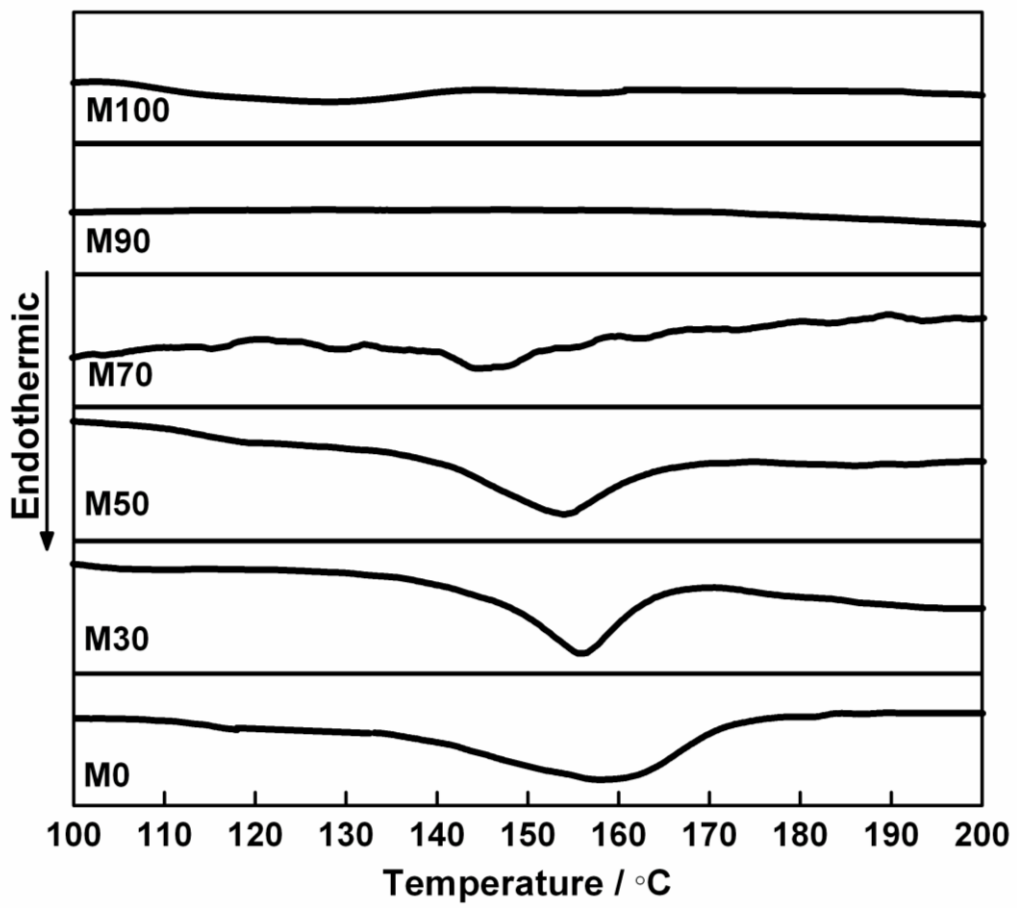

Figure 8.4. DSC curves of pure PVDF, pure PMMA, and polymer blend membranes.

Table 8.2. Degree of crystallization of PVDF/PMMA blended membranes.

Porous membrane	**Melting temperature of crystalline form, T_m (°C)**	**Enthalpy of fusion for crystalline form, ΔH_m (J g^{-1})**	**Crystallization degree, X_c (%)**
M0	159.4	32.5	31
M30	156.0	25.5	24
M50	153.6	22.8	22
M70	144.9	16.3	16
M90	-	-	-
M100	-	-	-

Figure 8.5(a) shows the ionic conductivity at room temperature for all the polymer electrolytes. With the addition of PMMA, it can be observed that the ionic conductivity of the polymer blend increases from 5.73×10^{-6} S cm^{-1} to a maximum of 1.21×10^{-3} S cm^{-1} as electrolyte uptake increases from 15% to 204%. According to Saito et al. [437], there are three possible ways that carrier ions could be transferred within the porous polymer electrolyte: (1) through liquid electrolyte trapped in pores, (2) through an amorphous domain that is swelled by liquid electrolyte, and (3) along molecular chains in the polymer. Since the carrier ion movements along the molecular chains in the polymer is much slower, the increase in ionic conductivity could be attributed to the large amount of trapped liquid electrolyte in the pores that then penetrates into the polymer chains to swell the amorphous domains [253, 430, 435, 437]. The temperature dependence of the ionic conductivity for the polymer electrolyte is presented in Figure 8.5(b). Typical behavior for a polymer electrolyte was observed, that is, ionic conductivity increases with increasing temperature. Higher temperature not only promotes the migration of carrier ions, but also results in the expansion of polymer [253]. This expansion produces local empty space and increases the free volume, which promotes the motion of polymer segments and carrier ions. The conductivity-temperature plot has a regression value, $R^2 \geq 0.99$, indicating that the ionic conductivity follows the Arrhenius equation, which is shown in Eq. (8.5).

$$\sigma = \sigma_o \exp\left(\frac{-E_a}{RT}\right) \tag{8.5}$$

where σ is the conductivity of the polymer electrolyte, σ_o is a pre-exponential factor, E_a is the activation energy, R is the gas constant, and T is the temperature. From the gradient of the Arrhenius plot, the activation energy, E_a, for the polymer electrolytes was calculated (Figure 8.5(c)). The results suggest that the polymer electrolyte with the

highest ionic conductivity has the lowest activation energy. Therefore, the migration of lithium ions is much easier with more tunnels in the polymer membranes [438].

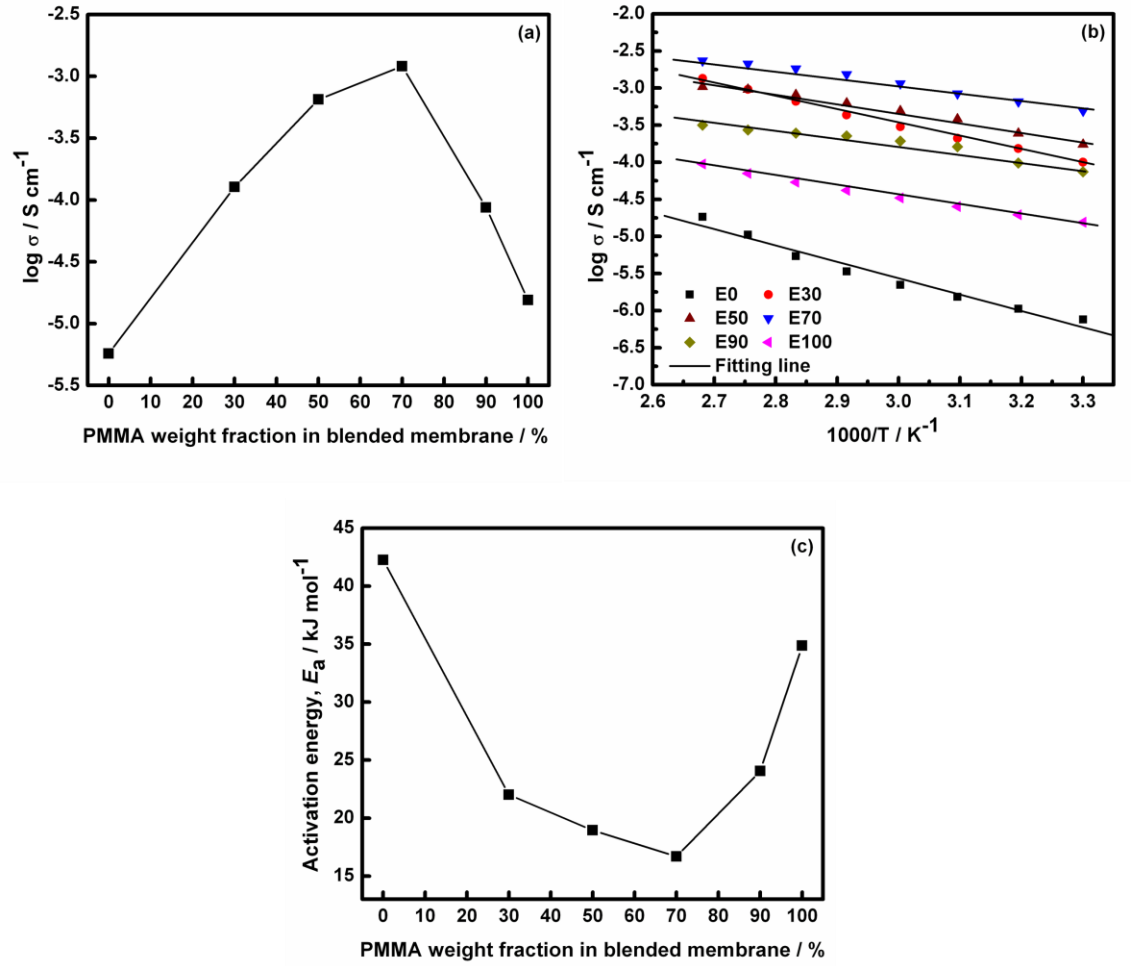

Figure 8.5. (a) Plots of ionic conductivity as a function of PMMA weight fraction in the polymer membranes at room temperature, (b) Arrhenius plots of the ionic conductivities of the polymer electrolytes, and (c) activation energy of polymer electrolytes.

A Li/E70/$LiFePO_4$ coin-type cell was fabricated and subjected to cycle testing at room temperature. The voltage range was 2.5 to 4.2 V at a current density of 8.5 mA g^{-1} (corresponding to a C/20 rate). Sample E70 was chosen as the electrolyte, lithium metal

as the anode, and $LiFePO_4$ as the cathode. The cell operates on the two-phase reversible process:

$$Li + LiFePO_4 \leftrightarrow 2Li + FePO_4 \quad (8.6)$$

with a theoretical specific capacity of 170 mAh g^{-1} [14, 439]. The specific capacity versus cycle number of the cell is presented in Figure 8.6(a). The charge capacity was higher than the discharge capacity in the first cycle. This irreversible capacity was considered to be due to the irreversible capacity loss related to the formation of the passivation layer at the lithium anode [440, 441]. The charge and discharge capacities of the cell are 150 and 129 mAh g^{-1}, respectively, at the first cycle. After the second cycle, the capacity increases to a maximum at 15 cycles, and then the cell capacity remains at about 135 mAh g^{-1} up to 50 cycles. The capacity is stable, and the coulombic efficiency approaches 100% over the 50 cycles. The charge-discharge profiles of the Li/E70/$LiFePO_4$ cell at the 1^{st}, 2^{nd}, 5^{th}, 10^{th}, 20^{th}, 30^{th}, 40^{th}, and 50^{th} cycles are shown in Figure 8.6(b). All charge-discharge curves exhibit a flat plateau at 3.4 and 3.5 V, which is a typical characteristic of $LiFePO_4$. Linear sweep polarization was performed to investigate the electrochemical stability window of Sample E70. For comparison, current-voltage measurements on commercial liquid electrolyte composed of 1 M $LiPF_6$ in EC:DMC (1:1 by volume) were carried out. As shown in Figure 8.6(c), it was found that the polymer electrolyte is stable up to 4.7 V, which meets the requirement for a practical lithium-ion battery. This is consistent with other reported gelled polymer electrolytes, since the electrochemical oxidation potential is mainly due to the absorbed liquid electrolyte [253, 412, 429, 438, 442]. Further research is necessary to improve the high rate performance of the lithium-ion batteries. It is well-known that the lithium-polymer battery performs better at high temperature. Therefore, ways to improve the capacity may consist in operating at high temperature. Another strategy to achieve high

capacity in the lithium-polymer battery is by soaking the porous membrane in highly conductive electrolyte solution.

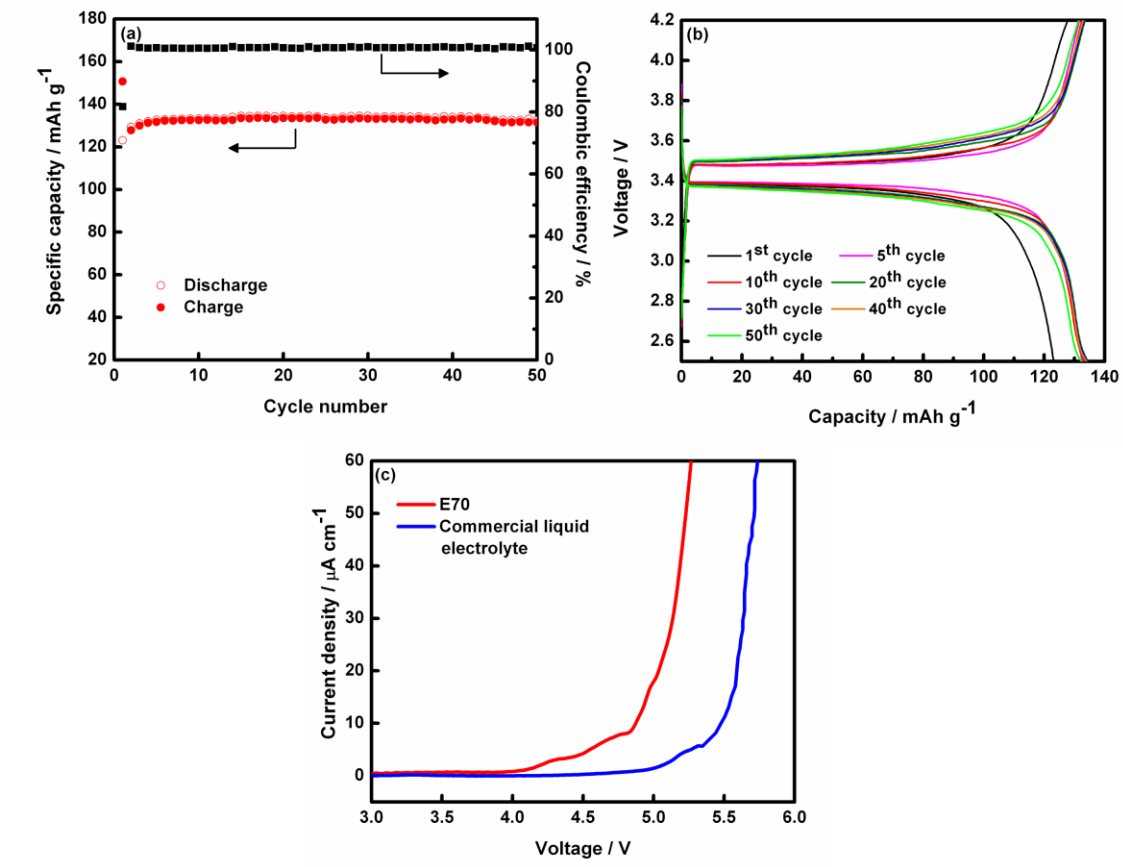

Figure 8.6. Electrochemical performance of Li/E70/$LiFePO_4$ cells: (a) cyclic performance and coulombic efficiency beyond 50 cycles at 8.5 mA g^{-1} (corresponding to a C/20 rate); (b) charge-discharge profiles for selected cycles; (c) linear sweep voltammograms of Sample E70 and commercial liquid electrolyte with a stainless steel working electrode and a lithium metal counter electrode at a scan rate of 1 mV s^{-1}.

8.4 Summary

In summary, PVDF/PMMA blend membranes have been successfully prepared via the phase separation method, followed by immersion in commercial liquid electrolyte to

activate the membrane. The conformation of the PVDF/PMMA membranes was verified through attenuated total reflectance-Fourier transformation infrared spectroscopy (ATR-FTIR). The degree of crystallinity of a polymer blend membrane decreases as the PMMA concentration increases. The addition of PMMA to the PVDF membrane not only increases the porosity, but also increases the liquid electrolyte uptake. SEM observations showed that Sample M70 has a large pore size (~ 1 μm) when compared with the pure PVDF and the pure PMMA membranes. The ionic conductivity at room temperature of Sample E70 was 1.21×10^{-3} S cm^{-1}, and this sample has the lowest activation energy of 16.68 kJ mol^{-1}. The Li/E70/$LiFePO_4$ cell showed stable electrochemical performance up to 50 cycles and an electrochemical stability window that extended up to 4.7 V. This research suggests that PVDF/PMMA polymer electrolyte could be suitable for use as electrolyte for lithium-ion rechargeable batteries.

Chapter 9

Conclusions and outlook

9.1 General conclusions

This thesis examines three components in the lithium-ion battery system. These are gel polymer electrolytes, anode materials, and cathode materials. Several methods have been adopted in order to obtain nanostructured/nanocomposite materials. Their physical and structural features have been characterized, as well as their electrochemical performances. In the case of NiO as anode material, the effects of coating PPy and graphene onto NiO were studied. LiV_3O_8/carbon nanocomposite was also investigated as cathode material. In the case of NiS prepared at different reaction temperatures, the morphology and electrochemical performance were compared. Finally, the potential of PVDF/PMMA gel polymer electrolyte in an electrochemical cell is discussed. Based on the work presented in this dissertation, NiO nanocomposite, LiV_3O_8 carbon composite, and NiS have the potential to improve the electrochemical performance of lithium ion batteries, in terms of both high specific capacity and cycleability.

9.2 Negative electrodes for Li storage

Hollow spherical NiO powders synthesized via spray pyrolysis, followed by NiO-PPy nanocomposite produced using chemical polymerization, have been demonstrated. It was strongly confirmed by SEM images that the nanosized PPy had a cauliflower-like

morphology, coating the surface of the NiO. The electrochemical results showed that NiO-PPy nanocomposite performed better in terms of higher discharge capacity and better life cycle than the pure NiO. This excellent performance of the nanocomposite could be mainly due to the role of PPy as a conducting medium, binder, diluting agent, and cushioning medium to protect the electrode from pulverization during Li insertion/extraction.

NiO-graphene nanocomposites have been successfully synthesized by a simple hydrothermal method, followed by calcination in air at 500 °C. The NiO-graphene nanocomposite samples showed very stable cycling up to 100 cycles compared to the bare NiO. The electrochemical results suggest that a lower content of NiO in the composite is suitable for fast charge-discharge applications, whereas higher content of NiO in the composite is suitable for high capacity requirements at moderate rate of charge-discharge.

9.3 Positive electrodes for Li storage

Novel LiV_3O_8/carbon composites have been synthesized by the hydrothermal method, followed by a carbon coating process. The LiV_3O_8/carbon composite electrodes show a significantly improved cycle life compared to that of the bare LiV_3O_8 electrode. The improvements can be attributed to the carbon coating in the matrix, which is responsible for improving the electrical conductivity of the LiV_3O_8 materials, as well as preventing aggregation and effectively accommodating volume variation.

A facile, one-step, hydrothermal autoclave microwave method was developed for the preparation of NiS powder within 15 minutes at temperatures of 160-180 ^{o}C. It was found that the temperature is the key factor that greatly influences the phase of the final NiS product. At 140 °C, pure hexagonal NiAs-type α-NiS phase was identified from the XRD patterns. With increasing reaction temperature (160-180 ^{o}C), XRD evidence indicates that an increasing fraction of rhombohedral millerite-like β-NiS is formed as a secondary phase. The α-NiS-β-NiS sample synthesized at 160 ^{o}C yielded good electrochemical performance in term of high reversible capacity and could be operated at a good fraction of its capacity at high rates. Due to the simple and low temperature synthesis, the α-NiS-β-NiS sample has been demonstrated to be a highly promising cathode material for Li rechargeable battery application.

9.4 Gel polymer electrolytes

Films of blended PVDF/PMMA were derived from a phase-separation method using DMF as the solvent and glycerin as non-solvent. The influence of PMMA addition into the PVDF membranes on the morphology and structure, electrolyte uptake of the porous membrane, and ionic conductivity of the activated membranes was investigated. The resulting PVDF/PMMA gel polymer electrolytes at 30:70 ratio (w/w) showed the highest ionic conductivity at room temperature and exhibited the lowest activation energy for the transportation of ions. The cycle performance and the storage stability of the Li/gel polymer electrolyte/$LiFePO_4$ cell containing the above electrolyte were found to be acceptable for practical utility.

9.5 Outlook

Future work based on this doctoral thesis that may be interesting could focus on the improvement of the energy density and safety of the lithium-ion battery by using room temperature ionic liquid (IL) electrolyte. As a matter of fact, the commercial systems nowadays available use electrolytes commonly based on organic carbonates (e.g. EC, DEC, EMC), but since these electrolytes are flammable and volatile, their use poses a serious safety risk and strongly reduces the battery operating temperature range. For this reason, alternative electrolytes with improved safety and the ability to work in a broader operation temperature range are urgently needed. More recently, the use of ionic liquids (ILs) as electrolyte for lithium batteries has become a major focus of interest. The main advantages of ILs over organic solvents are their non-flammability, negligible vapor pressure, high chemical and thermal stability, and, in some cases, hydrophobicity.

Production of electrode nanoparticles/nanocomposites in one step could perhaps be done, which is favorable for industrial manufacturing. Recently, microwave-assisted synthesis methods have been proved to be particularly effective, as they can yield the product rapidly with controlled particle size and morphology. In the case of NiS, poor capacity retention could be avoided by complete coating of the nanoparticles with carbon, graphene, or conducting polymers. Coating NiS nanoparticles with these materials would improve the overall and local electrical conductivity of the electrode, and likely lead to an improved electrochemical performance.

As for PVDF/PMMA gel polymer electrolytes, further research is necessary to improve the high rate performance of the lithium-polymer batteries. It is well known that the

lithium-polymer battery performs better at high temperature. Therefore, ways to improve the capacity may consist in operating at high temperature. Another strategy to achieve high capacity in the lithium-polymer battery is by soaking the porous membrane in highly conductive electrolyte solution.

References

[1] M.S. Whittingham, MRS Bull. 33 (2008) 411.

[2] M.R. Palacin, Chem. Soc. Rev. 38 (2009) 2565.

[3] D. Linden, T.B. Reddy, Handbook of Batteries, 2002.

[4] M. Winter, R.J. Brodd, Chem. Rev. 104 (2004) 4245.

[5] R.M. Dell, D.A.J. Rand, Lithium batteries, in: Understanding Batteries, The Royal Society of Chemistry, Cambridge, 2001, pp. 143.

[6] M. Anderman, Briefing to the US Senate Committee in Energy and Natural Resources (2007).

[7] US DOE Office of Basic Energy Sciences, Report of the Basic Energy Sciences Workshop on Electrochemical Energy Storage (2007) http://www.science.doe.gov/bes/reports/files/EES_rpt.pdf.

[8] J. Liu, G. Cao, Z. Yang, D. Wang, D. Dubois, X. Zhou, G.L. Graff, L.R. Pederson, J.-G. Zhang, ChemSusChem 1 (2008) 676.

[9] M.S. Whittingham, Chem. Rev. 104 (2004) 4271.

[10] E. Antolini, Solid State Ionics 170 (2004) 159.

[11] J. Akimoto, Y. Gotoh, Y. Oosawa, J. Solid State Chem. 141 (1998) 298.

[12] M.M. Thackeray, A. de Kock, W.I.F. David, Mater. Res. Bull. 28 (1993) 1041.

[13] C. Li, H.P. Zhang, L.J. Fu, H. Liu, Y.P. Wu, E. Rahm, R. Holze, H.Q. Wu, Electrochim. Acta 51 (2006) 3872.

[14] A.K. Padhi, K.S. Nanjundaswamy, C. Masquelier, S. Okada, J.B. Goodenough, J. Electrochem. Soc. 144 (1997) 1609.

[15] A. Ritchie, W. Howard, J. Power Sources 162 (2006) 809.

[16] M. Endo, C. Kim, K. Nishimura, T. Fujino, K. Miyashita, Carbon 38 (2000) 183.

[17] J.S. Gnanaraj, M.D. Levi, E. Levi, G. Salitra, D. Aurbach, J.E. Fischer, A. Claye, J. Electrochem. Soc. 148 (2001) A525.

[18] Y.S. Hu, P. Adelhelm, B.M. Smarsly, S. Hore, M. Antonietti, J. Maier, Adv. Funct. Mater. 17 (2007) 1873.

[19] Y.P. Wu, C. Jiang, C. Wan, R. Holze, Solid State Ionics 156 (2003) 283.

[20] W.-J. Zhang, J. Power Sources 196 (2011) 13.

[21] D. Larcher, S. Beattie, M. Morcrette, K. Edstrom, J.-C. Jumas, J.-M. Tarascon, J. Mater. Chem. 17 (2007) 3759.

[22] W.J. Weydanz, M. Wohlfahrt-Mehrens, R.A. Huggins, J. Power Sources 81-82 (1999) 237.

[23] Y. Idota, T. Kubota, A. Matsufuji, Y. Maekawa, T. Miyasaka, Science 276 (1997) 1395.

[24] J.W. Kim, J.H. Ryu, K.T. Lee, S.M. Oh, J. Power Sources 147 (2005) 227.

[25] S.-H. Ng, J. Wang, D. Wexler, K. Konstantinov, Z.-P. Guo, H.-K. Liu, Angew. Chem. Int. Ed. 45 (2006) 6896.

[26] P. Poizot, S. Laruelle, S. Grugeon, L. Dupont, J.M. Tarascon, Nature 407 (2000) 496.

[27] W.Y. Li, L.N. Xu, J. Chen, Adv. Funct. Mater. 15 (2005) 851.

[28] F. Zhan, B. Geng, Y. Guo, Chem. Eur. J. 15 (2009) 6169.

[29] J.-Z. Wang, C. Zhong, D. Wexler, N.H. Idris, Z.-X. Wang, L.-Q. Chen, H.-K. Liu, Chem. Eur. J. 17 (2011) 661.

[30] F. Azeez, in: Ph.D Thesis, North Carolina State University 2009.

[31] J.B. Goodenough, Y. Kim, Chem. Mater. 22 (2010) 587.

[32] B. Garcia, S. Lavallée, G. Perron, C. Michot, M. Armand, Electrochim. Acta 49 (2004) 4583.

[33] Y. Wang, K. Zaghib, A. Guerfi, F.F.C. Bazito, R.M. Torresi, J.R. Dahn, Electrochim. Acta 52 (2007) 6346.

[34] E. Markevich, V. Baranchugov, D. Aurbach, Electrochem. Commun. 8 (2006) 1331.

[35] F.B. Dias, L. Plomp, J.B.J. Veldhuis, J. Power Sources 88 (2000) 169.

[36] B. Scrosati, Chem. Rec. 5 (2005) 286.

[37] A. Patil, V. Patil, D. Wook Shin, J.-W. Choi, D.-S. Paik, S.-J. Yoon, Mater. Res. Bull. 43 (2008) 1913.

[38] D. Berndt, Electrochemical Energy Storage, in: H.A. Kiehne (Ed.) Battery Technology Handbook, Marcel Dekker Inc., New York, 2003, pp. 1.

[39] D. Von Handorf, Plat. Surf. Finish. 89 (2002) 84.

[40] G. Eggert, Skeptical Inquirer (0194-6730) 20 (1996) 31.

[41] R.M. Dell, D.A.J. Rand, Energy Storage in Batteries, in: Understanding Batteries, The Royal Society of Chemistry, Cambridge, 2001, pp. 1.

[42] J.A. Fleming, in: Proceedings of the Physical Society of London, London, England, 1885, pp. 161.

[43] G.W. Heise, N.C. Cahoon, The Primary Battery, Wiley, New York, 1971.

[44] P. Kurzweil, J. Power Sources 195 (2010) 4424.

[45] H. Manchester, Nickel-Cadmium Battery Lasts as Long as the Car in: Popular Science, Godfrey Hammond, New York, 1948, pp. 112.

[46] A.J. Salkind, P. Israel, J. Power Sources 136 (2004) 356.

[47] D.C.R. Espinosa, J.A.S. Tenório, J. Power Sources 157 (2006) 600.

[48] B. Scrosati, Renewable Energy 5 (1994) 285.

[49] R.M. Dell, D.A.J. Rand, Lithium Batteries, in: Understanding Batteries, 2001, pp. 143.

[50] F. Cheng, J. Liang, Z. Tao, J. Chen, Adv. Mater. 23 (2011) 1695.

[51] J.M. Tarascon, M. Armand, Nature 414 (2001) 359.

[52] G.M. Ehrlich, Lithium-ion Batteries, in: D. Linden, T.B. Reddy (Eds.) Handbook of Batteries, McGraw-Hill Professional, New York, 2001, pp. 35.1.

[53] D. Guyornard, J.-M. Tarascon, Adv. Mater. 6 (1994) 408.

[54] D.E. Fenton, J.M. Parker, P.V. Wright, Polymer 14 (1973) 589.

[55] M. Armand, M. Duclot, French Patent 78 329 76, 1978.

[56] F.M. Gray, Solid Polymer Electrolytes-Fundamentals and Technological Applications, VCH, New York, 1991.

[57] T.B. Reddy, S. Hossain, Rechargeable Lithium Batteries (Ambient Temperature), in: D. Linden, T.B. Reddy (Eds.) Handbook of Batteries, McGraw-Hill Professional, New York, 2001, pp. 34.1.

[58] F. Groce, B. Scrosati, J. Power Sources 43 (1993) 9.

[59] M. Liu, S.J. Visco, L.C. De Jonghe, J. Electrochem. Soc. 138 (1991) 1891.

[60] M.-Y. Chu, L. De Jonghe, S. Visco, in: Proceedings of the 11th Annual Battery Conference on Applications and Advances, California, 1996, pp. 163.

[61] H. Oman, in: Proceedings of the 12th Annual Battery Conference on Applications and Advances, California State University Long Beach, USA, 1997, pp. 31.

[62] Y. Nishi, Recent progress in batteries and future problems, in: T. Minami, M. Tatsumisago, M. Wakihara, C. Iwakura, S. Kohjiya, I. Tanaka (Eds.) Solid State Ionics for Batteries, Springer-Verlag, Tokyo, 2005, pp. 5.

[63] D. Linden, Basic Concepts, in: D. Linden, T.B. Reddy (Eds.) Handbook of Batteries, McGraw-Hill Professional, New York, 2003, pp. 1.3.

[64] Delta Gear Inc. (http://www.deltagearinc.com/BatteryGuide.htm).

[65] P.R. Bueno, C. Gabrielli, Electrochemistry, Nanomaterials, and Nanostructures, in: E.R. Leite (Ed.) Nanostructured Materials for Electrochemical Energy Production and Storage, Springer Science + Business Media, New York, 2009, pp. 81.

[66] Application Note, Gamry Instruments Inc. http://www.gamry.com.

[67] Electrochemical Impedance Spectroscopy (EIS): A Powerful and Cost-Effective Tool for Fuel Cell Diagnostics. Scribner Associates, Inc. www.scribner.com

[68] I. Kuribayashi, M. Yamashita, S. Muraoka, K. Nagasawa, J. Power Sources 63 (1996) 121.

[69] P.G. Bruce, C.A. Vincent, J. Chem. Soc. Faraday Trans. 89 (1993) 3187.

[70] L.A. de Picciotto, K.T. Adendorff, D.C. Liles, M.M. Thackeray, Solid State Ionics 62 (1993) 297.

[71] B.E. Conway, Electrochim. Acta 38 (1993) 1249.

[72] R. Jasinski, B. Burrows, J. Electrochem. Soc. 116 (1969) 422.

[73] N. Kumagai, A. Yu, J. Electrochem. Soc. 144 (1997) 830.

[74] M. Wakihara, Mater. Sci. Eng. R 33 (2001) 109.

[75] G.X. Wang, L. Yang, Y. Chen, J.Z. Wang, S. Bewlay, H.K. Liu, Electrochim. Acta 50 (2005) 4649.

[76] J.K. Lee, K.B. Smith, C.M. Hayner, H.H. Kung, Chem. Commun. 46 (2010) 2025.

[77] H. Gleiter, Prog. Mater Sci. 33 (1989) 223.

[78] S.C. Tjong, H. Chen, Mater. Sci. Eng. R 45 (2004) 1.

[79] M.-K. Song, S. Park, F.M. Alamgir, J. Cho, M. Liu, Mater. Sci. Eng. R 72 (2011) 203.

[80] M. Fernandez-Garcia, A. Martinez-Arias, J.C. Hanson, J.A. Rodriguez, Chem. Rev. 104 (2004) 4063.

[81] G. He, J. Eckert, W. Loser, L. Schultz, Nat. Mater. 2 (2003) 33.

[82] M.A. Meyers, A. Mishra, D.J. Benson, Prog. Mater Sci. 51 (2006) 427.

[83] H. Gleiter, Prog. Mater Sci. 33 (1989) 223.

[84] C.E. Hamm, R. Merkel, O. Springer, P. Jurkojc, C. Maier, K. Prechtel, V. Smetacek, Nature 421 (2003) 841.

[85] P.G. Bruce, B. Scrosati, J.M. Tarascon, Angew. Chem. Int. Ed. 47 (2008) 2930.

[86] A.S. Arico, P. Bruce, B. Scrosati, J.-M. Tarascon, W. van Schalkwijk, Nat. Mater. 4 (2005) 366.

[87] Y.S. Hu, L. Kienle, Y.G. Guo, J. Maier, Adv. Mater. 18 (2006) 1421.

[88] J. Maier, Nat. Mater. 4 (2005) 805.

[89] J. Jamnik, J. Maier, Phys. Chem. Chem. Phys. 5 (2003) 5215.

[90] P. Balaya, Energy Environ. Sci. 1 (2008) 645.

[91] Q. Wang, H. Li, L. Chen, X. Huang, Carbon 39 (2001) 2211.

[92] N.A. Kaskhedikar, J. Maier, Adv. Mater. (2009) 2664.

[93] P. Balaya, A.J. Bhattacharyya, J. J. Jamnik, Y.F. Zhukovskii, E.A. Kotomin, J. Maier, J. Power Sources 159 (2006) 171.

[94] P.M. Ajayan, Chem. Rev. 99 (1999) 1787.

[95] P. Benard, R. Chahine, Carbon nanostructures for hydrogen storage, in: G. Walker (Ed.) Solid-state hydrogen storage. Materials and chemistry, CRC Press LLC, Florida, USA, 2008, pp. 261.

[96] J. Yamaura, Y. Ozaki, A. Morita, A. Ohta, J. Power Sources 43 (1993) 233.

[97] J.L. Tirado, Mater. Sci. Eng. R 40 (2003) 103.

[98] M.S. Mauter, M. Elimelech, Environ. Sci. Technol. 42 (2008) 5843.

[99] E.H.L. Falcao, F. Wudl, J. Chem. Technol. Biotechnol. 82 (2007) 524.

[100] M. Dresselhaus, M. Endo, G. Dresselhaus, P. Avouris, Relation of Carbon Nanotubes to Other Carbon Materials Carbon Nanotubes, in, Springer Berlin / Heidelberg, 2001, pp. 11.

[101] K.S. Novoselov, A.K. Geim, S.V. Morozov, D. Jiang, Y. Zhang, S.V. Dubonos, I.V. Grigorieva, A.A. Firsov, Science 306 (2004) 666.

[102] Y.B. Zhang, Y.W. Tan, H.L. Stormer, P. Kim, Nature 438 (2005) 201.

[103] H.B. Heersche, P. Jarillo-Herrero, J.B. Oostinga, L.M.K. Vandersypen, A.F. Morpurgo, Nature 446 (2007) 56.

[104] © Airi Iliste/The Royal Swedish Academy of Sciences

[105] E. Yoo, J. Kim, E. Hosono, H.S. Zhou, T. Kudo, I. Honma, Nano Lett. 8 (2008) 2277.

[106] G. Wang, X. Shen, J. Yao, J. Park, Carbon 47 (2009) 2049.

[107] J.R. Dahn, T. Zheng, Y.H. Liu, J.S. Xue, Science 270 (1995) 590.

[108] Y.H. Liu, J.S. Xue, T. Zheng, J.R. Dahn, Carbon (1996) 193.

[109] A.N. Dey, J. Electrochem. Soc. 118 (1971) 1547.

[110] M. Winter, J.O. Besenhard, M.E. Spahr, P. Novák, Adv. Mater. 10 (1998) 725.

[111] R.A. Huggins, Solid State Ionics 113-115 (1998) 57.

[112] C.M. Park, H.J. Sohn, Adv. Mater. 22 (2010) 47.

[113] R. Teki, M.K. Datta, P. Krishnan, T.C. Parker, T.M. Lu , P.N. Kumta, N. Koratkar, Small 5 (2009) 2236.

[114] M. Wachtler, J.O. Besenhard, M. Winter, J. Power Sources 94 (2001) 189.

[115] M. Wachtler, M. Winter, J.O. Besenhard, J. Power Sources 105 (2002) 151.

[116] B. Gao, S. Sinha, L. Fleming, O. Zhou, Adv. Mater. 13 (2001) 816.

[117] H. Kim, J. Choi, H.J. Sohn, T. Kang, J. Electrochem. Soc. 146 (1999) 4401.

[118] J. Yang, M. Wachtler, M. Winter, J.O. Besenhard, Electrochem. Solid-State Lett. 2 (1999) 161.

[119] C. Wang, A.J. Appleby, F.E. Little, J. Power Sources 93 (2001) 174.

[120] J.H. Ryu, J.W. Kim, Y.E. Sung, S.M. Oh, Electrochem. Solid-State Lett. 7 (2004) A306.

[121] A. Ulus, Y. Rosenberg, L. Burstein, E. Peled, J. Electrochem. Soc. 149 (2002) A635.

[122] L.Y. Beaulieu, K.W. Eberman, R.L. Turner, L.J. Krause, J.R. Dahn, Electrochem. Solid-State Lett. 4 (2001) A137.

[123] M. Stjerndahl, H. Bryngelsson, T. Gustafsson, J.T. Vaughey, M.M. Thackeray, K. Edstrom, Electrochim. Acta 52 (2007) 4947.

[124] M.R. Wagner, P.R. Raimann, A. Trifonova, K.C. Moeller, J.O. Besenhard, M. Winter, Electrochem. Solid-State Lett. 7 (2004) A201.

[125] H. Zhao, Z. Zhu, C. Yin, H. Guo, D.H.L. Ng, Mater. Chem. Phys. 110 (2008) 201.

[126] P. Limthongkul, Y.I. Jang, N.J. Dudney, Y.M. Chiang, J. Power Sources 119-121 (2003) 604.

[127] P.P. Ferguson, R.A. Dunlap, J.R. Dahn, J. Electrochem. Soc. 157 (2010) A326.

[128] H. Li, L. Shi, Q. Wang, L. Chen, X. Huang, Solid State Ionics 148 (2002) 247.

[129] S. Matsuno, M. Noji, T. Kashiwagi, M. Nakayama, M. Wakihara, J Phys Chem C 111 (2007) 7548.

[130] H. Lia, X. Huang, L. Chen, G. Zhou, Z. Zhang, D. Yu, Y.J. Mo, N. Pei, Solid State Ionics 135 (2000) 181.

[131] G.W. Zhou, H. Li, H.P. Sun, D.P. Yu, Y.Q. Wang, X.J. Huang, L.Q. Chen, Z. Zhang, Appl. Phys. Lett. 75 (1999) 2447.

[132] H. Li, L. Shi, W. Lu, X. Huang, L. Chen, J. Electrochem. Soc. 148 (2001) A915.

[133] A. Trifonova, M. Wachtler, M.R. Wagner, H. Schroettner, C. Mitterbauer, F. Hofer, K.C. Moller, M. Winter, J.O. Besenhard, Solid State Ionics 168 (2004) 51.

[134] U. Kasavajjula, C.S. Wang, A.J. Appleby J. Power Sources 163 (2007) 1003.

[135] O. Mao, R.L. Turner, I.A. Courtney, B.D. Fredericksen, M.I. Buckett, L.J. Kausee, J.R. Dahn, Electrochem. Solid-State Lett. 2 (1999) 3.

[136] F. Quan, P.J. Chupas, M.S. Whittingham, Electrochem. Solid-State Lett. 10 (2007) A274.

[137] J. Yang, Y. Takeda, N. Imanishi, O. Yamamoto, J. Electrochem. Soc. 146 (1999) 4009.

[138] K.E. Aifantis, S. Brutti, S.A. Hackney, T. Sarakonsri, B. Scrosati, Electrochim. Acta 55 (2010) 5071.

[139] J.S. Chen, Y.L. Cheah, Y.T. Chen, N. Jayaprakash, S. Madhavi, Y.H. Yang, X.W. Lou, J Phys Chem C 113 (2009) 20504.

[140] G. Du, C. Zhong, P. Zhang, Z. Guo, Z. Chen, H. Liu, Electrochim. Acta 55 (2010) 2582.

[141] M.-S. Park, S.A. Needham, G.-X. Wang, Y.-M. Kang, J.-S. Park, S.-X. Dou, H.-K. Liu, Chem. Mater. 19 (2007) 2406.

[142] C. Park, Y.U. Kim, H. Kim, H.J. Sohn, J. Power Sources 158 (2006) 1451.

[143] H.Y. Lee, S.M. Lee, Electrochem. Commun. 6 (2004) 465.

[144] J. Saint, M. Morcrette, D. Larcher, L. Laffont, S. Beattie, J.P. Peres, D. Talaga, M. Couzi, J.M. Tarascon, Adv. Funct. Mater. 17 (2007) 1765.

[145] M. Yoshio, H. Wang, K. Fukuda, T. Umeno, N. Dimov, Z. Ogumib, J. Electrochem. Soc. 149 (2002) A1598.

[146] W. Liu, Z. Guo, W. Young, D. Shieh, H. Wu, M. Yang, N. Wu, J. Power Sources 140 (2005) 139.

[147] A. Magasinski, P. Dixon, B. Hertzberg, A. Kvit, J. Ayala, G. Yushin, Nat. Mater. 9 (2010) 353.

[148] D. Chen, L. Tang, J. Li, Chem. Soc. Rev. 39 (2010) 3157.

[149] D. Choi, D. Wang, V.V. Viswanathan, I.-T. Bae, W. Wang, Z. Nie, J.-G. Zhang, G.L. Graff, J. Liu, Z. Yang, T. Duong, Electrochem. Commun. 12 (2010) 378.

[150] S.-L. Chou, J.-Z. Wang, M. Choucair, H.-K. Liu, J.A. Stride, S.-X. Dou, Electrochem. Commun. 12 (2010) 303.

[151] Y. Ding, Y. Jiang, F. Xu, J. Yin, H. Ren, Q. Zhuo, Z. Long, P. Zhang, Electrochem. Commun. 12 (2010) 10.

[152] A.K. Geim, Science 324 (2009) 1530.

[153] A.K. Geim, K.S. Novoselov, Nat. Mater. 6 (2007) 183.

[154] Z. Ji, J. Wu, X. Shen, H. Zhou, H. Xi, J Mater Sci 46 (2011) 1190.

[155] P. Lian, X. Zhu, S. Liang, Z. Li, W. Yang, H. Wang, Electrochim. Acta 55 (2010) 3909.

[156] D. Wang, D. Choi, J. Li, Z. Yang, Z. Nie, R. Kou, D. Hu, C. Wang, L.V. Saraf, J. Zhang, I.A. Aksay, J. Liu, ACS Nano 3 (2009) 907.

[157] D. Wang, R. Kou, D. Choi, Z. Yang, Z. Nie, J. Li, L.V. Saraf, D. Hu, J. Zhang, G.L. Graff, J. Liu, M.A. Pope, I.A. Aksay, ACS Nano 4 (2010) 1587.

[158] G.X. Wang, B. Wang, X.L. Wang, J. Park, S.X. Dou, H. Ahn, K. Kim, J. Mater. Chem. 19 (2009) 8378.

[159] J. Yao, X. Shen, B. Wang, H. Liu, G. Wang, Electrochem. Commun. 11 (2009) 1849.

[160] E. Yoo, J. Kim, E. Hosono, H.-s. Zhou, T. Kudo, I. Honma, Nano Lett. 8 (2008) 2277.

[161] S.-M. Paek, E. Yoo, I. Honma, Nano Lett. 9 (2009) 72.

[162] Z.P. Guo, J.Z. Wang, H.K. Liu, S.X. Dou, J. Power Sources 146 (2005) 448.

[163] L. Yuan, J. Wang, S.Y. Chew, J. Chen, Z.P. Guo, L. Zhao, K. Konstantinov, H.K. Liu, J. Power Sources 174 (2007) 1183.

[164] J.-J. Cai, P.-J. Zuo, X.-Q. Cheng, Y.-H. Xu, G.-P. Yin, Electrochem. Commun. 12 (2010) 1572.

[165] S.Y. Chew, Z.P. Guo, J.Z. Wang, J. Chen, P. Munroe, S.H. Ng, L. Zhao, H.K. Liu, Electrochem. Commun. 9 (2007) 941.

[166] X.-W. Zhang, C. Wang, A.J. Appleby , F.E. Little, J. Power Sources 109 (2002) 136.

[167] H. Li, P. Balaya, J. Maier, J. Electrochem. Soc. 151 (2004) A1878.

[168] F.G. Morin, Phys. Rev. B 93 (1954) 1199.

[169] P. Lukenheimer, A. Wide, C.R. Ottermann, K. Bange, Phys. Rev. B 44 (1991) 5927.

[170] S.W. Oh, H.J. Bang, Y.C. Bae, Y.-K. Sun, J. Power Sources 173 (2007) 502.

[171] L. Yuan, Z.P. Guo, K. Konstantinov, P. Munroe, H.K. Liu, Electrochem. Solid-State Lett. 9 (2006) A524.

[172] X.H. Huang, J.P. Tu, C.Q. Zhang, X.T. Chen, Y.F. Yuan, H.M. Wu, Electrochim. Acta 52 (2007) 4177.

[173] X.H. Huang, J.P. Tu, C.Q. Zhang, J.Y. Xiang, Electrochem. Commun. 9 (2007) 1180.

[174] M.M. Rahman, S.L. Chou, C. Zhong, J.Z. Wang, D. Wexler, H.K. Liu, Solid State Ionics 180 (2010) 1646.

[175] X.H. Huang, J.P. Tu, X.H. Xia, X.L. Wang, J.Y. Xiang, Electrochem. Commun. 10 (2008) 1288.

[176] M. Okubo, E. Hosono, J. Kim, M. Enomoto, N. Kojima, T. Kudo, H. Zhou, I. Honma, J. Am. Chem. Soc. 129 (2007) 7444.

[177] A.R. Armstrong, P.G. Bruce, Nature 381 (1996) 499.

[178] L. Croguennec, P. Deniard, R. Brec, A. Lecerf, J. Mater. Chem. 5 (1995) 1919.

[179] Q. Liu, Y. Li, Z. Hu, D. Mao, C. Chang, F. Huang, Electrochim. Acta 53 (2008) 7298.

[180] J.B. Goodenough, D.G. Wickham, W.J. Croft, J. Appl. Phys. 29 (1958) 382.

[181] S. Yamada, M. Fujiwara, M. Kanda, J. Power Sources 54 (1995) 209.

[182] Y. Nishida, K. Nakane, T. Satoh, J. Power Sources 68 (1997) 561.

[183] M. Hirayama, H. Tomita, K. Kubota, R. Kanno, J. Power Sources 196 (2011) 6809.

[184] Y. Sakurai, H. Arai, S. Okada, J.-i. Yamaki, J. Power Sources 68 (1997) 711.

[185] Y.S. Lee, S. Sato, Y.K. Sun, K. Kobayakawa, Y. Sato, Electrochem. Commun. 5 (2003) 359.

[186] K. Mizushima, P.C. Jones, P.J. Wiseman, J.B. Goodenough, Mater. Res. Bull. 15 (1980) 783.

[187] J.N. Reimers, J.R. Dahn, J. Electrochem. Soc. 139 (1992) 2091.

[188] T. Ohzuku, A. Ueda, M. Nagayama, J. Electrochem. Soc. 140 (1993) 1862.

[189] J.R. Dahn, O. von Sacken, C.A. Michal, Solid State Ionics 44 (1990) 87.

[190] W. Li, J.N. Reimer, J.R. Dahn, Phys. Rev. B 46 (1992) 3236.

[191] A. Rougier, I. Saadoune, P. Gravereau, P. Willnann, C. Delmas, Solid State Ionics 90 (1996) 83.

[192] J. Xiao, N.A. Chernova, M.S. Whittingham, Chem. Mater. 22 (2010) 1180.

[193] T. Maegawa, A. Nozaki, S. Miyashita, F. Uchikawa, in: Extended Abstract of "The 39th Battery Symposium in Japan", Sendai, Japan, 1998, pp. 319.

[194] M.M. Thackeray, Prog. Solid State Chem. 25 (1997) 1.

[195] H. Ji, G. Yang, X. Miao, A. Hong, Electrochim. Acta 55 (2010) 3392.

[196] J. Cho, Y.J. Kim, T.J. Kim, B. Park, J. Electrochem. Soc. 149 (2002) A127.

[197] J. Cho, T.J. Kim, B. Park, J. Electrochem. Soc. 149 (2002) A288.

[198] Q. Liu, D. Mao, C. Chang, F. Huang, J. Power Sources 173 (2007) 538.

[199] S.-T. Myung, S. Komaba, N. Kumagai, Electrochim. Acta 47 (2002) 3287.

[200] S. Komaba, S.-T. Myung, N. Kumagai, T. Kanouchi, K. Oikawa, T. Kamiyama, Solid State Ionics 152-153 (2002) 311.

[201] M. Wu, A. Chen, R. Xu, Y. Li, Microelectron. Eng. 66 (2003) 180.

[202] M.Q. Wu, Q.Y. Zhang, H.P. Lu, A. Chen, Solid State Ionics 169 (2004) 47.

[203] G. Wang, H. Liu, J. Liu, S. Qiao, G.M. Lu, P. Munroe, H. Ahn, Adv. Mater. 22 (2010) 4944.

[204] O. Toprakci, H.A.K. Toprakci, L. Ji, X. Zhang, KONA Powder and Particle J. 28 (2010) 50.

[205] A.S. Andersson, J.O. Thomas, J. Power Sources 97-98 (2001) 498.

[206] G.X. Wang, S. Bewlay, S.A. Needham, H.K. Liu, R.S. Liu, V.A. Drozd, J.F. Lee, J.M. Chen, J. Electrochem. Soc. 153 (2006) A25.

[207] J. Yao, K. Konstantinov, G.X. Wang, H.K. Liu, J. Solid State Electrochem. 11 (2007) 177.

[208] A.S. Andersson, B. Kalska, L. Haggstrom, J.O. Thomas, Solid State Ionics 130 (2000) 41.

[209] B. Jin, E.M. Jin, K.H. Park, H.B. Gu, Electrochem. Commun. 10 (2008) 1537.

[210] Y. Wang, Y. Wang, E. Hosono, K. Wang, H. Zhou, Angew. Chem. Int. Ed. 47 (2008) 7461.

[211] Y.-H. Huang, J.B. Goodenough, Chem. Mater. 20 (2008).

[212] J.-Z. Wang, S.-L. Chou, J. Chen, S.-Y. Chew, G.-X. Wang, K. Konstantinov, J. Wu, S.-X. Dou, H.K. Liu, Electrochem. Commun. 10 (2008) 1781.

[213] B.L. Ellis, W.R.M. Makahnouk, Y. Makimura, K. Toghill, L.F. Nazar, Nat. Mater. 6 (2007) 749.

[214] N. Recham, J.N. Chotard, L. Dupont, C. Delacourt, W. Walker, M. Armand, J.M. Tarascon, Nat. Mater. 9 (2010) 68.

[215] M.E. Arroyo-deDompablo, R. Dominko, J.M. Gallardo-Amores, L. Dupont, G. Mali, H. Ehrenberg, J. Jamnik, E. Morán, Chem. Mater. 20 (2008) 5574.

[216] B.L. Ellis, W.R.M. Makahnouk, W.N.R. Weetaluktuk, D.H. Ryan, L.F. Nazar, Chem. Mater. 22 (2010) 1059.

[217] J. Desilvestro, O. Haas, J. Electrochem. Soc. 137 (1990) C5.

[218] K. Nassau, D.W. Murphy, Journal of Non-Crystalline Solids 44 (1981) 297.

[219] G. Pistoia, S. Panero, M. Tocci, R.V. Moshtev, V. Manev, Solid State Ionics 13 (1984) 311.

[220] G. Pistola, M. Pasquali, M. Tocci, V. Manev, R.V. Moshtev, J. Power Sources 15 (1985) 13.

[221] K. West, B. Zachau-Christiansen, S. Skaarup, Y. Saidi, J. Barker, I.I. Olsen, R. Pynenburg, R. Koksbang, J. Electrochem. Soc. 143 (1996) 820.

[222] H.Y. Xu, H. Wang, Z.Q. Song, Y.W. Wang, H. Yan, M. Yoshimura, Electrochimica Acta 49 (2004) 349.

[223] H. Liu, Y. Wang, K. Wang, Y. Wang, H. Zhou, Journal of Power Sources 192 (2009) 668.

[224] X. Li, P. Li, M. Luo, X. Chen, J. Chen, J. Solid State Electrochem. 14 (2010) 1325.

[225] Y. Gu, D. Chen, X. Jiao, F. Liu, J. Mater. Chem. 16 (2006) 4361.

[226] C.J. Cui, G.M. Wu, J. Shen, B. Zhou, Z.H. Zhang, H.Y. Yang, S.F. She, Electrochim. Acta 55 (2010) 2536.

[227] A.S. Arico, P. Bruce, B. Scrosati, J.M. Tarascon, W. van Schalkwijk, Nat. Mater. 4 (2005) 366.

[228] K. Aso, H. Kitaura, A. Hayashi, M. Tatsumisago, J. Mater. Chem. 21 (2011) 2987.

[229] S.C. Han, H.S. Kim, M.S. Song, J.H. Kim, H.J. Ahn, J.Y. Lee, J. Alloys Compd. 351 (2003) 273.

[230] S.C. Han, K.W. Kim, H.J. Ahn, J.H. Ahn, J.Y. Lee, J. Alloys Compd. 361 (2003) 247.

[231] D. Golodnitsky, E. Peled, Electrochim. Acta 45 (1999) 335.

[232] R. Fong, J.R. Dahn, C.H.W. Jones, J. Electrochem. Soc. 136 (1989) 3206.

[233] A. Débart, L. Dupont, R. Patrice, J.M. Tarascon, Solid State Sci. 8 (2006) 640.

[234] T. Matsumura, K. Nakano, R. Kanno, A. Hirano, N. Imanishi, Y. Takeda, J. Power Sources 174 (2007) 632.

[235] J. Wang, S.Y. Chew, D. Wexler, G.X. Wang, S.H. Ng, S. Zhong, H.K. Liu, Electrochem. Commun. 9 (2007) 1877.

[236] T. Takeuchi, H. Sakaebe, H. Kageyama, K. Handa, T. Sakai, K. Tatsumi, J. Electrochem. Soc. 156 (2009) A958.

[237] J.-W. Choi, G. Cheruvally, H.-J. Ahn, K.-W. Kim, J.-H. Ahn, J. Power Sources 163 (2006) 158.

[238] J.S. Chung, H.J. Sohn, J. Power Sources 108 (2002) 226.

[239] G. Kullerud, R.A. Yund, J. Petrol. 3 (1962) 126.

[240] B.T. Zhu, Z. Wang, S. Ding, J.S. Chen, X.W. Lou, RSC Adv. 1 (2011) 397.

[241] W. Wang, S.Y. Wang, Y.L. Gao, K.Y. Wang, M. Liu, Mater. Sci. Eng. B 133 (2006) 167.

[242] J.R. Chetia, A. Dutta, N.N. Dass, Characterization and conductivity study of poly(2-dimethylamino ethylmethacrylate) and its hydrochloride salt in solid state, in: B.V.R. Chowdari (Ed.) Solid State Ionics: Trends in the New Millennium, World Scientific, Singapore, 2002, pp. 345.

[243] M.B. Armand, J.M. Chabagno, M. Duclot, Poly-ethers as solid electrolytes, in: P. Vashitshta, J.N. Mundy, G.K. Shenoy (Eds.) Fast Ion Transport in Solids, Elsevier, Amsterdam, 1979, pp. 131.

[244] M. Jaipal Reddy, S. Sreepathi Rao, E. Laxminarsaiah, U.V. Subba Rao, J. Mater. Sci. Lett. 14 (1995) 1129.

[245] Y. Ito, K. Syakushiro, M. Hiratani, K. Miyauchi, T. Kudo, Solid State Ionics 18-19 (1986) 277.

[246] Z. Ogumi, Y. Uchimoto, Z. Takehara, J. Electrochem. Soc. 136 (1989) 625.

[247] A. Kumar, M. Deka, Nanofiber Reinforced Composite Polymer Electrolyte Membranes, in: A. Kumar (Ed.) Nanofibers, INTECH, Croatia, 2010, pp. 438.

[248] R.C. Agrawal, G.P. Pandey, J. Phys. D: Appl. Phys. 41 (2008) 223001.

[249] I.S. Elashmawi, N.A. Hakeem, Polym. Eng. Sci. 48 (2008) 895.

[250] A.M.M. Ali, M.Z.A. Yahya, H. Bahron, R.H.Y. Subban, M.K. Harun, I. Atan, Mater. Lett. 61 (2007) 2026.

[251] Y.-J. Wang, D. Kim, Electrochim. Acta 52 (2007) 3181.

[252] M. Nookala, B. Kumar, S. Rodrigues, J. Power Sources 111 (2002) 165.

[253] Z.-Y. Cui, Y.-Y. Xu, L.-P. Zhu, J.-Y. Wang, Z.-Y. Xi, B.-K. Zhu, J. Membr. Sci. 325 (2008) 957.

[254] Y. Wang, X. Ma, Q. Zhang, N. Tian, J. Membr. Sci. 349 (2010) 279.

[255] K.H. Lee, J.K. Park, W.J. Kim, Electrochim. Acta 45 (2000) 1301.

[256] B. Scrosati, F. Croce, L. Persi, J. Electrochem. Soc. 147 (2000) 1718.

[257] K.M. Kim, K.S. Ryu, S.G. Kang, S.H. Chang, I.J. Chung, Macromol. Chem. Phys. 202 (2001) 866.

[258] K.M. Kim, N.-G. Park, K.S. Ryu, S.H. Chang, Polymer 43 (2002) 3951.

[259] M. Watanabe, M. Itoh, K. Sanui, N. Ogata, Macromolecules 20 (1987) 569.

[260] M. Mucha, React. Funct. Polym. 38 (1998) 19.

[261] J.A. Galloway, K.J. Koester, B.J. Paasch, C.W. Macosko, Polymer 45 (2004) 423.

[262] P.A.R.D. Jayathilaka, M.A.K.L. Dissanayake, I. Albinsson, B.E. Mellander, Solid State Ionics 156 (2003) 179.

[263] A. Martinelli, M.A. Navarra, A. Matic, S. Panero, P. Jacobsson, L. Börjesson, B. Scrosati, Electrochim. Acta 50 (2005) 3992.

[264] S. Ramesh, A.K. Arof, J. Power Sources 99 (2001) 41.

[265] N.-S. Choi, J.-K. Park, Electrochim. Acta 46 (2001) 1453.

[266] G. Girish Kumar, S. Sampath, Solid State Ionics 176 (2005) 773.

[267] S. Ahmad, S. Ahmad, S.A. Agnihotry, J. Power Sources 140 (2005) 151.

[268] H.S. Kim, P. Periasamy, S.I. Moon, J. Power Sources 141 (2005) 293.

[269] D. Saikia, A. Kumar, Eur. Polym. J. 41 (2005) 563.

[270] D.E. Fenton, J.M. Parker, P.V. Wright, Polymer 14 (1973) 589.

[271] P.V. Wright, British Polym. J. 7 (1975) 319.

[272] M. Kovac, M. Gaberscek, J. Grdadolnik, Electrochim. Acta 44 (1998) 863.

[273] M. Marzantowicz, J.R. Dygas, F. Krok, A. Molenda, E. Zygadao-Monikowska, Z. Florjanczyk, Mol. Phys. Rep. 35 (2001) 65.

[274] Z. Li, J. Wei, F. Shan, J. Yang, X. Wang, J. Polym. Sci., Part B: Polym. Phys. 46 (2008) 751.

[275] H.S. Choe, J. Giaccami, M. Alamgir, K.M. Abraham, Electrochim. Acta 40 (1995) 2289.

[276] M. Watanabe, M. Kanba, K. Nagaoka, I. Shinohara, E. Tsuchida, K. Tsunemi, Makromol. Chem. Rapid Commun. 2 (1981) 741.

[277] C.-Y. Chiang, Y.J. Shen, M. Jaipal Reddy, P.P. Chu, J. Power Sources 123 (2003) 222.

[278] T. Iijima, Y. Toyoguchi, N. Eda, Denki Kagaku 53 (1985) 619.

[279] O. Bohnke, C. Rousselot, P.A. Gillet, C. Truche, J. Electrochem. Soc. 139 (1992) 1862.

[280] E. Tsuchida, H. Ohno, K. Tsunemi, N. Kobayashi, Solid State Ionics 11 (1983) 227.

[281] D.J. Bannister, G.P. Davies, I.M. Ward, J.E. McIntyre, Polymer 25 (1984) 1291.

[282] F.M. Gray, J.R. MacCallum, C.A. Vincent, Solid State Ionics 18-19 (1986) 282.

[283] Z. Florjanczyk, E. Zygadlo, K. Such, D. Raducha, W. Wieczorek, Electrochim. Acta 37 (1992) 1555.

[284] W. Wieczorek, K. Such, S.H. Chung, J.R. Stevens, J. Phys. Chem. 98 (1994) 9047.

[285] Z.H. Li, P. Zhang, H.P. Zhang, Y.P. Wu, X.D. Zhou, Electrochem. Commun. 10 (2008) 791.

[286] J. Xi, X. Qiu, J. Li, X. Tang, W. Zhu, L. Chen, J. Power Sources 157 (2006) 501.

[287] B. Oh, Y.R. Kim, Solid State Ionics 124 (1999) 83.

[288] T.A. Walker, Y.B. Melnichenko, G.D. Wignall, J.S. Lin, R.J. Spontak, Macromol. Chem. Phys. 204 (2003) 2064.

[289] B.R. Hahn, O. Hermann-Schonherr, J.H. Wendorff, Polymer 28 (1987) 201.

[290] W. Ma, J. Zhang, X. Wang, S. Wang, Appl. Surf. Sci. 253 (2007) 8377.

[291] R. Gregorio, Jr., M.J. Cestari, J. Polym. Sci. 32 (1994) 859.

[292] R. Gedye, F. Smith, K. Westaway, A. Humera, L. Baldisera, L. Laberge, L. Rousell, Tetrahedron Lett. 27 (1986) 279.

[293] P.L. Taberna, S. Mitra, P. Poizot, P. Simon, J.M. Tarascon, Nat. Mater. 5 (2006) 567.

[294] B. Varghese, M.V. Reddy, Z. Yanwu, C.S. Lit, T.C. Hoong, G.V. Subba Rao, B.V.R. Chowdari, A.T.S. Wee, C.T. Lim, C.-H. Sow, Chem. Mater. 20 (2008) 3360.

[295] G.X. Wang, Y. Chen, K. Konstantinov, M. Lindsay, H.K. Liu, S.X. Dou, J. Power Sources 109 (2002) 142.

[296] S.-L. Chou, J.-Z. Wang, H.-K. Liu, S.-X. Dou, J. Electrochem. Soc. 155 (2008) A926.

[297] W.-M. Zhang, X.-L. Wu, J.-S. Hu, Y.-G. Guo, L.-J. Wan, Adv. Funct. Mater. 18 (2008) 3941.

[298] H. Qiao, L. Xiao, Z. Zheng, H. Liu, F. Jia, L. Zhang, J. Power Sources 185 (2008) 486.

[299] I.A. Courtney, W.R. McKinnon, J.R. Dahn, J. Electrochem. Soc. 146 (1999) 59.

[300] J. Wang, J. Chen, K. Konstantinov, L. Zhao, S.H. Ng, G.X. Wang, Z.P. Guo, H.K. Liu, Electrochim. Acta 51 (2006) 4634.

[301] A.D. Pasquier, F. Orsini, A.S. Gozdz, J.M. Tarascon, J. Power Sources 81-82 (1999) 607.

[302] C. Zhong, J.-Z. Wang, S.-L. Chou, K. Konstantinov, M. Rahman, H.-K. Liu, J. Appl. Electrochem. 40 (2010) 1415.

[303] Y.-C. Liu, B.-J. Hwang, W.-J. Jian, R. Santhanam, Thin Solid Films 374 (2000) 85.

[304] K. Nishio, M. Fujimoto, O. Ando, H. Ono, T. Murayama, J. Appl. Electrochem. 26 (1996) 425.

[305] X.H. Huang, J.P. Tu, X.H. Xia, X.L. Wang, J.Y. Xiang, L. Zhang, Y. Zhou, J. Power Sources 188 (2009) 588.

[306] S. Grugeon, S. Laruelle, R. Herrera-Urbina, L. Dupont, P. Poizot, J.M. Tarascon, J. Electrochem. Soc. 148 (2001) A285.

[307] B. Veeraraghavan, J. Paul, B. Haran, B. Popov, J. Power Sources 109 (2002) 377.

[308] S.H. Ng, J. Wang, K. Konstantinov, D. Wexler, J. Chen, H.K. Liu, J. Electrochem. Soc. 153 (2006) A787.

[309] J. Fan, P.S. Fedkiw, J. Power Sources 72 (1998) 165.

[310] C. Liu, F. Li, L.-P. Ma, H.-M. Cheng, Adv. Mater. 22 (2010) E28.

[311] Y.-G. Guo, J.-S. Hu, L.-J. Wan, Adv. Mater. 20 (2008) 2878.

[312] C. Berger, Z.M. Song, X.B. Li, X.S. Wu, N. Brown, C. Naud, D. Mayou, T.B. Li, J. Hass, A.N. Marchenkov, E.H. Conrad, P.N. First, W.A. de Heer, Science 312 (2006) 1191.

[313] X.L. Li, X.R. Wang, L. Zhang, S.W. Lee, H.J. Dai, Science 319 (2008) 1229.

[314] D. Pan, S. Wang, B. Zhao, M. Wu, H. Zhang, Y. Wang, Z. Jiao, Chem. Mater. 21 (2009) 3136.

[315] F. Ji, Y.-L. Li, J.-M. Feng, D. Su, Y.-Y. Wen, Y. Feng, F. Hou, J. Mater. Chem. 19 (2009) 9063.

[316] Z.-S. Wu, W. Ren, L. Wen, L. Gao, J. Zhao, Z. Chen, G. Zhou, F. Li, H.-M. Cheng, ACS Nano 4 (2010) 3187.

[317] C. Xu, X. Wang, L. Yang, Y. Wu, J. Solid State Chem. 182 (2009) 2486.

[318] Y.J. Mai, X.L. Wang, J.Y. Xiang, Y.Q. Qiao, D. Zhang, C.D. Gu, J.P. Tu, Electrochim. Acta 56 (2011) 2306.

[319] W.S. Hummers, R.E. Offeman, J. Am. Chem. Soc. 80 (1958) 1339.

[320] C. Nethravathi, M. Rajamathi, Carbon 46 (2008) 1994.

[321] S. Wang, S.P. Jiang, X. Wang, Electrochim. Acta 56 (2011) 3338.

[322] R.J. Lagow, R.B. Badachhape, J.L. Wood, J.L. Margrave, J. Chem. Soc., Dalton Trans. (1974) 1268.

[323] N.I. Kovtyukhova, P.J. Ollivier, B.R. Martin, T.E. Mallouk, S.A. Chizhik, E.V. Buzaneva, A.D. Gorchinskiy, Chem. Mater. 11 (1999) 771.

[324] A.C. Ferrari, J. Robertson, Phys. Rev. B 61 (2000) 14095.

[325] O. Akhavan, Carbon 48 (2010) 509.

[326] T.-L. Lai, Y.-L. Lai, J.-W. Yu, Y.-Y. Shu, C.-B. Wang, Mater. Res. Bull. 44 (2009) 2040.

[327] F. Portemer, A. Delahaye-Vidal, M. Figlarz, J. Electrochem. Soc. 139 (1992) 671.

[328] P. Jeevanandam, Y. Koltypin, A. Gedanken, Nano Lett. 1 (2001) 263.

[329] Y. Li, X. Xie, J. Liu, M. Cai, J. Rogers, W. Shen, Chem. Eng. J. 136 (2008) 398.

[330] H.O. Pierson, Handbook of Carbon, Graphite, Diamond and Fullerenes - Properties, Processing and Applications, William Andrew Publishing/Noyes, 1993.

[331] X. Wang, S.M. Tabakman, H. Dai, J. Am. Chem. Soc. 130 (2008) 8152.

[332] D. Aurbach, J. Power Sources 89 (2000) 206.

[333] M.Y. Cheng, B.J. Hwang, J. Power Sources 195 (2010) 4977.

[334] X.H. Huang, J.P. Tu, B. Zhang, C.Q. Zhang, Y. Li, Y.F. Yuan, H.M. Wu, J. Power Sources 161 (2006) 541.

[335] B. Kang, G. Ceder, Nature 458 (2009) 190.

[336] I.R.M. Kottegoda, Y. Kadoma, H. Ikuta, Y. Uchimoto, M. Wakihara, Electrochem. Solid-State Lett. 5 (2002) A275.

[337] I.R.M. Kottegoda, Y. Kadoma, H. Ikuta, Y. Uchimoto, M. Wakihara, J. Electrochem. Soc. 152 (2005) A1595.

[338] K.J. Takeuchi, A.C. Marschilok, S.M. Davis, R.A. Leising, E.S. Takeuchi, Coord. Chem. Rev. 219-221 (2001) 283.

[339] S.L. Chou, J.Z. Wang, J.Z. Sun, D. Wexler, M. Forsyth, H.K. Liu, D.R. MacFarlane, S.X. Dou, Chem. Mater. 20 (2008) 7044.

[340] X. Liu, J. Wang, J. Zhang, S. Yang, J Mater Sci 42 (2007) 867.

[341] G.Q. Liu, C.L. Zeng, K. Yang, Electrochim. Acta 47 (2002) 3239.

[342] Q. Liu, H. Liu, X. Zhou, C. Cong, K. Zhang, Solid State Ionics 176 (2005) 1549.

[343] S. Panero, M. Pasquali, G. Pistoia, J. Electrochem. Soc. 130 (1983) 1225.

[344] S.Y. Chew, C. Feng, S.H. Ng, J. Wang, Z. Guo, H. Liu, J. Electrochem. Soc. 154 (2007) A633.

[345] G. Pistoia, M. Pasquali, G. Wang, L. Li, J. Electrochem. Soc. 137 (1990) 2365.

[346] M. Pasquali, G. Pistoia, Electrochim. Acta 36 (1991) 1549.

[347] G. Pistoia, G. Wang, D. Zane, Solid State Ionics 76 (1995) 285.

[348] X. Li, P. Li, M. Luo, X. Chen, J. Chen, J Solid State Electrochem 14 1325.

[349] X. Lou, D. Deng, J. Lee, J. Feng, L. Archer, Adv. Mater. 20 (2008) 258.

[350] K.M. Shaju, F. Jiao, A. Debart, P.G. Bruce, Phys. Chem. Chem. Phys. 9 (2007) 1837.

[351] Z.R. Chang, H.J. Lv, H.W. Tang, H.J. Li, X.Z. Yuan, H. Wang, Electrochim. Acta 54 (2009) 4595.

[352] H.S. Kim, M. Kong, K. Kim, I.-J. Kim, H.-B. Gu, J. Power Sources 171 (2007) 917.

[353] X.H. Rui, C. Li, C.H. Chen, Electrochim. Acta 54 (2009) 3374.

[354] X. Li, F. Kang, W. Shen, Electrochem. Solid-State Lett. 9 (2006) A126.

[355] M.M. Rahman, J.Z. Wang, N.H. Idris, Z. Chen, H. Liu, Electrochim. Acta 56 (2010) 693.

[356] L. Wang, Y. Huang, R. Jiang, D. Jia, J. Electrochem. Soc. 154 (2007) A1015.

[357] X.M. Liu, Z.D. Huang, S. Oh, P.-C. Ma, P.C.H. Chan, G.K. Vedam, K. Kang, J.-K. Kim, J. Power Sources 195 (2010) 4290.

[358] D.W. Wang, F. Li, Z.S. Wu, W. Ren, H.M. Cheng, Electrochem. Commun. 11 (2009) 1729.

[359] Y. Wang, Z. Shi, Y. Huang, Y. Ma, C. Wang, M. Chen, Y. Chen, J Phys Chem C 113 (2009) 13103.

[360] F. Leroux, B.E. Koene, L.F. Nazar, J. Electrochem. Soc. 143 (1996) L181.

[361] E. Perez-Cappe, Y. Mosqueda, R. Martinez, C.R. Milian, O. Sanchez, J.A. Varela, A. Hortencia, E. Souza, P. Aranda, E. Ruiz-Hitzky, J. Mater. Chem. 18 (2008) 3965.

[362] C. Li, E.T. Thostenson, T.W. Chou, Compos. Sci. Technol. 68 (2008) 1445.

[363] W. Zheng, S.C. Wong, Compos. Sci. Technol. 63 (2003) 225.

[364] D. Im, A. Manthiram, Solid State Ionics 159 (2003) 249.

[365] H. Takahara, T. Takeuchi, M. Tabuchi, H. Kageyama, Y. Kobayashi, Y. Kurisu, S. Kondo, R. Kanno, J. Electrochem. Soc. 151 (2004) A1539.

[366] N. Ravet, Y. Chouinard, J.F. Magnan, S. Besner, M. Gauthier, M. Armand, J. Power Sources 97-98 (2001) 503.

[367] A. Guerfi, M. Kaneko, M. Petitclerc, M. Mori, K. Zaghib, J. Power Sources 163 (2007) 1047.

[368] M.M. Rahman, S.-L. Chou, C. Zhong, J.-Z. Wang, D. Wexler, H.-K. Liu, Solid State Ionics 180 1646.

[369] J. Li, R.B. Lewis, J.R. Dahn, Electrochem. Solid-State Lett. 10 (2007) A17.

[370] H. Joachin, T.D. Kaun, K. Zaghib, J. Prakash, J. Electrochem. Soc. 156 (2009) A401.

[371] T.J. Patey, R. Büchel, S.H. Ng, F. Krumeich, S.E. Pratsinis, P. Novák, J. Power Sources 189 (2009) 149.

[372] A. Sakunthala, M. Reddy, S. Selvasekarapandian, B. Chowdari, H. Nithya, P. Chirstopher Selvin, J. Solid State Electrochem. 14 (2009) 1847.

[373] Y. Liu, X. Zhou, Y. Guo, Electrochim. Acta 54 (2009) 3184.

[374] L.J. Fu, H. Liu, C. Li, Y.P. Wu, E. Rahm, R. Holze, H.Q. Wu, Prog. Mater Sci. 50 (2005) 881.

[375] D. Liu, G. Cao, Energy Environ. Sci. 3 (2010) 1218.

[376] B. Scrosati, J. Garche, J. Power Sources 195 (2010) 2419.

[377] G. Amatucci, J.M. Tarascon, J. Electrochem. Soc. 149 (2002) K31.

[378] Y.M. Choi, S.I. Pyun, J.S. Bae, S.I. Moon, J. Power Sources 56 (1995) 25.

[379] I. Taniguchi, C.K. Lim, D. Song, M. Wakihara, Solid State Ionics 146 (2002) 239.

[380] D. Belov, M.H. Yang, Solid State Ionics 179 (2008) 1816.

[381] D. Belov, M.H. Yang, J. Solid State Electrochem. 12 (2008) 885.

[382] C.H. Doh, D.H. Kim, H.S. Kim, H.M. Shin, Y.D. Jeong, S.I. Moon, B.S. Jin, S.W. Eom, H.S. Kim, K.W. Kim, D.H. Oh, A. Veluchamy, J. Power Sources 175 (2008) 881.

[383] A. Yamada, S.C. Chung, K. Hinokuma, J. Electrochem. Soc. 148 (2001) A224.

[384] T. Amriou, B. Khelifa, H. Aourag, S.M. Aouadi, C. Mathieu, Mater. Chem. Phys. 92 (2005) 499.

[385] H. Liu, Y. Yang, J. Zhang, J. Power Sources 173 (2007) 556.

[386] A. Rougier, P. Gravereau, C. Delmas, J. Electrochem. Soc. 143 (1996) 1168.

[387] D. Marmorstein, T.H. Yu, K.A. Striebel, F.R. McLarnon, J. Hou, E.J. Cairns, J. Power Sources 89 (2000) 219.

[388] E. Peled, D. Golodnitsky, E. Strauss, J. Lang, Y. Lavi, Electrochim. Acta 43 (1998) 1593.

[389] X. Yu, J. Xie, J. Yang, K. Wang, J. Power Sources 132 (2004) 181.

[390] L.A. Montoro, J.M. Rosolen, J.H. Shin, S. Passerini, Electrochim. Acta 49 (2004) 3419.

[391] J. Wang, S.Y. Chew, Z.W. Zhao, S. Ashraf, D. Wexler, J. Chen, S.H. Ng, S.L. Chou, H.K. Liu, Carbon 46 (2008) 229.

[392] J.Z. Wang, S.L. Chou, S.Y. Chew, J.Z. Sun, M. Forsyth, D.R. MacFarlane, H.K. Liu, Solid State Ionics 179 (2008) 2379.

[393] Y. Nishio, H. Kitaura, A. Hayashi, M. Tatsumisago, J. Power Sources 189 (2009) 629.

[394] A.V. Murugan, T. Muraliganth, A. Manthiram, J. Electrochem. Soc. 156 (2009) A79.

[395] A.V. Murugan, T. Muraliganth, A. Manthiram, J Phys Chem C 112 (2008) 14665.

[396] P. Ragupathy, H.N. Vasan, N. Munichandraiah, Mater. Chem. Phys. 124 (2010) 870.

[397] A.V. Murugan, T. Muraliganth, A. Manthiram, Electrochem. Commun. 10 (2008) 903.

[398] A.V. Murugan, T. Muraliganth, P.J. Ferreira, A. Manthiram, Inorg. Chem. 48 (2009) 946.

[399] M.M. Rahman, J.Z. Wang, M.F. Hassan, D. Wexler, H.K. Liu, Adv. Energy Mater. 1 (2011) 212.

[400] J. Jamnik, J. Maier, Phys. Chem. Chem. Phys. 5 (2003) 5215.

[401] L.Y. Beaulieu, D. Larcher, R.A. Dunlap, J.R. Dahn, J. Electrochem. Soc. 147 (2000) 3206.

[402] M.M. Rahman, J.Z. Wang, M.F. Hassan, S. Chou, D. Wexler, H.K. Liu, J. Power Sources 195 (2010) 4297.

[403] E. Kim, D. Son, T.-G. Kim, J. Cho, B. Park, K.-S. Ryu, S.-H. Chang, Angew. Chem. Int. Ed. 43 (2004) 5987.

[404] X. Liu, Mater. Sci. Eng. B 119 (2005) 19.

[405] H. Li, L. Chai, X. Wang, X. Wu, G. Xi, Y. Liu, Y. Qian, Crystal Growth & Design 7 (2007) 1918.

[406] G. Yang, G. Wang, W. Hou, J. Phys. Chem. B 109 (2005) 11186.

[407] V. Sreeja, P.A. Joy, Mater. Res. Bull. 42 (2007) 1570.

[408] A. Putnis, Am. Mineral. 61 (1976) 322.

[409] S.N. Black, D.A. Jefferson, P. Henderson, J. Solid State Chem. 53 (1984) 76.

[410] M.M. Rahman, J.Z. Wang, M.F. Hassan, S. Chou, Z. Chen, H.K. Liu, Energy Environ. Sci. 4 (2011) 952.

[411] A. Manuel Stephan, Eur. Polym. J. 42 (2006) 21.

[412] H.P. Zhang, P. Zhang, Z.H. Li, M. Sun, Y.P. Wu, H.Q. Wu, Electrochem. Commun. 9 (2007) 1700.

[413] Y.P. Wu, H.P. Zhang, F. Wu, Z.H. Li, Polymer Lithium-Ion Batteries, Chemical Industry Press, Beijing, 2007.

[414] B. Scrosati, Applications of Electroactive Polymers, Chapman Hall, London, 1993.

[415] F.M. Gray, Polymer Electrolytes, The Royal Society of Chemistry, Cambridge, 1997.

[416] J.R. MacCallum, Polymer Electrolytes Reviews-I, Elsevier, London, 1987.

[417] J.R. MacCallum, Polymer Electrolytes Reviews-II, Elsevier, London, 1987.

[418] X.J. Wang, J.J. Kang, Y.P. Wu, S.B. Fang, Electrochem. Commun. 5 (2003) 1025.

[419] L.-Z. Fan, J. Maier, Electrochem. Commun. 8 (2006) 1753.

[420] F. Croce, L. Settimi, B. Scrosati, Electrochem. Commun. 8 (2006) 364.

[421] J.J. Xu, H. Ye, Electrochem. Commun. 7 (2005) 829.

[422] M. Oliver, US Patent 5658685 (1997).

[423] G. Li, Z. Li, P. Zhang, H. Zhang, Y. Wu, Pure Appl. Chem. 80 (2008) 2553.

[424] Q. Shi, M. Yu, X. Zhou, Y. Yan, C. Wan, J. Power Sources 103 (2002) 286.

[425] R.E. Kesting, in: D.R. Lloyd (Ed.) Materials Science of Synthetic Membrane, ACS Symposium Series No. 269, American Chemical Society, Washington, D.C, 1985, pp. 131.

[426] X.X. Zhu, K. Banana, H.Y. Liu, M. Krause, M. Yang, Macromolecules 32 (1999) 277.

[427] A. Subramania, N.T. Kalyana Sundaram, A.R. Sathiya Priya, G. Vijaya Kumar, J. Membr. Sci. 294 (2007) 8.

[428] J.M. Tarascon, A.S. Gozdz, C. Schmutz, F. Shokoohi, P.C. Warren, Solid State Ionics 86-88 (1996) 49.

[429] G.C. Li, P. Zhang, H.P. Zhang, L.C. Yang, Y.P. Wu, Electrochem. Commun. 10 (2008) 1883.

[430] Z. Li, G. Su, X. Wang, D. Gao, Solid State Ionics 176 (2005) 1903.

[431] J.Y. Song, Y.Y. Wang, C.C. Wan, J. Power Sources 77 (1999) 183.

[432] A. Du Pasquier, P.C. Warren, D. Culver, A.S. Gozdz, G.G. Amatucci, J.M. Tarascon, Solid State Ionics 135 (2000) 249.

[433] Y. Saito, A.M. Stephan, H. Kataoka, Solid State Ionics 160 (2003) 149.

[434] S. Rajabzadeh, T. Maruyama, Y. Ohmukai, T. Sotani, H. Matsuyama, Sep. Purif. Technol. 66 (2009) 76.

[435] J.-H. Cao, B.-K. Zhu, Y.-Y. Xu, J. Membr. Sci. 281 (2006) 446.

[436] J. R. Gregorio, N.C.P.d.S. Nociti, J. Phys. D: Appl. Phys. 28 (1995) 432.

[437] Y. Saito, H. Kataoka, E. Quartarone, P. Mustarelli, J. Phys. Chem. B 106 (2002) 7200.

[438] Z. Li, G. Su, D. Gao, X. Wang, X. Li, Electrochim. Acta 49 (2004) 4633.

[439] V. Gentili, S. Panero, P. Reale, B. Scrosati, J. Power Sources 170 (2007) 185.

[440] Q. Hu, S. Osswald, R. Daniel, Y. Zhu, S. Wesel, L. Ortiz, D.R. Sadoway, J. Power Sources 196 (2011) 5604.

[441] E. Peled, D. Golodnitsky, G. Ardel, J. Electrochem. Soc. 144 (1997) L208.

[442] P. Zhang, H.P. Zhang, G.C. Li, Z.H. Li, Y.P. Wu, Electrochem. Commun. 10 (2008) 1052.

Acronyms

AFM:	Atomic force microscopy
ATR-FTIR:	Attenuated total reflectance-Fourier transform infrared
BET:	Brunauer-Emmett-Teller
BSE:	Back-scattered electrons
CNTs:	Carbon nanotubes
CPE:	Constant phase element
CPEs:	Composite polymer electrolytes
CV:	Cyclic voltammetry
DBP:	Dibutyl phthalate
DMC:	Dimethyl carbonate
DSC:	Differential scanning calorimetry
EC:	Ethylene carbonate
EDS:	Energy dispersive spectroscopy
EIS:	Electrochemical impedance spectroscopy
emf:	Electromotive forces
FESEM:	Field-emission scanning electron microscopy
GNS:	Graphene nanosheet
GPE:	Gel polymer electrolytes
IR:	Infrared
LiTFSI:	Lithium bis(trifluoromethylsulfonyl)imide
LSV:	Linear sweep voltammetry
MWCNTs:	Multi-walled carbon nanotubes
PAN:	Poly (acrylonitrile)

PANI:	Polyaniline
PC:	Propylene carbonate
PEG:	Poly (ethylene glycol)
PEO:	Poly(ethylene oxide)
PMMA:	Poly(methyl methacrylate)
PPy:	Polypyrrole
PTC:	Positive temperature coefficient
PTh:	Polythiophene
PVC:	Poly (vinyl chloride)
PVDF:	Poly(vinylidene fluoride)
RTILs:	Room-temperature ionic liquids
SAED:	Selected area electron diffraction
SEI:	Solid-electrolyte interphase
SEM:	Scanning electron microscopy
SPE:	Solid polymer electrolytes
TEGDME:	Tetra(ethylene glycol) dimethyl ether
TEM:	Transmission electron microscopy
TGA:	Thermogravimetric analysis
XRD:	X-ray diffraction

Publications during PhD study

Nurul Hayati Idris, M.M. Rahman, Jia-Zhao Wang, Zhi-Xin Chen and Hua-Kun Liu. *Synthesis and electrochemical performance of LiV_3O_8/carbon nanosheet composite as cathode material for lithium-ion batteries*. Composites Science and Technology 71 (2011) 343-349. (I.F. 2.856).

Nurul H. Idris, Jiazhao Wang, Shulei Chou, Chao Zhong, Md. Mokhlesur Rahman and Huakun Liu. *Effects of polypyrrole on the performance of nickel oxide anode materials for rechargeable lithium-ion batteries*, Journal of Materials Research 26 (2011) 860-866. (I.F. 1.395).

Nurul Hayati Idris, Md Mokhlesur Rahman, Shu-Lei Chou, Jia-Zhao Wang and Hua-Kun Liu. *Rapid synthesis of binary α-NiS-β-NiS by microwave autoclave for rechargeable lithium-ion batteries*, Electrochimica Acta 58 (2011) 456-462. (I.F. 3.642).

Nurul Hayati Idris, Md. Mokhlesur Rahman, Jia-Zhao Wang and Hua-Kun Liu. *Microporous gel polymer electrolytes for lithium rechargeable batteries*, Journal of Power Sources 201 (2011) 294-300. (I.F. 4.283).

Iresha R.M. Kottegoda, **Nurul Hayati Idris**, Lin Lu, Jia-Zhao Wang and Hua-Kun Liu. *Synthesis and characterization of graphene-nickel oxide nanostructures for fast charge-discharge application*, Electrochimica Acta 56 (2011) 5815-5822. (I.F. 3.642).

M.M. Rahman, Jia-Zhao Wang, **Nurul Hayati Idris**, Zhixin Chen and Huakun Liu. *Enhanced lithium storage in a VO_2(B)-multiwall carbon nanotube microsheet composite prepared via an in situ hydrothermal process*, Electrochimica Acta 56 (2010) 693-699. (I.F. 3.642).

Jia-Zhao Wang, Chao Zhong, David Wexler, **Nurul Hayati Idris**, Zhao-Xiang Wang, Li-Quan Chen and Hua-Kun Liu. *Graphene-encapsulated Fe_3O_4 nanoparticles with 3D laminated structure as superior anode in lithium ion batteries*, Chemistry-A European Journal 7 (2011) 661-667. (I.F. 5.476).